# MID-IR OBSERVATIONS AND MODELING OF ASTROPHYSICAL DUST

## AGB CIRCUMSTELLAR ENVELOPES AND ICM DUST

Thesis submitted for the degree of
“Doctor Philosophiæ”

CANDIDATE
Massimo Marengo

SUPERVISORS
Professor D.W. Sciama
Dr. G.G. Fazio

CO-SUPERVISOR
Professor J.C. Miller

International School for Advanced Studies
SISSA–ISAS

Harvard-Smithsonian Center for Astrophysics

June 2000

To Mayli

# ACKNOWLEDGMENTS

Writing a thesis is just the last, hectic, step of a long journey. For me, that journey started at the end of a bright october day, when I was stunned by the most incredible sunset on the gulf of Trieste, and by the news that I was admitted to graduate school in SISSA. Many years have passed since then. As I look back, I see all the fond memories of the many persons that shared this journey with me. To all of them I am indebted.

Among all, the fondest memory goes to Dennis Sciama. Entering in contact with his rich personality, in the very moment when I was doing my first steps as a scientist, was a true privilege. He rescued me when I was lost, unable to decide between the many paths to follow. He supported me when I took the route across the ocean that lead me to CfA. He gave me a much broader vision of my work, showing how physics is a whole and that a true comprehension of astrophysical phenomena only comes by a careful analysis of both theory and observations. Since he left all of us, he is deeply missed, both as a mentor and a friend.

With him I want to thank all the wonderful people I met in Trieste. John Miller, always available for all of us, students at SISSA, and who kindly offered to be my thesis co-advisor after Dennis left us. All the people of the staff, who provided the most enjoyable working environment I had ever experienced. The people in the computational facility, who introduced me to the cult of Linux and to the job of system administrator. My fellow students and friends at the ICTP, with whom I shared so many special moments. And finally the other people that make Trieste a special place: the family of Mitú, who used to run the Hostel down the sea, and the community of cavers (especially the "Gruppo Triestino Speleologi") who introduced me to the misteries of the underworld and to the Gran Pampel.

I am also indebted to all the people at the Harvard-Smithsonian Center for Astrophysics. Giovanni Fazio welcomed me as his student, as a Smithsonian Predoctoral fellow at the CfA. During my stay at the CfA, he was always available for support, guiding me with the right advise and a clear insight on the direction to take. With him I want to thank the other people in the MIRAC collaboration, among them Joe Hora and William Hoffman, from which I learned so much on infrared astronomy. And Margarita Karovska, who offered me the possibility to stay at the CfA after my graduation, and was very helpful in the revision of this manuscript.

Before starting my Ph.D. in Trieste, I graduated at the University of Torino, with Professor Giovanni Silvestro. He introduced me to astronomy;

I want to thank him for that, and for being my friend ever since. When I left Torino to go to Trieste, and then to CfA, I maintained strong collaborations with the University and the Observatory of Torino, and with the Institute of Space Astrophysics of the CNR in Rome. Much of the work in this thesis is the product of this collaboration. I am very indebted to all the people who made this possible, and especially to Maurizio Busso, who has been, and still is, a central figure in my scientific life.

During the many years of this thesis work, I have been observing at many telescopes around the world. There, I have met many wonderful people always eager to help and support my work, doing miracles in sometime seemingly prohibitive conditions. To all of them, at the TIRGO, Asiago, Loiano, Mt. Hopkins and IRTF telescopes, go all my thanks for their hospitality. And to the people at the "Service d'Astrophysique" at CEA near Paris, where I spent a few weeks learning how to reduce TIRGO data and did my first scuba immersion.

Of the many other people with whom I collaborated during this work, I want to especially thank Avery Meiksin and Željko Ivezić. From Avery I learned how to do my first serious numerical simulation. Without Željko, and his insights in radiative transfer modeling, a central part of my thesis would have not been possible. I am grateful to both of them, for their availability, their advise and their ideas when I most needed them.

Finally, I want to thank my family. My parents did not have the slightest idea of what an astrophysicist would do. They thought that astronomers stay late at night on their chairs contemplating the stars in the sky. They never imagined that I would end up traveling the world in a single year more than they have in their entire life. Nevertheless they always supported me unconditionally, knowing that I had to do what I felt was my way in this world. I could not have asked more.

At the end of this journey, there is a special person to which this thesis is dedicated. Mayli, my wife, who in the short span of a weekend completely changed my life. Without her, I would not have come to Boston, "adopted" a platypus, and this work would have been left incomplete. She brought serenity and equilibrium to my life, making it whole.

# Abstract

Astrophysical dust plays a major role in stellar formation and evolution, and in the chemical enrichment of the Galaxy. However, the processes which lead to its formation in the circumstellar environment of evolved stars, and describe its interactions with the Interstellar Medium, are largely unknown. Mid-IR observations, combined with radiative transfer modeling aimed to derive the dust physical parameters from its thermal emission, are our best tool to investigate the physics of dust in many astrophysical contexts.

In this thesis, I first analyze the current status of mid-IR observations of circumstellar envelopes around Asymptotic Giant Branch (AGB) stars. I then propose a new set of tools, based on the photometric system available in mid-IR imaging cameras, aimed to derive the chemical and evolutionary status of the envelopes from their mid-IR colors. A large sample of sources, observed in the IR and radio, is used to test the effectiveness of the proposed tools, and to derive the correlations between mid-IR colors and mass loss rates in the AGB.

Next, I explore the connections between the pulsational characteristics of Long Period Variables of Mira, Semiregular and Irregular type, with the temporal modulation of their mass loss rates. The mid-IR emission of a large sample of AGB variables is studied, with the aid of spherically symmetric radiative transfer models of circumstellar dust in local thermodynamical equilibrium. This technique allows to analyze the thermal structure of the envelopes, and the timescales of their dust production. A deficiency of hot dust in the majority of Semiregular variables is found, suggesting the frequent occurrence of circumstellar dust shell detachment in these sources, and a different efficiency of the mass loss processes between the Mira and the Semiregular class.

I then study a sample of 46 AGB and post-AGB sources, by analyzing the images I have collected with several mid-IR cameras. The photometry of the envelopes is used to determine their chemical and evolutionary status. The spatial distribution of the dust and the envelope symmetry is measured from the collected data. These observations show how sub-arcsecond resolution can be obtained with ground-based mid-IR imaging, by using a special technique here described.

MIRAC images of the Young Stellar Object AFGL 2591 at 11.7, 12.5 and 18.0 $\mu$m are also presented. I discuss the discovery of a previously unknown dust ejection episode, associated to the molecular outflow of the source. By measuring the photometry of the object, the total mass of the ejection ($\sim$0.1 $M_\odot$) is derived.

Finally, I present a new numerical code, able to compute the stochastic temperature distribution of dust surviving in a hot astrophysical plasma. Applications of this code, which has been parallelized to increase the computational efficiency with multi-processor computer clusters, are discussed. A particular emphasis is given on dust in the intracluster medium of cluster of galaxies, and the consequences of its dust emission on the Sunyaev-Zel'dovich effect.

# Contents

# List of Figures

# List of Tables

# Chapter 1

# Introduction

## 1.1 Dark regions of the sky

The presence of dark regions in the stellar fields of the Milky Way was first noted by William Herschel, who referred to them as “vacancies”. These starless regions of the sky were not of particular interest for the great astronomer, except for their close association with bright nebulæ often found in their proximity. Well aware of this connection, he was used to call for his sister Caroline each time one of these empty regions was sweeping into the field of view of his telescope, to record the new patches of luminosity that were expected to follow.[1]

But it wasn’t until Edward Emerson Barnard, in 1889, started to take pictures of the Milky Way, that a photographic record of Herschel’s vacancies was available for scientific study. In 1919 he first published a catalogue of 182 “dark markings”, based on observations made with a telescope he built himself, using a 6 inches photographic lens bought second hand in San Francisco. Intrigued by the presence of these black empty patches of sky in regions otherwise bright of starlight, he was among the first to suspect their true nature: not just a coincidence in the distribution of stars, but the consequence of some dark opaque medium absorbing the background stellar radiation.

It is now well known that Herschel “vacancies” and Barnard “dark markings” were obscuring clouds of dust and gas, but it took more than 30 years since their photographic discovery, for this explanation to be widely accepted. As early as 1926, thanks to the counts of “extragalactic nebulæ”

---

[1] See the excellent narration in “The Dust of Space” by Seares (1940).

Fig. 1.1.— The Horsehead Nebula, object No. 33 in Barnard's catalogue, is a typical example of thick dust lane obscuring a background bright nebula and stellar field. Barnard thought of it as one of the most convincing cases for the existence of a dark absorbing medium in the galaxy: "*clearly a dark body projected against, and breaking the continuity of, the brighter nebulosity*" (Barnard, 1913). Digital image from NOAO.

(galaxies) by Edwin Hubble[2], it was recognized the presence of a diffuse absorbing stratus (less opaque than Barnard's dark nebulæ), symmetrically placed along the galactic plane. Extinction measurements based on similar techniques (Trumpler, 1940) were finally able to determine the amount of obscuration, leading to the conclusion that the interstellar medium (ISM) was filled with tenuous amounts of fine solid particles. The selective absorption of light by these particles was found to cause a measurable "reddening" in the spectra of background stars, similar in nature to the red tint of the sunset radiation, given by the dust particles suspended in the Earth atmosphere.

The composition and origin of the interstellar dust grains was identified twenty years later, in a fundamental work by Hoyle & Wickramasinghe (1969). By comparing the wavelength dependence of interstellar extinction with the absorption index of various laboratory materials, they were able to conclude that "[...] *interstellar grains may be a mixture of graphite particles formed in carbon stars and of silicates in oxygen-rich giants*"[3].

---

[2] See Hubble (1926) and the more extensive survey in Hubble (1934)

[3] Hoyle & Wickramasinghe (1969)

After the turn of the century, their basic assumptions are still valid, and the advances of the observational techniques covering the whole electromagnetic spectrum, together with the availability of new theoretical and laboratory opacities, have shown the presence of dust in a rich mineralogic variety, and in many different astrophysical contexts. The aim of this work is to analyze the observations of astrophysical dust in the mid-IR region (5–20 $\mu$m ), where its thermal radiation is emitted. This thesis focuses on the two extremes in the life cycle of cosmic dust grains: its formation around cool giants in late evolutionary stages, and the possibility of its survival (and ultimately its destruction) in the hostile spaces between the galaxies.

In the next section the conditions of dust grains in these environments are briefly described. The following chapter introduces the theoretical basis of the interactions between dust, radiation and matter, which take place in the circumstellar and intergalactic environments.

Basic tools for the mid-IR analysis of circumstellar dust are then introduced in chapter 3. Chapter 4 shows an application of these techniques, making use of radiative transfer modeling in order to study the mass loss processes of variable stars in the Asymptotic Giant Branch (AGB) phase.

Chapter 5 describes a succesful project of direct mid-IR imaging of circumstellar dust, around AGB sources modeled in the previous chapter, and along a molecular outflow in a Young Stellar Object (YSO). The observations are analyzed and compared with the theoretical predictions, in order to test their recent mass loss history and geometry.

In chapter 6, the chances to observe the emissions of dust surviving at the center of cluster of galaxies (IntraCluster Medium, or ICM) are finally evaluated, and some applications are proposed.

## 1.2 Dust grains in the galaxy and beyond

Since the existence of a dark diffuse medium able to absorb the stellar radiation in the ISM was first recognized, the presence of dust has been discovered in a multitude of different environments. In this section the dust metamorphosis in the Galaxy is briefly described, by discussing with particular emphasis the properties of dust in the ISM, around giant stars (where it is formed) and in the intergalactic medium (where it is finally destroyed).

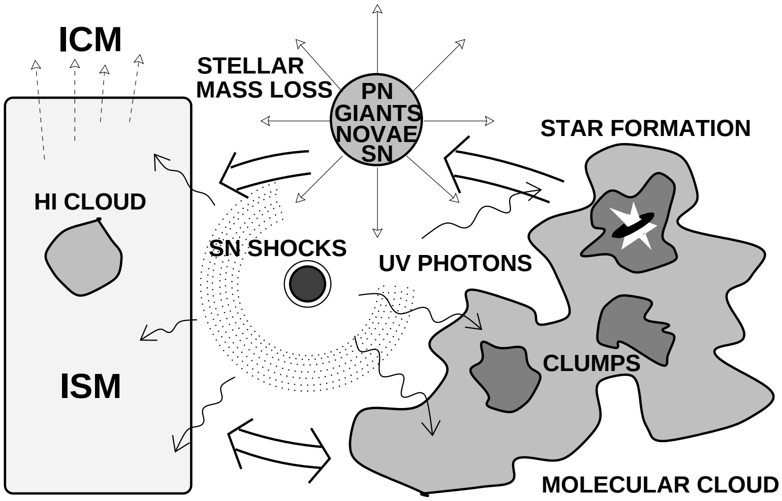

Fig. 1.2.— Creation and destruction cycles of dust in the Galaxy. Adapted from Tielens (1989).

### 1.2.1 Dust metamorphosis in the galaxy

Dust is a fundamental constituent of the Galaxy, and plays a major role in its evolution. Dust grains created around giant stars drifts into the diffuse interstellar medium, where they are eroded by the hot component of the ISM and the energetic UV background. Part of this dust, however, is eventually accumulated in dense molecular clouds, where it is protected from the more energetic photons, and finds a favorable environment for its survival and growth. Here, far-infrared radiation emitted by dust removes the gravitational energy of collapsing molecular clouds, thus allowing for star formation to occur. In these processes dust becomes part of protostellar disks, feeding the young stars with metals, and ultimately providing the building material for planetary systems. Some of the ISM dust, finally, is assumed to became part of the intergalactic medium, blown away from the galactic plane by the action of strong galactic winds (Matteucci & Gibson, 1995), or by means of ram pressure stripping as the host galaxy crosses the denser central regions of the ICM (Gunn & Gott, 1972).

This complex interplay between processes of formation, destruction, and growth of galactic dust, summarized in figure 1.2, is crucial for the chemical evolution of the Galaxy, and the chemical enrichment of the extragalactic medium.[4]

---

[4] See, e.g. the review in Dorschner & Henning (1995).

The term *stardust* coined by Ney (1977) is well justified by the fact that the main source of cosmic dust is the stellar mass loss. The formation of small grains in dense molecular clouds and the growth of refractory dust in the diffuse ISM, however, have recently turned out to be processes of at least comparable importance. To these well recognized dust sources, one may add the possibility of dust formation in *cooling flows* at the core of clusters of galaxies (Fabian et al., 1994), even though this idea is quite controversial. The fact that cosmic dust grains originates and are reprocessed in many different environments is well reflected by the large variety of mineralogical composition and grain sizes encountered in the galactic and extragalactic dust.

The destruction of dust, on the other end, is mainly due to the interactions with energetic UV photons and SuperNova Remnants (SNRs) shocks in the ISM, and to sputtering by hot plasma and the X background radiation in the ICM. The physics of these interactions in the interstellar, circumstellar and ICM environment is briefly discussed in the following sections.

### 1.2.2 Interstellar dust

Dust in the ISM is subjected to many chemical and physical processes, including grain-grain collisions, erosion by sputtering, irradiation effects and grain growth due to recondensation of evaporated and sputtered grain material.

Grain growth in the ISM is necessary to maintain the observed interstellar dust density, due to the high depletion rate by the hotter surrounding medium. The lifetime of ISM dust is estimated to be $\sim 4 \cdot 10^8$ yr for carbonaceous grains, and $\sim 2 \cdot 10^8$ yr for silicate material (Jones et al., 1994). The timescale for ISM dust replenishment by stellar mass loss is, however, ten times larger ($2.5 \cdot 10^9$ yr, see e.g. Jones & Tielens 1994), and is thus insufficient to keep the balance.

Two mechanisms are invoked to solve this deficiency: formation of small grains and Polycyclic Aromatic Hydrocarbons (PAH) triggered by Supernova (SNs) shocks and $C^+$ ion chemistry (probably responsible for the interstellar gas heavy metal depletion), and migration of ISM dust in molecular clouds, where it is protected from the more energetic radiation and finds more favorable conditions for grain growth. By comparing the lifetime of dust in the diffuse ISM with the fraction of the ISM that is part of molecular clouds (about 30%), and the molecular clouds lifetimes ($\sim 10^8$ yr), one can assume that each ISM dust particle will be processed in a cloud for more than 10 times during its mean lifetime (Mathis, 1990). While in the clouds, dust grains undergo chemical processing that modify their size distribution, leading to the formation of larger grains coated with ice mantles.

The grain size distribution and chemical composition of dust in the diffuse ISM and in clouds is thus different. From the fitting of the observed galactic extinction curve, Mathis, Rumpl & Nordsieck (1977) derived a power-law for the diffuse ISM grain size distribution ("standard" MRN distribution):

$$n_d(a) \propto a^{-k} \qquad \text{for} \quad a_{min} \lesssim a \lesssim a_{max} \tag{1.1}$$

where $k \sim 3.5$, $a_{min} \sim 0.005$ $\mu$m and $a_{max} \sim 0.25$ $\mu$m. Further analysis by Kim, Martin & Hendry (1994) using a larger number of observational constraints, found deviations from the MRN distribution required to explain the UV extinction curve, and an exponential cutoff for $a \gtrsim 0.2$ $\mu$m, that allows a better fitting of the dust far-infrared radiation:

$$n_d(a) \propto a^{-k} e^{-a/a_o} \tag{1.2}$$

with $k \sim 3.06$ for silicates and $k \sim 3.48$ for graphite. The details of the deviations from the simple MRN distribution and the position and slope of the exponential cutoff are different between diffuse ISM and dust in molecular clouds, and result in a relative decrease of small particles in the clouds, accompanied by the presence of larger grains.

As already shown, extinction measurements are the main source to determine the composition of ISM dust. Emission is also important, however, because it probes the composition of the most extincted regions, opaque at optical wavelengths, and allows the determination of the less abundant components. The dust thermal emission, in fact, amounts to about the 30% of the total luminosity of the Galaxy, mainly at far infrared wavelengths. Strong Unidentified Infrared Bands (UIB), have also been observed in the 3.3 – 11.3 $\mu$m range, and their interpretation is a strong constraint on the proposed models of ISM detailed composition.

The current accepted models of the diffuse ISM assume a mixture of refractory grains, mainly carbonaceous and oxidic. Among the C-based material, the main components are graphite, Hydrogenated Amorphous Carbon (HAC) and PAH, with this last ingredient introduced to explain the observed UIB. The oxidic part of the ISM dust is in turn made of amorphous (Mg-dominated) silicates and Mg-Fe oxides. Apart from these main chemical components, minor species are also found, as e.g. sulfides grains (Begemann et al., 1994). SiC is also expected, due to its high rate of production in C

TABLE 1.1 TOTAL GALACTIC STELLAR MASS LOSS.

| Source | Total $\dot{M}$ $M_\odot$ yr$^{-1}$ | fraction % |
|---|---|---|
| Thermally pulsing AGB stars | $5.5 \cdot 10^{-1}$ | 73 |
| Supernovæ | $7.5 \cdot 10^{-2}$ | 10 |
| RGB stars | $5.5 \cdot 10^{-2}$ | 7 |
| Wolf Rayet stars | $2.5 \cdot 10^{-2}$ | 3 |
| Red and Yellow Supergiant stars | $2.0 \cdot 10^{-2}$ | 3 |
| Early AGB stars | $2.0 \cdot 10^{-2}$ | 2.5 |
| Main Sequence stars | $1.0 \cdot 10^{-2}$ | 1.5 |

Adapted from Sedlmayr (1994)

stars, but is probably not abundant, as inferred by the absence of interstellar absorption at 11.3 $\mu$m, where its main feature is located.

### 1.2.3 Circumstellar dust

High luminosity giant stars are the main stellar source of dust, since they provide up to 90% of the total stellar mass loss. Stars in the AGB and the post-AGB, in particular, account for the greater part of the total yield, as shown in table 1.1.

Supernovæ (SN) are also important, being the main contributors of elements heavier than carbon, and thus playing a major role in providing refractory grains to the ISM. Their total yield, however, is not well known, due to the uncertainties in their dust production efficiencies, and because it is difficult to estimate the grain survival rate after the SN explosion. Wolf Rayet stars (WR), Red Giants Branch stars (RGB) and Main Sequence stars (MS) are instead secondary contributors.

The initial evidences for a circumstellar origin of dust came from the reddened spectra of the parent stars, which show various degrees of extinction at optical wavelengths (first suggested by Loreta 1934), and strong mid-IR infrared excess. A better understanding of the circumstellar dust composition came with the development of infrared spectroscopy. At the end of the 1960s, it was confirmed the assumption that stars with M spectral type were forming silicate particles, while carbon stars were the sources of carbonaceous grains.

With the IRAS satellite mission, a database of 5,425 Low Resolution Spectra (LRS, 1986) was collected in the 7.7–22.6 $\mu$m range. Since most of the observed sources were AGB, post-AGB and supergiant stars, it was possible for the first time to attempt a precise classification of the circumstellar dust mineralogy.

The presence of a broad 9.8 $\mu$m feature, either in emission or absorption, and a secondary one between 16 and 20 $\mu$m, was readily associated with vibrations of the Si-O bond in silicate dust. A mixture of olivines ($[Mg_xFe_{2-x}]SiO_4$) and pyroxenes ($[Mg_xFe_{1-x}]SiO_3$) with amorphous structures is now accepted as the main component of dust in O-rich circumstellar envelopes. Recent SWS spectra obtained with the infrared satellite ISO (see e.g. Waters et al., 1996), however, suggest the presence of minor quantities of crystalline grains in the envelopes of some very evolved AGB and post-AGB objects. Secondary features already observed in the IRAS database, as the famous 13 $\mu$m emission feature, were instead attributed to corundum ($Al_2O_3$, see e.g. Onaka et al. 1989), or other oxides (as $SiO_2$, see Speck 1998).

The LRS of C-rich envelopes, on the other end, exhibit a rather flat spectrum, where the main feature is a narrow emission line at 11.2 $\mu$m, associated to SiC. The main component of carbonaceous dust, however, is amorphous carbon, consisting of graphite crystals arranged in an amorphous conglomerate ("sooth", making these stars similar to "smoking chimneys"). Another important component of C-rich envelopes are the PAH, which are known to play a central role in carbonaceous dust formation processes (Cherchneff et al., 1992). Their observation, however, is limited to post-AGB end Planetary Nebulæ (PN) halos, where they are excited by the energetic UV photons emitted by the hot central star.

The dichotomy between O-rich and C-rich dust in circumstellar envelopes is largely regulated by the chemistry of the CO molecule (Dominik et al., 1993). A strongly bonded compound, CO does not interact with the other circumstellar particles. Since it is one of the very first molecules to form, CO rapidly depletes the circumstellar gas from the less abundant element between O and C. Stars with $C/O \lesssim 1$ (O-rich stars) will thus be forced to form oxidic dust, while carbon stars ($C/O \gtrsim 1$) will be left with an overabundance of C atoms, leading to the formation of dust in a C-rich chemistry. There are exceptions, to this rather strict rule: the 9.8 $\mu$m silicate feature was in fact observed in a few IRAS carbon star spectra (Little-Marenin, 1986; Willems & de Jong, 1986). The meaning of these observations is still quite uncertain, even though binarity, or changes in the parent star, have been proposed to solve the mystery.

The efforts to better understand the mineralogy of circumstellar dust and the details of its formation have dominated the research of the last decade, with two basic approaches: theoretical and laboratory determination of dust opacities (see Speck 1998 for a recent review), and modeling of dust condensation in circumstellar environments (Winters et al., 1994; Windsteig et al., 1997; Höfner & Dorfi, 1997). Despite the advances in the last years, there are still various degrees of uncertainties, mainly due to radiative transfer effects limiting our ability to derive dust opacities from observational data, and because the dust composition of individual sources can be very different (see discussion in section 4).

To conclude this section, it is worth noting that a completely independent confirmation of the stellar origin of interstellar dust is obtained by the analysis of meteorites, which in some cases contain small inclusions of refractory grains characterized by anomalous isotopical composition. The measured isotopical abundances, that cannot be explained if the grain where formed inside the presolar nebula, demonstrate their provenience from the circumstellar envelopes of AGB stars (Gallino et al., 1990). This exciting discovery realizes an ancient dream of astronomers, allowing the direct analysis of "stardust" and stellar materials in the comfort of their own laboratory.

### 1.2.4 Extragalactic dust

In June 1957 Fritz Zwicky presented at the Flagstaff meeting of the Astronomical Society of the Pacific the results of a large scale investigation on the "Non-Uniformities in the Apparent Distribution of Cluster of Galaxies". The statistical analysis, carried out on fields photographed with the Mount Palomar 18-inch and 48-inch Schmidt telescopes, as well as the 200-inch Hale reflector, contained the first real indication of a non uniform distribution of clusters of galaxies. By finding an average lower density of faint galaxies in proximity of intrinsically brighter ones, he suggested that "*... [intergalactic] dust exists in all intergalactic space, but is preferentially located in the rich clusters of galaxies*"[5]. Unfortunately, he went so far to predict the existence of extragalactic dust everywhere in the universe, to the point of negating his own evidences of superclustering, by explaining the cluster anisotropy as an extinction effect only.

His observations of the anticorrelation between faint galaxies and rich clusters, however, was confirmed many years later by Bogart & Wagoner (1973) while looking for clustering effects between quasars (QSO) and clus-

---

[5] Zwicky (1957)

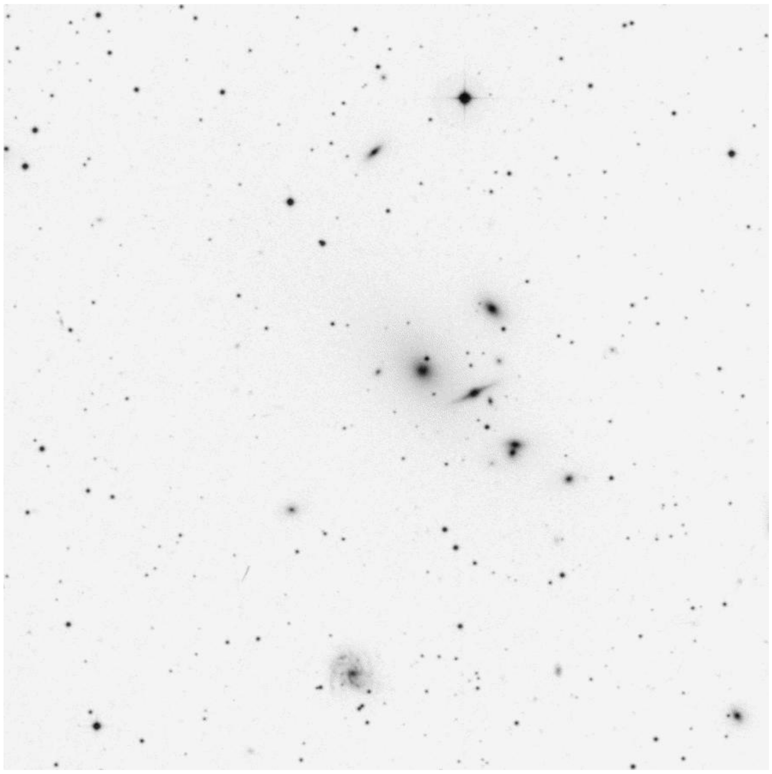

Fig. 1.3.— Digitized Sky Survey image of Abell cluster 262.

ters of galaxies. They found this discovery "*somewhat contradictory*" and rejected as unlikely the hypothesis of dust extinction as the explanation. In their conclusions, however, they mentioned that Karachentsev & Lipovetskii (1969) and de Vancouleurs et al. (1972) did measure an average obscuration of about 0.2 magnitudes of the background galaxies.

More recently, Boyle et al. (1988) made a new search looking for correlations between the position of high-redshift quasars and low redshift galaxies. They did not find it, but were perplexed to obtain a significant ($4\sigma$) deficiency of QSOs (up to 30%) in a radius of 4 arcmin from galaxies lying in a cluster. They attributed the effect as a result of dust extinction, measuring again $A_B \simeq 0.2$. A later survey (Romani & Maoz, 1992) concluded that an average value of $A_B \sim 0.5$ mag (or a very patchy distribution) was necessary to explain the observed anticorrelation between quasars and their sample of Abell clusters. However, when Ferguson (1993), and later Maoz (1995) searched for the reddening that should accompany such strong extinction, they didn't find any positive results, raising new doubts about the presence of substantial amounts of dust in clusters of galaxies. Hu (1992), on the other end, in a series of papers looking at the UV-to-optical line ratio from the emission of background galaxies in *cooling flow* clusters, measured an $E_{B-V}$ reddening of about the expected value ($\sim 0.19$).

In an attempt to reconcile the contradicting observations, the amount of reddening that should be expected for the measured extinction was computed by Aguirre (1999), with the assumption of a grain population biased towards small sizes. He concluded that such dust would be too gray to produce an observable reddening, but opaque enough to count for the observed type I supernova dimming, thus reconciling cosmological models with observational data *without* requiring an accelerating universe! As in the case of Zwicky, this is another example of the really profound consequences that the inclusion of dust may have in our view of the structure of the universe.

It should be clear, by now, that the presence of dust in the ICM is highly controversial, not only because of the difficult task of providing observational evidences, but also for the important consequences that dust in cluster of galaxies would have for many fundamental cosmological questions.

The main reason why it is so difficult to accept the presence of dust in the extragalactic space is that the ICM environment is very hostile to the survival of dust. With temperatures ranging between $10^6$ and $10^9$ K, and densities of the order of $10^{-6} - 10^{-2}$ cm$^{-3}$, the gas in the ICM is very efficient to destroy dust grain on timescales of $10^6 - 10^8$ yr (see discussion in section 2.3.3). If dust exist in such conditions, it either implies a recent episode of dust injection from the galaxies in the cluster, or a mechanism for dust formation *in situ*. As anticipated in section 1.2.1, there are evidences that support both possibilities.

The fact that ICM is chemically enriched, suggests some sort of interaction with the ISM of the galaxies in the clusters, since any trace of metals in the ICM should be traced back to stellar nucleosynthesis. Strong stellar winds in starburst galaxies can throw into the gravitational well of the cluster a fraction of their newly enriched ISM (gas *and dust*), as explained in Matteucci & Gibson (1995). Ram pressure stripping at the passage of a galaxy in the central regions of a cluster can also contribute in maintaining a certain amount of ICM dust.

Radiative cooling in the denser regions of some clusters, acting as *cooling flows*, can also give rise to the conditions for dust formation. As predicted by Fabian et al. (1994), when cold matter slowly accumulates at the core of the cluster, it may form cold clouds, and maybe even stars, explaining the alignment of some cooling flows with their optical emission.

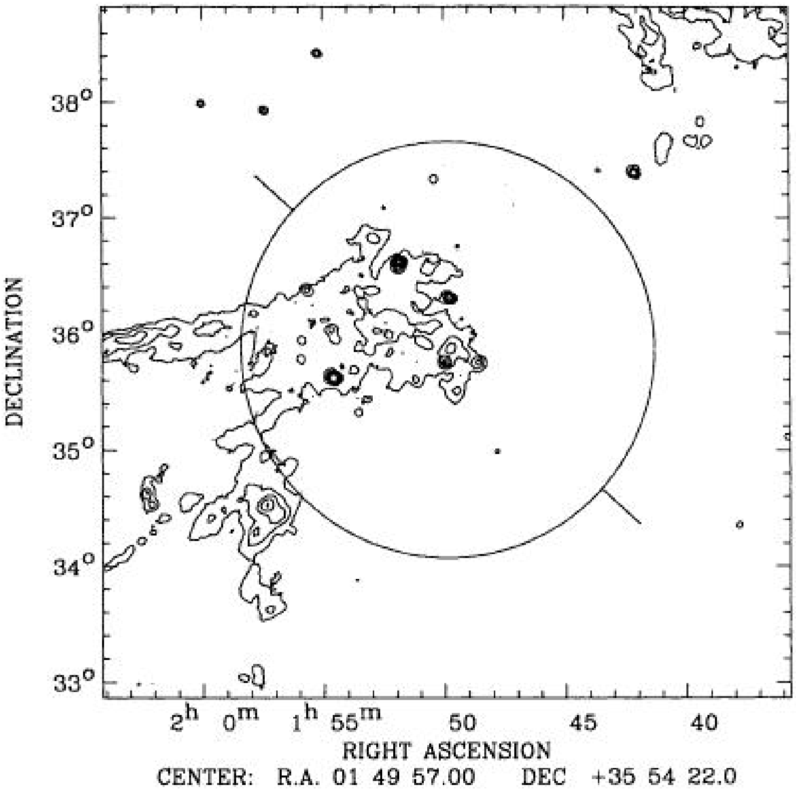

Fig. 1.4.— IRAS image of Abell cluster 262 at 100 $\mu$m. The circle marks the cluster radius, and the vectors indicate the cluster's major axis. Contours show intensity levels ranging from 2 to 10 $\sigma$ above the mean background noise, in steps of 1 $\sigma$. Adapted from Wise et al. (1993).

A more direct way to solve the controversy, looking for direct evidences of ICM dust, would be to search for the thermal emission of grains heated by the hot ICM plasma. Since the expected "mean" temperature of the grains, is $\sim$ 30 K, the spectral region of choice for a detection should be the far-infrared/millimetric domain.

Several groups have attempted to scan the IRAS database in search of diffused far-IR emissions (60 – 100 $\mu$m) from cluster of galaxies (Bregman et al., 1990; Wise et al., 1993; Cox et al., 1995; Bregman & Cox, 1997). These surveys obtained mixed results, finding a "positive" detection of "warm" (24 – 33 K) dust emission for about 10% of the observed clusters, but with a rather low statistical significance (between 3 and 5 $\sigma$). Similar searches in the sub-millimeter by Annis & Jewitt (1993) and at the wavelength of the CO (J=1→0) line by Grabelsky & Ulmer (1990) did not give positive results.

An example of positive detection in Wise et al. (1993) is given in figure 1.4; the low spatial resolution of the IRAS scan does not allow to determine the exact position of the diffuse emission, thus making impossible to distinguish if the dust is diffused in the hot ICM, or included in the dominant member of the cluster. A more careful analysis and calibration of ISO data may be able to solve the puzzle, but there are no conclusive answers thus far (Cox & Bregman, 1997). In the meantime, and waiting for the upcoming SIRTF observatory, the available observations suggest that ICM dust may be a short lived phase that occurs in particular conditions, for only a fraction of the clusters of galaxies.

# Chapter 2

# Theoretical basis: dust, radiation and matter interactions

This chapter introduces the basic theoretical tools used in this thesis work.

The propagation of radiation in a dusty medium is described in section 2.1. The formal solution of radiative transfer problem in presence of dust is given, and applied to the case of dusty circumstellar envelopes. The methods developed in this section are then used in the following chapters to model the circumstellar environment of AGB stars.

Section 2.2 introduces the physics of interactions between dust matter and radiation. The optical properties of dust minerals are summarized, and discussed in term of the "opacities" characterizing astrophysical dust. These opacities are a basic component to compute the spectral properties of radiation emitted and absorbed by dust.

The last section finally examines the interactions between dust and other particles, namely the positive ions an the electrons of a plasma in which dust grains can be embedded. The survival of dust in this conditions is analyzed, and the effects of the dust-particles interactions are described from the point of view of the grain thermodynamics. The basic equations shown in this section are then used to study the behaviour of dust in the ICM.

## 2.1 Radiative transfer in a dusty medium

With the exceptions of refractory grains in meteorites, the only observables for the study of cosmic dust are in most cases the bolometric flux and the spectral flux distribution coming from the dust medium. In these cases the solution of a radiative transfer problem is necessary to connect the observations with the physical and thermodynamical status of the dust.

In this section the general equation of radiative transfer is introduced, and discussed in the case of a dusty medium. The condition of local thermodynamical equilibrium, in which the dust radiative emission balances the energy input from all heating sources, is introduced, and a solution method for the problem in a spherically symmetric geometry is given.

The case of spherical symmetry and thermal equilibrium is the typical approximation used to describe dusty circumstellar envelopes, in which the only heating source is the radiation field generated from the central star. A more general problem, in which the interactions between dust and matter give a substantial contribution to the energy balance, and the thermodynamical equilibrium does not apply due to different timescales between the heating and cooling processes, is discussed separately in section 2.3.4.

### 2.1.1 Spectral intensities and flux units

The *spectral intensity* $I_\nu$ of a radiation field is defined as the amount of energy $\mathrm{d}E$ in the frequency beam $\mathrm{d}\nu$ that, coming from the solid angle $\mathrm{d}\Omega$, crosses the surface $\mathrm{d}A$ in the time $\mathrm{d}t$:

$$I_\nu = \frac{\mathrm{d}E}{\mathrm{d}\nu\,\mathrm{d}t\,\mathrm{d}\Omega\,\mathrm{d}A} \tag{2.1}$$

The integral over the solid angle of the normal component of the intensity $I_\nu$ with respect to the collecting area is called *spectral flux*, and is the quantity measured by astronomical detectors:

$$F_\nu = \int_{4\pi} I_\nu \cos\theta \,\mathrm{d}\Omega \tag{2.2}$$

The *bolometric flux* is instead defined as the total collected flux over all frequencies, and is thus related to $F_\nu$ by the integral:

$$F_{bol} = \int_0^\infty F_\nu \,\mathrm{d}\nu \tag{2.3}$$

Spectral fluxes are measured in units of erg cm$^{-2}$ s$^{-1}$ Hz$^{-1}$. A commonly adopted unit, called Jansky, is defined as:

$$1\,\mathrm{Jy} \,=\, 10^{-23}\,\mathrm{erg\ cm^{-2}\ s^{-1}\ Hz^{-1}} \tag{2.4}$$

Fluxes are also expressed in *magnitudes*, which is a logarithmic scale unit based on the *zero point* flux of the standard star $\alpha$ Lyr:

$$m = -2.5 \log \left( \frac{F_\nu}{F_{\nu,0}} \right) \tag{2.5}$$

This system, which imitates the way the human retina perceives luminous fluxes, was introduced by Hipparcos in 120 B.C., and is still widely used.

To compute the flux emitted by a dust cloud, one has to solve the problem of how electromagnetic radiation propagated in the dusty medium. This is done by the "radiative transfer equation", described in the following section.

### 2.1.2 The general equation of radiative transfer

Barionic matter and electromagnetic radiation interacts in three basic forms: absorption, scattering, and emission.

Consider a volume of material with cross section $\mathrm{d}A$ and length $\mathrm{d}\ell$, which is illuminated by a radiation field of intensity $I_\nu$. In case of absorption, an amount $\mathrm{d}E^{(a)}$ of energy is removed from the incident flux, and converted into internal energy of the absorbing material. The amount of energy that is absorbed is proportional to the intensity $I_\nu$, and the constant of proportionality is called *absorption opacity* $k_\nu^{(a)}$:

$$\mathrm{d}E^{(a)} \; = \; k_\nu^{(a)} \, I_\nu \, \mathrm{d}\nu \, \mathrm{d}t \, \mathrm{d}\Omega \, \mathrm{d}A \, \mathrm{d}\ell \tag{2.6}$$

In the case of scattering, the fraction of incident radiation that is removed is immediately reflected in the same wavelength bin but at different solid angle. The scattered radiation is also proportional to $I_\nu$, and the constant of proportionality is called *scattering opacity* $k_\nu^{(\sigma)}$:

$$\mathrm{d}E^{(\sigma)} \; = \; k_\nu^{(\sigma)} \, I_\nu \, \mathrm{d}\nu \, \mathrm{d}t \, \mathrm{d}\Omega \, \mathrm{d}A \, \mathrm{d}\ell \tag{2.7}$$

In the case of emission, the material releases into the radiation field an energy $\mathrm{d}E^{(\epsilon)}$, proportional to a quantity $j_\nu$, called *emissivity*. The emitted energy is not necessarily proportional to the intensity $I_\nu$, but rather depends on the physical characteristics of the emitting material, and its energetic state:

$$\mathrm{d}E^{(\epsilon)} \; = \; j_\nu \, \mathrm{d}\nu \, \mathrm{d}t \, \mathrm{d}\Omega \, \mathrm{d}A \, \mathrm{d}\ell \tag{2.8}$$

For the conservation of energy, the total variation of the incident flux in the solid angle $\mathrm{d}\Omega$ is given by the difference between the emitted, absorbed and scattered energy:

$$\mathrm{d}I_\nu = \frac{\mathrm{d}E^{(\epsilon)} - \mathrm{d}E^{(a)} - \mathrm{d}E^{(\sigma)}}{\mathrm{d}\nu\,\mathrm{d}t\,\mathrm{d}\Omega\,\mathrm{d}A} \tag{2.9}$$

which gives the *general equation of radiative transfer*:

$$\frac{\mathrm{d}I_\nu}{\mathrm{d}\ell} = j_\nu - k_\nu\, I_\nu \tag{2.10}$$

In this equation $k_\nu = k_\nu^{(a)} + k_\nu^{(\sigma)}$ is the *total opacity*, that describes the interactions between radiation and matter at a microscopic level.By defining the *source function* $S_\nu$ as the ratio between the emissivity and the total opacity, one can rewrite the radiative transfer equation in the more usual form:

$$\frac{\mathrm{d}I_\nu}{\mathrm{d}\ell} = k_\nu\,(S_\nu - I_\nu) \tag{2.11}$$

The source function describes the interactions between matter and radiation at a macroscopic level; its general form for a dusty medium is given in the next section.

### 2.1.3 The source function for a dusty medium

The radiative transfer equation is more properly expressed in terms of a non dimensional quantity, called *optical depth* which is proportional to the total opacity integrated along an optical path $\mathcal{P}$:

$$\mathrm{d}\tau_\nu = k_\nu\,\mathrm{d}\ell \quad \Rightarrow \quad \tau_\nu = \int_{\mathcal{P}} k_\nu\,\mathrm{d}\ell \tag{2.12}$$

By introducing the optical depth, the only term in the equation 2.11 which depends on the properties of the interacting matter is the source function $S_\nu$:

$$\frac{\mathrm{d}I_\nu}{\mathrm{d}\tau_\nu} = S_\nu - I_\nu \tag{2.13}$$

With this change of variable, the radiative transfer equation can be formally solved in terms of the optical depth:

$$I_\nu(\mathcal{P}) = \underbrace{I_\nu(0)\, e^{-\tau_\nu(\mathcal{P})}}_{\text{background component}} + \underbrace{\int S_\nu(\tau'_\nu)\, e^{-[\tau'_\nu - \tau_\nu(\mathcal{P})]}\, \mathrm{d}\tau'_\nu}_{\text{source component}} \tag{2.14}$$

where the *background component* gives the amount of incident radiation extincted along the path $\mathcal{P}$, and the *source component* is the contribution to $I_\nu$ given by the emission and scattering of the interacting matter.

For a dusty medium, the source component can be split in two separate contributions, one relative to the dust emission, and one giving the total dust scattering:

$$S_\nu = \frac{j_\nu}{k_\nu} = \frac{j_\nu^{(\epsilon)} + j_\nu^{(\sigma)}}{k_\nu^{(a)} + k_\nu^{(\sigma)}} \tag{2.15}$$

If $T_d$ is the dust temperature (generally a function of the heating sources, among which the radiation field itself), then the emission component is equal to the black body emission $B_\nu(T_d)$, multiplied by the efficiency factor given by the absorption opacity $k_\nu$:

$$j_\nu^{(\epsilon)} = k_\nu^{(a)}\, B_\nu(T_d) \tag{2.16}$$

The scattering component, on the other end, is obtained by integrating the scattered radiation over the total solid angle:

$$j_\nu^{(\sigma)} = \frac{1}{4\pi} \int_{4\pi} k_\nu^{(\sigma)}\, I_\nu(\Omega')\, g(\Omega', \Omega)\, \mathrm{d}\Omega' \tag{2.17}$$

where $g(\Omega', \Omega)$ is the angular phase function for coherent scattering from direction $\Omega'$ to direction $\Omega$ (see e.g. Mihalas, 1978).

By introducing the *albedo* $\varpi_\nu = k_\nu^{(\sigma)}/k_\nu$, the formal expression of the source function for a dusty medium becomes:

$$S_\nu = (1 - \varpi_\nu)\, B_\nu(T_d) + \frac{\varpi_\nu}{4\pi} \int_{4\pi} I_\nu(\Omega')\, g(\Omega', \Omega)\, \mathrm{d}\Omega' \tag{2.18}$$

By substituting equation 2.18 in equation 2.13 the radiative transfer problem can in principle be solved, once the thermal structure of the dust is determined. In the next section this problem is discussed, in the simplified case in which dust and radiation are thermalized.

### 2.1.4 Dust in local thermodynamical equilibrium

The thermal state of a single dust grain is defined by the balance between its heating and cooling sources. In general, these two processes can have very different timescales, $\tau_{heat}$ and $\tau_{cool}$. If $\tau_{cool} \ll \tau_{heat}$, the temperature of the grain is subjected to fluctuation in time. In this case a common temperature for the dust cannot be defined, since each grain, at any given moment in time, may have a different temperature. In this situation, common for dust in a hot plasma (like dust in the ICM or SN remnants), a *statistical distribution* of dust temperature have to be used.

If $\tau_{cool} \sim \tau_{heat}$, the grains in the cloud can reach an equilibrium temperature $T_d$, which is described by the balance between emitted and absorbed radiation. In this case, the dust is said to be in *local thermodynamical equilibrium*, or LTE. This equilibrium is described by the following equation, in which the left hand side is the total flux irradiated on all solid angles, and the right hand side is the total absorbed flux:

$$\int \mathrm{d}\Omega \int k_\nu \, S_\nu \, \mathrm{d}\nu = 4\pi \int k_\nu \, J_\nu \, \mathrm{d}\nu \tag{2.19}$$

where $J_\nu$ is the average flux intensity over all solid angles:

$$J_\nu = \frac{1}{4\pi} \int I_\nu \, \mathrm{d}\Omega \tag{2.20}$$

In the hypothesis in which radiative cooling is the only active process, the source function in equation 2.18 can be used to describe the LTE condition of a dust grain:

$$\int \mathrm{d}\Omega \int k_\nu \, (1 - \varpi_\nu) \, B_\nu(T_d) \, \mathrm{d}\nu = 4\pi \int k_\nu \, (1 - \varpi_\nu) \, J_\nu \, \mathrm{d}\nu \tag{2.21}$$

where the scattering term is eliminated by the solid angle integration.

### 2.1.5 Scaling properties of radiative transfer

As described in Ivezić & Elitzur (1997), the radiative transfer equation for dusty media possesses a number of scaling properties, that can be used to simplify the modeling of dusty clouds, and the interpretation of the observational results.

The first of these properties is *scale invariance*. Consider a generic path $\mathcal{P}$, and the adimensional coordinate $y = \ell/R_1$ along the path, with $R_1$ an arbitrary length scale. Then equation 2.11 can be written as:

$$\frac{\mathrm{d}I_\nu}{\mathrm{d}y} = \tau_\nu(\mathcal{P})\ \eta(y)\ [S_\nu(y) - I_\nu(y)] \tag{2.22}$$

where $\eta(y)$ is a dimensionless function describing the variations of the opacity with position:

$$\eta(y) = \frac{1}{\tau_\nu(\mathcal{P})} \cdot \frac{\mathrm{d}\tau_\nu(y)}{\mathrm{d}y} = \frac{k_\nu(y)}{\int k_\nu(y)\,\mathrm{d}y} \tag{2.23}$$

Note that $\eta(y)$ generally depends on the wavelength, but if the optical properties of the individual absorbers do not change with position, this dependence disappears. In the case in which the relative abundance is constant along $\mathcal{P}$, then the function $\eta(y)$ reduces to the normalized dimensionless density:

$$\eta(y) = \frac{n_d(y)}{\int n_d(y)\,\mathrm{d}y} \tag{2.24}$$

Equation 2.22 does not explicitly depend on quantities having the dimensions of length, since the absolute spatial scale has disappeared from the formulation of the problem, and is only necessary to express the total optical depth in terms of the physical size of the system. The properties of the radiation described by equation 2.22, are instead fully described by the adimensional variable $y$, showing that the problem is in fact scale invariant with respect to the spatial scale.

A second important property of the radiative transfer equation, is the way it scales with respect to the absolute normalization of the radiation intensity and flux. As shown in Ivezić & Elitzur (1997) for a dusty medium in LTE, if the only energy source is an external energy field $I_\nu^E$, then the radiative transfer problem is fully specified by the temperature $T_1$ at the dust heated boundary, which defines the *scaling function*:

$$\Psi = \frac{4\sigma T_1^4}{F_1^E} \tag{2.25}$$

where

$$F_1^E = \int \mathrm{d}\nu \int I_\nu^E\ \cos\theta\,\mathrm{d}\Omega = \frac{L^E}{4\pi R_1^2} \tag{2.26}$$

is the bolometric flux at the heating boundary layer, produced by an external source of luminosity $L^E$, placed at a distance $R_1$. In the case of circumstellar envelopes, $T_1$ is the temperature at the radius $R_1$ of the central cavity of the envelope, $L_* = L^E$ is the parent star luminosity and $F_1^E$ its bolometric flux.

In a system in which the position of the boundary layer is determined by the dust condensation (or sublimation) temperature $T_{cond}$ (dust as close as possible to the hot external source), then the absolute scale of the bolometric flux is determined by the value of $T_1 = T_{cond}$, and the only relevant property of the input radiation is its adimensional spectral shape:

$$f_\nu^E = \frac{F_\nu^E}{\int F_\nu^E \, \mathrm{d}\nu} \tag{2.27}$$

For a circumstellar dust envelope, the spectral energy distribution of the emitted radiation can be fully determined by specifying the spectral shape of the central stellar radiation, the optical depth $\tau_\nu$ and the temperature $T_1$ at the inner envelope radius. This radius can either be the dust condensation radius for a system that is currently producing dust, or the radius of the central cavity in the case of a detached dust shell.

### 2.1.6 Solution for the spherically symmetric case

The solution of a radiative transfer problem is simplified in case of spherical symmetry, which makes it one-dimensional. For this reason, spherical symmetry is often adopted as an approximation for the real geometry. This is the case, for example, of dusty circumstellar envelopes: even though there are evidences for departures from spherical symmetry (see discussion in section 5), the quality of the data and the low spatial resolution of the images justify in most cases this kind of approximation.

The problem of radiative transfer for a spherical dusty shell was first developed by Rowan-Robinson (1980), which gave a solution method for this geometry. In this section we repeat his procedure, following the formalism developed by Ivezić & Elitzur (1997), in order to provide a description of the modeling procedure employed in the following chapters for AGB circumstellar envelopes.

In spherical symmetry the system is described by the radial adimensional coordinate $y$; in the case of a dust shell, this coordinate can be defined to have the value $y = 1$ at the inner envelope boundary (so that $T_1$ is the inner temperature of the envelope). In this geometry, the optical depth along an optical path $\mathcal{P}$ is described by the following integral (see figure 2.1):

$$\tau_\nu(y, \theta) = \tau_\nu^T \int_0^{y\,\cos\theta} \eta\left(\sqrt{u^2 + y^2\,\sin^2\theta}\right) \mathrm{d}u \tag{2.28}$$

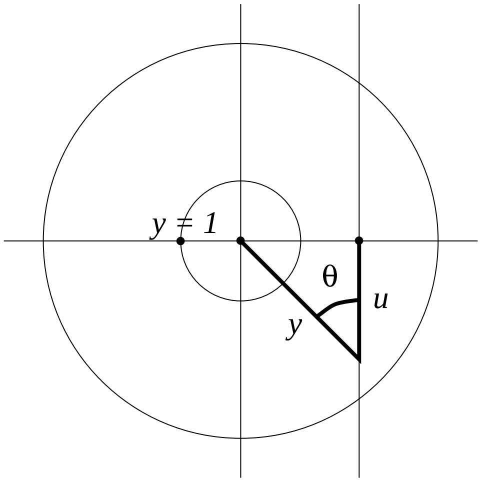

FIG. 2.1.— Geometry of a spherically symmetric dust envelope: $y$ is the radial distance from the center of symmetry and $u$ is the coordinate along the optical path intersecting the radial direction at an angle $\theta$.

where $\tau_\nu^T$ is the total optical depth along the radial direction:

$$\tau_\nu^T = \int_1^\infty k_\nu(y)\,\mathrm{d}y \tag{2.29}$$

In this assumptions, the formal solution of the radiative transfer equation can be written as:

$$I_\nu(y,\theta) = I_\nu^E\,e^{-\tau(y)}\,\Theta\left[\frac{\theta_1^E}{y} - \theta\right] + I_\nu^d(y,\theta) \tag{2.30}$$

where $\Theta$ is the step function which limits the central star contribution only inside its angular size $\theta_1^E$, and the last term is the dust component of the radiative intensity:

$$I_\nu^d = \int S_\nu(y',\theta)\,e^{-[\tau_\nu(y',\theta)-\tau_\nu(y,\theta)]}\,\mathrm{d}\tau_\nu(y',\theta) \tag{2.31}$$

In a similar way, the angle averaged intensity, necessary to derive the dust thermal structure in the hypothesis of LTE, can be written as:

$$J_\nu(y) = \frac{F_1^E}{4\pi y^2}\,f_\nu^E\,e^{-\tau_\nu(y)} + J_\nu^d(y) \tag{2.32}$$

where $J_\nu^d$ is the dust diffuse average intensity, which is determined by the dust source function, and thus by the dust temperature. This last quantity require the solution of the LTE equation, that can be rewritten as:

$$k_P(T_d)\,T_d^4 = k_P(T_1)\,T_1^4\,\frac{\int k_\nu\,(1-\varpi_\nu)\,J_\nu(y)\,\mathrm{d}\nu}{\int k_\nu(1-\varpi_\nu)\,J_\nu(1)\,\mathrm{d}\nu} \tag{2.33}$$

where $k_P(T)$ is the *Planck-averaged opacity* at the temperature $T$:

$$k_P(T) = \frac{k_\nu\,B_\nu(T)\,\mathrm{d}\nu}{\int B_\nu(T)\,\mathrm{d}\nu} \tag{2.34}$$

The flux scale $\Psi$, defined as $F_1 = 4\sigma T_1^4\,\Psi$ can also be rewritten as a function of the angle averaged intensity $J_\nu(y)$; in the case of isotropic scattering, in which $g(\Omega',\Omega) = 1$:

$$\Psi = \frac{\int k_\nu\,f_\nu^E\,\mathrm{d}\nu}{k_P(T_1)}\cdot\frac{1}{1-\epsilon} \tag{2.35}$$

where

$$\epsilon = \frac{\int k_\nu\,(1-\varpi_\nu)\,J_\nu^d(1)\,\mathrm{d}\nu}{\int k_\nu\,(1-\varpi_\nu)\,B_\nu(T1)\,\mathrm{d}\nu} \tag{2.36}$$

In the optically thin limit ($\tau_\nu \to 0$) the problem can be solved analytically:

$$\frac{k_P(T)}{k_P(T_1)}\left(\frac{T}{T_1}\right)^4 = \frac{1}{y^2} \qquad , \qquad \Psi = \frac{\int k_\nu\,f_\nu^E\,\mathrm{d}\nu}{k_P(T1)} \tag{2.37}$$

From this result, it is clear that the thermal structure and flux scale are fully determined by the spectral shape $f_\nu^E$ of the external energy source (the central star), and by the temperature $T_1$ of the inner shell boundary. If $k_\nu \propto \lambda^{-\beta}$, it is easy to find the well known result (first derived by Sopka et al., 1985):

$$T = T_1\,y^{-\frac{2}{4+\beta}} \tag{2.38}$$

where $\beta \simeq 1$–$2$ for silicates and carbonaceous dust (Marengo et al., 1997).

In the case of an optically thick dust shell, the problem must be solved numerically, using an iterative method. By giving the optical properties $k_\nu$ and $\varpi_\nu$ of the dust, the initial temperature $T_1$, the dust density distribution $\eta(y)$ and the spectral shape $f_\nu^E$ of the central star, one can solve equation 2.32 for $J_\nu(y)$, with the dust temperature derived from equation 2.33

and the flux scale given by equation 2.35. This method is applied in the public domain radiative code DUSTY (Ivezić et al., 1999), where an initial guess for the solution is provided by an analytical approximation, which is then iterated until convergence.

## 2.2 Interaction between dust and radiation

The interactions between dust grains and radiation, from a microscopic point of view, are described by the absorption and scattering opacities $k_\nu^{(a)}$ and $k_\nu^{(\sigma)}$. These two quantities are related to the electrical properties of the solid material of which the dust is made.

As discussed earlier, cosmic dust grains are in general amorphous conglomerates of crystalline materials. If the molecules and atoms that form the crystalline lattice are polar, their interactions with radiation are a consequence of Maxwell laws. In particular, part of the energy of an incident electromagnetic wave is absorbed by the dipoles in the lattice, and converted into internal energy associated to molecular and atomic vibrational states, or electronic population levels. Part of this internal energy is then emitted again, at characteristic frequencies of the material dipolar structure.

In this section the physics of the microscopic interactions between dust and radiation is reviewed. Since astronomical dust exists in the form of microscopic grains, its optical properties are best described by Mie theory, which allows to approximate the opacities of particulates with a rather simplified set of assumptions. The optical properties of bulk materials are instead derived by using the Kramers-Kronig relations, widely used in laboratory measurements of opacity from thin films of material. These methods are discussed in the last section.

### 2.2.1 The refractive index of solids

Consider a single oscillator of charge $q$ and mass $m$ in an electric field $\vec{E}$ of harmonic frequency $\omega$. In a dust grain this can be the case of a polar molecule, an ion in the lattice, or a free or bound electron. The equation of motion of the oscillator displacement around its rest position $\vec{x}$ is:

$$\ddot{\vec{x}} + \gamma\dot{\vec{x}} + \omega_0^2\vec{x} = \frac{q\vec{E}}{m} \tag{2.39}$$

where $\gamma$ is a *dumping* coefficient that counts for the "friction" opposed to the oscillator motion and $\omega_0$ is the *natural frequency* of the oscillator (in a classical physics analogy, $m\omega_0$ would be the oscillator "spring constant").

The induced dipolar moment $\vec{p} = q\vec{x}$ is derived by solving the differential equation 2.39:

$$\vec{p} = \frac{-q^2\vec{E}}{m} \cdot \frac{1}{(\omega_0^2 - \omega^2) - i\gamma\omega} = \alpha(\omega)\,\vec{E} \tag{2.40}$$

where $\alpha(\omega)$ is the *polarizability* $\alpha(\omega)$ of the oscillator:

$$\alpha(\omega) = \frac{-q^2}{m} \cdot \frac{1}{(\omega_0^2 - \omega^2) - i\gamma\omega} \tag{2.41}$$

The macroscopic polarizability $\vec{P}$ of a medium made of $N$ molecules per unit volume is $\vec{P} = N\alpha(\omega)\vec{E}$. From Maxwell equation the electric displacement of such material is $\vec{D} = \epsilon\vec{E} = \vec{E} + 4\pi\vec{P}$, where:

$$\epsilon = 1 + 4\pi N\alpha(\omega) \tag{2.42}$$

is the complex dielectric constant of the material. From equation 2.41 the dielectric constant can be expressed in terms of the natural frequency $\omega_0$ and the dumping factor $\gamma$:

$$\epsilon = 1 + \frac{4\pi Nq^2}{m} \cdot \frac{1}{(\omega_0^2 - \omega^2) - i\gamma\omega} \tag{2.43}$$

With this formalism, $\epsilon$ is a complex function of $\omega$, and can thus be decomposed in its real and imaginary part:

$$\epsilon' = 1 + \frac{4\pi Nq^2}{m} \cdot \frac{(\omega_0^2 - \omega^2)}{(\omega_0^2 - \omega^2)^2 + \gamma^2\omega^2} \tag{2.44}$$

$$\epsilon'' = \frac{4\pi Nq^2}{m} \cdot \frac{\gamma\omega}{(\omega_0^2 + \omega^2)^2 + \gamma^2\omega^2} \tag{2.45}$$

Figure 2.2 shows the behavior of the dielectric constant around a natural frequency $\omega_0$ of the solid. The real part $\epsilon'$ in general *increases* with the frequency $\omega$ (*normal dispersion*). When $\omega \sim \omega_0$, however, the value of $\epsilon'$ *decreases* with $\omega$ and this is known as *anomalous dispersion*. The width of the anomalous dispersion is related to the value of $\gamma$: the larger the dumping coefficient of the oscillating dipole, the larger the anomalous dispersion region is. Similarly, the imaginary part $\epsilon''$ has a peak for $\omega \sim \omega_0$, whose width is also related to $\gamma$. Since $\gamma$ measures the efficiency of a medium to "dump" an incident electromagnetic field, e.g. to extract energy from it, it is related to the opacity of the material. The anomalous dispersion region

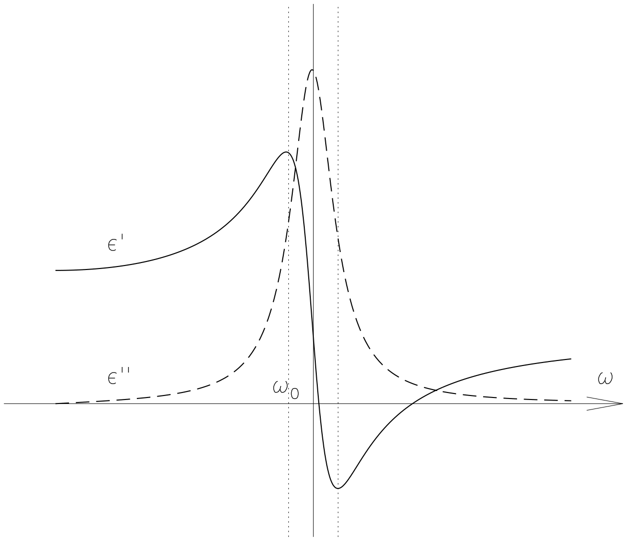

FIG. 2.2.— Real and imaginary part of the dielectric constant $\epsilon = \epsilon' + i\epsilon''$, plotted around the natural frequency $\omega_0$ of the oscillating dipole

is where the absolute value of $\epsilon$ is larger, e.g. where the radiation is mostly absorbed. A material will thus be opaque at wavelengths close to its natural frequencies $\omega_0$, and the amount of opacity is related to the magnitude of $\gamma$.

To make this explicit, one can translate the dielectric constant in terms of the complex refractive index $\mathbf{n} = n + ik$, defined as ratio between the speed of the radiation in the vacuum and in the solid. By writing the incident radiation as an idealized harmonic wave with frequency $\omega$ and wavelength $\lambda$:

$$A = A_0\, e^{i\left(\omega t + \frac{2\pi}{\lambda} x\right)} \tag{2.46}$$

the same radiation will propagate in the medium as:

$$\tilde{A} = A_0\, e^{i\left(\omega t - \frac{2\pi}{\lambda} n x\right)}\, e^{-\frac{2\pi}{\lambda} k x} \tag{2.47}$$

The imaginary part $k$ of the refraction index is thus responsible for the absorption of the incident radiation, while $n$ is the optical refraction index related to the phase shift in the transmitted electromagnetic wave. By solving equation 2.39 with a solution in the form 2.47, one can derive the relation between $\mathbf{n}$ and the complex refraction index $\epsilon$:

$$\epsilon' = n^2 - k^2 = \Re\big[\mathbf{n}^2\big] \tag{2.48}$$

$$\epsilon'' = 2nk = \Im\big[\mathbf{n}^2\big] \tag{2.49}$$

The real and imaginary part of the refraction index, and the complex dielectric function, are thus complementary parameters describing the optical properties of a certain material. They depend on the atomic and molecular constants of the medium, and in particular on the natural frequencies and dumping factors of the dipolar oscillators. In general, a solid can have as many $\omega_0$ and $\gamma$, as the number of its possible dipolar oscillators. These can be due to: (i) the orientation of polar molecules in the solid, (ii) the ionic polarization due to the relative movements of ions in the solid, and (iii) the electronic polarization due to the displacement of atomic electrons with respect to their nuclei. These three types of oscillators have different $\omega_0$, characteristic of separate regions of the electromagnetic spectrum. Solids with polar molecules will have absorption features at frequencies around $\sim 10^{11}$ Hz (millimetric wavelengths), ionic polarization will give rise to features at $\sim 10^{13}$ Hz (infrared), while electron displacement will have effects on the spectra at $\sim 10^{15}$ Hz (UV).

Since we are mainly interested to the properties of dust in the mid-IR, the optical constant of the grains at such wavelengths will be dominated by features related to the ionic vibrations in the dust lattice.

### 2.2.2 Mie Theory

Mie theory describes how spherical, homogeneous particles interact with electromagnetic radiation. It rests on the following assumptions:

- the only significant interactions are between single particles and radiation of arbitrary wavelength
- the frequency dependent optical constants ($\epsilon$ or $\mathbf{n}$) fully describe the optical properties of the particles
- the scattering of radiation from the particles is *elastic* (the wavelength of scattered radiation is the same as that of incident light)
- there is no systematic phase relation between the radiation scattered by the particles

- the medium in which the particles are distributed is *homogeneous* and *isotropic*

With Mie theory one can express the scattering and absorption opacities as a function of the optical constants. This is done by assuming the medium as made of $N$ identical particles per unit volume, interacting with a radiation of intensity $I_\nu$. From equations 2.6 and equation 2.7, the intensity of the absorbed and scattered radiation is:

$$I_\nu^{(a)} = k_\nu^{(a)} I_\nu \tag{2.50}$$

$$I_\nu^{(\sigma)} = k_\nu^{(\sigma)} I_\nu \tag{2.51}$$

The opacities $k_\nu^{(a)}$ and $k_\nu^{(\sigma)}$ are in general proportional to the number density and the geometrical cross section of the particles. The constants of this proportionality are the efficiencies of the particles material in absorbing and scattering the radiation, and are defined as:

$$Q_\nu^{(a)} = \frac{k_\nu^{(a)}}{\pi a^2 N} \tag{2.52}$$

$$Q_\nu^{(\sigma)} = \frac{k_\nu^{(\sigma)}}{\pi a^2 N} \tag{2.53}$$

By using Mie theory, the efficiencies $Q_\nu^{(a)}$ and $Q_\nu^{(\sigma)}$ can be written in terms of $\epsilon$ (see e.g. van de Hulst, 1957):

$$Q_\nu^{(a)} = \frac{8\pi a}{\lambda} \Im\left[\frac{\epsilon - 1}{\epsilon + 2}\right] \tag{2.54}$$

$$Q_\nu^{(\sigma)} = \frac{8}{3}\left(\frac{2\pi a}{\lambda}\right)^4 \Re\left[\frac{\epsilon - 1}{\epsilon + 2}\right] \tag{2.55}$$

### 2.2.3 Kramers-Kronig dispersion relations

For a bulk material, generally opaque to an incident radiation, a transmission spectra from which to measure $\mathbf{n}$ (and thus $Q_\nu^{(a)}$ and $Q_\nu^{(\sigma)}$) is not always available. In this case, the only observable is the *reflectance power* $R$, that is the ratio between the incident and reflected intensity at wavelength $\omega$:

$$R(\omega) = \frac{I_\nu^R}{I_\nu^I} \tag{2.56}$$

$R(\omega)$ is a wavelength dependent quantity related to the *reflectivity* $r(\omega)$, that gives the efficiency in which the electric field of an electromagnetic wave is reflected by the material:

$$E^R = r(\omega)\, E^I \tag{2.57}$$

As a complex quantity, $r(\omega)$ can be written in the form $r(\omega) = \rho(\omega)e^{i\theta(\omega)}$, where $\rho(\omega)$ is the magnitude of the reflectivity and $\theta(\omega)$ the phase shift between the reflected and incident wave. By solving the wave equation for $E$, one gets:

$$r(\omega) = \frac{1-\mathbf{n}}{1+\mathbf{n}} \tag{2.58}$$

Since $R(\omega) = r(\omega)r^*(\omega) = \rho^2(\omega)$, then:

$$R = \left|\frac{1-\mathbf{n}}{1+\mathbf{n}}\right| \tag{2.59}$$

thus allowing to express the real and imaginary part of the refraction index as a function of $R$ and $\theta$:

$$n = \frac{1-R}{1+R-2\sqrt{R}\cos\theta} \tag{2.60}$$

$$k = \frac{-2\sqrt{R}\sin\theta}{1+R-2\sqrt{R}\cos\theta} \tag{2.61}$$

If $R$ can be measured in the laboratory, $\theta$ is much more complex to obtain. A relation between $R(\omega)$ and $\theta(\omega)$ is however given by the Kramers-Kronig relations, which connect the real and imaginary part of any analytic function (see e.g. Jackson, 1962, p. 311). Using the Kramers-Kronig relations one can compute the value of $\theta(\omega)$ from the measured values of $R(\omega)$:

$$\theta(\omega) = \frac{-\omega}{\pi}\,\mathrm{P}\int_0^\infty \frac{\ln R(\omega') - \ln R(\omega)}{\omega' - \omega}\,\mathrm{d}\omega' \tag{2.62}$$

where P stands for the *principal part* of the integral.

### 2.2.4 Experimental determination of dust opacities

Mie theory and the Kramers-Kronig relations allow the determination of the optical constants of solids in an experimental setup, and can thus be used, in principle, to measure the opacity of cosmic dust in the laboratory. The problem, however, is the general unavailability of cosmic dust to perform the experiments (given that the meteoritic dust grains cannot be isolated in the required quantities).

Astronomical spectra should then be used, and this is possible in the case of optically thin sources, when the main component of the observed spectra is either the extincted background radiation (as for interstellar dust), or the thermal emission from a dusty envelope.

Consider the formal solution of the radiative transfer equation 2.14 for $\tau_\nu \ll 1$. In the first case (background component prevailing), the source function contribution can be neglected, and:

$$I_\nu(\mathcal{P}) \sim I_\nu(0)\,\tau_\nu(\mathcal{P}) \tag{2.63}$$

In the second case, instead, if the scattered radiation can be ignored (in a circumstellar envelope, the scattering contribution to the mid-IR spectra is usually less than 1%):

$$I_\nu(\mathcal{P}) \sim I_\nu(0)\,\tau_\nu(\mathcal{P}) + B_\nu(T_d)\,\tau_\nu(\mathcal{P}) \tag{2.64}$$

where $T_d$ is the dust temperature in the region of the dust cloud where the radiation is emitted (the dust *photosphere*).

In both cases, the observed radiation intensity is proportional to the total optical depth of the dust. If the external source spectrum $I_\nu(0)$ and the dust continuum thermal radiation $B_\nu(T_d)$ can be modeled, the observed dust spectrum can be *rectified* in order to measure $\tau_\nu$ directly from the data.

Once $\tau_\nu$ is known, the total absorption efficiency $Q_\nu = Q_\nu^{(a)} + Q_\nu^{(\sigma)}$ is derived by equations 2.52 and 2.53:

$$Q_\nu = \frac{\tau_\nu}{\pi a^2 N D} \tag{2.65}$$

where $N$ is the dust number density, and $D$ the length of the optical path $\mathcal{P}$, estimated by the physical dimensions of the dust cloud (or the circumstellar envelope).

Once the absorption efficiency $Q_\nu$ is measured for a certain astronomical source, the comparison with laboratory spectra is necessary for the mineralogical identification of the dust, and to have a set of optical constants physically consistent. The laboratory measurement of opacity is made with one of the following procedures:

- measurements of refractive angles, which allow to derive the real part of the refractive index by use of Schnell's Law. A sample of high transparency is required.

- measurement of transmittance and reflectance at near normal incidence; the sample should also be quite transparent, but not as much as in the above case. The optical constants are then derived using Mie theory.
- measurements of reflectance at near-normal incident over a wide range of frequencies. The optical constants are derived by use of the Kramers-Kronig relations.
- ellipsometric techniques, which measures amplitude ratios and phase shifts directly, but are very difficult to use.
- measurements of reflectance for incident light of various polarization states and two oblique angles of incidence. This method is also difficult to perform, since it requires large sample surfaces, usually not available.

In practice, most of the "astronomical dust" opacities are derived by measuring the transmittance and reflectance of particulates embedded in a matrix of potassium bromide (KBr) that is supposedly transparent and linear for infrared measurements. This point, however, is controversial, since (Dorschner et al., 1978) found a wavelength shift between opacities measured with this method and from bulk material. The correction they introduced is widely used, but has recently been criticized on the basis of new measurements by (Speck, 1999).

To overcome these problems, many of the most recent opacities are now measured with the reflectance method, applied to thin films of bulk material enclosed in a diamond anvil.

## 2.3 Interaction between dust and matter

Even though most of the optical extinction and infrared emission of ISM and circumstellar envelopes is provided by dust, 99% of the total mass is due to the gaseous component of the circumstellar and interstellar medium. This is even more true for the ICM, where the presence of dust is uncertain, but large amounts of hot gas are responsible for the observed strong X ray emission. The interactions between dust grains and gas can in general give rise to physical and chemical modifications of the grains, and can play an important role in the dust thermodynamic and survival.

In circumstellar envelopes and molecular clouds, dust/gas interactions are responsible for the dynamics of mass loss around giant stars, and for the chemical reactions that give rise to grain nucleation and growth. This processes are briefly discussed in chapter 4, in relation to the stellar winds of variable AGB stars.

This section focuses instead on the physical interactions mediated by the collisions of gaseous particles with the grains. If the kinetic energy of the colliding gas particles is high enough, compared with the energy density of the radiation, the heating processes of dust grains is dominated by such collisions, and the thermodynamical state of the dust can be very far from LTE. Grain charging and momentum transfer are also important, and should be considered when the dust is embedded in hot plasma, as in the case of SN remnants and ICM.

### 2.3.1 Grain charging

If the gas particles interacting with a grain are ionized, or can be ionized during the impact, then an electric charge can be transferred to the grain. The amount of the electric charge that builds up after several collisions can be very important, because determines the cross section of the grain with respect to impinging charged particles. Charging can also lead to the grain disintegration, when the accumulated charge is too high for the solid state forces that maintain the grain structure (Draine & Salpeter, 1979). Secondary particle emissions, electrons in negatively charged grains, or ions in grains with total positive charge, may however limit the total charge, thus preventing the grain destruction.

In steady state conditions, the total charge assumed in dust/ion collision is determined by the following equation:

$$\left(\frac{\mathrm{d}\mathcal{Q}}{\mathrm{d}t}\right)_{tot} = \left(\frac{\mathrm{d}\mathcal{Q}}{\mathrm{d}t}\right)_{e} + \sum_{Z} \left(\frac{\mathrm{d}\mathcal{Q}}{\mathrm{d}t}\right)_{Z} = 0 \tag{2.66}$$

where the first term refers to the electronic components of the plasma, and the sum over $Z$ is made over the positive ions. In the presence of ionizing radiation fields, a contribution $(\mathrm{d}\mathcal{Q}/\mathrm{d}t)_{ph}$ due to photoelectric effects should also be taken into account, as can increase the positive charge of the grains, when the photoelectrons escape through the grain surface (see e.g. Spitzer, 1978).

In the case of hot plasma ($T \gtrsim 10^7$ K) the grains become transparent to electrons, and are charged positively. The efficiency of grain charging is however limited by secondary electron emission. As a result, the acquired dust electric potential is significantly smaller than the mean kinetic energy of the gas particles ($q\mathcal{U}/kT \ll 1$), and the collisional cross section is thus simply given by the geometrical one (Dwek & Arendt, 1992).

### 2.3.2 Grain dynamics

Dust/gas collisions provide momentum transfer between dust grains and the gas. If $\theta$ is the incident angle in such a collision, the transferred momentum is:

$$\Delta p = \begin{cases} 2mv\cos\theta & \text{for elastic scattering} \\ mv\cos\theta & \text{for inelastic scattering} \end{cases} \tag{2.67}$$

The first case applies if the gaseous particle is reflected from the grain surface, while inelastic scattering occurs in case of absorption. If the trapped gas particle is subsequently emitted with a Maxwellian distribution of velocities at dust temperature, the final momentum can be larger than $mv\cos\theta$. This process is called *diffuse reflection* (Baines et al., 1965), and is more efficient when dust and gas temperatures are coupled and similar, as in dense molecular clouds.

In hot plasma, where the dust temperature is negligible with respect to the temperature of the gas, the momentum transfer in the release of the particle is very small, and $\Delta p \sim mv\cos\theta$. Then:

$$\frac{\Delta p_p}{\Delta p_e} \simeq \sqrt{\frac{m_p}{m_e}} \tag{2.68}$$

where $m_p$ and $m_e$ are the masses of the positive and negative charged particles (the latter are usually electrons, in which case most of the momentum transfer is due to the positive ions).

In circumstellar envelopes gas and dust are not coupled dynamically, and elastic reflection prevails, giving rise to the dragging force responsible for the envelope expansion in the winds of evolved stars (see chapter 4).

### 2.3.3 Grain destruction

The two main mechanisms for grain destruction are *thermal evaporation* and *sputtering*. The first process occurs when the grain temperature is high enough that the thermal energy $kT_d$ of the surface atoms in the high energy tail of the kinetic distribution overcomes the lattice binding energy. In this process the grain cools down, preventing further evaporation. Only when $T_d$ exceeds the dust sublimation temperature ($T_{subl} \simeq 1000$ K for carbonaceous

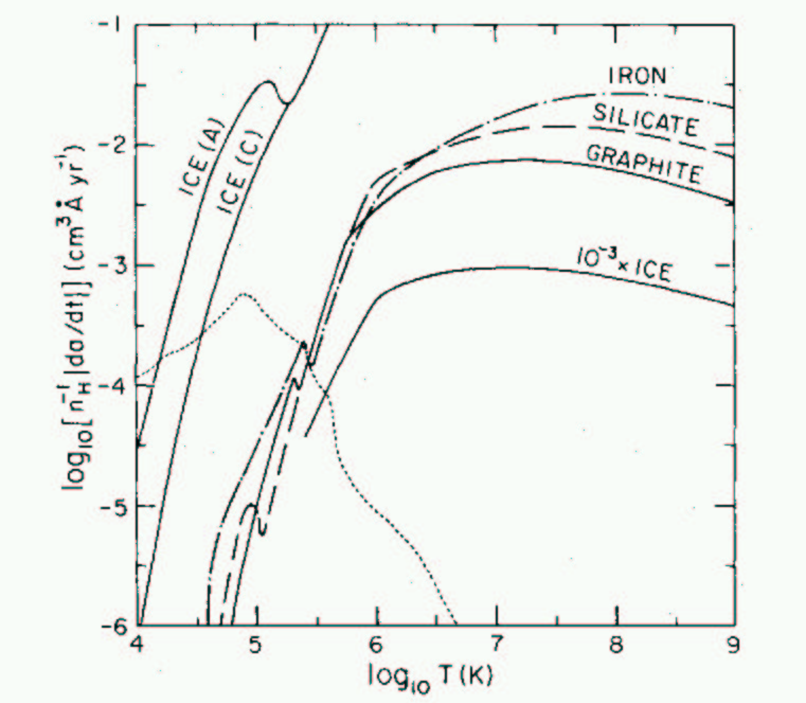

Fig. 2.3.— Sputtering rates for grains of different composition, as a function of gas kinetic temperature. From Draine & Salpeter (1979).

grains, and ≃ 1500 K for silicates), the grain completely evaporates in a short time.

*Physical sputtering* consists in the extraction of grain surface atoms by incident particles, primarily ions because of the larger energy and momentum transfers (Scalo et al., 1977). This process is to be distinguished from *chemical sputtering*, in which an incident particle bounds with a surface atom, creating an unstable molecule that eventually disintegrates, ejecting both particles from the grain (see e.g. Roth, 1983).

Dust sputtering is the main destructive process for dust in hot gas. It can be described as a cascade process, in which the incident particle first sets in motion a few target atoms, that in turn accelerate other atoms transferring enough energy to make them escape the grain. In the extreme cases in which all the atoms of the dust grain are involved, a complete evaporation takes place, and the grain is destroyed.

The sputtering lifetime is defined as the inverse of the rate in which a population of grains is depleted by sputtering, and is proportional to the grain volume $V \propto a^3$ (the number of atoms to be removed) and inversely proportional to the grain cross section $\propto \pi a^2$ and gas density $n_g$:

$$\tau_{sputt} = \frac{1}{N} \left[\frac{\mathrm{d}N}{\mathrm{d}t}\right]^{-1} \propto \frac{V}{\pi a^2\, n_g} \sim \frac{a}{n_g} \tag{2.69}$$

The sputtering rate in general depends on the grain composition and the kinetic temperature of the sputtering gas (see e.g. figure 2.3). If the temperature range is between $10^6$ and $10^9$ K this dependence can be ignored, and the following approximation is valid within a factor of 2 (Draine & Salpeter, 1979):

$$\tau_{sputt}\ (\mathrm{yr}) \simeq 10^6\, \frac{a\ (\mu\mathrm{m})}{n\ (\mathrm{cm}^{-3})} \tag{2.70}$$

### 2.3.4 Grain thermodynamics

The energy deposited by incident particles in dust/gas collisions can dominate the dust grain thermodynamics if the gas kinetic energy is higher than the energy density of the ambient radiation field. This is typical for dust surviving in a hot plasma, subjected to electrons and ions collisions.

To evaluate the separate contribution of the positive and negative ions to the collisional heating of the dust grains, assume the plasma is thermalized to a temperature $T$. Then the individual ions of mass $m$ have a Maxwellian energy and velocity distributions $f(E)$, and $v(E)$ respectively :

$$f(E) = \frac{2}{\sqrt{\pi}}\, \frac{E^{\frac{1}{2}}}{(kT)^{\frac{3}{2}}}\, e^{-\frac{E}{kT}} \tag{2.71}$$

$$v(E) = \int \left(\frac{2E}{m}\right)^{\frac{1}{2}} f(E)\, \mathrm{d}E \tag{2.72}$$

The *heating rate* of a grain is proportional to the grain cross section, the gas density, and the average energy transfer of the collisions is:

$$H_{coll} = \pi a^2 n_g \int_0^\infty f(E)\, v(E)\, E \zeta(E)\, \mathrm{d}E \tag{2.73}$$

where $\zeta(E)$ is the efficiency in which the energy of the ionic particle is transferred to the dust grain. In the case of incident electrons, this function is given by Dwek & Werner (1981):

$$\zeta(E) = \begin{cases} 1 & \text{for}\, E \lesssim E_* \\ 1 - \left[1 - \left(\frac{E_*}{E}\right)^{\frac{3}{2}}\right]^{\frac{2}{3}} & \text{for}\, E > E_* \end{cases} \tag{2.74}$$

This approximation reflects the idea that for impact energy lower than a critical value $E_*(\mathrm{erg}) \simeq 3.7 \cdot 10^{-8} a^{2/3}(\mu\mathrm{m})$ the electron energy is completely absorbed, while for higher energies the grains starts to become transparent to the impinging electrons.

By substituting the explicit form of the Maxwell distributions in equation 2.73, one obtains:

$$H_{coll} = \sqrt{\frac{8}{\pi m}} \frac{n_g}{(kT)^{3/2}} \int_0^\infty x^2 e^{-x}\, \zeta(E)\, \mathrm{d}x \tag{2.75}$$

Notice that $H_{coll} \propto m^{1/2}$, and thus electron collisions prevails as heating sources of dust in a hot plasma. The average *time* between successive ion/grains collisions is defined as the reciprocal of the *collision rate*:

$$R_{coll} = \pi a^2 n_g \int_0^\infty v(E)\, f(E)\, \mathrm{d}E \tag{2.76}$$

Since $\tau_{coll} = (R_{coll})^{-1} \propto m^{1/2}$, again electronic collisions due to the lower mass particle prevails.

If a grain is not evaporated by the energy input of an electron collision, its initial temperature is gradually restored by radiative cooling. The *radiative cooling rate* is given by the total flux irradiated by the dust grains, as in equation 2.19:

$$\Lambda_{rad}(T) = \int_0^\infty k_\nu B_\nu(T)\, \mathrm{d}\nu \tag{2.77}$$

$$= 4\pi a^2\, Q_P(T)\, \sigma T^4 \tag{2.78}$$

where $Q_P(T)$ is the *Plank averaged absorption efficiency* defined similarly to the Planck averaged opacity $k_P$ in equation 2.34:

$$Q_P(T) = \int_0^\infty Q_\nu\, B_\nu(T)\, \mathrm{d}\nu \tag{2.79}$$

The *radiative cooling time* $\tau_{cool}$ is defined as the total time needed by a grain to change its temperature from $T_i$ to $T_f$:

$$\tau_{cool}(T_i, T_f) = \int_{T_i}^{T_f} \left| \frac{\mathrm{d}T}{\mathrm{d}t} \right|^{-1} \mathrm{d}T \tag{2.80}$$

where

$$\frac{\mathrm{d}T}{\mathrm{d}t} = \frac{1}{c_V(T)} \left[ H_0 - \Lambda_{rad}(T) \right] \tag{2.81}$$

is inversely proportional to the volume heat capacity of the grain material at the given temperature $c_V(T)$, and to the difference between the radiative cooling and the minimum heating rate $H_0$ provided by the background radiation field. This last term can in principle be expressed as a function of the temperature $T_0$ which the grain would have if in equilibrium with the ambient radiation field:

$$H_0 = 4\pi a^2 \, Q_P(T_0) \, \sigma T_0^4 \tag{2.82}$$

Note that if $H_0 \sim \Lambda_{rad}$ then the cooling time will be infinite, and the grains will be at the equilibrium temperature $T_0$ of the radiation field. This is the case, for example, of dust in circumstellar envelopes that is in LTE with the radiation (and $T_0$ is the local equilibrium dust temperature $T_d$). In the case of ICM dust, however, $\Lambda_{rad} \gg H_0$, and the main source of energy for the dust are the collisions with the electrons in the ICM plasma; the minimum temperature $T_0$ is defined as the temperature of the cosmic background radiation, or the equilibrium temperature that the dust would have with respect of the X-ray radiation emitted by the gas.

According to the ratio between the cooling and collision time, dust grains are in thermal equilibrium with the gas, or will oscillate between successive heating and cooling at each collision: in this case the thermal status of the dust is described by a statistical distribution of temperatures, in what is called a *stochastic heating* process. An example of stochastic heating is provided by dust in the ICM, and is discussed in chapter 6.

# Chapter 3

# Tools for mid-IR analysis of AGB dust

Mid-IR is the ideal spectral range to study circumstellar dust. The presence of broad features in the opacity of grain commonly formed in the extended atmosphere of giant stars, in principle allows a precise identification of the mineralogical species by analyzing the 10 $\mu$m spectra. The temperature gradients in circumstellar envelopes, with dust in equilibrium with the environmental radiation field, are such that the bulk of the grain thermal radiation is emitted in the 10 $\mu$m region. Since the optical thickness of many circumstellar envelopes, especially around AGB stars, is high enough to make them completely opaque at visible wavelengths, mid-IR is the only accessible spectral window for probing the central region of these systems.

For these basic reasons the IRAS database has been widely used for the development of diagnostic tools able to probe the chemical and physical status of circumstellar envelopes from their infrared emission. This approach, however, is limited by the low spatial and spectral resolution of IRAS data, and the impossibility to make repeated observations of variable sources. Even though a limited number of sources have been subjected to new observations with the european satellite ISO, these issues have not been completely resolved, due to the short duration of the mission, serious calibration problems and the still inadequate spatial resolution. These limitations confirm the need for ground based high resolution facilities, monitoring the status of AGB circumstellar envelopes in the mid-IR over long periods of time.

This chapter is devoted to the presentation of a new set of tools for the analysis of ground-based mid-IR photometry of AGB circumstellar envelopes. The results of this analysis have been presented in the paper Marengo et al. (1999), and have been obtained in collaboration with Maurizio Busso at the Astronomical Observatory of Torino (Italy), Giovanni Silvestro at the “Dipartimento di Fisica Generale”, University of Torino (Italy), Paolo Persi at the “Istituto di Astrofisica Spaziale” of the Italian National Research Council (C.N.R. Roma) and Pierre-Olivier Lagage at the “Service d’Astrophysique”, CEA Saclay (France).

A sample of AGB sources with known mass loss rates, introduced in section 3.3.2, is used for calibration purposes, and to explore the correlations between the infrared emissions and mass loss of the selected sources. The calibration is then confirmed by radiative transfer modeling of spherically symmetric AGB systems, as it is described in detail in section 3.2.

## 3.1 Asymptotic Giant Branch Stars

It has already been pointed out that AGB stars are collectively the main source of *stardust* in the Galaxy. Providing a large fraction of the carbon from which the solar system (and ultimately, the biological life) is made, AGB stars play an important role in the chemical evolution of the ISM. AGB stars contribute a large fraction of the infrared luminosity of galaxies, and are thus one of the main components of stellar population synthesis models aiming to reproduce galactic spectra in the IR. Finally, stars on the AGB represent an almost ideal laboratory for nuclear physics and stellar evolution theories, since convection reaching their internal burning shells drags to the surface recently synthesized nuclei, exposing them to direct observation.

In all these processes, the less known ingredient is probably the strong mass loss that characterize the AGB phase, which is enhanced by the presence of dust, and powered by even less known processes of dust nucleation in the stellar extended atmosphere.

The analysis of the AGB circumstellar envelopes from the point of view of mid-IR astronomy, to which a large part of this thesis is devoted, should thus be seen as an effort to open a new channel for researching one of the key factors in the evolution of the Galaxy, and the physics involved.

In this section the relevant facts about AGB stars are given. For a more general discussion of AGB evolution and nucleosynthesis the reader is referred to Busso et al. (1999) and Wallerstein & Knapp (1998), where the various classes of carbon stars are discussed in length.

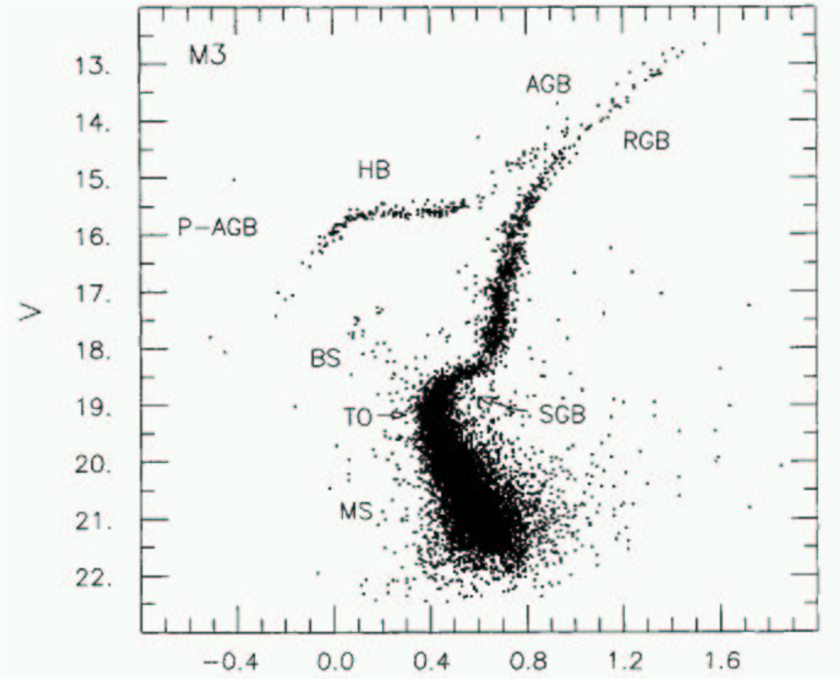

FIG. 3.1.— The Asymptotic Giant Branch in the Hertzsprung-Russel diagram of the globular cluster M3. Adapted from Renzini & Fusi Pecci (1988)

### 3.1.1 Evolution of low and intermediate mass stars

The Asymptotic Giant Branch phase represents the second ascent of intermediate and low mass stars in the red giant region of the Hertzsprung-Russel diagram (see figure 3.1). Stars with main sequence mass below 6-8 $M_{\odot}$, after the exhaustion of H core burning, rise the Hayashi tracks in the HR diagram, gradually reaching higher luminosities and lower effective temperatures. This is done with the expansion of their convective envelope by several orders of magnitude, ending with a stellar radius of the order of a few A.U. Sustained by nuclear burning of H in a shell, around an inert He core, these stars populate the region of the HR diagram known as Red Giant Branch (RGB).

Towards the end of the RGB, the convective envelopes of giants reach the internal layers of these stars, processed by previous nucleosynthesis. As a result, the surface abundance of $^{14}$N is doubled, $^{12}$C is reduced by 30% and Li and Be are diluted by several orders of magnitude (Iben & Renzini, 1983). This process is called *first dredge-up*.

The RGB phase ends with the ignition of the He shell, which replaces the H shell as main energy source; the star contracts, increase its effective temperature, and enters in the *Horizontal Branch* (HB). Low mass stars, having $M_i \lesssim 1.8$–$2.2$ $M_\odot$ (Chiosi et al., 1992), which develop a degenerate He core during the RGB, experience the so-called He-flash, in which the degeneration is removed. Intermediate mass stars, on the contrary, start core He burning in normal conditions, in the *blue band* region of the HR diagram, which ends with a rapid contraction of the H convective envelope (*blue loop*).

In both cases, the HB phase ends with the creation of an inert C-O core, around which a burning He shell is active. Stars with $M_i \gtrsim 6$–$8$ $M_\odot$will instead ignite C burning in the core, starting a path which will ultimately lead to their explosion as Type II supernovæ.

The Sun is a low mass stars, and will thus become a Red Giant after leaving the main sequence. This moment in the solar evolution will mark the destruction of the inner solar system, among which the planet Earth.

### 3.1.2 The Early-AGB phase

The AGB starts with the exhaustion of He core burning, and is divided in two phases: Early-AGB (E-AGB) in which the He burning shell provides all the energy necessary to sustain the stellar structure, and the thermal pulsing AGB (TP-AGB) which is characterized by the alternate ignition of two concentric He and H shells.

The E-AGB is accompanied by a progressive contraction of the core, which become highly degenerate ($\rho_c \sim 10^6$ g cm$^{-3}$) and isothermal, due to the high conductivity of the Fermi pressure of free degenerate electrons. The high efficiency of neutrino cooling processes (Urca) helps to mantain a low core temperature ($Tc \sim 2 \cdot 10^8$K), well below the C ignition temperature.

At the end of the E-AGB, intermediate mass stars experience a *second dredge-up*, in which elements processed by the CNO cycle are taken to the surface, which increases in abundance of $^4$He and $^{14}$N, at the expense of $^{12}$C and $^{16}$O.

The E-AGB phase ends when the He shell is extinguished, and the H burning starts again in a new external shell. This typically happens when the mass of the H depleted core reaches the critical value of $\sim 0.5$–$0.6$ $M_\odot$ (Becker & Iben, 1979).

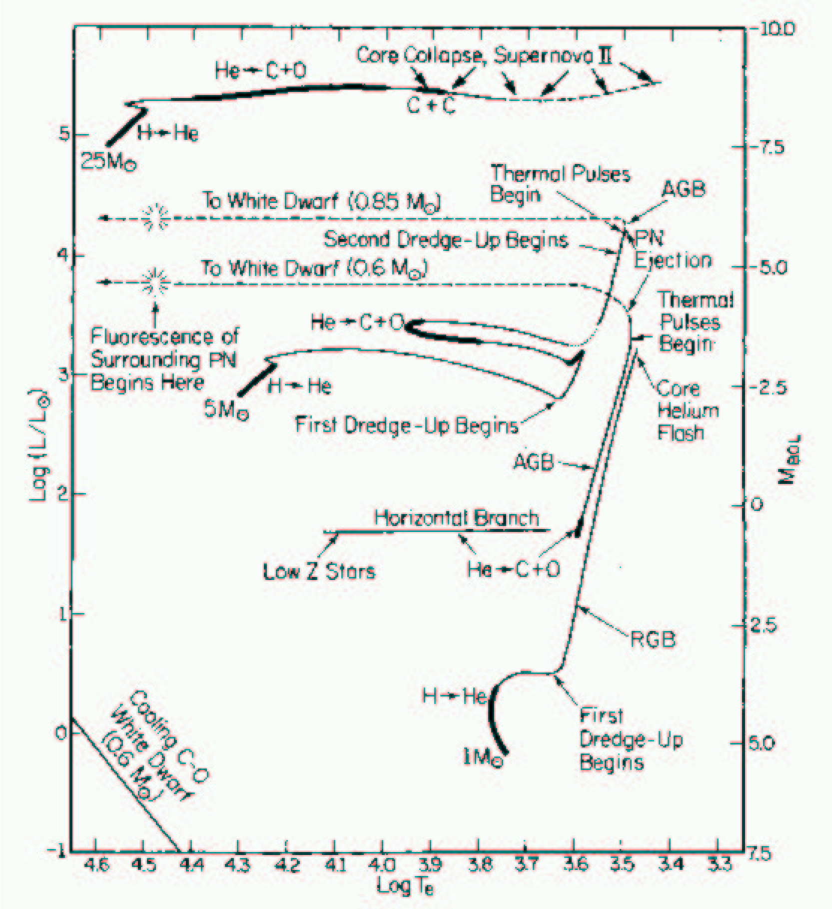

FIG. 3.2.— Tracks on the HR diagram of theoretical model stars of low (1 $M_\odot$), intermediate (5 $M_\odot$) and high (25 $M_\odot$) mass. From Iben (1991)

### 3.1.3 The TP-AGB phase and the third dredge-up

The second part of the AGB is characterized by thermal instabilities called *thermal pulses*. A thermal pulse occurs when the He shell, which continously increases in mass due to the burning of the external H shell, is momentarily ingnited and expands. This expansion is reversed when the temperature drops below the minimum necessary for He burning; the He shell is extinguished again and the H burning restarts. The duration of the He shell activity is very short ($\sim 10^2$ yr), and the cycle is repeated every $10^3$-$10^4$ yr. The lenght of the interpulse period is a function of the C-O core mass, and can thus be quite different between low and intermediate mass stars:

$$\tau_{ip} \sim 2 \cdot 10^5\,\mathrm{yr}\left(\frac{0.6\mathrm{M}_\odot}{M_{C-O}}\right)^{10} \tag{3.1}$$

In fact, since the core mass is increased at each thermal pulse with the C and O produced during the He burning, the interpulse period becomes shorter at the very end of the TP-AGB, when a rapid sequence of thermal pulses is experienced. During a thermal pulse, the luminosity produced by the star is largely increased; in the long interpulse phase, however, the total luminosity tends asymptotically to a value controlled by the H depleted core mass (Paczynski, 1970; Uus, 1970):

$$L_{max} = 5.925 \cdot 10^4 \left(\frac{M_H}{1\,\mathrm{M}_\odot} - 0.495\right)\mathrm{L}_\odot \tag{3.2}$$

Immediately after a thermal pulse, the base of the convective envelope penetrates (in mass) in the regions that contains freshly produced elements, causing a new dredge-up (*third dredge-up*). The third dredge-up is responsible for the increase of surface abundance of C, in stars which are initially O-rich M giants. Neutron rich elements produced during the thermal pulses by repeated exposures with intense neutron fluxes (*s-elements*) are also dragged to the surface. Since many s-elements are short lived radioactive nuclei (as in the case of Tc), their detection in a stellar spectra is the best evidence that the object is presently in the TP-AGB phase.

Recently updated stellar models (Straniero et al., 1995, 1997) found that, for solar metallicity, stars above the 1.5–2 $\mathrm{M}_\odot$ can undergo a sufficient number of third dredge-up episodes to drive an increase of the C/O ratio above unity. When this happens, a *carbon star* is born. On the other end, AGB stars with $M_i \gtrsim$ 5-6 $\mathrm{M}_\odot$ experience partial H burning at the base of the convective envelope, or Hot Bottom Burning, HBB, (see e.g. Sugimoto, 1971; Renzini & Voli, 1981; Blöcker & Schönberner, 1991; Sackmann & Boothroyd, 1992; Vassiliadis & Wood, 1993; Frost et al., 1998). This consumes the newly produced C, preventing the star from becoming C-rich, and enriches the stellar surface with Li (however, see Frost et al., 1998, for an alternative evolutionary path). As a result, C stars can probably be formed at the end of the AGB evolution, only for a quite narrow mass range (2–4 $\mathrm{M}_\odot$), with more massive stars remaining as Li-rich objects, generally of class S if the abundance of s-elements is high enough to be observable (Smith & Lambert, 1989).

During the TP-AGB phase, the mass loss already present in the RGB and E-AGB is enhanced, due to the formation of dust in the stellar extended

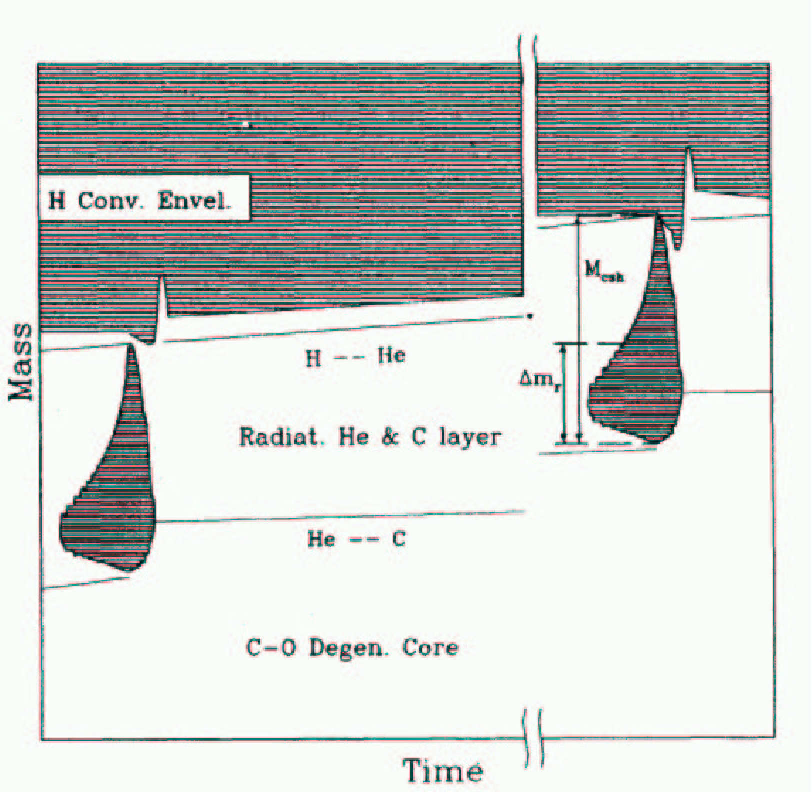

FIG. 3.3.— Simplified sketch of the structure of the stellar layers outside the degenerate C-O core, during two successive thermal pulses. Shaded regions are convective, and dredge-up from the convective envelope is shown after each pulse. From Busso et al. (1995)

atmosphere, powering strong stellar winds at the expenses of the stellar convective envelope. The end of the AGB comes when the star is totally depleted of its convective envelope, and the hot degenerate core is exposed. The star then becomes a post-AGB object, on its way to its final state of white dwarf.

### 3.1.4 The AGB mass loss

Mass loss is a common characteristic of giant stars; what is peculiar of the AGB phase, however, is the *magnitude* of the mass loss rate, which in just a few final stellar pulses transforms an intermediate mass star into a 0.5–0.6 $M_\odot$ white dwarf. Where does all the convective envelope mass go? It

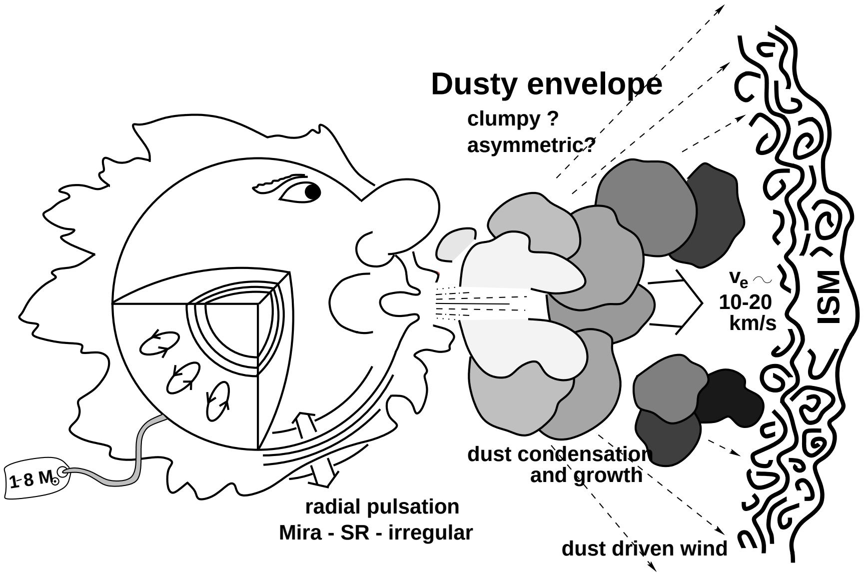

FIG. 3.4.— The main components of an AGB system: the central TP-AGB star producing a strong *dust driven* stellar wind, and the dusty circumstellar envelope merging with the ISM. From Marengo et al. (2000b)

ends up dispersed in the circumstellar environment, with the creation of a circumstellar envelope of gas and dust which will ultimately merge with the ISM (see section 1.2.3).

A complete theory able to explain the required mass loss rates (up to $10^{-4}$ $M_\odot$ yr$^{-1}$) is presently unavailable. The RGB mass loss can be easily explained by using a *Reimers wind* formula, in which the mass loss rates is a function of the stellar luminosity, radius and mass (Reimers, 1975):

$$\dot{M} \sim 4 \cdot 10^{-13}\,\mathrm{M}_\odot\,\mathrm{yr}^{-1}\,\eta\,\left(\frac{L_*}{1\,\mathrm{L}_\odot}\right)\left(\frac{R_*}{1\,\mathrm{R}_\odot}\right)\left(\frac{1\,\mathrm{M}_\odot}{M_*}\right) \tag{3.3}$$

where $\eta$ is a fudge factor between 1/3 and 3. The mass loss predicted by the Reimers formula is largely insufficient to describe the AGB mass loss rates. Larger values of $\dot{M}$ can be obtained applying a semi-empirical formula derived by Salpeter (1974), in which is assumed that the total momentum of the expanding envelope is given by the radiation pressure acting on the circumstellar dust grains:

$$\dot{M} \sim 2 \cdot 10^{-8}\,\mathrm{M}_\odot\,\mathrm{yr}^{-1}\,\tau_V\,\left(\frac{L_*}{1\,\mathrm{L}_\odot}\right)\left(\frac{1\,\mathrm{km\ s}^{-1}}{v_e}\right) \tag{3.4}$$

where $\tau_V$ is the total optical depth of the envelope (mainly given by the dust), $v_e$ is the envelope expansion speed, and $L_*$ the stellar luminosity.

Many modifications of these two mass loss formulas, specifically written for the AGB phase, have been proposed; a good review is given in Habing (1996). As in the case of Salpeter's wind, the main idea is that the AGB wind is powered by the stellar radiation acting on the dust grains, which then transfers the momentum to the gaseous component of the envelope (*dust driven winds*). The only difficulty with this idea is that it requires a separate "engine" to accumulate enough material to start up the process at a suitable distance from the star, where the temperature is low enough to allow dust grain condensation. To solve this problem, the effects of radial pulsations related to the long period variability of many AGB stars, are invoked: this scenario is discussed in detail in chapter 4, where the correlation between mass loss and stellar variability via radiative transfer modeling of the observed IR spectra is analyzed.

In any case, the AGB mass loss is strong enough to enshroud low and intermediate mass stars with optically thick circumstellar envelopes made at the expense of the stellar convective envelopes, thus preventing such stars to grow their core mass above the limits that would otherwise lead to a Type II supernova event, as is the case for the fast evolving massive stars. The death of an AGB star (and thus of our Sun) is a quiet one, and happens hidden inside dusty cocoon: "*old soldiers never die, they simply fade away*" (from Habing, 1990).

### 3.1.5 The post-AGB phase, and beyond

The post-AGB is a brief transition phase in which the star leaves the tip of the AGB, crossing the HR diagram at constant luminosity towards the white dwarf region. Most of the post-AGB objects are heavily obscured by their optically thick dust envelopes, that dissipate only when the effective temperature of the star becomes high enough to trigger the formation of a fast pressure-driven *superwind*, which blows away the AGB envelope. When this happens, the energetic radiation from the hot central object, now a white dwarf, ionizes and excites the circumstellar molecular gas, creating a Planetary Nebula.

The creation of a planetary nebula is a complex phenomenon which involves time dependent hydrodynamics and radiative transfer. A simplified model was created by Kwok et al. (1978), by assuming a process of *interacting stellar winds* (the slow moving AGB wind, responsible for the dusty circumstellar envelopes, and the fast post-AGB superwind). This model shows that, after the onset of the superwind, the shock front that propagates through the fossil AGB envelope completely changes its structure, making worthless any attempt to reconstruct the mass loss history of the AGB precursor from the density profile of the PN dusty halo. High resolution imaging of the AGB and post-AGB phases, which are before the start of the superwind, are thus necessary to probe the history of mass loss by observing the circumstellar envelope.

The interacting stellar winds model, however, cannot deal with the complex morphology observed in PN. As shown in the gorgeous gallery collected by the Hubble Space Telescope, many, if not all, of the planetary nebulæ possess various degree of asymmetry. HST and Mid-IR imaging surveys have revealed that these asymmetric structures are already present in the post-AGB phase (Ueta et al., 2000; Meixner et al., 1999); it is not clear, however, when the departure from sphericity starts, since AGB stars are presumed to be spherically symmetric systems.

## 3.2 Modeling the mid-IR spectra of AGB envelopes

The main tool to study the infrared spectral energy distribution of AGB circumstellar envelopes is represented by radiative transfer modeling. This is a common practice, that has been applied to derive the physical parameters of AGB dust shells by many authors (Rowan-Robinson, 1980; Griffin., 1990; Justtanont & Tielens, 1992; Hashimoto, 1995; Ivezić & Elitzur, 1995; Marengo et al., 1997, and many others). All these works have been using a model based on the fundamental equations described in section 2.1, in the approximation of spherical symmetry, and envelope radial density structure determined by the hypothesis of steady mass loss ($n_d \propto y^{-2}$) or static dust driven wind (Ivezić & Elitzur, 1995). More recently, sophisticated models taking into account time dependent hydrodynamics (Steffen et al., 1998), dust formation and dynamic coupling between the base of the circumstellar envelope and a fully self-consistent pulsating AGB stellar atmosphere (Winters et al., 1994; Windsteig et al., 1997; Höfner & Dorfi, 1997) have been developed. Two dimensional models able to deal with complex envelope geometries (Lopez et al., 1995) have also been applied to specific sources, whose images were showing actual departures from spherical symmetry.

Due to the nature of the data to which our analysis is aimed (photometry of low resolution spectra of unresolved sources), we have chosen to adopt the DUSTY code (Ivezić et al., 1999) to provide 1D radiative transfer modeling of stationary circumstellar envelopes in spherical symmetry. Although

DUSTY does offer the option to solve the hydrodynamic of self consistent radiative driven winds, we have chosen to disable this feature, in order to simplify the basic assumptions in our parameter grid.

As described in sections 2.1.5 and 2.1.6, a complete model of spherically symmetric AGB dusty envelopes is essentially described by the following parameters: (1) the total optical depth $\tau_V$ of the envelope, (2) the temperature $T_1$ of the inner boundary of the dust shell, (3) the shape of the spectral energy distribution of the central star and (4) the optical properties of the dust. In the following sections our choices for these modeling parameters are described. The models thus produced are then used in section 3.3 for the calibration of our mid-IR tools. In chapter 4 the same models are used to study correlations between AGB long period variability and the temporal modulation of their mass loss, and in chapter 5 to analyze our mid-IR images of selected AGB sources.

### 3.2.1 Opacities for AGB circumstellar dust

The chemical characterization of AGB circumstellar envelopes enters in the modeling procedure with the choice of a suitable opacity. According to the C/O abundance ratio, the chemistry of dust formation favors the condensation of either C-rich (around carbon stars) or O-rich dust (in low mass M-stars, or intermediate mass HBB AGBs). Separate opacities for the two cases are needed, in order to simulate the two classes of objects.

Since its discovery (Wolf & Ney, 1969), the 9.8 $\mu$m feature observed in the spectra of O-rich AGB stars was associated with the presence of silicate dust in the circumstellar environment. Early attempts to reproduce the energy distribution of the observed sources using the optical properties of laboratory grains failed, due to the inadequacy of crystalline terrestrial silicates (pyroxenes, olivines) to explain the high opacity of astronomical dust in the near-IR. The concept of *dirty silicates* was thus introduced by Jones & Merrill (1976), referring to an undetermined mixture of amorphous and crystalline materials, containing various types of impurities responsible for the required increase in opacity.

A widely used opacity for astronomical silicates was then derived by Volk & Kwok (1988), by manually adjusting the dust absorption coefficients used in their radiative transfer model, in order to reproduce the average spectra of O-rich envelopes with low optical depth and similar colors. From this opacity, Ossenkopf et al. (1992) computed two sets of optical constants, chemically and physically consistent according to the Kramers-Kronig relations and Mie theory (see sections 2.2.3 and 2.2.2). The two set of opacities

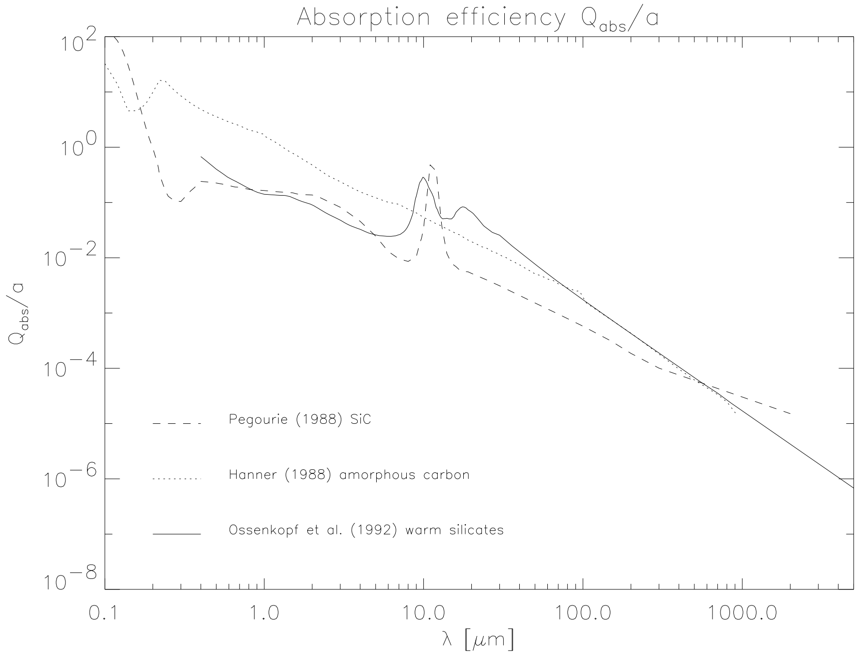

FIG. 3.5.— Dust opacities used in DUSTY modeling of our AGB envelopes. Amorphous carbon from Hanner (1988) (dotted line), SiC from Pégourié (1988) (dashed line), and "astronomical" silicates from Ossenkopf et al. (1992), warm set (solid line)

take into account the possibility of dust annealing in the circumstellar environment, as described by Stencel et al. (1990) and Nuth & Hecht (1990). The first set is optimized for "warm" silicates (expected to be found in sources with low optical depths, in which the oxidation of the silicate grains is not complete), and the second for the "cold" silicates (characteristics of very opaque envelopes, with "evolved" dust having higher content of Fe).

Since most of the sources in our test sample have low or intermediate optical depth, we have based our analysis on the adoption of the Ossenkopf et al. warm silicates opacity only, that are available in the standard DUSTY distribution.

A word of caution: is evident by the process in which such opacities have been produced, that they should be considered only as an "average" for the whole class of O-rich AGB circumstellar envelopes with low optical depth. By no means they can reproduce the exact shape of the 9.8 $\mu$m silicate feature for all sources, since a certain mineralogical variability should be expected between sources having different evolutionary status and metallicity.

In particular, Volk & Kwok arbitrarily set the ratio between the 10 and 18 $\mu$m features to be 0.5, while finding a possible range between 0.4 and 0.7, and this problem has only been partially fixed by Ossenkopf et al. increasing the ratio to the value of 0.55, which provides a better fit of laboratory data. A variation in this number, however, should still be expected, according to the relative abundance between Fe and Mg in the silicate structure. Furthermore, Ossenkopf et al. opacities cannot reproduce the observed 13 $\mu$m feature found in the IRAS spectra of many sources (tentatively associated to the presence of $Al_2O_3$ grains, see e.g. Onaka et al. 1989), or fit the crystalline silicate features observed in the ISO spectra of other envelopes. Even though suitable opacities for many amorphous and crystalline silicates and oxide materials are now available, and have been used to test the detailed chemical composition of individual envelopes (see e.g. Speck, 1998), such kind of analysis is outside the scope of this work. We are more interested in the determination of the thermal and density structure of AGB envelopes as a class, and thus our priority lies in fitting the whole LRS spectral region, and not in the details of the silicate feature alone. For this reason, the choice of the "warm" Ossenkopf et al. opacity appears to be adequate.

Concerning the opacity of dust in C-rich envelopes found around carbon stars, at least two main components are required, as many sources show the 11.2 $\mu$m SiC emission feature, along with a continuum associated to amorphous carbon. Even though SiC is present in nature in two main forms, the hexagonal-romboedric $\alpha$-SiC, and $\beta$-SiC with cubic crystalline structure, only $\alpha$-SiC produces a stable feature at 11.2 $\mu$m. For this reason we have chosen the opacity by Pégourié (1988) which was derived by applying Mie theory to $\alpha$-SiC laboratory data. To simulate the continuum opacity due to amorphous carbon, we have adopted the optical constants measured by Hanner (1988), also implemented in the DUSTY code.

Since different AGB envelopes having the same infrared excess (e.g. similar total optical depth) does show SiC features with different intensity, it will be assumed that the relative abundance of SiC and amorphous carbon can be variable. In principle, the combined opacities of amorphous carbon and SiC should depend on the way the two species are mixed (SiC micrograin embedded in an amorphous carbon matrix, or coating of one material around a core of the other, etc...). In the absence of experimental data on this subject, we have chosen to produce the total opacity $Q_{abs}^{tot}$ as the weighted average of the two single absorption coefficients:

$$Q_{abs}^{tot} = (1-x)\, Q_{abs}^{amC} + x\, Q_{abs}^{SiC} \tag{3.5}$$

where $x$ is the relative abundance (in number density) between the number density of SiC grains and the total. Our model grid for the C-rich envelopes is characterized by $x$ from 0 (no SiC) to 0.14.

From equations 2.54 and 2.55 it is evident that the total opacity, at least in the range of sizes of AGB circumstellar grains, depends linearly on the radius $a$; the global optical properties of the dust in each envelope will thus depend on the adopted grain size distribution. For our grid of models, we have chosen to use the standard MRN distribution (see section 1.2.2), with grain size in the interval $0.005 \lesssim a \lesssim 0.25$ $\mu$m. This choice is justified by the greater uncertainty that are present the dust optical constants themselves, but should be regarded as a crude approximation of the real distribution, which may be enhanced toward larger grains in envelopes where grain growth is favored.

### 3.2.2 Model spectra for the central AGB star

At mid-IR wavelengths, where the dust thermal emission is maximum, the radiation of the central star contributes for only a small fraction of the total source spectra. For this reason, the spectrum of the AGB star powering the envelope can be in many cases approximated with a warm black body ($T_{eff} \sim$ 2000–3500 K). After running a number of test model grids with various $T_{eff}$, we concluded that the best results for the whole test sample of sources was obtained with $T_{eff} \sim 2000$ K; we have thus adopted this value for our full grid of models. One should take into account, however that in the mid-IR range the final spectra is not really sensitive to small variations in $T_{eff}$, and the chosen value is thus only representative of the observed spread in the effective temperature along the Asymptotic Giant Branch of the HR diagram.

A corollary of the scarce sensitivity of mid-IR to the stellar effective temperature, is the low precision in attempting to estimate the distance of AGB sources by fitting the mid-IR spectra. Due to the scaling properties of radiative transfer (see section 2.1.5), once the scaling factor $\Psi$ is determined by fitting the source spectra, the spatial scale of the system is given by the ratio between $T_1$ and the $T_{eff}$:

$$\Psi = 4 \left(\frac{R_1}{R_*}\right)^2 \left(\frac{T_1}{T_{eff}}\right)^4 \tag{3.6}$$

Due to the poor determination of $T_{eff}$ (and the fact that the ratio $T_1/T_{eff}$ is elevated at the fourth power), also $R_1$ (and thus the bolometric

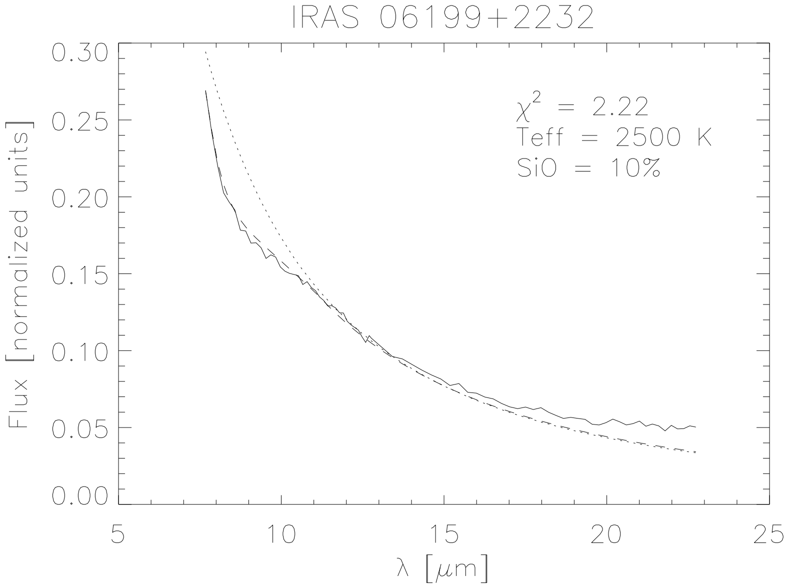

FIG. 3.6.— The spectrum of $\mu$ Gem (solid line) compared with an Engelke function of $T_{eff}$ = 2500 K and SiO absorption of 10% (dashed line), and a black body with the same $T_{eff}$ (dotted line). The source is a "naked photosphere" of spectral type M3III. Note the lower quality of the fit for $\lambda \gtrsim 15$ $\mu$m: an accurate model at larger wavelengths requires to add a dust cold shell with $\tau_V \simeq 10^{-3}$ and $T_1 \simeq 140$ K, showing that even this source (not an AGB) is surrounded by dust.

flux, see equation 2.25), cannot be well measured. A much better determination of the source distance requires a more precise fit of $T_{eff}$, that can be obtained only by detailed modeling of the stellar spectra, when the dust extinction is not excessive at optical and near infrared wavelengths.

For optically thin sources, a larger contribution from the central star should be expected. For these sources we have tested an alternative spectral distribution for the AGB star, that in principle should be more accurate in reproducing the continuum of late type giant stars. As described in Cohen et al. (1992), the main shortcoming of black bodies, when used to reproduce the spectrum of cool O-rich (M type) stars, is the presence of neutral hydrogen absorption and SiO line blending in the 8–10 $\mu$m range. This first feature can be effectively modeled using a wavelength dependent modification of the Planck black body, known as "Engelke function" (Engelke, 1992):

$$B_\nu^{(Engelke)}(T_{eff}) = B_\nu^{(Planck)}(T_b) \tag{3.7}$$

$$T_b = 0.738 \cdot T_{eff} \left( \frac{79450}{\lambda \cdot T_{eff}} \right)^{0.182} \tag{3.8}$$

where $T_b$ is the color dependent *Engelke temperature*, which substitutes the effective temperature $T_{eff}$ in the Planck function.

As a model for the SiO absorption, we have used the $\alpha$ Tau spectrum collected by Cohen et al. (1992). By subtracting an appropriate Engelke function with $T_{eff}$ = 10,000 K from the $\alpha$ Tau spectrum, we extracted the features related to SiO absorption for that star. In order to produce a model of such absorption scalable for different amount of SiO, we have fitted the $\alpha$ Tau SiO feature with a 5th order polynomial. The generic AGB model spectra with given $T_{eff}$ and SiO is then produced adding to the Engelke function the SiO fit polynomial, renormalized to produce the requested absorption at the nominal wavelength of 8 $\mu$m.

Even though this approximation is not a real SiO absorption spectrum, it can considerably improve the fitting of optically thin AGB sources and other “dustless” giants at IRAS LRS wavelengths, as shown in Sloan & Price (1995); an example is given in figure 3.6. This modified Engelke function with arbitrary $T_{eff}$ and SiO absorption is part of the DUSTY distribution since version 2.0.

In the following discussion, to provide the best possible stellar photosphere without having too many free parameters, we have adopted, along with the “standard” black body with $T_{eff}$ = 2500 K, an Engelke function with $T_{eff}$ = 2500 K and SiO absorption of 10% as model photosphere for a second set of DUSTY simulations of O-rich envelopes.

### 3.2.3 Model parameter space

In order to reduce the number of models necessary to fit all the sources in our sample, we have restricted the free parameters in our DUSTY simulations to the optical depth $\tau_V$, and the dust temperature $T_1$ at the inner envelope radius. This last quantity can either be seen as the dust condensation temperature for systems which are actively producing dust at present time, or the temperature at radius $R_1$ of the central cavity, which forms when the shell is detached due to a quiescent phase in the dust production. If the radius $R_1$, due to the scaling properties described in section 2.1.5, is completely determined by the choice of $T_1$, we set the outer radius $R_2$, which depends on the duration of the mass loss phase, to the fixed value of $1000 \cdot R_1$ for all models.

As described previously, we adopted the Ossenkopf et al. "warm" silicates as dust opacity of O-rich envelopes, and Hanner amorphous carbon mixed with a variable amount of Pégourié SiC for C-rich sources. The central AGB sources were modeled with both a 2000 K black body, and a 2500 K Engelke function with 10% SiO absorption (see previous section). All models were computed in spherical geometry, and the radial density distribution of the dust was assumed to be $n_d(r) \sim r^{-2}$ (steady mass loss for the period in which the dust shell was created). A set of models in which the radial structure was determined by full hydrodynamic dust driven stationary wind was also computed, by turning on this feature in DUSTY. This test showed only small differences between the spectra of "steady mass loss" and "radiatively driven winds" models; for this reason the discussion that follow will be made using the models with $n_d(r) \sim r^{-2}$.

As shown in Marengo et al. (1999), the modeling of O-rich sources of intermediate optical depth can be tricky, because the combination of low $\tau_V$ and high $T_1$ can produce silicate features very similar to the ones of models with higher opacity and low temperature shells. The two families of models, however, have different continuum slopes that can help in the discrimination. A fine grid of models is required to attempt the identification of a correct set of parameters on individual sources from their spectra. For this reason we run our models on a logarithmic grid with $\tau_V$ from $10^{-3}$ to 231, and $T_1$ from 100 to 1400 K for silicates, and 1000 K for carbonaceous dust (close to the respective dust condensation temperatures), with 60 steps in $\tau_V$ and 31 in $T_1$. A test with a finer grid of models didn't show any improvement in fitting individual sources, while a coarser grid did produce unreliable results.

## 3.3 Mid-IR colors of AGB dusty envelopes

The current size of available infrared telescopes, combined with the sensitivity of modern mid-IR imaging cameras, allow to spatially resolve only a minority of dusty circumstellar envelopes around AGB stars. The physical, chemical and evolutionary status of unrefolved sources can however be derived with the diagnostic tools here presented. This tools are calibrated with the help of our grid of radiative transfer models and the test sample of AGB sources. An application of these instruments is then given in chapter 4 to study the correlations between AGB long period variability and mass loss, and in chapter 5 to analyze the photometry of a sample of AGB envelopes imaged at various mid-IR telescopes.

### 3.3.1 A mid-IR photometric systems

The so-called "mid-IR window" is the spectral region between 7 and 13 $\mu$m in which the atmosphere is transparent enough to allow ground based astronomical observations. To make a use of this wavelength range, the first "thermal infrared" bolometers were using a broad band filter ($\Delta\lambda \sim 5$ $\mu$m) centered at the wavelength of 10 $\mu$m (N band filter). With the progresses in manufacturing more and more sensitive semiconductor arrays tuned to the infrared, the possibility of using filters with a smaller passband ($\Delta\lambda/\lambda \sim 0.1$, or 10% passband filters) allowed the development of a multiband photometric system in the mid-IR.

Modern mid-IR imaging cameras are equipped with a full set of 10% filters, designed to select specific features of thermal emission from dust and molecules emitting in the 10 $\mu$m region. In particular, two filters are used to image the continuum emissions at 8.5 and 12.5 $\mu$m, beginning and ending points of the mid-IR window. Another filter at 9.8 $\mu$m is designed to select the emissions at the center of the silicate feature, while a filter at 11.2 $\mu$m is centered with the SiC feature. More recently, with the further improvements in detectors sensitivity, filters at 18-20 $\mu$m have been introduced to take advantage of the relative resurgence of atmospheric transparency at these wavelengths.

Narrow band 2% filters are now available as part of "circular variable filters" (or CVF), able to perform low resolution imaging spectra of bright objects, and pin-point the wavelengths of specific features such as PAH emission lines. However, we use here the 10% passband filters at 8.5, 9.8, 11.2, 12.5 and 18 $\mu$m, since they are more specific to the emission of AGB dust, and are a "standard" set in all mid-IR infrared cameras.

The ability of a specific filter to transmit the radiation at the wavelength $\lambda$ is described by the transmission function $\phi(\lambda)$. In the ideal case $\phi(\lambda)$ should be a top-hat function having maximum transparency in the passband $\Delta\lambda$, and zero outside. In practice, since the *profile* $\phi(\lambda)$ is determined by the manufacturing process, it can change between different filters, and have an irregular shape. To standardize our analysis without limiting the conclusions to a specific set of filters, we adopt for each filter a symmetric gaussian profile having FWHM equal to $\lambda/10$:

$$\phi_{\lambda_0}(\lambda) = N_0 \exp\left[-\frac{(\lambda-\lambda_0)^2}{\sigma^2_{\lambda_0}}\right] \tag{3.9}$$

where the normalization coefficient $N_0$ is defined to have $\int \phi(\lambda) = 1$, and

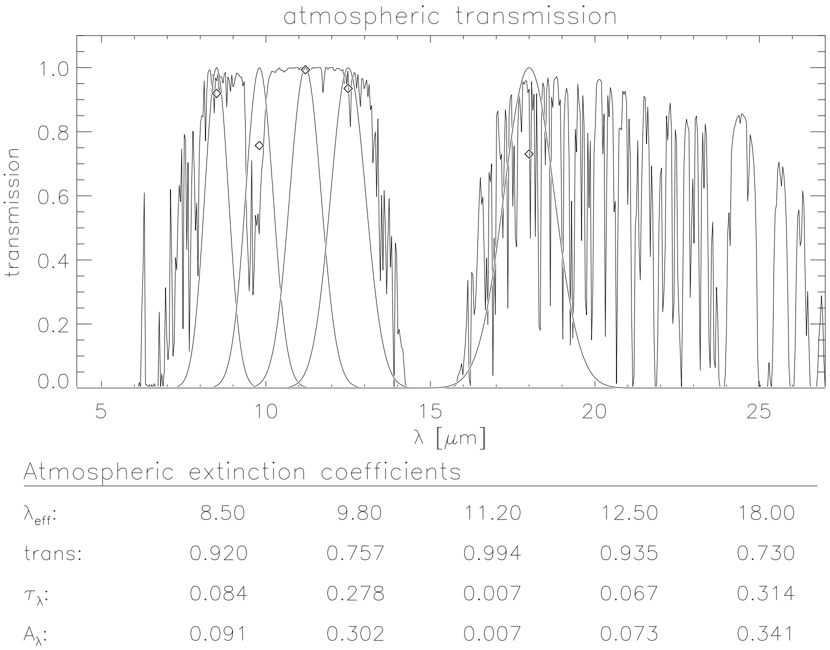

Atmospheric extinction coefficients

| | | | | | |
|---|---|---|---|---|---|
| $\lambda_{\rm eff}$: | 8.50 | 9.80 | 11.20 | 12.50 | 18.00 |
| trans: | 0.920 | 0.757 | 0.994 | 0.935 | 0.730 |
| $\tau_\lambda$: | 0.084 | 0.278 | 0.007 | 0.067 | 0.314 |
| $A_\lambda$: | 0.091 | 0.302 | 0.007 | 0.073 | 0.341 |

Fig. 3.7.— Atmospheric transparency in the mid-IR, measured at Mauna Kea, Hawaii (from United Kingdom Infra-Red Telescope (UKIRT) web site, program IRTRANS4). The gaussian profile of the filters in our mid-IR photometric system is superposed, and the average transparency in each filter passband is plotted (diamonds). In the lower panel the effective wavelength, average transparency, atmospheric optical depth and extinction of each filter is given.

$$\sigma_{\lambda_0} = \frac{\Delta\lambda_0}{2\sqrt{\log 2}} \tag{3.10}$$

These photometric bands can be combined to give a set of *colors* sensitive to the mid-IR dust features and continuum, defined as:

$$[\lambda_1] - [\lambda_2] = 2.5 \log \left[\frac{F_{\lambda_2}}{F_{\lambda_1}}\right] \tag{3.11}$$

The following colors are of interest in analyzing the emission of dusty circumstellar envelopes: the "blue continuum" color [8.5]-[12.5] sensitive to the slope of the dust thermal emission, the "red continuum" [12.5]-[18.0] measuring the infrared excess at longer wavelength, the "silicate" color [8.5]-[9.8] tuned to the 9.8 $\mu$m silicate feature and the "SiC" color [8.5]-[11.2] aimed to detect the presence of the SiC emission feature in C-rich envelopes.

We propose to show that this multiband photometric system is particularly suitable for exploring the characteristics of AGB circumstellar envelopes, and allows a simple immediate comparison with the predictions of sophisticated radiative transfer models.

### 3.3.2 A test sample of AGB sources

Since the aim of this analysis is to look into the correlations between AGB mass loss and mid-IR photometry, our working sample was extracted from a catalog of AGB stars with known mass loss rates, compiled by Loup et al. (1993) using millimetric observations of CO and HCN line observations.

The catalog (hereafter L93) consists of 444 sources, for which $^{12}$CO(1→0), $^{12}$CO(2→1) and HCN(1→0) circumstellar line observations have been published from 1995 through September 1992. This catalog is not complete, nor statistically significant, since it is clearly biased toward strong CO emitters. It is however a large sample, indicative of the general properties of AGB stars.

For each source in the L93 catalog, identified with an IRAS point source, the authors give an estimate of the total bolometric flux, based on the fit of the IRAS photometry at 12, 25 and 60 $\mu$m given in the IRAS Point Source Catalog (PSC, 1986). An estimate of the source distance is also available for 349 catalog objects, derived by assuming a “standard” luminosity of $10^4$ $L_\odot$, and in some cases by modeling the CO and HCN emission.

For each source in the sample, L93 also gives an estimate of the total mass loss rate $\dot{M}$, by consistently determining the photodissociation radius $R_{CO}$ (from which the CO emission is originated) with a numerical fit provided by Mamon et al. (1988). When detailed radiative transfer modeling of the CO line profile is made by the original authors of the observations more than one estimate is given. For all sources, the kinematic expansion velocity $v_e$ of the CO/HCN shell is provided, inferred from the line profile.

In order to combine the mass loss information provided by the radio millimetric data with mid-IR photometry, we have extracted all the sources in L93 catalog for which a good quality IRAS LRS is available. With this additional criteria we ended up having a sublist of 154 O-rich, 7 S-type and 167 C-rich sources; note again that by construction this test sample suffers from the bias in the original L93 catalog, and also from the specific biases in the IRAS LRS, among which source confusion on the galactic plane.

The IRAS data were obtained for all sources from the Astrophysics Data Facility at NASA’s Goddard Space Flight Center internet web server (`http://space.gsfc.nasa.gov/astro/iras`).

Table 3.1 IRAS color-color diagram regions

| Region | Characteristic type of object |
|---|---|
| I | O-rich non variable stars without circumstellar shells |
| II | variable stars with "young" O-rich circumstellar shells |
| IIIa | variable stars with more evolved O-rich circumstellar shells |
| IIIb | variable stars with thick O-rich circumstellar shells |
| IV | variable stars with very thick O-rich circumstellar shells |
| V | planetary nebulæ and non variable stars with very cool circumstellar shells |
| VIa | non variable stars with relatively cold dust at large distances; a significant part of the stars is carbon rich |
| VIb | variable stars with relatively hot dust close to the star and relatively cold dust at large distances; some of the objects have proven to be O-rich |
| VII | variable stars with more evolved C-rich circumstellar shells |
| VIII | other objects |

Each original spectrum was divided in two separate segments, corresponding to the *blue* and a *red* detectors of IRAS spectrometer (sensitive in the 8–13 and 11-22 $\mu$m wavelength range, respectively). We joined the two half of each LRS by superposing the overlapping region between 11 and 13 $\mu$m, as explained in the IRAS Explanatory Supplement (1988). The spectra were then rectified to correct for the wrong assumptions made on the spectrum of the LRS calibrating standard source ($\alpha$ Tau), as described in Cohen et al. (1992). The amount of this corrections is however generally small, and mainly affects the shorter wavelengths in the "blue" segment. The joint rectified spectra were then recalibrated to match the 12 $\mu$m IRAS PSC flux, by convolving the spectra with the IRAS 12 $\mu$m filter profile.

The IRAS LRS catalog provides an automatic classification two-digit code for each spectrum. The first digit (main class) is related to the spectral index $\beta$ of the continuum (assuming $F_\lambda \propto \lambda^\beta$), while the second indicates the strength of the main feature, in emission or absorption, present in the mid-IR window. In particular, spectra of O-rich sources are identified by the strength of the 9.8 $\mu$m silicate feature, that is found in emission or absorption in the LRS classes 2n and 3n respectively. C-rich envelopes are

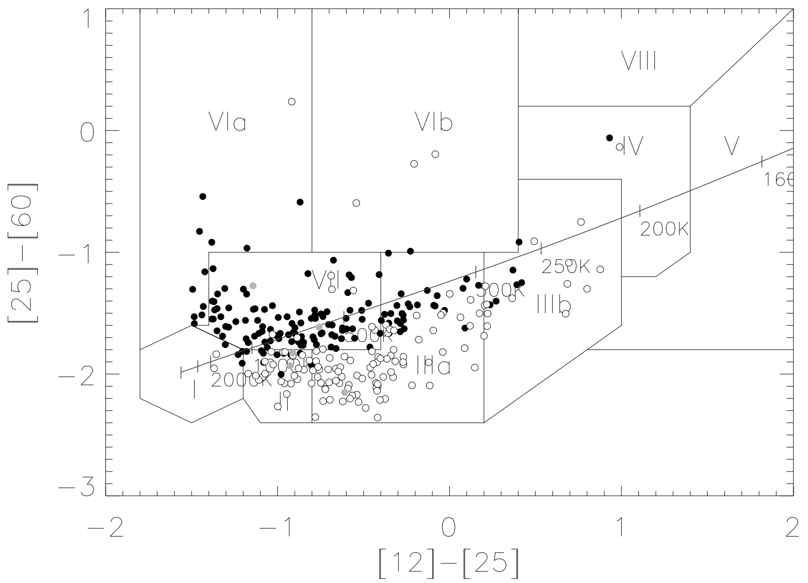

Fig. 3.8.— IRAS [25]-[60] vs. [12]-[25] color color diagram of test sources selected from Loup et al. (1993) catalog. Filled circles are C-rich sources, open symbols are O-rich and S-stars are plotted in gray. The regions in which the plot is divided are the ones defined by van der Veen & Habing (1988). The colors of black bodies at different temperatures are also indicated.

mainly found in the 4n class, defined by the strength of the 11.2 $\mu$m SiC feature in emission. Post-AGB objects of both types are in the main classes 6n and 7n, characterized by very large infrared excesses. Finally, both O-rich and C-rich sources may fall in classes 1n and 0n (featureless spectra), where a few LRS with self-absorbed SiC features can be found (Omont et al., 1993).

This classification is correlated to the infrared excess of the sources in the IRAS PSC photometry, as put in evidence by the IRAS [25]-[60] vs. [12]-[25] color-color diagram introduced by van der Veen & Habing (1988). Figure 3.8 shows the van der Veen & Habing color-color diagram of the test sample sources. The regions plotted on the diagram were identified according to the distribution of IRAS PSC sources on the diagram (see table 3.1).

The distribution of L93 sources is consistent with the van der Veen & Habing classification. Most of the O-rich sources are distributed in the

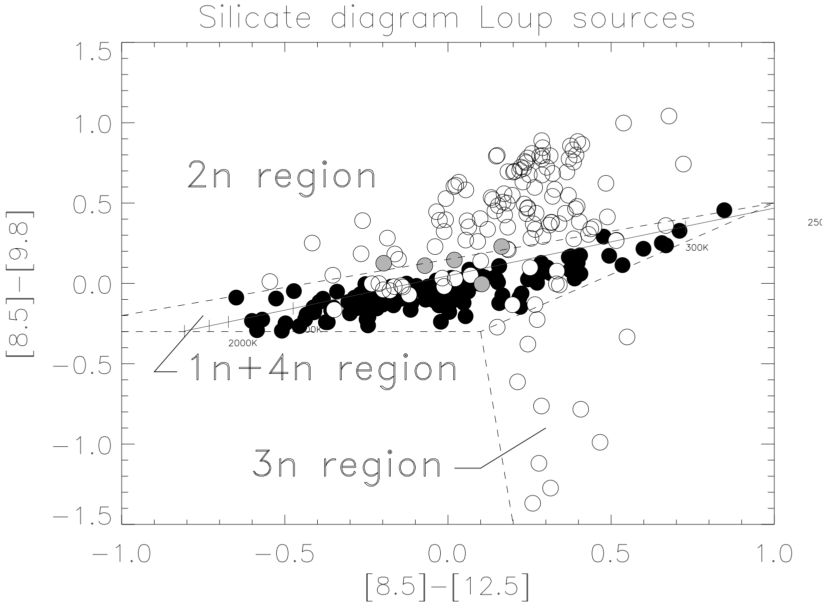

FIG. 3.9.— Silicate feature color color diagram of test sources selected from Loup et al. (1993) catalog. Filled circles are C-rich sources, open symbols are O-rich and S-stars are plotted in gray. The colors of black bodies with different temperatures are plotted, and the diagram is divided in three regions according to the LRS automatic classification of the sources.

II, IIIa and IIIb regions, in a sequence indicating a progressive increase in the source optical depth. Most of the C-rich sources are in region VII, as expected, even though some of them are located along the black body curve in region IIIa and IIIb. Only two sources are in region V, and are associated to post-AGB objects. The high 60 $\mu$m excess of the few sources in region VIa (mostly C-rich) and VIb (O-rich), may be due to the presence of a cold detached envelope, or to galactic cirrus contamination.

In order to simulate the mid-IR photometry for all the selected sources, we first converted the IRAS spectral energy distribution $\lambda F_\lambda$ in flux density units $F_\nu = \lambda^2 F_\lambda / c$, and then convolved $F_\nu$ with the gaussian filter profiles defined in section 3.3.1 for our photometric system:

$$F_{\lambda_0} = \int_0^\infty \phi_{\lambda_0}(\lambda) \cdot F_\nu(\lambda)\, \mathrm{d}\lambda \tag{3.12}$$

The derived photometry is then used to compute the mid-IR colors defined in section 3.3.1 for each source in the test sample.

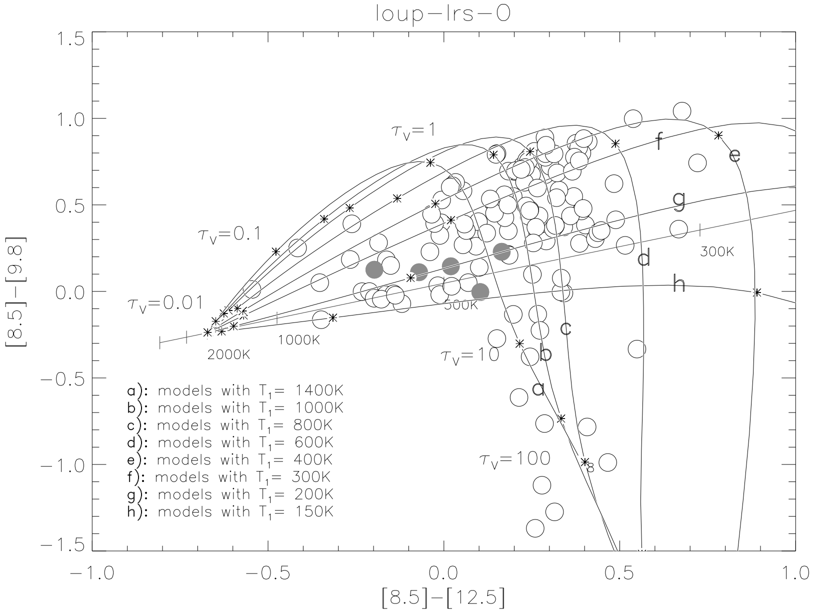

FIG. 3.10.— Silicate feature color color diagram of O-rich and S-stars with silicate dust DUSTY model tracks having $T_1$ of 1400, 1000, 600, 400 and 200 K; marks on each track indicate models having $\tau_V$ of 0.01, 0.1, 10 and 100.

### 3.3.3 The silicate feature color color diagram

A diagram sensitive to the strength of the 9.8 $\mu$m silicate feature is made by combining the [8.5]-[9.8] and the [8.5]-[12.5] colors. The distribution of our test sources is shown in figure 3.9. The diagram can be divided in three regions. The first is above the black body curve, and all the O-rich sources of LRS class 2n (with the silicate feature in emission) are found there. The second is aligned along the black body line, and groups all the C-rich sources plus the O-rich ones without the silicate feature (classes 4n and 1n respectively). Finally the third region is below the black body, and collects all the O-rich envelopes of class 3n (with the silicate feature in absorption).

The distribution of the C-rich sources on the diagram is apparently only a function of their increasing infrared excess, which causes a redder [8.5]-[12.5] color of thicker envelopes.

Concerning the O-rich sources, the explanation is apparently more complex, since a larger spread in both colors is present. This can be investigated by adding to the plot the colors of the silicate dust model envelopes computed in section 3.2, derived from the model spectra by applying equation 3.12, similarly to what done for the sources. The result is shown in figure 3.10. Models with the "standard" black body of $T_s \simeq 2500$ K are used.

Each curve corresponds to a different temperature $T_1$, and is generated by models with increasing optical depth $\tau_V$. Note that curves with a large ranges of $T_1$ are necessary to cover the whole area in which the sources are distributed. Envelopes located along the black body, having weak silicate feature and low color temperature, require $T_1$ as low as 200 K. Since dust cannot form efficiently at such low temperatures, this implies that a relatively large fraction of O-rich envelopes have shells which are detached from the dust forming stellar extended atmosphere, and have expanded to distances where the equilibrium temperature is consistently lower. In chapter 4 this hypothesis is tested on a sample of variable AGB stars, and correlated with the low period variability type (Mira, SR or Irregular).

It is important to note that model tracks for different $T_1$ join in the region of maximum source density. This means that the same silicate feature strength, relative to the continuum, can be obtained either with high $T_1$ and $\tau_V \gtrsim 1$ or with low $T_1$ and $\tau_V \lesssim 1$, and the two cases cannot be well separated on the basis of the mid-IR colors alone. To derive in a unique way the physical parameters of O-rich AGB circumstellar envelopes thus require considering the whole LRS distribution, or fitting colors in a larger wavelength range, in order to measure with higher sensitivity the slope of the continuum. The IRAS PSC fluxes can in principle provide the requested sensitivity, but in many cases produce spurious results due to galactic cirrus contamination at 60 and 100 $\mu$m.

Despite these limitations, the position of the model tracks on the diagram does explain the sources distribution. Sources above the black body have low and intermediate optical depths, as expected for LRS class 2n. Sources of class 1n appear instead as a combination between cold envelopes with low $\tau_V$ and hot shells with $\tau_V \sim 10$ (opacity at 10 $\mu$m close to unity), in which the silicate feature is partially self absorbed. Sources below the black body, on the other end, are below the black body line, due to their high $\tau_V$ which is responsible for the silicate feature in absorption.

### 3.3.4 The SiC color color diagram

The SiC color diagram, shown in figure 3.11 is very similar to the silicate color diagram. The O-rich sources, however do show a smaller spread, because the 11.2 micron filter still intercepts the last part of the 9.8 $\mu$m silicate

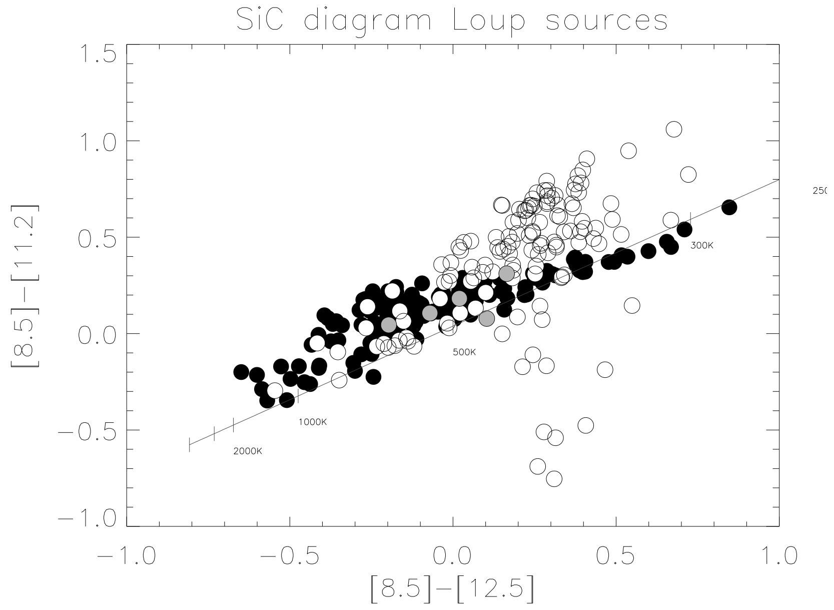

FIG. 3.11.— SiC feature color color diagram of all the sources in our test sample. Again filled circles are C-rich sources, grey symbols are S-stars and empty ones are O-rich. The black body line for different temperatures is also shown.

feature. The C-rich sources show instead a larger spread, and are located above the black body line; this is a direct consequence of the presence of the SiC emission feature in many sources.

This last statement is confirmed in figure 3.12, where carbonaceous dust radiative transfer model tracks are overplotted on the sources. Different lines are characterized by increasing amounts of SiC with respect to amorphous carbon, from 0 to 0.14 in number density of grains. Note that the displacements of the models for $\tau_V \sim 1$ is proportional to the abundance of SiC, as it increases the strength of the 11.2 $\mu$m feature. By fitting the two colors of the diagram, it should in principle be possible to estimate the SiC/amC ratio in the envelope of each source; the rather low S/N of most IRAS LRS, unfortunately, makes this task quite unpractical, and more accurate high resolution measurements of the 11 $\mu$m region are necessary. The plot, however, shows that for the L93 sample the maximum amount of SiC in the dust mixture is of the order of 14%, confirming that these grains are not a major component of C-rich dust.

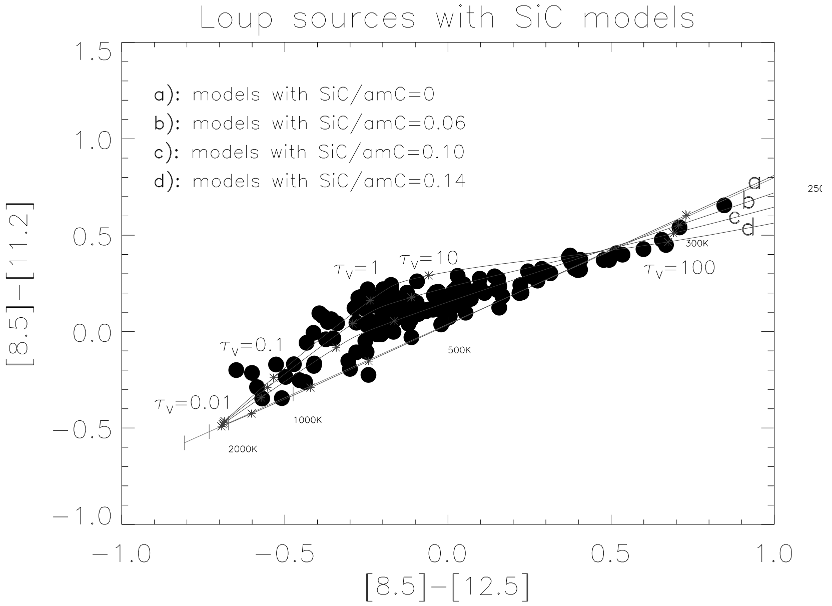

FIG. 3.12.— SiC feature color color diagram of C-rich sources with DUSTY model tracks having $T_1$ of 1000 K and SiC/amC abundance of 0, 0.06, 0.10 and 0.14. Marks on each track indicate models having $\tau_V$ of 0.01, 0.1, 10 and 100.

### 3.3.5 Mid-IR colors and mass loss rates

Equation 3.4 suggests that the mass loss rate of a dust-driven AGB wind should be proportional to the envelope optical depth $\tau_V$ and the stellar luminosity $L_*$, and inversely proportional to the outflow velocity $v_e$. Since the last two quantities, together with the total mass loss rate $\dot{M}$, are available for all sources in L93 catalog, we have defined a *mass loss parameter*

$$\mu = 2.5 \log \left[ \left( 10^5 \, \frac{\mathrm{d}M}{\mathrm{d}t} \right) \frac{v_e}{L_4} \right] \tag{3.13}$$

where $L_4$ is the luminosity in units of $10^4$ $\mathrm{L}_\odot$. This quantity should be proportional to the optical depth $\tau_V$.

As the infrared excess expressed by the [8.5]-[12.5] continuum color is related to $\tau_V$ (as demonstrated by the model tracks in figure 3.10 and 3.12) we tested this hypothesis with the diagram in figure 3.13.

The sources of different chemical type are not completely separated in the plot, but the C-rich sources appear to be more concentrated in the upper

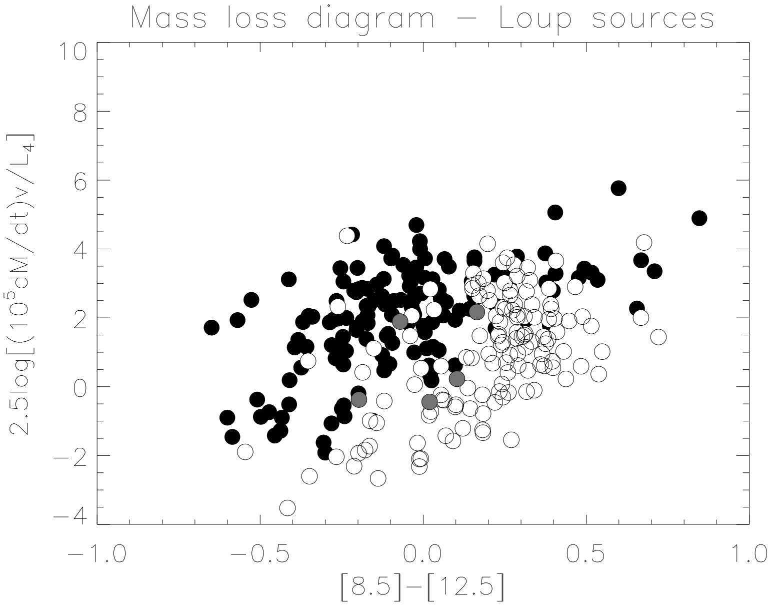

FIG. 3.13.— Mass loss rate parameter vs. infrared excess for L93 sources in test sample. C-rich envelopes are filled symbols, O-rich are empty and S-stars are grey circles.

left side of the diagram (higher mass loss, lower infrared excess), while the O-rich ones are grouped in the lower right side (redder colors and lower mass loss rates), with the few S-stars in between. The general increase of the mass loss parameter with the infrared excess, confirms that AGB mass loss is sustained by dust driven winds.

The partial segregation of the sources is explained by the different optical properties of the two dust opacities. Figure 3.5 shows that in the 10 $\mu$m window (and only in this region, due to the silicate features) the opacity of oxidic dust is higher than the absorption coefficient of carbonaceous material. As a result, the same quantity of dust in the circumstellar environment produces a larger infrared excess in O-rich sources than in C-rich envelopes.

Even though the error bars on the estimates of mass loss rate in the L93 sample are quite large, it is unlikely that the errors on $\dot{M}$ alone can explain the large spread in the source distribution shown in figure 3.13. This suggests that the spread is intrinsic for the sample, and possibly due to temporal variations in the mass loss rates on timescales smaller than the crossing time of the circumstellar envelope at the stellar wind speed. The L93 mass loss measurements are based on the CO emission taking place in a shell of radius $R_{CO}$, of the order of $10^{17}$ cm, while the mid-IR photosphere is usually at a distance of about $10^{14}$–$10^{15}$ cm. To break the correlation between the gaseous and the dusty shells is required a temporal variation of $\dot{M}$ on timescales of the order of $10^3$ yr (assuming an outflow velocity of 10 km $s^{-1}$), or shorter. This timescale is in general too short to be associated with the thermal pulses of the TP-AGB, and too long with respect to the long period variability ($P \sim 1$ yr) which characterize the AGB phase. They are however compatible with the temporal separation of structures observed in the remnant AGB shells of post-AGB objects like the Egg nebula (Sahai et al., 1998), or the evolved carbon star IRC+10216 (Mauron & Huggins, 1999) which have been associated to recurrent variations in the mass loss rate.

# Chapter 4

# AGB mass loss and stellar variability

In this chapter the relations between the mid-IR emission and pulsation properties of O-rich AGB stars with known long period variability type are studied. The analysis is made by using the tools developed in the previous chapter, and by modeling the sources with steady state spherically symmetric radiative transfer. By fitting the IRAS Low Resolution Spectra of the circumstellar envelopes around each star, the thermal structure, optical depth and mass loss rate are derived. The best fit parameters are then correlated with the central source variability type.

This work has been made in collaboration with Željko Ivezić, Princeton University, and has been presented at the International Workshop "The changes in Abundances in Asymptotic Giant Branch Stars", held in Rome, September 16–18, 1999 (Marengo et al., 2000b). [Results of this analysis finally published on Marengo et al. (2001)]

## 4.1 Long Period Variability in the AGB phase

On August 3, 1596, David Fabricius, an amateur astronomer native of Friesland (The Netherlands) started a series of observations, aimed to determine the position of a planet which he believed to be Mercury (it was, in fact, Jupiter). He used as reference point a nearby unidentified star of magnitude 3 which, surprisingly, by August 21 had already increased to magnitude 2. When the star faded and finally disappeared in October, Fabricius assumed he had just observed a nova, and then forgot about it. On February 15, 1609, he observed the star reappear, which was quite unusual. Fabricius, who was a minister, unfortunately did not live to enjoy the appreciation of its discovery, being murdered by a peasant whom he accused from the pulpit of having stolen one of the minister's geese.[1]

The mysterious star was then forgotten, until Johann Fokkens, also of Friesland, saw it again in 1638, determining that it was a variable star with a period of 11 months. The star was finally named *Mira*, which means "The Wonderful" by Johann Hevelius of Danzig, and *o* (omicron) Ceti by Johann Bayer in 1603.

Today, Mira is taken as the prototype for a whole class of variable stars, with periods that can be as long as several hundred days, and whose light curves can be of several magnitudes in the optical. Mira, as other *Long Period Variables* (LPV), is an AGB star, characterized by pulsational instabilities in the atmospheric layers. Radial pulsations, with not fully understood dynamics, are responsible for periodic contraction and relaxation of the stellar photosphere, and thus for the variations of the stellar luminosity.

In the inner part of the LPV atmosphere, the passing shocks cause a periodic modulation of the structure; in the upper layers the dissipation of mechanical energy leads to a levitation, i.e. a density enhancement of up to several orders of magnitude, compared to an hydrostatic atmosphere. Both of these effects can influence the formation of molecules and dust grains, and thus the mass loss properties of the star (Höfner, 1999).

If Long Period Variability is in some way one of the ingredients in dust formation processes in AGB stars, some correlation between the infrared properties of LPVs, which are a function of dust production, and the pulsational characteristics, should be expected. This is what this chapter aims to explore.

### 4.1.1 Types of Long Period Variability

There are four main types of LPVs that are associated with the AGB phase: Miras (of which *o* Ceti is the prototype), Semiregulars of type "a" and "b", and Irregulars of type "Lb". According to the General Catalogue of Variable Stars (GCVS, Kopolov et al. 1998), they are defined as follows:

Mira: long-period variables with characteristic late-type emission spectra (Me, Ce, Se) and light amplitudes from 2.5 to 11 magnitudes in V. Their periodicity is well pronounced, and the periods lie in the range between 80 and 1000 days. Infrared amplitudes are usually less than

---

[1] see Hoffleit (1996) for an historical account on Mira discovery.

in the visible, and may be less than 2.5 magnitudes; for instance, in the K band they usually do not exceed 0.9 mag.

SRa: Semiregular variables of type a, which are late-type (M, C, S or Me, Ce and Se) giants displaying persistent periodicity and usually small (less than 2.5 magnitudes in V) light amplitude. Amplitudes and light-curves generally vary, and periods are in the range 35–1200 days. Many of these stars differ from Miras only by showing smaller light amplitudes.

SRb: Semiregular late-type (M, C, S or Me, Ce, Se) giants with poorly defined periodicity (mean cycles in the range of 20 to 2300 days), or with alternating intervals of periodic and slow irregular changes, and even with light constancy intervals. Every star of this type may be assigned a certain main period, but the simultaneous presence of two or more periods of light variation is observed.

Lb: Slow irregular variables of late spectral type (K, M, C and S), which shows no evidence of periodicity, or any periodicity present is very poorly defined and appears only occasionally. Lb stars are in general poorly studied, and may in fact belong to the semiregular type (SRb).

The length of the pulsational period, in the SR class, can be related to the evolutionary phase of the pulsators along the AGB. Two independent studies made by Jura & Kleinmann (1992) and Kerschbaum & Hron (1992) arrived at the conclusion that SRs having period $P < 100^d$ are characterized by low mass loss rates ($\dot{M} \sim 10^8$ $\mathrm{M}_\odot$ $\mathrm{yr}^{-1}$) and seem to be on the E-AGB phase. Semiregulars with longer periods have instead a higher mass loss, and presumably are in the TP-AGB. This classification is supported by the detection of the s-element Tc in SRs with $P \gtrsim 100^d$ (Little et al., 1987); Tc is otherwise not observed in most SRs with shorter period. Miras, on the other end, appears to be all in the TP-AGB phase.

However, it is clear from the above classification that the subdivision between the various categories is rather thin, and can be easily biased by the quality and frequency of the observations used for the construction of variable light curve.

According to Kerschbaum & Hron (1996), for example, SRa should be considered not as a class by themselves, but as a mixture of “intrinsic” Miras and SRb. Jura & Kleinmann (1992) ignored this subdivision, arguing that, for an infrared selected sample, SRs can all be considered as a single class.

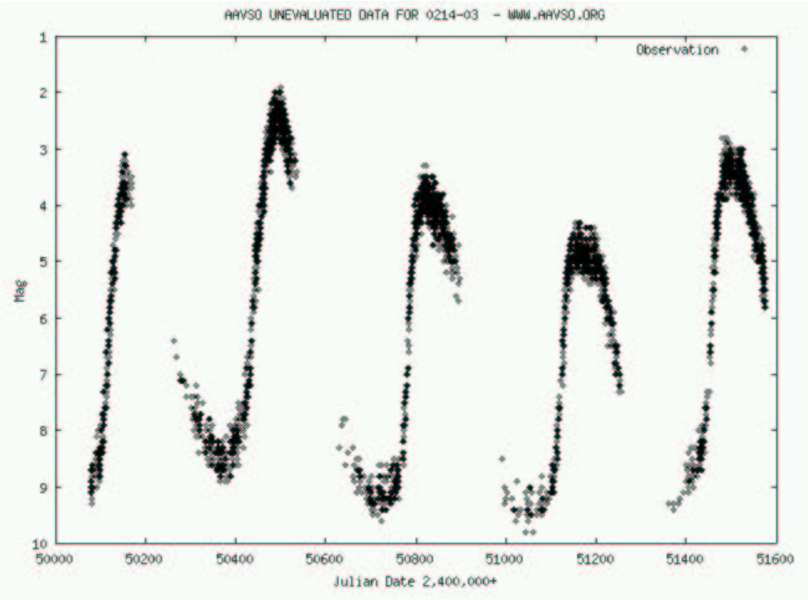

FIG. 4.1.— Light-curve of Mira (*o* Ceti) during several pulsational cycles. From the American Association of Variable Star Observers (AAVSO) web site (`http://www.aavso.org`).

A cautious approach is thus necessary, to avoid reaching erroneous conclusions by analyzing samples of sources which are in general difficult to define, and can be contaminated by pulsators in a different state.

### 4.1.2 Pulsation modes in Miras and SRs

An open problem concerning the dynamics of pulsations in Long period Variables is the determination of the pulsational mode. This is somewhat surprising, since the ratio of the fundamental mode and first overtone period in an AGB variable is larger than 2 (Wood & Sebo, 1996). Any reasonable estimate of the radius and mass of an LPV should thus be enough to determine the pulsational mode. This is unfortunately untrue, since a number of observational difficulties can make this measurement rather awkward, and still leave the problem open.

A mass of 1 $M_\odot$ is usually adopted in these computations, based on kinematics studies of LPVs in the Galaxy. This value, however, tends to favor first overtone pulsations over fundamental mode, thus biasing the measurement. The determination of the angular radii, also suffers of serious problems, mainly due to the wavelength dependence of the measured diameters, which requires accurate model atmosphere predictions to be usable. The determination of the distance is also uncertain, even after the HIPPARCOS mission, which provides a large set of reasonable parallaxes. The theoretical models used to analyze the pulsations are also a source of confusion, being not at all clear if classical pulsation theory is applicable to LPVs, or if more refined models are required (Tuchman, 1999).

Fourier analysis of LPV light-curves, can also give direct information on the pulsational mode. An extensive analysis of Mira itself (Barthès & Mattei, 1997) showed a main period of 332.9 days, which is interpreted as first overtone, and a second periodicity of 1503.8 days associated to the fundamental mode. Other analysis of Mira stars made with similar techniques found pulsations which can be interpreted as first overtone pulsation modes. Semiregulars, on the contrary, are often associated to combinations of the first overtone with higher pulsational modes.

Wood et al., (1999), however, by analyzing the relative position in the period luminosity plane of LMC Miras and SRs in the MACHO database, found five distinct period-luminosity sequences. These sequences allowed them to conclude that Miras are *unambiguously* fundamental mode pulsators, while SRs pulsates on a combination of the various overtones.

Even though different analyses are producing contradicting answers, a common result seems to be that SRs appear to pulsate as a combination of higher overtones with respect to Miras. More data and a better understanding of the physics of pulsations in the perturbed atmospheres of variable AGB, are still necessary to provide a reliable answer on this important question.

## 4.2 A sample of Mira, Semiregular and Irregular variables

In order to test the link between AGB long period variability and mass loss, we have selected a sample of LPVs for which the IRAS mid-IR spectra were available. This sample is characterized in the next section, and then analyzed from the point of view of the mid-IR properties in the LRS spectral region, by studying its mid-IR colors and the shape of the silicate feature.

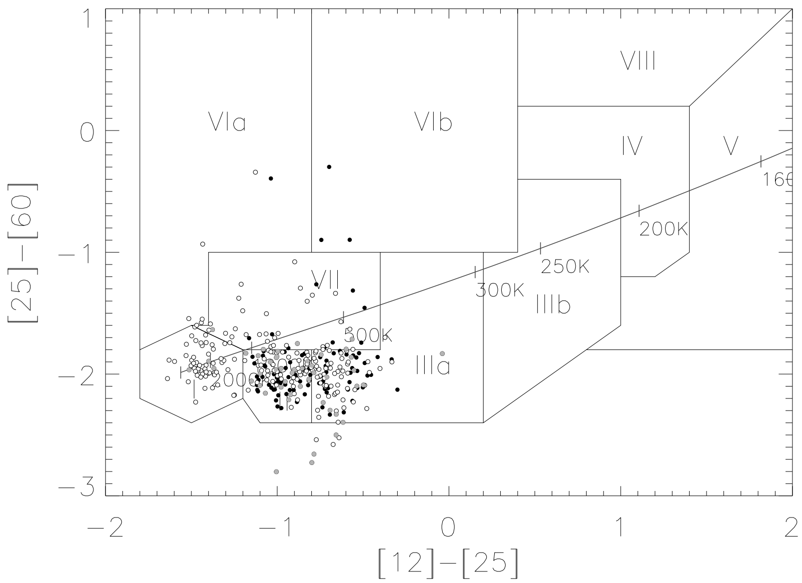

FIG. 4.2.— IRAS [25]-[60] vs. [12]-[25] color color diagram of sources in our KH sample. Miras are filled circle, NMs empty symbols and SRa are grey. The regions are defined according to van der Veen & Habing (1988). The solid line crossing the plot shows the colors of a black body with different temperatures.

### 4.2.1 Characterization of KH sample

In Ivezić & Knapp (1998) a sample of AGB stars, variable as Mira, SRb and Lb were analyzed in terms of the IRAS [12]-[25] and [12]-K colors. A discrimination was found according to the chemical composition (O-rich vs. C-rich) and the variability type, with SRb and Lb having redder colors than Miras. This evidence was interpreted as a consequence of missing hot dust in the envelopes of SRb and Lb, indicating a recent (order of 100 yr) decrease in the mass loss rate. The sample used in Ivezić & Knapp (1998) was compiled from data published in a series of papers by Kerschbaum, Hron and collaborators (Kerschbaum & Hron, 1996, and references therein), for which the spectral and variability type was known. In this work we have extended the sample in order to include also the stars of type SRa.

We have then limited our analysis to the sources with an O-rich circumstellar chemistry around stars with spectral type M, thus excluding all the S and C stars. This choice was determined by the different optical properties of O-rich and C-rich dust. The 9.8 $\mu$m silicate feature of O-rich envelopes, as shown in section 3.3.3, makes the spectrum of these sources particularly sensitive to small variations of the physical parameters and temperature structures of the envelopes. The almost featureless opacities of amorphous carbon dust present in C-rich envelopes, on the other end, are much less dependent on changes in the dust grain temperature distribution. For this reason, fitting mid-IR spectra (and in particular the inner envelope temperature $T_1$) is potentially more accurate in the case of oxidic dust.

Of all the sources in the original Kerschbaum & Hron (1996) list, we have excluded also the ones for which the IRAS LRS was unavailable, ending with a list of 432 sources (KH sample, hereafter). In our KH sample 96 are Miras, 48 SRa, 140 SRb and 58 Lb. We have then combined the SRa, SRb and Lb in a single sample of 246 non-Miras (NMs).

To test the possibility that SRa are a spurious class containing a mixture of Mira and SR variables, we have cross correlated the results with a separate sample of SRa sources alone, as a precaution to check if our NMs are "contaminated" by erroneous classified Miras.

The distribution of KH sources in the IRAS color color diagram described in section 3.3.2 is shown in figure 4.2. Note that most of the sources are distributed in regions II and IIIa of the diagram (containing variable stars with young circumstellar envelopes). NMs, however, are also present in region I, where sources without a circumstellar shell (or, rather, having an optically thin one) are located. We have finally cross correlated our sample with the General Catalogue of Variable Stars (GCVS, Kopolov et al. 1998), in order to derive the pulsational period of all sources, when available.

Our sample contains 57 SRs with $P < 100^d$ and 130 with $P \gtrsim 100^d$ which, according to Jura & Kleinmann (1992) and Kerschbaum & Hron (1992) should be in the Early- and TP-AGB phase, respectively. The analyses performed in the following sections are then checked against this subdivision, in order to verify that any eventual difference between Miras and NMs is due to the pulsational mode, and not to the evolutionary status of the sources.

Due to the nature of the samples from which our KH list is derived, and in particular to the limitations in the IRAS catalog, affected by source confusions in the galactic plane, our sample is not statistically complete. Nevertheless, it provides significant indications for the whole class of O-rich galactic AGB variables.

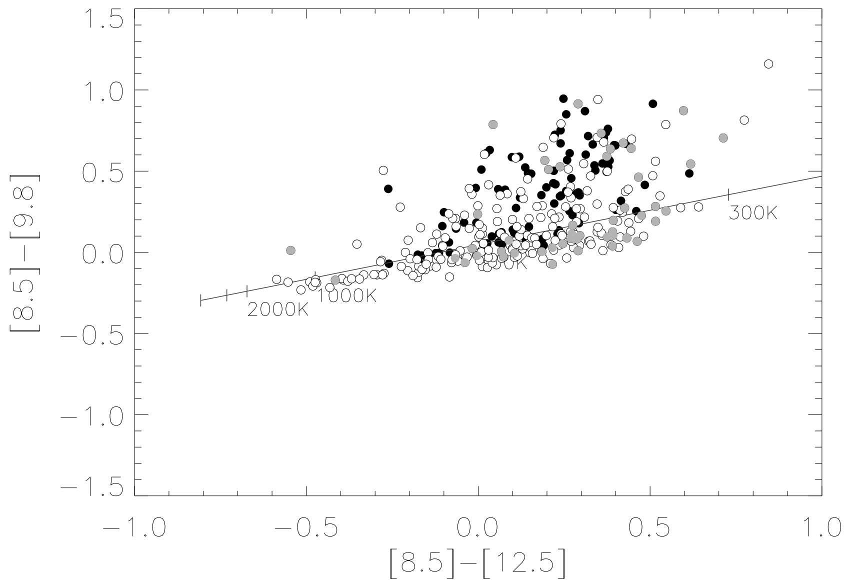

FIG. 4.3.— Silicate color diagram of sources in KH sample. Miras are filled circle, NMs empty symbols and SRa are grey.

### 4.2.2 Mid-IR colors and variability

Preliminary information on the physical and chemical status of dusty circumstellar envelopes can be obtained by using a suitable photometric system tuned for mid-IR observations, as shown in chapter 3.

As for the test sources used to calibrate our mid-IR color color diagrams, we have derived the photometry in the 8.5, 9.8, 12.5 and 18.0 "standard" gaussian filters by convolving the LRS spectra with the filter profiles, as explained in section 3.3.2. Since all KH sources are O-rich, the "silicate color" diagram is the natural choice to probe the properties of the dust thermal emission in the mid-IR. The plot, shown in figure 4.3, brings into evidence that NMs, and among them most of the SRa, are distributed along the black body line, with a large spread in the [8.5]-[12.5] color. Miras, on the contrary, are clumped above the black body, with $-0.1 \lesssim$ [8.5]-[12.5] $\lesssim 0.5$. This region, as shown in figure 3.10, is mostly populated by envelopes with intermediate optical depth ($1 \lesssim \tau_V \lesssim 30$).

The [8.5]-[9.8] color shows that Miras have a tendency to have a stronger 9.8 $\mu$m silicate feature, while NMs and especially SRa tends to be found

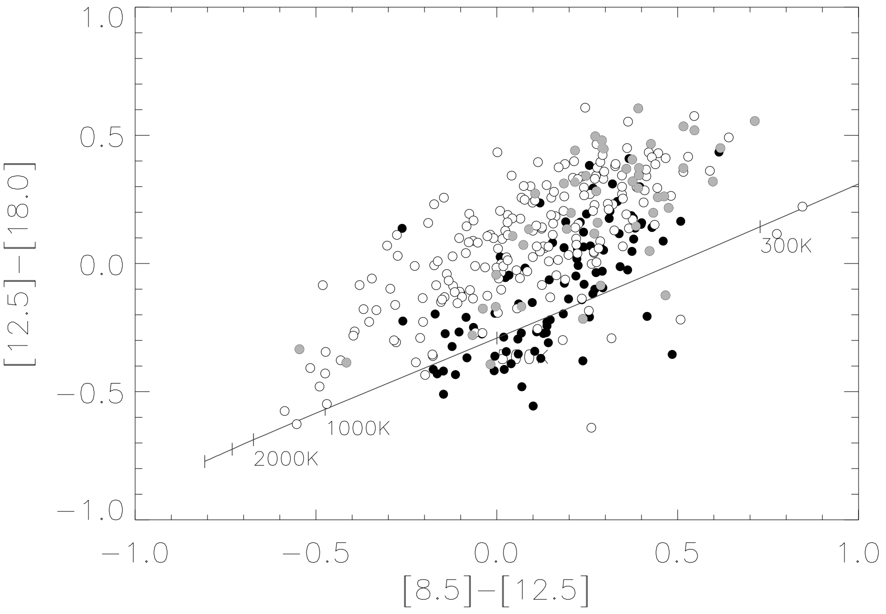

FIG. 4.4.— Dust continuum color diagram of sources in KH sample. Miras are filled circle, NMs empty symbols and SRa are grey.

closer to the black body, where featureless 1n class spectrum are usually located. The absence of a complete separation between Miras and NMs, does not allow to discuss the detailed properties of the silicate feature in the two groups on the basis of the [8.5]-[9.8] color alone. A specific test on the shape of the silicate feature requires the analysis of the full LRS spectra, as described in the next section.

The absence of sources below the black body, in the region otherwise occupied by the 3n class of objects, indicates that the optical depth of KH sources is never high enough to produce a silicate feature self absorbed.

The "thermal continuum" diagram [12.5]-[18.0] vs. [8.5]-[12.5], shown in figure 4.4, does highlight a difference between Miras and NMs, as NMs have an average redder [12.5]-[18.0] color. This cannot be due to a higher optical depth of NM envelopes, which would affect also the "silicate feature" color diagram; it suggests instead the presence of colder circumstellar dust around NMs, as found in Ivezić & Knapp (1998). SRa have a distribution similar to the NMs, but [8.5]-[12.5] $\gtrsim -0.1$ (as for the Miras).

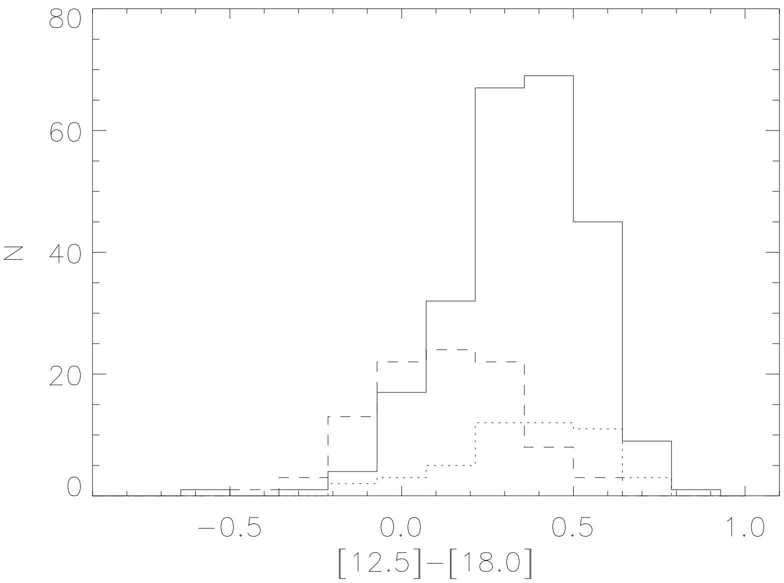

FIG. 4.5.— Distribution of the [12.5]-[18.0] excess colors for Miras (dashed line), NMs (solid line) and SRa (dotted line) for the KH sample.

A quantitative test is provided by the histogram in figure 4.5, and summarized in table 4.1. The histogram plots the distribution of Miras, SRa and NMs in the [12.5]-[18.0] color excess, defined for each source as the difference between its color and the color of a black body with the same [8.5]-[12.5] color temperature. The mean value for this quantity is $\sim 0.11$ for Miras, $\sim 0.32$ for NMs and $\sim 0.33$ for SRa. The 0.2 magnitude difference between the Miras and NMs distribution is larger than the dispersion of the two samples, measured by the variance $\sigma \simeq 0.18$ of both Miras and NMs. We tested this result with a Student's t-test for the mean values, finding that the difference between the two population is indeed statistically significant (see table 4.1 for further details). We then performed the same analysis upon the two SR subsamples with $P < 100^d$ and $P \gtrsim 100^d$, finding a similar color excess in the two cases (0.36 and 0.30 magnitudes), which is not significant with respect to the 0.01 Studen't t-test significance level.

This two tests suggest that, from the point of view of the color temperature of their circumstellar dust, Miras and NMs are two different populations. Among the SR sources, the physical characteristics of the circum-

Table 4.1 [12.5]−[18.0] color excess.

| Sample | Median [mag] | Mean [mag] | $\sigma$ [mag] | N sources |
|---|---|---|---|---|
| Mira | 0.10 | 0.11 | 0.18 | 96 |
| NM | 0.34 | 0.32 | 0.18 | 246 |
| SRa | 0.37 | 0.33 | 0.19 | 48 |
| SR ($P < 100^d$) | 0.37 | 0.36 | 0.17 | 57 |
| SR ($P \gtrsim 100^d$) | 0.32 | 0.30 | 0.20 | 130 |

Significance of statistical tests

| Sample | F-test | t-test | Result at 0.01 significance[a] |
|---|---|---|---|
| Mira vs. NM | 0.90 | $6 \cdot 10^{-20}$ | Same $\sigma$ and different mean |
| SRa vs. Mira | 0.70 | $2 \cdot 10^{-10}$ | Same $\sigma$ and different mean |
| SRa vs. NM | 0.60 | 0.71 | Same $\sigma$ and mean |
| SR $P<100^d$ vs. $P \gtrsim 100^d$ | 0.16 | 0.05 | Same $\sigma$ and mean |

[a] Samples have different $\sigma$ if the variance F-test returns a significance of 0.01 or smaller, and different mean values if Student's t-test returns a significance of 0.01 or smaller

stellar envelopes are instead homogeneous across all pulsational periods. Assuming the validity of the Kerschbaum & Hron (1992) correlation between pulsational periods and AGB evolution, this is suggestive that SRs form similar circumstellar envelopes in the Early- and TP-AGB phases. The similarity of SRa with NMs, may indicate that there is not a large contamination of Miras in the KH sample.

### 4.2.3 Variability and the main silicate feature

The shape and characteristics of the 9.8 $\mu$m silicate feature observed in the spectra of O-rich AGB circumstellar envelopes is in general affected by many different factors, intrinsic as the grain chemical composition, size distribution, structure (crystalline of amorphous) and degree of processing (e.g. annealing), or extrinsic as the radiative transfer effects due to the envelope optical depth, thermal structure and geometry.

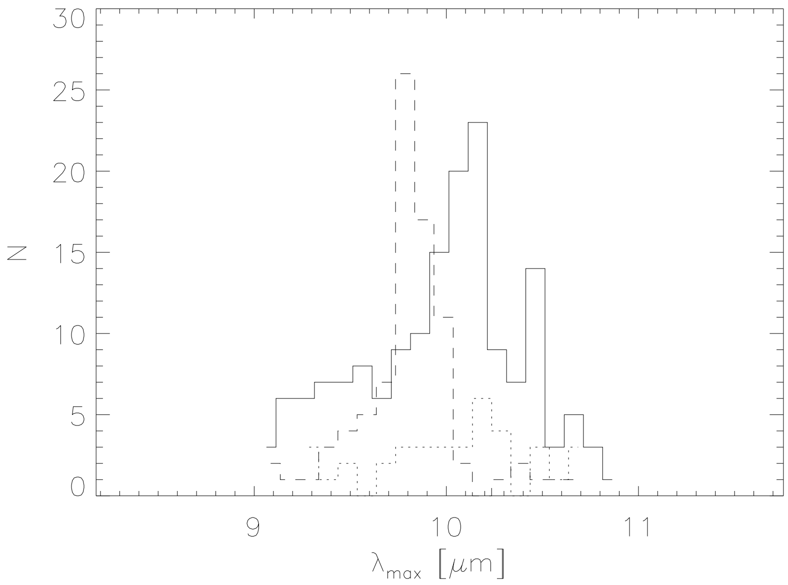

FIG. 4.6.— Distribution of the 10 $\mu$m silicate feature peak of KH sources. Dashed line is for Miras distribution, solid line for NMs and dotted line for SRa.

Little-Marenin & Little (1990) first tried to classify a large sample of O-rich AGB variables from the point of view of their silicate feature in the IRAS LRS spectra. They found that their sample of SR and Irregulars was showing a narrower silicate feature, shifted to the red, compared to the Miras. A similar analysis was performed by Hron et al. (1997) with larger statistics, and taking into account the dust continuum emission by fitting it with a separate black body. This later work confirmed the differences between the two classes, finding a shift of about 0.3 $\mu$m in the peak position.

In order to probe the KH sources in terms of the shape of their silicate feature, we have fitted each individual IRAS LRS with the best 5 degree polynomial in the 9-11 $\mu$m wavelength range. The fitting procedure removes the effect of noise and eventual secondary features, producing "smooth" spectra where the position of the maximum can be easily recognized. The wavelength of the maximum of the best fit polynomial in the given interval is then assumed to be the position of the "true" silicate peak.

With this technique we measured the position of the silicate peak of 85 Miras and 162 NMs; for the remaining sources (11 Miras and 84 NMs) the

TABLE 4.2 SILICATE PEAK POSITION FOR KH SOURCES.

| Sample | Median [$\mu$m] | Mean [$\mu$m] | $\sigma$ [$\mu$m] | N sources |
|---|---|---|---|---|
| Mira | 9.87 | 9.86 | 0.28 | 85 |
| NM | 10.07 | 10.01 | 0.42 | 162 |
| SRa | 10.10 | 10.08 | 0.41 | 37 |
| SR ($P < 100^d$) | 10.09 | 10.04 | 0.43 | 31 |
| SR ($P \gtrsim 100^d$) | 10.07 | 10.02 | 0.38 | 95 |

Significance of statistical tests

| Sample | F-test | t-test | Result at 0.01 significance[a] |
|---|---|---|---|
| Mira vs. NM | $5 \cdot 10^{-5}$ | $5 \cdot 10^{-4}$ | Different $\sigma$ and mean[b] |
| SRa vs. Mira | $6 \cdot 10^{-3}$ | $4 \cdot 10^{-3}$ | Different $\sigma$ and mean[b] |
| SRa vs. NM | 0.82 | 0.43 | Same $\sigma$ and mean |
| SR $P<100^d$ vs. $P\gtrsim100^d$ | 0.41 | 0.87 | Same $\sigma$ and mean |

[a] Samples have different $\sigma$ if the variance F-test returns a significance of 0.01 or smaller, and different mean values if Student's t-test returns a significance of 0.01 or smaller.
[b] Student's t-test performed in the "unequal variance" case.

fitting procedure failed either because of the excessive noise in the spectrum, or for the absence of a significant feature. Many of the sources for which the silicate feature is too weak are in fact Lb stars of LRS class 1n. Note that the infrared colors of such sources are generally too low (having a color temperature below 1000 K), to identify them as "naked photospheres" (AGB stars without a circumstellar envelope). More probably, they are instead Lb stars with circumstellar envelopes of intermediate optical depth, having the silicate feature partially in self absorption. This is consistent with the distribution of these sources in figure 4.3.

The results are shown in table 4.2, and the histogram with the distribution of $\lambda_{max}$ is plotted in figure 4.6. We found the mean values for Miras and NMs to be $\langle\lambda_{max}\rangle_{Mira} \simeq 9.86$ $\mu$m and $\langle\lambda_{max}\rangle_{NM} \simeq 10.01$ $\mu$m respectively, and the median values 9.87 and 10.08 $\mu$m. The standard deviation $\sigma_\lambda$ is also very different in the two samples, almost twice for NMs ($\sim 0.42$ $\mu$m) than for Miras ($\sim 0.28$ $\mu$m), indicating a larger dispersion in the silicate feature

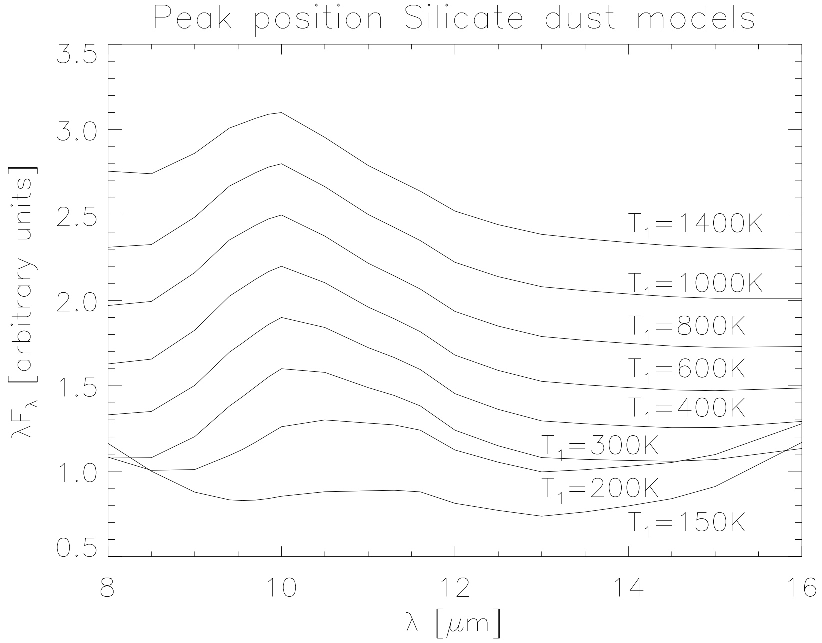

FIG. 4.7.— The position of the 10 $\mu$m silicate feature peak for a sequence of models with $\tau_V = 2.9$ and $T_1$ equal to 1400, 1000, 800, 600, 400, 300, 200 and 150 K.

position for the NMs; this difference is statistically significant with respect to the F-test 0.01 significance level. The Student's t-test for the mean values, performed between the two samples (with unequal variances), confirms the separation of the Mira and NM populations with high significance (0.0005). This result is in agreement with the shift of about 0.2–0.3 $\mu$m observed in previous analysis (Hron et al., 1997).

We performed the same test on the SRa class, finding $\langle\lambda_{max}\rangle_{SRa} \simeq$ 10.08 $\mu$m, and $\sigma_\lambda \simeq 0.41$, very close to the general NM class statistics. This is a further indication that KH SRa do not contain a significant fraction of misclassified Miras. The $\langle\lambda_{max}\rangle$ values for the SR subset with $P \gtrsim 100^d$ and $P < 100^d$ are 10.07 and 10.9 $\mu$m respectively, and the $\sigma_\lambda$ are 0.43 and 0.39 $\mu$m. Again this indicates that the two subclasses are part of the same population.

There are many different reasons that can explain the 0.2 $\mu$m shift in the silicate feature position between Miras and NMs. The first possibility is that the composition of dust, and/or oxidation state of the silicate material in the two classes is different, as suggested by various authors (Vardya et al., 1986;

Little-Marenin & Little, 1988; Onaka et al., 1989; Sloan & Price, 1998). A second explanation is that the grain size distribution may be different. This possibility has been explored by Simpson (1991). The results of her work, however, show that to produce a noticeable change in the silicate feature of the envelope spectra, a variation in the dust grain size of at least a factor 7 is required. As argued by Hron et al. (1997), current dynamical models for dust driven winds (Höfner & Dorfi, 1997) indicate that such large variations in the particle size are unlikely to be produced.

There is, however, a third possibility, that is to invoke radiative transfer as the cause of the peak shift. Envelopes with fixed optical depth $\tau_V$ and decreasing dust temperature emit an increasing fraction of their thermal radiation at longer wavelengths. This translates in “flat” spectra in which the contribution from the silicate feature, gradually self absorbed, is bound to disappear, until the thermal continuum produces a “bump” in the spectrum which can be interpreted as a shift in the peak of the feature. This effect is shown in figure 4.7 for a sequence of models with $\tau_V \simeq 2.9$ and gradually decreasing dust temperature $T_1$. Note how the shift becomes very pronounced; this suggests that cold envelopes would have a much larger dispersion in the $\lambda_{max}$ distribution (as in fact is observed for our NM variables), than envelopes with hotter dust.

## 4.3 Modeling the mid-IR spectra

To quantify the color temperature difference between KH Miras and NMs, and separate the effects of dust thermal structure and optical depth, we have estimated $T_1$ and $\tau_V$ for each KH source by fitting its LRS spectrum. The adopted best fit procedure is based on $\chi^2$ minimization of the individual spectra with a series of DUSTY models, computed as described in section 3.2. Details on the fitting technique are given in section 4.3.2, and the efficiency in obtaining a good quality fit is discussed in 4.3.3.

As radiative transfer modeling with DUSTY requires to specify the geometry, dust radial density profile and grain size distribution, the dust mass loss rate needed to produce each model envelope is fully characterized by a certain combination of model parameters. The explicit relation between best fit parameters and $\dot{M}_d$ is given in section 4.4, where the statistical distribution of the dust temperature structure and optical depth is also discussed, in terms of the Mira vs. NM dichotomy suggested in the previous sections.

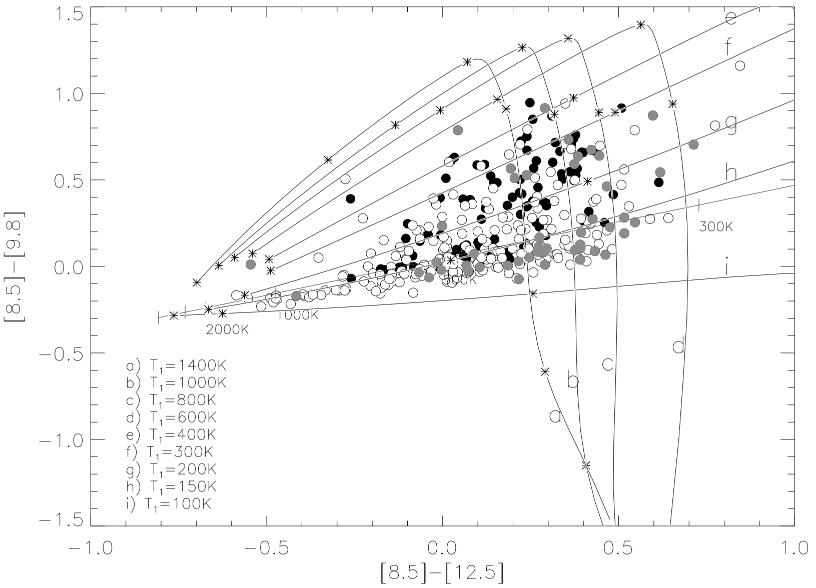

FIG. 4.8.— Silicate color diagram of KH sources with DUSTY models having 2500 K Engelke central source with 10% SiO absorption. Models with $T_1$ equal to 100, 150, 200, 300, 400, 600, 800, 1000 and 1400 K are plotted.

### 4.3.1 Model parameter space

Since our KH sample contains only O-rich sources, and has circumstellar envelopes with oxidic dust, we have adopted the full grid of models computed in section 3.2 with the Ossenkopf et al. (1992) dust. The models were run with "standard" MRN grain size distribution, and $n_d(r) \propto r^{-2}$ radial density profile (steady mass loss during the phase in which the current envelope was produced). The inner radius $R_1$ was fixed by the choice of the inner shell temperature $T_1$, and the outer envelope radius was scaled as $R_2 \simeq 1000 \cdot R_1$.

As for the brightness energy distribution of the central star, we have tested both the "standard" 2000 K black body, and the Engelke function with 10% SiO absorption described in section 3.2.2. Even though the Engelke + SiO function provides the best fits for dustless sources with "naked photosphere" and envelopes characterized by a very low optical depth, we found that a standard black body is in general a better choice for AGB envelopes with $\tau_V \sim 1$. As shown in figure 4.8 and 4.9: models computed with the Engelke + SiO function have the tendency to produce LRS spectra

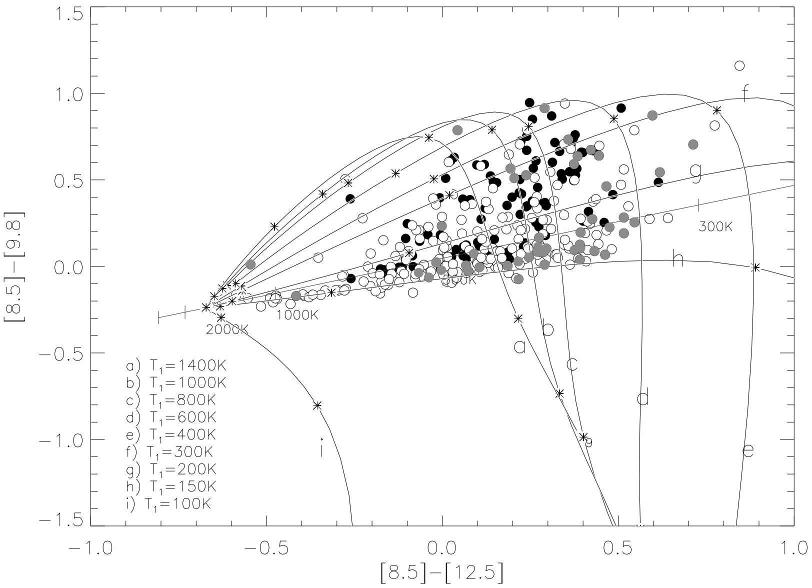

FIG. 4.9.— Silicate color diagram of KH sources with DUSTY models having 2000 K Planck black body central source. Models with $T_1$ equal to 100, 150, 200, 300, 400, 600, 800, 1000 and 1400 K are plotted.

with an excessive strength of the 10 $\mu$m silicate feature (resulting in too high [8.5]-[9.8] color). Models with the black body curve, on the contrary, can better reproduce the distribution of HK sources in the color color plane. For this reason, the analysis which follows has been entirely made using the DUSTY models with Planck black body central source.

A fine logarithmic grid of models with $\tau_V$ from $10^{-3}$ to 231, and $T_1$ from 100 to 1400 K was used, with 60 steps in $\tau_V$ and 31 in $T_1$, in order to provide the necessary precision in the best fit parameters. Note in figure 4.9 how the coldest dust family of models (track with $T_1 \simeq 100$ K) is totally inadequate to fit any source in the KH sample. The coldest models able to provide a good fitting of the sources, have $T_1 \simeq 150$ K, which can be assumed as a rough estimate of the minimum inner shell temperature in our sample of AGB envelopes.

A subset of models with $T_1$ restricted to the interval 630–1400 K ("hot dust" models hereafter) was then extracted from the full set, in order to test whether "cold dust" models with lower $T_1$ are really necessary to improve the fitting of certain classes of spectra.

### 4.3.2 Fitting technique

The best fit models for each source in our sample were found with a $\chi^2$ minimization routine applied to the source and model spectra in the IRAS LRS wavelength range only. Even though the IRAS point source photometry was available for all sources, and easily derived for the models, we decided to restrict the fitting procedure to the 7–23 $\mu$m interval. This decision was made in order to avoid galactic cirrus contamination at longer wavelengths, and the phase dependence of optical and near-IR photometry with the LPV of the sources.

For each source in the sample, the models were individually renormalized to match the absolute flux scale of the source LRS. The normalization factor $\alpha$ of each model was computed by least square minimization of the distance between model and source:

$$\alpha = \frac{\sum_{i=1}^{N} \left(\lambda_i F_\nu^S \cdot \lambda_i F_\nu^M\right)}{\sum_{i=1}^{N} \left(\lambda_i F_\nu^M\right)^2} \tag{4.1}$$

where $\lambda_i F_\nu^S$ is the source spectral energy distribution (the IRAS LRS) and $\alpha \cdot \lambda_i F_\nu^M$ the (renormalized) model, rebinned on the LRS wavelength grid, on which the summation index $i$ runs. The $\chi^2$ variable of each source-model pair was then defined as:

$$\chi^2 = \frac{1}{N-2} \sum_{i=1}^{N} \frac{\left[\lambda_i F_\nu^S\left(\lambda_i\right) - \alpha \cdot \lambda_i F_\nu^M\left(\lambda_i\right)\right]^2}{\sigma_S^2\left(\lambda_i\right) + \sigma_M^2\left(\lambda_i\right)} \tag{4.2}$$

The error $\sigma_S$ of the IRAS LRS was derived by subtracting the LRS with a smoothed version of themselves, while the error $\sigma_M$ was estimated as the difference between the two closest models in the parameter space. The $\chi^2$ variable was finally divided by the number of degrees of freedom $N-2$, where $N = 80$ is the number of wavelengths, and 2 are the fitting parameters measured in the fit ($\tau_V$ and $T_1$). Each source was then assigned to its best fit model, providing the minimum value of the $\chi^2$ variable.

As a consistency test for our fitting procedure, we have simulated a set of LRS spectra with known $T_1$ and $\tau_V$, covering the whole model parameter space, by introducing gaussian noise to our DUSTY model grid. The synthetic spectra were then fitted by using the same original models, without noise. The results are shown in figure 4.10 for $S/N = 10$ and $S/N = 5$ (the first case is the typical one for our sources, and the second corresponds to the most noisy sources in the sample). Each circle in the plots represent a

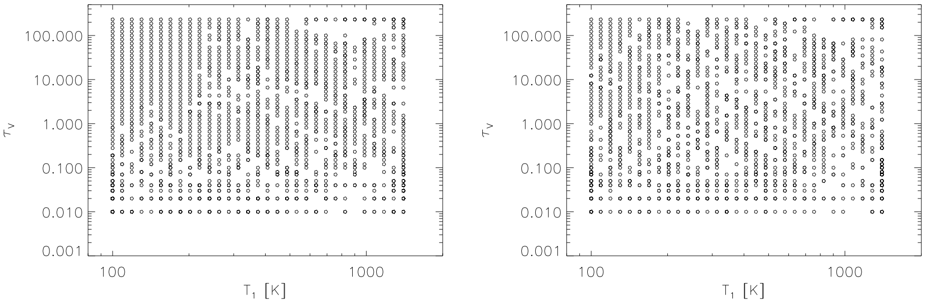

FIG. 4.10.— Test diagram of $\chi^2$ fitting procedure. Artificial gaussian noise have been added to the full grid of models and to the resulting spectra. This produced "noisyfied" spectra, with $S/N = 10$ (left) and 5 (right), which have been fitted using the unmodified grid. Each circle represents one point of the model grid for which the correspondent "noisyfied" model have been successfully fitted. Empty spaces in the regular grid pattern correspond to models not correctly fitted, as a consequence of the added noise.

point in the model grid; missing points are "noisyfied" models which have not been fitted correctly by our procedure.

The figure shows that increasing noise can reduce the effectiveness of our procedure, but within the limits of our sample is not likely to introduce biases in the fit results. The missing points in the grid are distributed uniformly, at least in the regions where the physical parameters of KH sources are expected to fall. Sources with $\tau_V \lesssim 0.02$ are likely to have their optical depth overestimated, due to constraints in the numerical accuracy of the models, which for very low $\tau_V$ are practically indistinguishable. The distribution of the incorrectly identified models in $T_1$ is completely uniform, validating our procedure for fitting this parameter.

### 4.3.3 Fit results

The quality of our fits is estimated by the value of the best $\chi^2$ variable. As shown in figure 4.11, best fit models with $\chi^2 \lesssim 3$ are in general able to reproduce the source LRS with great accuracy, matching the position of the two silicate features (at 9.8 and 18 $\mu$m), their relative height and width, and the slope of the continuum emission. Fits with $3 \lesssim \chi^2 \lesssim 5$, are still good, even though some peculiarity of the silicate feature are not exactly reproduced. The continuum slope, however, is still well modeled, and the small discrepancies are in most cases due to the presence of secondary features, or the unusual width of the source LRS silicate feature, in the 13–14 $\mu$m

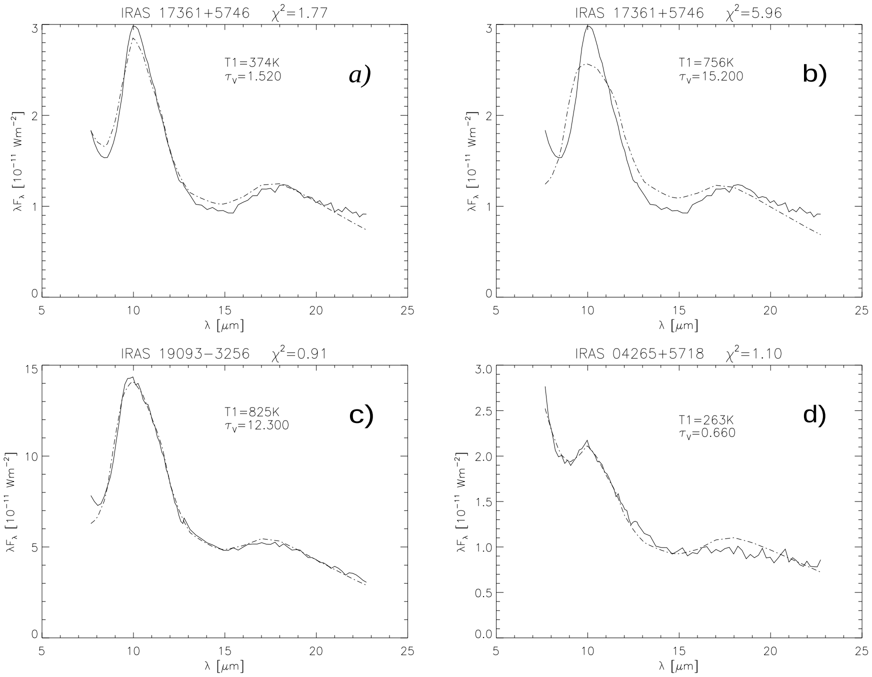

FIG. 4.11.— IRAS Low Resolution Spectra of Mira and NM sources (solid line) with best fit models (dashed dotted line). In panel *a* the SRb star TY Dra is fitted with a cold dust model ($T_1 \simeq 370$ K), resulting in a very small $\chi^2$. If the dust temperature is limited to the range 640–1400 K (as in the "hot dust" models), the fit is unable to reproduce the source spectral energy distribution (panel *b*). Panel *c* and *d* shows good quality fits of a Miras with relatively hot dust ($T_1 \simeq 825$ K) and a SRs with very low inner shell temperature ($T_1 \simeq 270$ K).

range, which cannot be fitted with the Ossenkopf et al. (1992) opacity. A better fit of these models probably requires a larger set of opacities, allowing variations in the dust composition. Models with $\chi^2 \gtrsim 5$, on the other hand, show more serious problems, as the wrong fit of dust continuum emission, or failure in the fitting routine convergence, due to insufficient $S/N$ in the source LRS. The best fit parameters obtained for these sources are less reliable, since a better fitting may require radically different opacities, or changes in the envelope geometry, such as the presence of multiple dust shells.

The statistics of the best fit $\chi^2$ for our KH sources is shown in table 4.3. The left side of the table reports the number of sources having $\chi^2$ larger than 3, 5 and 10 in the Miras, NMs, SRa and period selected SRs, fitted

Table 4.3 Sources which cannot be fitted with $\chi^2$ better than 3, 5 and 10.

| | all models | | | hot models | | |
|---|---|---|---|---|---|---|
| Sample | $\chi^2 \gtrsim 3$ | $\chi^2 \gtrsim 5$ | $\chi^2 \gtrsim 10$ | $\chi^2 \gtrsim 3$ | $\chi^2 \gtrsim 5$ | $\chi^2 \gtrsim 10$ |
| Mira | 35% | 19% | 3% | 42% | 31% | 12% |
| NM | 18% | 6% | 1% | 54% | 27% | 22% |
| SRa | 21% | 4% | 2% | 33% | 12% | 4% |
| SR ($P<100^d$) | 18% | 5% | 0% | 67% | 42% | 21% |
| SR ($P \gtrsim 100^d$) | 21% | 7% | 2% | 48% | 18% | 6% |

with the full grid of models. The right side present the same statistics, but with the use of the "hot dust" family of models (models with $T_1 \gtrsim 640$ K). Notice that all NM sources shows a significant improvement in the quality of their fits when "cold dust" models ($T_1 \lesssim 640$ K) are allowed (compare, e.g. panels *a* and *b* of figure 4.11), while Miras can be equally well fitted using "hot dust" models alone. This is a further evidence that the class of NM is more likely to show colder envelopes than the average Mira source.

## 4.4 Correlation between mass loss rate and shell temperature

The statistical distribution of the best fit parameters for our KH sample can be analyzed to test the separation between Miras and NMs suggested by the different colors and silicate feature position.

This statistical analysis is limited to sources with $\chi^2$ better than 10, in order to prevent unreliable fits to bias our conclusions. This restriction is aimed to exclude the sources in which the continuum emission is not exactly reproduced by the model, and thus the fitting procedure is suspected to have converged on mistaken best fit parameters. The excluded sources are 19% of the Miras, and 6% of the NMs.

This precautional measure, however, does not seem to affect the statistical validity of our results: similar tests performed on the whole sample yielded the same conclusions, within the approximations of our technique.

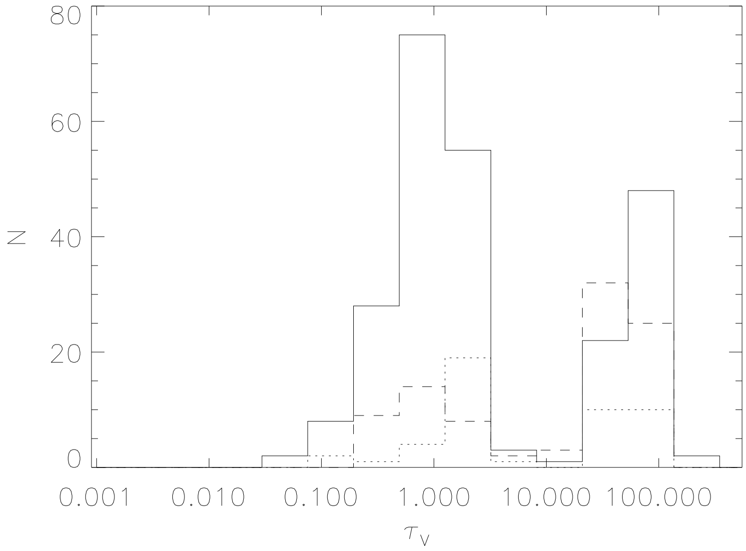

FIG. 4.12.— Distribution of the best fit optical depth $\tau_V$ for Miras (dashed line), NMs (solid line) and SRa (dotted line).

### 4.4.1 Distribution of envelope optical depths

Figure 4.12 shows the statistical distribution of the best fit optical depth for our KH sources. The histogram appears to be bi-modal, with a double-peak distribution centered at $\tau_V \sim 1$ and $\tau_V \sim 25$ respectively. NMs appears to be distributed mainly in the low $\tau_V$ bin, while Miras, although present in both categories, are mainly concentrated in the high optical depth bins. SRa appears to be equally distributed in the two categories, with a prevalence for low optical depths.

This diagram reflects a well known characteristic of LPVs: Miras in general possess higher optical depths than non-Miras, which on the contrary are in general brighter optically. From the analysis of our sample it is difficult to decide if the separation between the low and high $\tau_V$ distribution is statistically significant: larger statistics and a more accurate fit with better opacities is probably necessary to validate this result. The different average optical depth of the two main classes (Mira and NM), is however large enough to be confirmed by the statistical tests reported in table 4.4.

Note that the Student's t-test in table 4.4 underestimates the difference between the various populations, since it analyses the mean value assuming

TABLE 4.4 DISTRIBUTION OF BEST FIT $\tau_V$ FOR KH SOURCES.

| Sample | Median | Mean | $\sigma$ | N sources ($\chi^2 \lesssim 5$) |
|---|---|---|---|---|
| Mira | 23.1 | 25.4 | 21.8 | 81 (81%) |
| NM | 1.2 | 16.6 | 25.9 | 232 (94%) |
| SRa | 2.3 | 20.9 | 25.1 | 46 (96%) |
| SR ($P < 100^d$) | 0.8 | 10.5 | 25.8 | 54 (95%) |
| SR ($P \gtrsim 100^d$) | 1.5 | 20.2 | 26.2 | 121 (93%) |

Significance of statistical tests

| Sample | F-test | t-test | Result at 0.01 significance[a] |
|---|---|---|---|
| Mira vs. NM | 0.08 | $7 \cdot 10^{-3}$ | Same $\sigma$ and different mean |
| SRa vs. Mira | 0.28 | 0.30 | Same $\sigma$ and mean |
| SRa vs. NM | 0.83 | 0.29 | Same $\sigma$ and mean |
| SR $P{<}100^d$ vs. $P{\gtrsim}100^d$ | 0.92 | 0.02 | Same $\sigma$ and mean |

[a] Samples have different $\sigma$ if the variance F-test returns a significance of 0.01 or smaller, and different mean values if Student's t-test returns a significance of 0.01 or smaller.

a gaussian distribution. This is of course not valid for the bimodal distributions shown in figure 4.12. A much better comparison between the different subsamples is given by the median values of the best fit $\tau_V$, which are closer to the modal value for each sample. In this case, SRa appears to be more similar to NMs than to Miras, even though the Student's t-test cannot decide on the basis of the mean value. This confirms that our SRa does not have a large contamination of Miras. The two subclasses of NMs appears to have similar optical depths, even though short period NMs tends to have lower $\tau_V$.

### 4.4.2 Distribution of inner shell temperatures

If the segregation between Miras and NMs is related to an intrinsic difference in the underlying mass loss mechanism, a correlation between the best fit $\tau_V$ and $T_1$ should be expected. This is shown in figure 4.13, where the KH sources appear distributed in a strip crossing the diagram. Even though both classes of sources are present along the whole sequence, Miras tend to aggregate at the top of the strip, with higher optical depths and $T_1$. NMs, on the contrary, have in general lower $T_1$ and $\tau_V$. A discontinuity in the distribution of the sources for $T_1 \simeq 500$ K, suggests to divide the diagram in 4 separate regions, labeled counter-clockwise from I to IV, with most of the sources in quadrant I and III only. A quantitative distribution of the various subclasses in the four quadrants is given in table 4.5.

The sequence observed in figure 4.13 can be explained by assuming that low $T_1$ are the product of envelope expansion, after the interruption of the mass loss rate. At the end of an intense dust production phase, an envelope starting at the inner radius $R_c$ (dust condensation radius) will have a "steady state" radial profile $n_d(r) \simeq n_d(R_c) \cdot (R_c/r)^2$. If the dust production stops, the envelope would detach, expanding at a radius $R_1 = R_c + v_e t$, where $v_e$ is the expansion velocity and $t$ the time since the envelope detachment. From equations 2.29 and 2.65, the optical depth of the detached envelopes can be written as:

$$\tau_V \simeq \pi a^2 \cdot Q_V \cdot n_d(R_c)\,\frac{R_c^2}{R_1} \sim \tau_V(0)\left(\frac{1}{1+\frac{v_e t}{R_c}}\right) \tag{4.3}$$

where $\tau_V(0)$ is the optical depth that the envelope built-up just before detaching from the stellar atmosphere. Since the stellar flux scales as $r^{-2}$, and the cooling radiative flux of the grains as $T_d^4$, the equilibrium temperature of the dust at the inner envelope edge goes as $R_1^{-1/2}$. Taking into account radiative transfer effects, one has from equation 2.38:

$$T_1 \simeq T_c\left(\frac{R_c}{R_1}\right)^n \simeq T_c\left(\frac{1}{1+\frac{v_e t}{R_c}}\right)^n \tag{4.4}$$

with $n = 2/(4+\beta)$, and $\beta \sim$ 1–2 for silicate and amorphous carbon dust. Equations 4.3 and 4.4 describe a linear relation on the logarithmic $\tau_V$ - $T_1$ plane, parametrized on the time $t$ after the envelope detaches:

$$\log \tau_V \simeq \log\left[\tau_V(0)\right] + k\,\log\left[\frac{T_1}{T_c}\right] \tag{4.5}$$

where $k \simeq (4+\beta)/2 \sim$ 2.5–3.0. Linear interpolation of the sources in figure 4.13 gives a very similar result, with a best fit regression line, for all sources, that is approximately:

$$\log \tau_V \simeq \frac{3}{2} + \frac{5}{2} \cdot \log\left(\frac{T_1}{1000\mathrm{K}}\right) \tag{4.6}$$

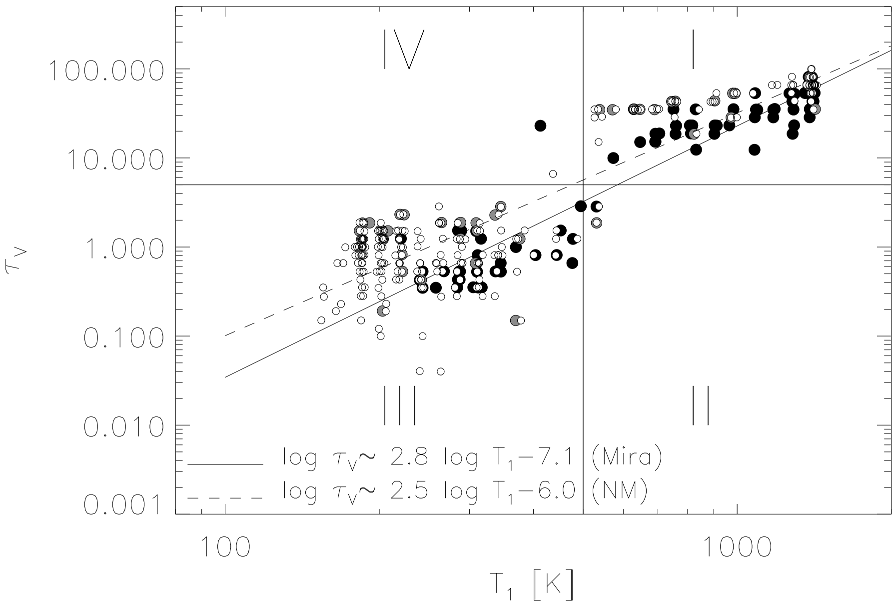

Fig. 4.13.— Model $\tau_V$ vs. $T_1$ for Miras (filled circle), non-Miras (empty circles) and SRa (grey symbols). A small random offset (less than 1/3 of the parameter grid step) has been added to each $T_1$ and $\tau_V$, in order to separate the symbols associated to sources with identical best fit parameters, which would otherwise appear as a single point on the diagram. The plot is divided in four regions, according to the source segregation; the counts in the four quadrants are given in table 4.5.Regression lines for Miras and NMs are plotted.

Table 4.5 KH sources distribution in $\tau_V$ vs. $T_1$ diagram.

| Sample | I | II | III | IV |
|---|---|---|---|---|
| Mira | 59 | 1 | 32 | 1 |
| NM | 72 | 2 | 169 | 1 |
| SRa | 20 | 1 | 26 | 0 |

This confirms that the distribution of the sources in the $T_1$ / $\tau_V$ space are well represented by the hypothesis of detached shells after a phase of enhanced mass loss.

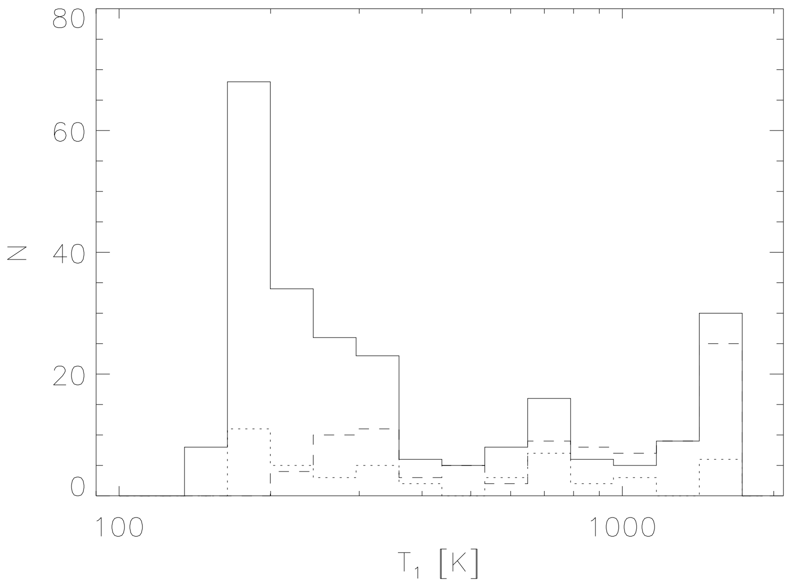

FIG. 4.14.— Histogram of $T_1$ distribution for KH Miras (dashed line), NM (solid line) and SRa (dotted line).

The details of the source distribution on the plot, and in particular the steep discontinuity in $\log \tau_V(0)$ shown by all sources around $T_1 \sim 500$ K may be due to a sudden drop in the dust production and growing processes when the temperature of the inner shell drops, due to its expansion, below a critical value, making inefficient the dust accumulation mechanisms.

The hypothesis of detached shells can also predict the distribution of the sources $\mathrm{d}N/\mathrm{d}T_1$ in each temperature bin:

$$\frac{\mathrm{d}N}{\mathrm{d}T_1} = \frac{\mathrm{d}N}{\mathrm{d}t} \cdot \frac{\mathrm{d}t}{\mathrm{d}T_1} \tag{4.7}$$

where $\mathrm{d}N/\mathrm{d}t$ is the distribution of sources as a function of the time $t$ in which the envelope detached. Assuming a constant expansion rate, $\mathrm{d}N/\mathrm{d}t \sim \mathit{const}$ and $\mathrm{d}T_1/\mathrm{d}t \propto \mathrm{d}T_1/\mathrm{d}R_1 \simeq R_1^{-n-1} \propto T_1^{n+1/n} \simeq T_1^3$ (using equation 4.4), and thus:

$$\frac{\mathrm{d}N}{\mathrm{d}\log T_1} \propto T_1 \cdot \frac{\mathrm{d}t}{\mathrm{d}T_1} \simeq T_1^{-2} \tag{4.8}$$

Table 4.6 Distribution of best fit $T_1$ for KH sources.

| Sample | Median [K] | Mean [K] | $\sigma$ [K] | N sources ($\chi^2 \lesssim 5$) |
|---|---|---|---|---|
| Mira | 830 | 870 | 430 | 81 (81%) |
| NM | 290 | 490 | 430 | 232 (94%) |
| SRa | 370 | 560 | 410 | 46 (96%) |
| SR ($P < 100^d$) | 200 | 360 | 350 | 54 (95%) |
| SR ($P \gtrsim 100^d$) | 310 | 480 | 450 | 121 (93%) |

Significance of statistical tests

| Sample | F-test | t-test | Result at 0.01 significance[a] |
|---|---|---|---|
| Mira vs. NM | 0.86 | $9 \cdot 10^{-11}$ | Same $\sigma$ and different mean |
| SRa vs. Mira | 0.72 | $1 \cdot 10^{-4}$ | Same $\sigma$ and different mean |
| SRa vs. NM | 0.78 | 0.35 | Same $\sigma$ and mean |
| SR $P<100^d$ vs. $P\gtrsim100^d$ | 0.04 | $2 \cdot 10^{-3}$ | Same $\sigma$ and different mean |

[a] Samples have different $\sigma$ if the variance F-test returns a significance of 0.01 or smaller, and different mean values if Student's t-test returns a significance of 0.01 or smaller.

The histogram shown in figure 4.14 agrees with this dependence for the sources on NM class. For example, there are about 6 times more sources in the $T_1 = 200$ K bin than in the $T_1 = 500$ K bin, in nice agreement with the prediction in equation 4.8.

The distribution of NMs is sharply truncated for $T_1 \sim 200$ K, even though our model grid continues as low as $T_1 = 100$ K. This results suggests that when the NMs envelope has expanded to a distance at which the equilibrium temperature is $\sim$ 150–200 K, a new hot shell is formed, bright enough to dominate the LRS spectrum from which the fit is made.

Note that the same lower value of $T_1$ was estimated by superposing the model tracks on the "silicate" diagram in figure 4.9. This lower limit in the dust inner shell temperature of all sources can be used to derive the maximum time in which the mass loss is suspended in NMs sources, by using the radial dependence $T_d(r)$ in equation 4.4. Since the distance $R_c$ at which the silicate dust can form ($T_c \simeq 1500$ K) is, for a typical O-rich AGB with $T_{eff} \simeq 200$ K, of the order of a few stellar radii ($R_c \simeq$ 5–8 $\cdot 10^{13}$ cm), one can write:

$$R_1 \sim 5 - 8 \cdot 10^{13}\,\mathrm{cm}\left(\frac{1500\mathrm{K}}{T_1}\right)^2 \tag{4.9}$$

being $R_s \sim 1$ A.U. the average stellar radius in the AGB phase. A dust shell with $T_1 \simeq 200$ K should thus be located at a distance $R_1 \simeq 0.9$–$1.7 \cdot 10^{16}$ cm. Assuming an expansion speed about 15 km/s, the required time to produce a detached shell at such distance is then 100–200 yr. Note that the estimated time scale is too long to compare with the Mira/SR pulsational period, and too short with respect to the interpulse time in the TP-AGB phase. It is however consistent with the timescales observed by Hashimoto et al. (1998); Sahai et al. (1998); Mauron & Huggins (1999), and by the independent estimate made in section 3.3.5 (see also Marengo et al., 1999).

The timescale of the high mass loss duration phase, in which the dust envelopes are created, can also be estimated by counting the fraction of NMs in the high temperature bins (e.g. $T_1 \gtrsim 500$ K). Since this fraction is about 30%, the phase of intense dust production should last no more than 30–60 yr, assuming 100-200 yr as the total period of the mass loss cycle.

Miras, on the contrary, show a flat distribution, truncated at a much higher $T_1$. This is an evidence that Mira sources have a higher dust production efficiency, which prevents the complete detachement of their circumstellar envelopes, and their cooling to very low temperatures.

The parameters of the $T_1$ distribution for the various subsamples are written in table 4.6. They confirm the separation between Miras and NMs and the homogeneity of SRa with the global NM class. The two subclasses of SRs with long and short pulsational period, however, does show a different mean value, with short period SRs having colder dust than the long period ones. This difference, however, has low statistical significance, and can be due to statistical fluctuations in our sample.

### 4.4.3 Distribution of mass loss rates

From the best fit parameters of each source, it is possible to estimate the mass loss rate. By integrating the differential optical depth along the path as in equation 4.3, with a "steady mass loss" radial density profile $n_d(r) \simeq n_d(R_1) \cdot (R_1/r)^2$, one obtains:

$$\tau_V \simeq \pi a^2 \cdot Q_V \cdot n_d(R_1) R_1 \tag{4.10}$$

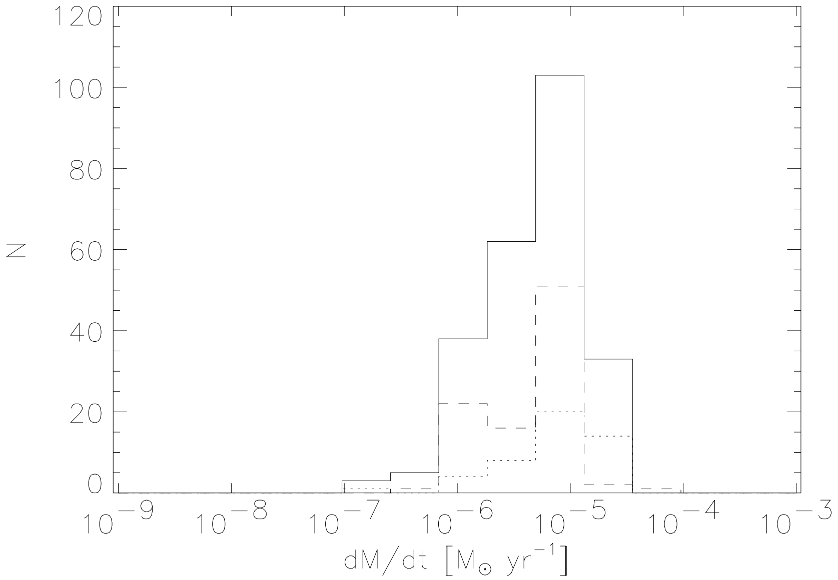

FIG. 4.15.— Distribution of best fit mass loss rate $\dot{M}$ for Miras (dashed line), NMs (solid line) and SRa (dotted line).

where $a$ is the dust average grain radius and $Q_V$ the opacity at optical wavelength. For a spherically symmetric dust envelope with constant expansion velocity $v_e$, the mass loss rate is:

$$\dot{M} \simeq 4\pi r^2 \cdot v_e \cdot \mu_d \rho_r \tag{4.11}$$

where $\mu_d$ is the dust to gas mass loss ratio and $\rho_r \simeq 4/3\pi a^3 \cdot \rho_d \cdot n_d(r)$ the mass density distribution of the circumstellar shell, made of individual dust grains having mass density $\rho_d$. Combining equation 4.10 with equation 4.11 one has:

$$\dot{M} \simeq \frac{16\pi a}{3} \cdot \frac{\mu_d \rho_d \cdot v_e}{Q_V} \cdot \tau_V \cdot R_1 \tag{4.12}$$

For the sources in our KH sample, one can assume $\rho_d \simeq 3.9$ g cm$^{-3}$ as in terrestrial silicates, $a \simeq 0.1$ $\mu$m, $Q_V \simeq 1$, $v_e \simeq 15$ km/s and $\mu_d \simeq 100$. Using equation 4.9, one finally obtains the following approximation for the mass loss rates, as a function of the two fitting parameters $\tau_V$ and $T_1$ alone:

TABLE 4.7 DISTRIBUTION OF BEST FIT $\log_{10}(\dot{M}/1\mathrm{M}_\odot\mathrm{yr}^{-1})$ FOR KH SOURCES.

| Sample | Median | Mean | $\sigma$ | N sources ($\chi^2 \lesssim 5$) |
|---|---|---|---|---|
| Mira | -5.3 | -5.4 | 0.3 | 81 (81%) |
| NM | -5.4 | -5.4 | 0.4 | 232 (94%) |
| SRa | -5.1 | -5.2 | 0.4 | 46 (96%) |
| SR ($P < 100^d$) | -5.5 | -5.5 | 0.4 | 54 (95%) |
| SR ($P \gtrsim 100^d$) | -5.3 | -5.3 | 0.4 | 121 (93%) |

Significance of statistical tests

| Sample | F-test | t-test | Result at 0.01 significance[a] |
|---|---|---|---|
| Mira vs. NM | 0.14 | 0.46 | Same $\sigma$ and mean |
| SRa vs. Mira | 0.14 | $2 \cdot 10^{-3}$ | Same $\sigma$ and different mean |
| SRa vs. NM | 0.66 | $6 \cdot 10^{-3}$ | Same $\sigma$ and different mean |
| SR $P<100^d$ vs. $P \gtrsim 100^d$ | 0.59 | $8 \cdot 10^{-3}$ | Same $\sigma$ and different mean |

[a] Samples have different $\sigma$ if the variance F-test returns a significance of 0.01 or smaller, and different mean values if Student's t-test returns a significance of 0.01 or smaller.

$$\dot{M} \simeq 0.1 \cdot \tau_V \left(\frac{1\mathrm{K}}{T_1}\right)^2 \tag{4.13}$$

Note that this quantity represent the mass loss rate at the time in which the dust shell was produced. In the case of detached envelopes, this is not the current mass loss rate, which may be significantly lower.

The histogram with the distribution of $\dot{M}$ is shown in figure 4.15. All classes reveal a similar distribution centered around $\log_{10}(\dot{M}/1\mathrm{M}_\odot\mathrm{yr}^{-1}) \simeq -5.3$, and a similar spread, with $\dot{M}$ in the interval $10^{-7}$–$5 \cdot 10^{-5}$ $\mathrm{M}_\odot$ $\mathrm{yr}^{-1}$. This result implies that Miras and NMs does have a similar total mass loss rate, at least during the high dust production phase which resulted in the creation of the dust shell.

Table 4.7 reports the statistics of the distribution. The similarity between Mira and NM mass loss is confirmed, even though a separation of SRa from the other classes, and between the two classes of SRs with different pulsational period, is suggested. The significance of the separation is however very low, and can be attributed to statistical fluctuations in our sample, or to the high uncertainties in the quantities assumed to derive equation 4.13 (and in particular the dust to gas mass loss ratio and the average grain size).

## 4.5 Conclusions

In this analysis we have investigated the connections between mass loss and variability for a sample of AGB LPV of Mira, SR and Irregular type, from the point of view of the mid-IR emission of their dusty circumstellar envelopes.

We found the continuum excess color in the 12.5 and 18.0 $\mu$m bands able to differentiate between sources of Mira and NM type. NMs showed a higher [12.5]-[18.0] color, which we interpreted as an indication of missing hot dust in the circumstellar envelope of these sources.

We then compared the position of 10 $\mu$m silicate feature in the LRS spectrum of Mira and NM sources, confirming the shift of $\sim 0.2$ $\mu$m already found by other authors. Even though this result may be taken as an evidence for mineralogical variability in the composition of oxidic dust in the two class of sources, we have pointed out how radiative transfer may mimic the same effect. If this is the case, the shift observed in the LRS of NMs can be another consequence of colder dust in their envelopes.

We then applied radiative transfer modeling to all sources in the sample, in order to derive their optical depth and temperature at the inner shell boundary by fitting their individual Low Resolution Spectra. Again we found a statistically significant difference between the temperature of NM and Mira circumstellar envelopes.

About 70% of all NMs in our sample show a $\tau_V$ vs. $T_1$ relation that is appropriate for detached envelopes, expanding freely at the AGB wind speed. For these sources, the inner boundary shell temperature is much lower than the dust condensation one, but never less than 150–200 K. This minimum temperature can be interpreted as a maximum limit of 100-200 yr in the period of time in which the envelopes are allowed to detach, before being replaced by newly formed hot structures. The remaining part of the NMs are instead characterized by much hotter envelopes with an estimated $T_1$ in the dust condensation and growth range ($Tc \sim$ 600–1400 K), in which the envelope is not complete detached. The frequency of these sources (~30%) suggests that the duration of the high mass loss phase in NMs is of the order of 30–60 yr. The two regimes are linked by an intermediate domain, in which $T_1 \sim 500$ K, where the optical depth of the envelope suddenly drops by one order of magnitude.

The proportion between "hot" and "cold" envelopes in the Mira class is reversed with respect to NMs, with 70% of Miras having $T_1 \gtrsim 500$ K. This dependence shows that fully detached shells are probably not common in the Mira class. The 1 magnitude drop in the total optical depth of the envelopes around $T_1 \sim 500$ K, is confirmed for this class of sources, and can thus be related to some basic property of the silicate dust condensation processes.

We did not find any significant difference in the total mass loss rates of Miras and NMs, even though the frequent occurrence of detached shells in NMs suggests the existence of intermittent phases in which the dust production is suspended for these sources.

All our statistical tests confirm that our subsample of SRa is coherent with the full sample of NMs (SRa, SRb and Irregulars) in our selection of KH sources. We also did not find any significant difference between SRs with long and short period pulsations, that can be associated with different phases in the AGB evolution.

As suggested by Ivezić & Knapp (1998), the absence of hot dust in NMs can be interpreted as a recent decrease ($\sim 10^2$ yr) in their mass loss rates. In the same paper were also found evidences for mass loss to resume on similar timescales, implying that AGB stars may oscillate between the Mira and NM phase, as proposed by Kerschbaum & Hron (1996). This idea is however discarded in a recent paper by Lebtzer & Hron (1999), in which the abundance of $^{99}$Tc in a large sample of SRs was compared with the analogous quantity in Miras. Since the Tc abundance is characterized by a quick increase during the first thermal pulse, after which it stays basically constant (Busso et al., 1992), a similar fraction of Tc-rich stars should be found in the Mira and SR samples. However, this is not the case, making it unlikely that TP-AGB variables oscillates between the two classes of pulsators.

Our analysis confirms the occurrence of shell detachment in NM variables, but suggests a different explanation. The discordant behavior of mass loss between Miras and NMs may be due to a different efficiency of oxidic dust formation in the two cases. This may be related to the characteristic pulsational mode of the two classes of variables.

Many separate evidences points toward the idea that SR variables pulsate as a combination of several overtones, while Miras are high amplitude pulsators (Wood et al.,, 1999), even though this subject is quite controversial (see e.g.Feast 1999, proceedings of the same I.A.U. conference). If this is the case, it is likely for Mira variables to have a greater efficiency in levitating their extended atmosphere to regions where the dust condensation is possible (see discussion of Icke et al. 1992 models in Sahai et al. 1998). As a consequence, Miras extended atmospheres would be able to support a continuous mass loss rate by providing enough molecules in the right density and temperature range for dust condensation and growth. NMs, on the contrary, would need several pulsation cycles to reach the critical density for dust formation to start. The increasing opacity resulting from dust nucleation would then trigger an outburst of dust production, lasting until the dust building elements are depleted, after which the envelope detaches. In this case, the active phase in which the mass loss is active in NM variables should be of the order of 30%, of the total cycle, according to the ratio of NMs which do not show a detached shell.

This dynamical mechanism has been partially reproduced in time dependent wind models (Winters, 1998), but the observed timescales (5–10 yr) are still too short to explain the observed shells. Based on our analysis, we cannot favor any particular mechanism for the occurrence of interrupted mass loss in NM sources. We feel, however, that dynamical models trying to reproduce the mass loss of AGB pulsators should take into account this link between the efficiency of dust production and the pulsational type, and the presence of detached dust shells found by analyzing the relations between $\tau_V$ and $T_1$ in the two classes of sources.

# Chapter 5

# Mid-IR observations of circumstellar dust

The previous chapters show how the analysis of the spectral energy distribution depends on the spatial distribution of the dust around the central source. Temporal variations in the mass loss rate give rise to complex radial density profiles, and thus affect the thermal structure and source spectra. Moreover, there are evidences of departures from spherical symmetry in many classes of circumstellar envelopes. Envelopes around Young Stellar Objects (YSOs) are formed in presence of dust disks or tori, and in many cases are perturbed by collimated molecular outflows. AGB stars are the precursors of Planetary Nebulæ, which show a wide array of axisymmetric, point symmetric or completely asymmetric shapes. It is not clear at which point of the transition between the AGB phase and PN the spherical symmetry is lost. Since a few AGB stars observed with high spatial resolution (Karovska et al., 1997; Lopez et al., 1997; Weigelt et al., 1998) do show asymmetric structures, it is not unlikely to imagine non spherical perturbations in the dusty envelopes during the AGB.

In this chapter the perspective of high resolution imaging of circumstellar envelopes with state of the art mid-IR imaging cameras are explored. The results obtained with several instruments at different telescopes are presented.

Section 5.3 describes the observations of a sample of AGB circumstellar envelopes performed with the mid-IR cameras TIRCAM (Tirgo InfraRed CAMera) and CAMIRAS at the TIRGO (Telescopio InfRarosso al GOrnergrat, Switzerland) and San Pedro Martir (SPM, Observatorio Astronomico National, Mexico) telescopes. These observations, are aimed to test the discriminating capability between the chemical and physical status of AGB envelopes with mid-IR observations. They have been made in collaboration with the TIRCAM and CAMIRAS team from 1992 to 1997, have been presented at several International Workshops and Meetings, and published in the papers Busso et al. (1996), Marengo et al. (1997) and Marengo et al. (1999).

Section 5.4 shows a new set of observations made with the camera MIRAC3 at the NASA Infrared Telescope Facility (IRTF, Mauna Kea, Hawaii). This project, was done under the supervision of Giovanni G. Fazio at the Harvard-Smithsonian Center for Astrophysics, in collaboration with the MIRAC team (G.G Fazio, W.F. Hoffmann, J.L Hora, A. Dayal and L.K. Deutsch). The goal of the project was to obtain direct information on the spatial structure of dusty circumstellar envelopes around AGB stars. The results have been presented at the International Conference "Asymmetrical Planetary Nebulæ II: from Origins to Microstructures", Cambridge MA, August 3-6, 1999 (see Marengo et al., 2000b). A paper is in preparation, discussing the detection of extended envelope emissions for a number of sources, and the constraints that the images provide for the geometry of the observed circumstellar envelopes.

In section 5.5, the observation of circumstellar dust around the massive YSO AFGL 2591 is described. The images, taken with MIRAC3 at IRTF in collaboration with the MIRAC team and Ray Jayawardhana, show the detection of a dust knot which may be evidence of a recent ejection event, in a source characterized by a well known molecular outflow. The results have been presented in a paper submitted to ApJ Letters (Marengo et al., 2000c).

## 5.1 Imaging with mid-IR cameras

Ground-based mid-IR observations are limited by high background emission. Thermal emission from the atmosphere and telescope, at ambient temperature (300 K), is peaked at 10 $\mu$m. Photons coming from astronomical sources are then mixed with a background flux that can be orders of magnitude more intense. Special techniques have thus to be employed in order to separate the source signal from the background.

This section describes the beam switching technique we used for the background subtraction in our observations, and the limitations, in sensitivity and spatial resolution, which affects mid-IR imaging.

### 5.1.1 Observations in background-limited conditions

To maximize the efficiency of observations in high background conditions, and minimize the residual background induced noise, special telescopes have to be used. An optimal infrared telescope requires:

1. a long focal length, providing a small pupil beam. This is necessary to minimize the physical size of the detector, which needs to be refrigerated at low temperature (a few K) in order to maintain a high quantum efficiency and low noise.
2. aluminum coated mirrors, which minimize the thermal emission and the IR reflectivity
3. small secondary mirror support and light screen baffles, in order to reduce the emissions from any metal surface which is not essential
4. a small secondary mirror, with an oscillating support for sky emission subtraction.

The background emission subtraction is made with the *beam switching* technique illustrated in figure 5.1. Rapid beam switching is obtained by oscillating the secondary mirror of the telescope (*chopping*), in order to point alternatively the target source and the nearby sky. The chopping motion should be carried out at the frequency of a few hertz, above the dominant frequency of sky and detector fluctuations. Additional slow beam switching is made by moving the telescope (*nodding*) at a frequency of a few hundredth of hertz, to remove from the image the effects of different telescope collimation in the two chop beams.

The beam switching sequence consists of several steps (Hoffmann & Hora, 1999). First, the telescope is set to image the source in one of the chop beams, while the camera coadds frames into two separate buffers for the required integration time. One buffers contains the source plus background (frame $A_+$), the other only background, or background plus the source in a different position (frame $A_-$). Next, the telescope is nodded to a different sky position, and two more background images are obtained and stored in two additional buffers (frames $B_+$ and $B_-$). If the *throw* of the nodding is smaller than the detector field of view, then frames $B_+$ and $B_-$ will contain images of the source in inverted positions with respect to the chopping $A_+$ and $A_-$ frames. After the observation is complete, the telescope is returned to its original position, the four images individually stored, and then combined to provide a realtime image with the background subtracted:

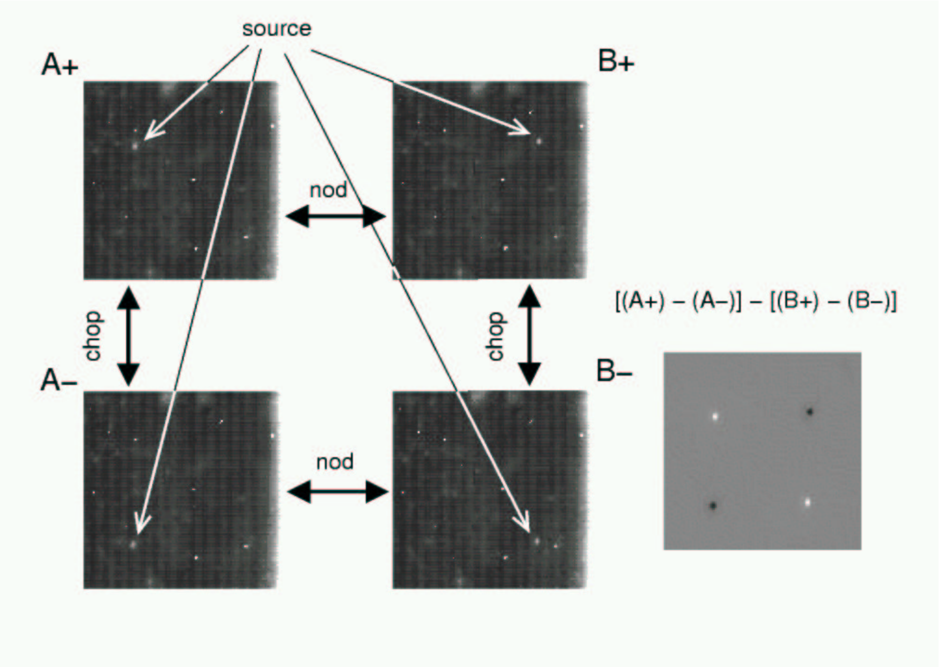

FIG. 5.1.— Schematic view of the beam switching technique for background subtraction in mid-IR imaging observations with the camera MIRAC3. The source is in all four beams.

$$\text{Image} = (A_+ - A_-) - (B_+ - B_-) \tag{5.1}$$

The total integration time on source is given by the combination of several parameters. If $t_{ch}$ is the time during which the source is chopped in each nodding positions, and $n_{nod}$ is the total number of nodding cycles in the observations, then:

$$t_{obs} = t_{ch} \cdot n_{nod} \cdot n_{beams} \tag{5.2}$$

where $n_{beams}$ is the number of chop/nod beams in which the source is imaged inside the detector field of view ($n_{beams} = 4$ in figure 5.1 example). To estimate the total time required for the observation, one should take into account overheads due to the movements of the telescope from one nod position to the other, time wait to settle oscillation jitter of the chopping secondary, and readout time of the detector.

### 5.1.2 $S/N$ ratio in background limited conditions

The total noise in the final image, expressed in "counts" of the analog to digital converters (A.D.U.) is given by different contributions:

$N_R$ read-out noise, introduced by the A/D converters

$i_s \cdot t$ signal current noise, given by the fluctuations of the source signal "current" $i_s$

$i_{BG} \cdot t$ background current noise, residual of the background signal not perfectly subtracted with the beam switching technique

$i_{DC} \cdot t$ dark current noise, due to currents that are generated by the detector electronics even when the the shutter is closed to incident photons

$\epsilon(t)$ flat-field noise, associated to the relative efficiency of the individual detector elements (*pixels*). This noise, when the flux in a given pixel is above the linear regime, can be described by an exponential law with time $\epsilon(t) \sim e^t$.

Signal, background and dark current noise depend on the Poissonian statistics of the incident photons ($P_k = \langle i \cdot t \rangle / k!\, e^{-\langle i \cdot t \rangle}$); they are thus proportional to the square roots of the individual currents and frame time: $\sigma_k = \sqrt{\langle i \cdot t \rangle}$. The total noise for each detector pixel then is:

$$N = \sqrt{N_R^2 + i_s \cdot t + i_{BG} \cdot t + i_{DC} \cdot t + \epsilon(t)} \tag{5.3}$$

According to the dominant source of noise, the observation is said to be "read-out noise limited" ($N \sim R_N$), "photon-noise limited" ($N \sim \sqrt{i_s \cdot t}$), "background noise limited" ($N \sim \sqrt{i_{BG} \cdot t}$) and "flat-field" limited ($N \sim \sqrt{e^t}$). The signal to noise ratio of the image is:

$$\frac{S}{N} = \frac{i_s \cdot t}{\sqrt{N_R^2 + i_s \cdot t + i_{BG} \cdot t + i_{DC} \cdot t + \epsilon(t)}} \tag{5.4}$$

which assumes the following time dependence in the various regimes:

$$\frac{S}{N} \sim \begin{cases} t & \text{if "read-out noise limited"} \\ \sqrt{t} & \text{if "background-noise limited"} \\ \sqrt{t} & \text{if "photon-noise limited"} \\ t \cdot \sqrt{e^{-t}} & \text{if "flat-field limited"} \end{cases} \tag{5.5}$$

For mid-IR observations, since the background current is much greater than the source and dark currents, and the integration times are limited to avoid the exponential regime of the flat-field noise, the resulting $S/N$ is dominated by the background. The total $S/N$ of a mid-IR image is thus proportional to the square root of the total integration time.

### 5.1.3 Point Spread Function in the mid-IR

The spatial resolution achievable with a mid-IR camera depends on the optics of the telescope and the quality of the atmosphere surrounding the telescope. In ideal conditions, the image of a point source (i.e. an unresolved star) is given by a bi-dimensional Dirac $\delta$-function. In a real system, the image observed on the focal plane of the detector is quite different, and is called *Point Spread Function*, or PSF.

The shape of the telescope and camera PSF is determined in part by diffraction, and in part by the atmospheric turbulence which deforms the wavefront of the stellar radiation.

The diffraction component can be derived by describing the the primary mirror as a circular aperture. The ideal diffraction limited PSF is then described by an Airy function:

$$F(x) = \left[ 2 \frac{J_1(x)}{x} \right]^2 , \qquad x = \frac{\pi \theta D}{\lambda} \tag{5.6}$$

where $\theta$ is the angular coordinate on the focal plane, $\lambda$ the wavelength of the image and $D$ the aperture of the telescope. In a real-life case, the presence of the secondary mirror and the camera secondary optics elements modify the standard Airy function to a more complex pattern. Deformations of the primary mirror due to different inclinations of the telescope, in absence of an active system able to compensate the non perfect rigidity of the system, can also change the shape of the ideal PSF. As a first approximation, equation 5.6 can be used to describe the PSF of an ideal system. In this case, the maximum angular resolution, given by the angular separation between the Airy function maximum and the first minimum, is:

$$\theta_{min}[\text{arcsec}] = 2.06 \cdot 10^5 \cdot 1.22 \frac{\lambda}{D} \tag{5.7}$$

The PSF is also affected by the "blurring" induced by turbulence in the atmospheric layers between the source and the detector (*seeing*). Temperature gradients in the turbulent cells of the atmosphere produce variations $\Delta n$ in the atmospheric refractive index. The variation $\Delta \mathcal{L}$ in the phase of the source radiation wavefront are proportional to the cell size $L$ and to the average number of cells along the optical path:

$$\Delta\mathcal{L} \simeq \sigma\sqrt{N} \cdot L \cdot \Delta n \tag{5.8}$$

If the telescope aperture $D$ is small with respect to $L$, then the effect of seeing is to move around in the focal plane a point source PSF, according to the random oscillations of $\Delta n$. In large aperture telescopes, the image results from sampling a large fraction of the wavefront; the final PSF is thus projected in a fixed position, but enlarged to a size similar to the PSF displacement produced in a small aperture telescope. By reducing the observation time to the same scale of atmospheric cell fluctuations, one can "freeze" the position of the oscillating PSF, or minimize its deformation due to seeing.

The seeing PSF can be represented analytically by a gaussian. More elaborate functional approximations use a bi-parametric function, which describes the width of the central profile and the lateral wings (Moffat, 1969; King, 1971). The "wings" of the seeing PSF are usually approximated by an exponential.

In the analysis performed in the following sections, the shape of the PSF was derived by observing a standard star, assumed to be an unresolved point source. We also simulated a synthetic PSF profile, obtained by coadding a number of Airy functions randomly shifted to simulate the atmospheric seeing. The random displacement was set using a normalized gaussian random number generator, having zero median value and the required standard deviation to generate the seeing FWHM:

$$\delta(\theta) = C_n \, e^{-\theta^2/\sigma^2} \qquad \sigma = \frac{FWHM_{seeing}}{4\ln 2} \tag{5.9}$$

where $C_n$ is a normalization constant.

In the visible, a medium aperture telescope provides a theoretical spatial resolution much higher than the seeing degradation of the image. In this case the observations are "seeing limited". In the mid-IR, on the contrary, the wavelength is 20 times longer, making the seeing less important. Typical mid-IR observations are thus "diffraction limited".

To have the correct spatial sampling of the instrumental PSF on the detector array, the magnification on the focal plane should be set to project the FWHM of the Point Spread Function on a matrix of 2×2 pixels (Nyquist criterium). These criteria fix the spatial scale on the array, which is thus decided by the aperture of the telescope.

## 5.2 Reduction of Mid-IR images

Mid-IR cameras usually store the collected data in some internal binary format, which has then to be converted to a format readable by the data reduction tools. This common file format is usually FITS (Flexible Image Transport System) (Wells et al., 1981; Greisen et al., 1981; Grøsbol et al., 1988; Harten et al., 1988).

Each camera has its own software to convert the stored data into FITS. In the case of TIRCAM and CAMIRAS this operation is performed by routines written in the IDL language by L. Corcione (Observatory of Torino, Italy) for TIRCAM and Philippe Galdemard (Service d'Astrophysique at Saclay, France) for CAMIRAS. The conversion of MIRAC3 data is instead performed by using the C program `mrc2fts` written by J.L Hora (Harvard-Smithsonian Center for Astrophysics, Cambridge MA) available at MIRAC web page `http://cfa-www.harvard.edu/~jhora/mirac/mirac.html`. At the same address the program `badcol` is also available, which corrects images that suffer from bad transmission of channels of data.

This section describes the data reduction pipeline adopted to process TIRCAM, CAMIRAS and MIRAC3 images, *after* their conversion to FITS format. It is assumed that the "positive" and "negative" chop-nod frames are already combined in the FITS files, as described in section 5.1.1.

The sequence which gives the single final image for each observation essentially consists of the following steps:

1. Determination of a bad pixel mask necessary to remove the contribution of individual unreliable detector pixels.
2. Flat field correction, which compensates for the different gains of the detector pixels.
3. Recentering of the individual frames in which the source integration has been splitted, shifting of the recentered frames with respect to the common centroid and coadding into a single image.
4. Photometric calibration of the final image, by using the observation of a reference star with known flux.
5. An optional further step consists in the deconvolution of the final image with a model PSF (usually derived from the image of a point source), in order to increase the spatial resolution.

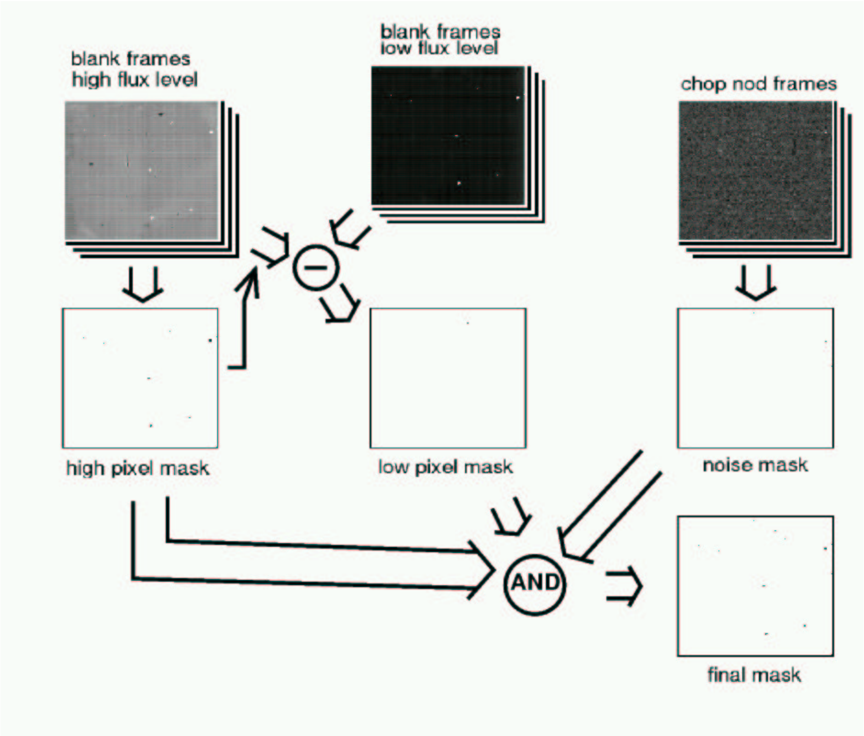

Fig. 5.2.— A bad pixel map is obtained from a set of individual frames in which the excessively high level, low level and high noise pixels are removed.

These operations have been performed on TIRCAM, CAMIRAS and MIRAC3 data with the aid of a specific package that I wrote in IDL, available at the MIRAC web page.

### 5.2.1 Masking bad pixels

The mask map specifies which image pixels should be combined in the final image from the single chop-nod frames. The reasons for which pixels have to be discarded are multiple:

1. Some pixels have an excessive dark current, which makes them appear like "hot spot" on the grabbed frames.

2. Other pixels are unresponsive, or suffer from vignetting of the pupil beam on the focal plane.

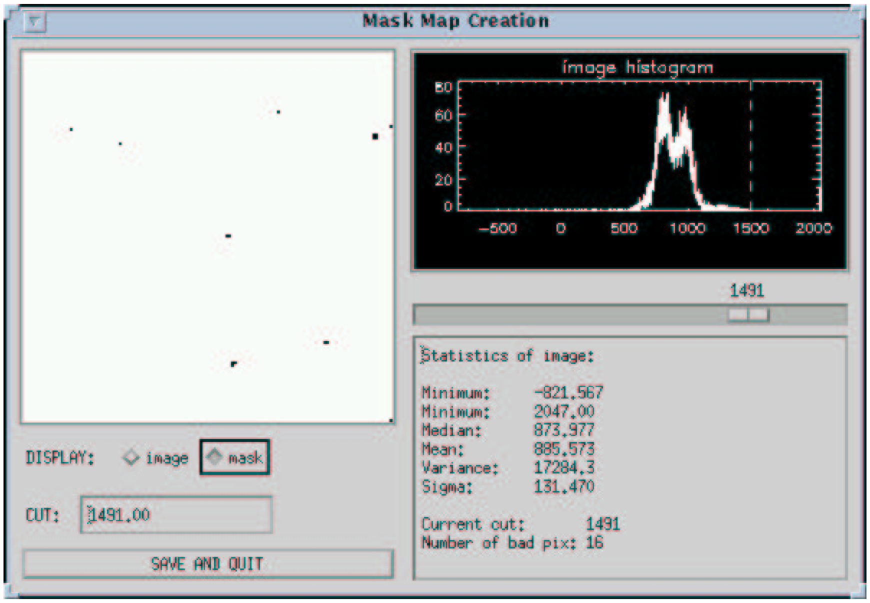

```
Statistics of image:

Minimum:      -821.567
Minimum:      2047.00
Median:       873.977
Mean:         885.573
Variance:     17284.3
Sigma:        131.470

Current cut:        1491
Number of bad pix: 16
```

FIG. 5.3.— Screenshot of the `xmask_ima` IDL program used to create a bad pixel mask. The selection of pixels for the high level pixel map is shown.

3. Some pixels should be removed because they have high noise, outside the statistics of the whole array.

A pixel mask map is an image in which the rejected pixels are set to zero (off) value, and the good ones to unity (on). Each detector frame image can then be filtered by multiplication (logical `AND`) with the mask. As shown in figure 5.2, the following sequence allows the creation of a mask (Hoffmann et al., 1998):

1. A blanked image ("grab") at a standard frame time is used to select the pixels with unusual high flux, due to high dark current. The selected pixels constitute the "high level pixel mask".
2. The difference between a blank image at moderately high flux level, and a low flux blank image masked with the high level pixel mask, allows to exclude low flux pixels. This generates a "low level pixel mask".
3. The standard deviation of a set of nod-chop off-source images is computed pixel by pixel; pixels with unusual high $\sigma$ are then set to zero in order to have a "noise pixel mask".

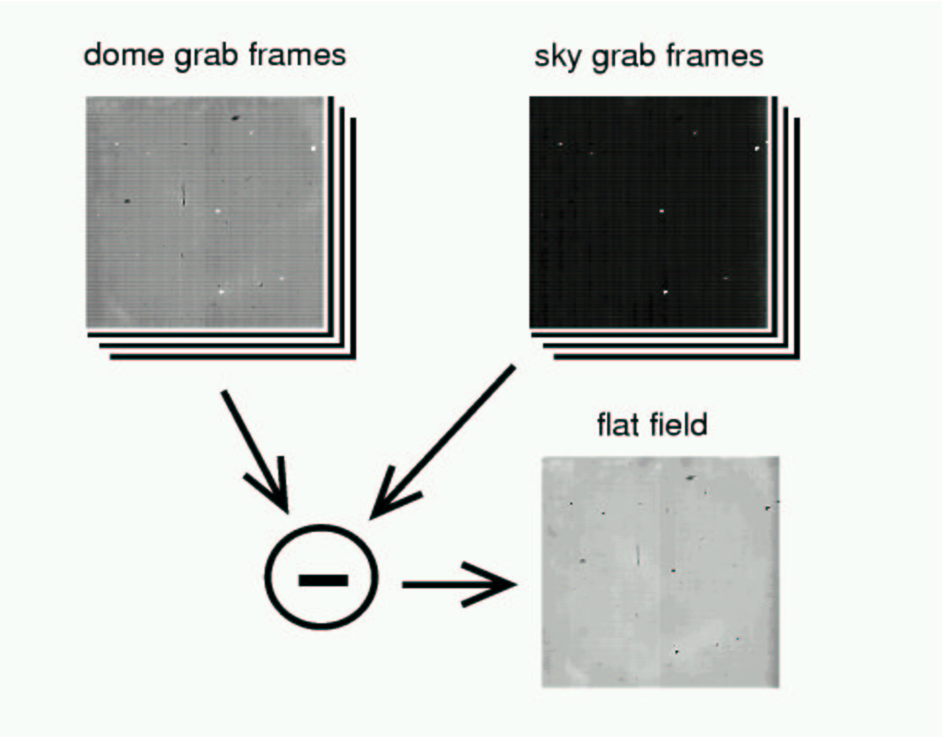

FIG. 5.4.— Process in which a flat field is derived. A sequence of low flux level frames is subtracted from a set of high flux level images. The result is normalized to unity.

4. The "high", "low" and "noise" masks are then combined in a single map, in which the "bad" pixels present in one of the intermediate masks are set to zero (logical `AND`).

The mask map used in the reduction of our data has been obtained with the aid of the IDL procedure `xmask_ima`, whose graphical user interface is shown in figure 5.3 while obtaining the high level pixel map.

### 5.2.2 Flat field correction

Each frame has what can be called a "zero-flux pattern" noise, that is the image obtained with zero luminous flux on the array, and with the same camera settings used during the real imaging. This pattern noise is introduced by the voltage offsets in the array and the signal processing electronics, and depends on the frame time because of the dark current. The pattern is also wavelength dependent, since the response of the detector pixels depends on the frequency of the incident radiation. To obtain a useful image it is necessary to remove the zero flux pattern by using a “flat field” map. The corrected frame is given by dividing, pixel by pixel, the original image with the flat field.

There is no standard way to derive a flat field map in the mid-IR, but in general this operation involves the subtraction of several black frames obtained at two different flux levels. The procedure followed in our data reduction is described in figure 5.4 (Hoffmann et al., 1998):

1. A series of frames is taken by imaging the dome, without chopping or nodding. The frame integration time is chosen in order to avoid the saturation of the array. Due to the high emissivity of the dome (at ambient temperature) in the mid-IR, these constitute the required high flux level frames.

2. A second set of frames is taken, *without changing the orientation of the telescope*, by imaging a portion of empty sky (off-source frames, no chop or nod). This can be practically accomplished by opening the dome shutter, without moving the telescope after taking the dome frames. The frame integration time should be the same as before. Due to the lower emissivity of the sky, these constitutes the low flux level frames.

3. The two set of frames are separately median coadded, and then subtracted one from the other. The result is finally normalized to unity (each pixel is divided by the median level of the array).

### 5.2.3 Recentering and coadding individual frames

The final image for each observation is performed by coadding recentered single frames, flat filed corrected and bad pixel masked. We have done this operation with the aid of the custom written IDL procedure `xcenter_ima`, whose graphical user interface is shown in figure 5.5. The sequence of operations in which this is done is described in figure 5.6.

1. A set of chop-nod frames is initially corrected by using the appropriate flat field map.

2. The frames are rebinned on a sub-pixel grid (we used 5×5 pixels for each camera detector pixel, in order to increase the spatial sampling of the sources.

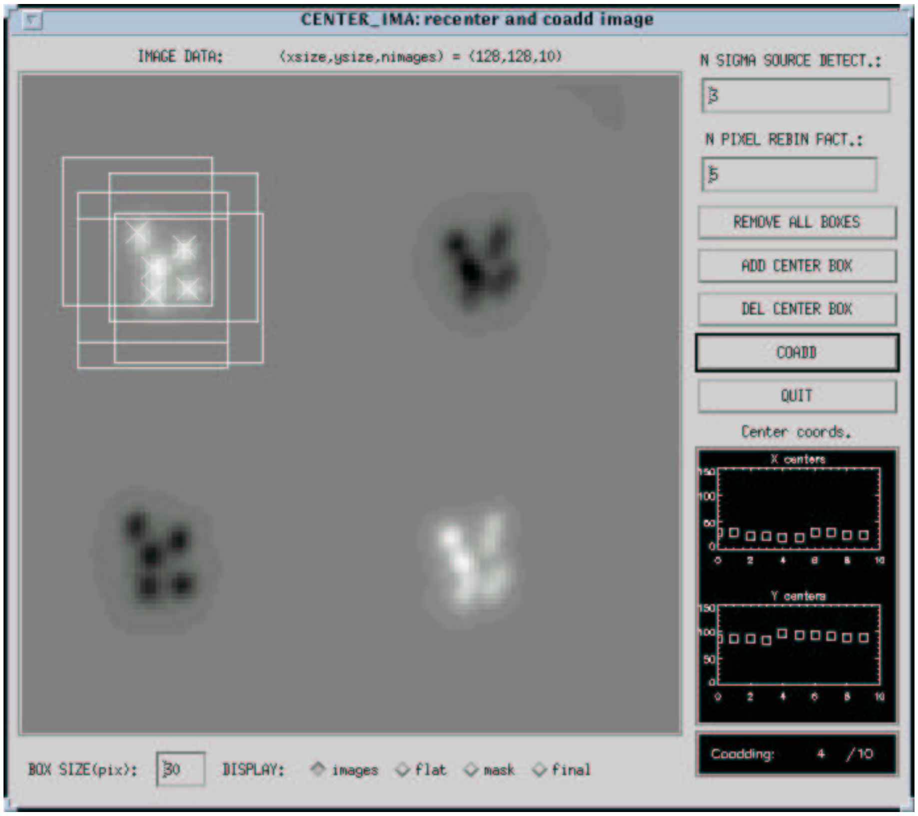

IMAGE DATA: (xsize,ysize,nimages) = (128,128,10)

N SIGMA SOURCE DETECT.: 3

N PIXEL REBIN FACT.: 5

BOX SIZE(pix): 30

DISPLAY: ◆ images ◇ flat ◇ mask ◇ final

Coadding: 4 /10

FIG. 5.5.— Screenshot of the `xcenter_ima` program, while performing the recentering of a set of chop-nod dithered observations. The display shows an un-recentered coadding of all frames, with the source in all four beams, and dithered in 5 positions in each beam. The crosses and boxes represent the hints of the user, entered with the cursor, for the position of the dithered source in the A+ beam. The source centroid coordinates are then computed inside each box, separately for each frame, by the recentering routine.

3. If the source was imaged in more than one chop-nod beam (as in figure 5.6, in which the source is in all four beams), the following steps should be performed for each beam which contains the source.

4. The coordinates of the source centroid are evaluated in each rebinned frame. This can be done computing the flux centroid of the source, by gaussian fitting, or by cross correlating the source brightness distribution in case of extended irregular sources.

5. The coordinates of each frame are recalculated in order to put the source centroid in a fixed position.

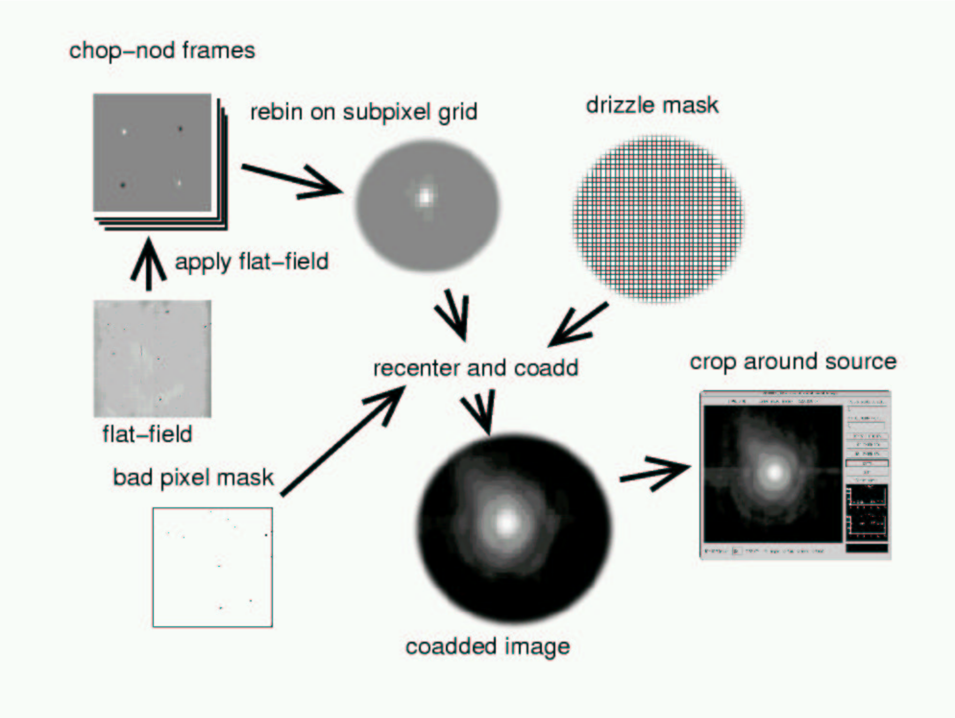

FIG. 5.6.— Steps in which a sequence of chop-nod observations are combined to produce a final image.

6. A rebinned bad pixel mask is associated to each frame, and shifted in the same way as the source frame.
7. An additional *drizzling mask* is added to the bad pixel mask (see below).
8. The source frames are coadded on the super-sampled grid, averaging the pixels with the same coordinate in the different frames. The average is computed by excluding the pixels masked-out by the bad pixel mask, and a weight can be associated to each frame, according to the square root of its integration time (to ensure uniform $S/N$ ratio, see equation 5.5).
9. The final image is then cropped at the required size around the source.

If the source was observed in more than one beam, the single beam images are coadded together (provided that their recentering is the same). It is a good idea to weigh the coadd with respect to each image's $S/N$ ratio.

This procedure ensures the flux normalization of the final image with respect to the single frame time. It also removes the effects of bad pixels in the final image, and provides a better spatial sampling of the source on the array. To maximize the efficiency of the spatial grid oversampling, the observations are usually made by dithering the source (with an offset of a few pixels) on the array, in order to project the image in different locations of the detector grid. To help the identification of the dithered source coordinates on the chop-nod frames, the `xcenter_ima` procedure allows cursor input on a preview of the coadded not recentered image (Figure 5.5).

The technique of *drizzling* can provide a better spatial resolution of the final image. Developed by Fructer & Hook (1998) to correct for the strong undersampling of the HST Wide Field Planetary Camera, it performs a coadding of rebinned frames without degrading the spatial resolution. The technique consists in "condensating" each detector pixel in a "*drop*", which occupies only a fraction of the original size of the detector pixel area projected on the super-sampled grid. This can be accomplished by masking out with a "drizzle mask" the sub-pixel grid columns and rows outside the required "drop" dimension, and then renormalizing the image to conserve the flux (see figure 5.6). We found the drizzling technique effective in improving the source spatial resolution when performed on a very large number of individual frames ($\gtrsim 250$), to ensure an uniform coverage of the image on the sub-pixel grid. This condition is typically met in our "fast mode" technique experimented with the camera MIRAC3 at IRTF.

### 5.2.4 Photometric calibration

The photometric calibration of the final images was made with the procedure `xphot_ima` whose graphical user interface is shown in figure 5.7. The program computes aperture photometry for each source by calibrating the final image with a reference star of known photometry, observed immediately before and after the source.

The aperture photometry is done in a similar fashion to the IRAF package `DAOPHOT` (Stetson, 1987). For both source and reference the user provides the aperture radius and the inner and outer radii of an annulus in which the sky emission level is estimated. The program computes the source counts as the difference between the counts in the source aperture, and the sky annulus, of equivalent aperture area:

$$counts = counts_{aper} - counts_{sky} \cdot \frac{A_{aper}}{A_{sky}} \tag{5.10}$$

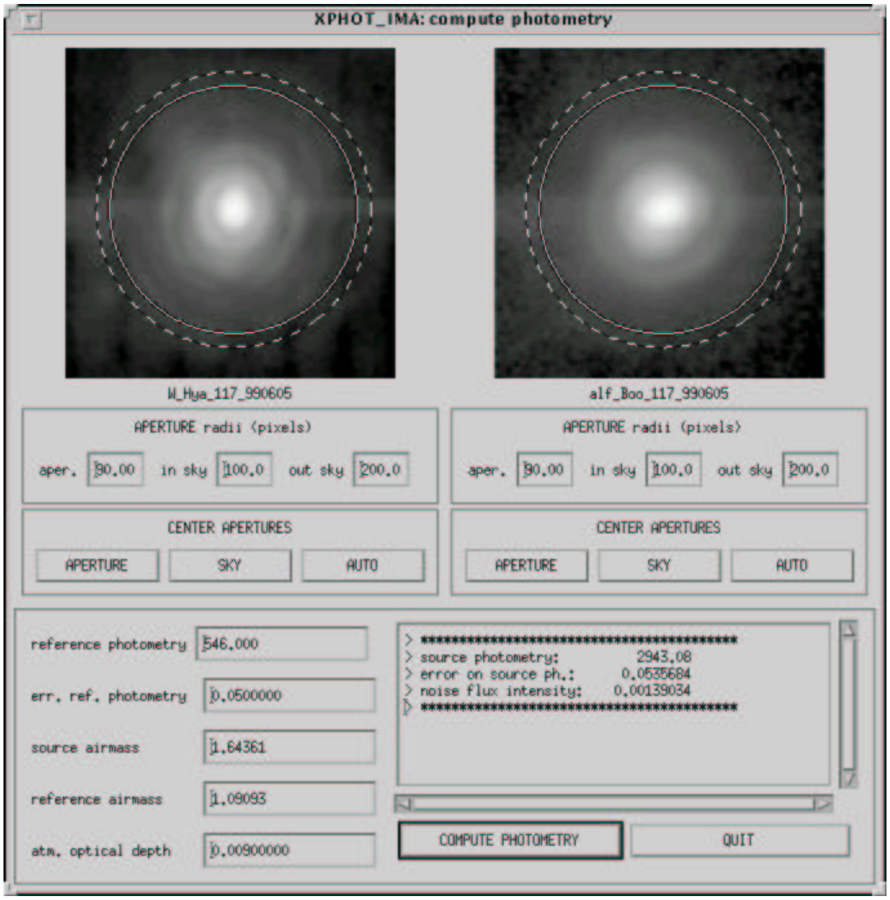

aper. 90.00 in sky 100.0 out sky 200.0

aper. 90.00 in sky 100.0 out sky 200.0

reference photometry 546.000

err. ref. photometry 0.0500000

source airmass 1.64361

reference airmass 1.09093

atm. optical depth 0.00900000

```
> ****************************************
> source photometry:          2943.08
> error on source ph.:      0.0535684
> noise flux intensity:    0.00139034
> ****************************************
```

FIG. 5.7.— Screenshot of the `xphot_ima` program, while computing the photometry of the SR AGB source W Hya. The source was observed with MIRAC3 in June 1999, with $\alpha$ Boo as photometric reference star. The aperture is identical for source and reference, and centered with the source and reference image. The sky annulus radius starts at the dashed circle, and ends outside the border of the two images. The coordinates and radii are given in units of the rebinned super-sampled image (1 pixel = 1/5 MIRAC3 pixels).

The calibration factor is the ratio between the reference star photometry and counts. The airmass correction is then computed from the ratio of the air mass of source and reference at the time of their respective observations:

$$f_{air} = e^{-\tau_{air} \cdot \frac{air_{source}}{air_{ref}}} \tag{5.11}$$

where the optical depth of the atmosphere is given (for our standard photometric system) in figure 3.7.

The source photometry is then measured by dividing the source counts with the calibration factor, and multiplying the result with the airmass correction.

The error of each measurement is computed as the geometric sum of the standard deviation of sky values in source and reference frames, the uncertainty in the mean sky brightness, and the relative error in the reference star photometry. The random photon noise in the source and reference image is not considered, since the major contributions to the total errors in mid-IR background limited conditions are due to the residual background noise (see equation 5.5).

### 5.2.5 Deconvolution techniques

Sources showing extended emission were deconvolved with the PSF, in order to achieve a better angular resolution. As explained in section 5.1.3, distortion of the source radiation while crossing the atmosphere and the telescope-camera optics degrade the spatial resolution of the image, and the image of a generic point source is spread into a PSF figure. The generic radial brightness profile $F_\nu(\theta)$ is thus imaged on the detector focal plane as the enlarged profile $F'_\nu(\theta)$:

$$F'_\nu(\vec{\theta}) = \int F_\nu(\vec{\theta}')\, PSF(\vec{\theta} - \vec{\theta}')\, \mathrm{d}\vec{\theta}' \tag{5.12}$$

If the shape of the PSF is known, it is in principle possible to attempt a deconvolution to reverse the image degradation. This operation, however, does not yield a unique solution. Several methods have thus been developed to compute the "most likely" deconvolved source image.

In section 5.4 we have tested two deconvolution procedures on all the observed sources, by using the (photometric) reference source as a model for the real PSF. This approach has its own limitations, mainly because of the instability of the real PSF, whose shape is sensitive to several factors:

- the telescope orientation (the telescope deforms under its own weight, and the deformation depends on its position)
- the seeing and the presence of wind
- the ambient temperature, which changes the distance between the primary and secondary mirror
- the focus of the camera and the distance of the image from the optical axis

In order to limit these complications, we made an effort to observe the reference stars as close as possible, in time and sky orientation, to the relative source. The absence of a reasonable number of bright infrared standards, however, makes this procedure relatively difficult.

The deconvolutions were made with two different algorithms, *maximum entropy* based on Hollis et al. (1992) and *maximum likelihood* based on Richardson (1972) and Lucy (1974). We applied both methods on each extended source, and the final results were then compared, to reduce the possibility of spurious detection in the deconvolved images.

## 5.3 Mid-IR colors of AGB circumstellar envelopes

This section describes the observational campaign carried on with the mid-IR cameras TIRCAM and CAMIRAS, aimed to collect images and photometry of AGB circumstellar envelopes.

The results of the observations are reviewed, and used as an observational test for the diagnostic tools developed in chapter 3, in preparation of the more extended imaging campaign described in section 5.4.

### 5.3.1 The cameras TIRCAM and CAMIRAS

The camera TIRCAM has been developed in a collaboration between the "Istituto di Astrofisica Spaziale" of the Italian National Research Council (C.N.R. Rome), the Astronomical Observatory of Torino (Italy) and the "Dipartimento di Fisica Generale" of the University of Torino (Italy). The camera is described in Persi et al. (1994), and at the time of the observational campaign was equipped with a 10×64 pixels Si:As array detector built by the Huges Aircraft Corporation (USA). The pixel scale of the array was 1.23"/pix and 1.38"/pix at TIRGO and SPM respectively. The photometric system of the camera included the full set of 10% passband filters described in section 3.3.1.

The camera CAMIRAS, developed at the Service d'Astrophysique at Saclay, France (Lagage, P.O., 1992), was equipped with a 192×128 Si:Ga/DVR array detector. The available photometric system was similar to the one of TIRCAM, and we performed our observations with the 10% filters having effective wavelength of 8.55, 9.56, 11.21, 12,45 and 16.64 $\mu$m. To maximize the $S/N$ and reduce the total observation time, we performed most of the observations with the source in all four chop-nod beams. The pixel scale of CAMIRAS at TIRGO was 0.72"/pix.

Table 5.1 TIRCAM/CAMIRAS AGB sources

| # | Source | Class | IRAS | LRS[a] | Var. type[b] |
|---|---|---|---|---|---|
| 1 | KU And | O-rich | 00042+4248 | 26 | M |
| 2 | WX Psc | O-rich | 01037+1219 | 4n | M |
| 3 | W And | S-star | 02143+4404 | 22 | M |
| 4 | *o* Cet | O-rich | 02168−0312 | 2n | M |
| 5 | AFGL 618 | C-rich | 04395+3601 | 62 | – |
| 6 | IRAS 06088+1909 | C-rich | 06088+1909 | – | – |
| 7 | Red Rect | C-rich | 06176−1036 | 80 | – |
| 8 | IRC+40156 | O-rich | 06297+4045 | 27 | – |
| 9 | X CnC | C-rich | 08525+1725 | 42 | SRb |
| 10 | R LMi | O-rich | 09425+3444 | 24 | M |
| 11 | R Leo | O-rich | 09448+1139 | 1n | M |
| 12 | IRC+10216 | C-rich | 09452+1330 | 43 | M |
| 13 | CIT 6 | C-rich | 10131+3049 | 04 | SRa |
| 14 | Y CVn | C-rich | 12427+4542 | 42 | SRb |
| 15 | RT Vir | O-rich | 13001+0527 | 21 | SRb |
| 16 | S CrB | O-rich | 15193+3132 | 24 | M |
| 17 | WX Ser | O-rich | 15255+1944 | 29 | M |
| 18 | V CrB | C-rich | 15477+3943 | 4n | M |
| 19 | U Her | O-rich | 16235+1900 | 23 | M |
| 20 | NSV 9118 | O-rich | 17297+1747 | 14 | SR |
| 21 | AFGL 2205 | O-rich | 18348−0526 | 3n | M |
| 22 | NSV 11225 | C-rich | 18397+1738 | 43 | – |
| 23 | CRL 3068 | C-rich | 23166+1655 | 02 | – |

[a] LRS class from Loup et al. (1993).

[b] Variability type derived from GCVS (Kopolov et al., 1998).

### 5.3.2 Observations

The target list was selected according to the mid-IR brightness and estimated distance of the sources, to maximize the $S/N$ ratio and possibly detect extended emission from the dust in the AGB envelopes.

Table 5.1 shows the list of the observed sources. For each source is indicated the chemical type, the IRAS name and LRS class, and the variability

Table 5.2 Photometry of TIRCAM sources

| #[a] | Source | $F_{8.8}$ [Jy] | $F_{9.8}$ [Jy] | $F_{11.7}$ [Jy] | $F_{12.5}$ [Jy] | epoch |
|---|---|---|---|---|---|---|
| 3 | W And | 97 | - | 143 | 205 | Dec 93 |
| 4a | *o* Cet | 3730 | 3670 | 4650 | 2650 | Oct 92 |
| 4b | *o* Cet | 2100 | 3330 | 3540 | 1780 | Dec 93 |
| 5 | AFGL 618 | 141 | 188 | 275 | 302 | Dec 93 |
| 9 | X CnC | 107 | 151 | 40 | - | Dec 93 |
| 10 | R LMi | 331 | 377 | 409 | 268 | Dec 93 |
| 11 | R Leo | 1780 | 1700 | 2780 | 1860 | Dec 93 |
| 12 | IRC+10216 | 28300 | 33100 | 37100 | 37200 | Dec 93 |
| 14 | Y CVn | 254 | 198 | 283 | 259 | May 93 |
| 15 | RT Vir | 369 | 468 | 556 | 325 | May 93 |
| 16 | S CrB | 183 | 187 | 224 | 134 | May 93 |
| 17 | WX Ser | 116 | 206 | 86 | - | May 93 |
| 18 | V CrB | 103 | 225 | 129 | 105 | May 93 |
| 19 | U Her | 547 | 619 | 553 | 403 | May 93 |
| 21 | AFGL 2205 | 133 | - | 340 | 656 | May 93 |
| 22 | NSV 11225 | 782 | 792 | 899 | 810 | May 93 |

[a] List number given according to table 5.1

type. The sample consists of 23 objects of which 12 O-rich, 10 C-rich and 1 S-star. Two sources are post-AGB (AFGL 618 and AFGL 2205), two are pre-PN (Red Rectangle and CRL 3068) and the others are in the AGB phase.

TIRCAM observations were performed in 1992 and 1993 at the 1.5 m italian “Telescopio InfraRosso al GornerGrat” (TIRGO) and at the 2.1 m infrared telescope of the Observatorio Astronomico National (Mexico) at San Pedro Martir (SPM), Baja California.

The camera used a set of 10% filters centered at 8.8 (continuum + PAH), 9.8 (main silicate feature), 11.7 (SiC + PAH) and 12.5 (continuum + PAH) $\mu$m. The data reduction was performed using IRAF, MIDAS and IDL packages, as described in section 5.2. The effective integration times were ranging from 10 sec to 5 min, according to the source brightness. The sources were imaged in one beam, due to the small size of the detector.

The measured photometry of the observed sources is listed in table 5.2. The photometric calibration was achieved by observing repeatedly the standard stars $\alpha$ Boo and $\alpha$ Tau. The zero point estimates show an uncertainty of about 5%; the nominal errors of the data in the table 5.2 ($1\sigma$) are $\lesssim$7% in the 8.8 and 9.8 $\mu$m filters, and $\lesssim$15% in the other two.

The data in table 5.2 was originally published in Busso et al. (1996),

Table 5.3 Photometry of CAMIRAS sources and standards

| #[a] | Source | $F_{8.55}$ [Jy] | $F_{8.57}$ [Jy] | $F_{9.56}$ [Jy] | $F_{11.21}$ [Jy] | $F_{12.24}$ [Jy] | $F_{12.45}$ [Jy] | $F_{16.64}$ [Jy] | epoch |
|---|---|---|---|---|---|---|---|---|---|
| 1 | KU And | 488 | 433 | 763 | 1030 | - | 497 | - | Nov 96 |
| 2 | WX Psc | 846 | 702 | 1050 | 1040 | - | 364 | 863 | Nov 96 |
| 3 | W And | 154 | 151 | 188 | 162 | - | 115 | - | Nov 96 |
| 5a | AFGL 618 | 226 | 192 | 322 | 378 | 413 | 484 | 882 | Nov 96 |
| 5b | | - | - | 272 | - | 559 | - | - | Feb 97 |
| 6 | 06088+1909 | 40 | - | 37 | 42 | - | 37 | - | Nov 96 |
| 7 | Red Rectangle | 235 | - | 937 | - | - | - | 3030 | Feb 97 |
| 8 | IRC+40156 | - | 54 | - | 76 | 50 | - | - | Nov 96 |
| 13 | CIT 6 | - | - | - | 3880 | 3070 | - | 1930 | Feb 97 |
| 20 | NSV 9118 | 221 | - | 283 | 222 | 290 | - | - | Feb 97 |
| 23 | CRL 3068 | 288 | - | 362 | 404 | - | 472 | 280 | Nov 96 |
| std | $\alpha$ Aur | 326 | 325 | 262 | 191 | 161 | 156 | 88 | |
| std | $\alpha$ Tau | 838 | 834 | 682 | 509 | 433 | 420 | 246 | |
| std | $\beta$ And | 354 | 352 | 286 | 212 | 179 | 174 | 100 | |
| std | $\beta$ Gem | 170 | 169 | 136 | 99 | 84 | 81 | 46 | |
| std | $\beta$ Peg | 524 | 522 | 429 | 323 | 276 | 268 | 159 | |

[a] List number given according to table 5.1; std indicates photometric standards.

where the photometry of the C-rich source FX Ser was also given. This measurement was subsequently rejected (Marengo et al., 1999), due to the presence of vignetting in the original images.

An additional number of 10 sources was observed with the camera CAMIRAS during two observing runs at TIRGO in November 1996 and February 1997. These observations were made with a set of 10% passband filters centered at 8.55, 9.56, 11.21, 12.45 and 16.65 $\mu$m, plus narrow band filters at 8.57 and 12.24 $\mu$m. The total integration time ranged between 5 and 15 minutes, according to the source brightness. The sources were observed in all four beams with a chop-nod throw of 20", in order to maximize the source $S/N$.

The standard stars $\alpha$ Aur, $\alpha$ Tau, $\beta$ And, $\beta$ Gem and $\beta$ Peg were observed to calibrate the images and derive the point-spread function (PSF). The calibration fluxes in the CAMIRAS photometric system were derived for each standard in a two step process: (1) a synthetic spectrum for each star was constructed by fitting available IR photometry data (Gezari, 1993) with the Engelke + SiO modified black body described in section 3.2.2, and (2) convolved with the CAMIRAS filter profiles to provide the flux at each wavelength. The reference fluxes computed with this procedure are listed in

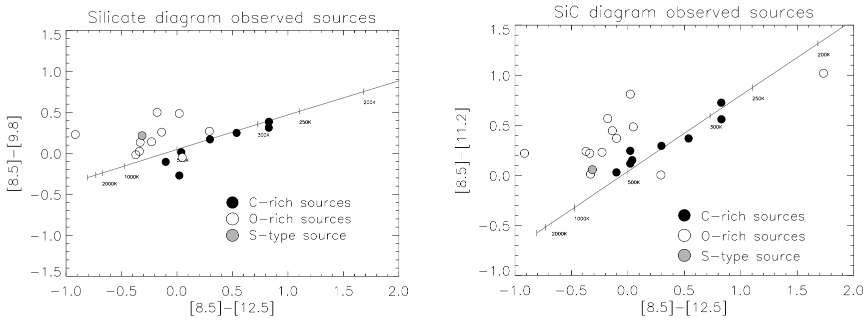

Fig. 5.8.— Silicate and SiC color diagram of TIRCAM/CAMIRAS sources. C-rich envelopes are filled circles, O-rich are empty and the S-star is grey.

table 5.3. The observed PSF were dependent on the local seeing conditions, varying from night to night. The mean value of the PSF FWHM was $\sim 2.2$” at 8.55 $\mu$m and $\sim 3$” at 12.45 $\mu$m.

Table 5.3 reports the integrated flux densities of CAMIRAS sources, already published in Marengo et al. (1999). The photometric statistical error (comprehensive of the calibration errors) is approximately 10%. Of all the sources in table 5.3, only WX Psc, IRC+10216, CRL 3068 and Red Rectangle appear to be spatially resolved (within our measured PSF) in at least one filter.

### 5.3.3 Mid-IR colors and mass loss

The affinity of TIRCAM and CAMIRAS filters with the “standard” photometric system introduced in section 3.3.1 allows an observational test of the color diagrams previously defined. A color correction to the measured photometry is in principle required to reconcile the small differences between CAMIRAS and TIRCAM set of filters, and the “standard” ones. This color correction was thus estimated by convolving the filters profile with the IRAS spectra of AGB stars with different LRS class. The values thus obtained, however, turned out to be much smaller than the uncertainty of the measurements in our photometry, and have therefore been ignored. For this reason we consider equivalent CAMIRAS 8.55 and 9.56 filters with TIRCAM 8.5 ans 9.8 $\mu$m fluxes.

The “silicate” and “SiC” feature color color diagram of the observed sources are plotted in figure 5.8. They confirm the results found in chapter 3, with C-rich sources along the black body, and [optically thin] O-rich envelopes in the upper part of the diagrams.

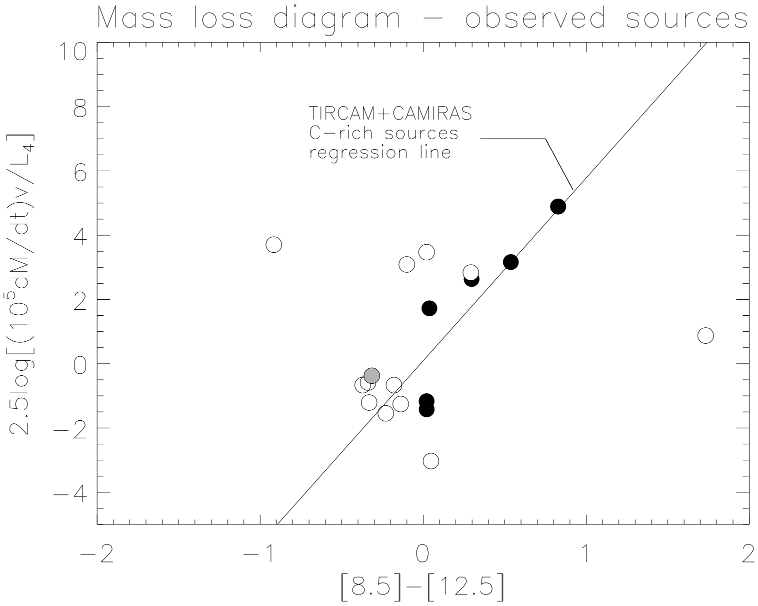

FIG. 5.9.— The mass loss parameter vs. mid-IR "continuum" color for TIRCAM/CAMIRAS sources. A regression line for C-rich sources is computed and drawn on the diagram.

One or more estimates for mass loss rate, bolometric flux, envelope outflow velocity and total luminosity are available in Loup et al. (1993) for 21 of the observed sources, and are listed in table 5.4. These values allow to compute the mass loss parameter defined in section 3.3.5, which we found related to the infrared continuum color [8.5]-[12.5]. The validity of this correlation can be tested by using MIRAC/CAMIRAS photometry for the observed sources.

Figure 5.9 shows the color - mass loss diagram for the observed sample. The plot uses the photometry listed in table 5.2 and 5.3. The mass loss parameter is derived from table 5.4 (the average value is computed for sources with multiple estimates of $\dot{M}$ and $L$).

The main difference with the similar plot in figure 3.13 is the much lower dispersion of the sources with respect to the mass loss parameter. C-rich sources, in particular, appear to be on a sequence, which is plotted on the diagram. A comparison with figure 3.13 shows that the regression line found for C-rich TIRCAM/CAMIRAS sources defines a lower boundary of the region populated by L93 (Loup et al., 1993) C-rich sources. This is a

Table 5.4 Physical parameters of TIRCAM/CAMIRAS AGB sources

| # | Source | $4\pi \cdot 1\mathrm{kpc}^2 F_{total}$ $L_\odot$ | $\dot{M}$ [$\mathrm{M}_\odot$ yr$^{-1}$] | $v_e$ [km s$^{-1}$] | d [kpc] | $L$ [$\mathrm{L}_\odot$] |
|---|---|---|---|---|---|---|
| 1 | KU And | $1.5 \cdot 10^4$ | $9.7 \cdot 10^{-6}$ | 21.7 | 0.82 | $1.0 \cdot 10^4$ |
| | | | $2.4 \cdot 10^{-5}$ | 21.7 | 1.10 | $1.8 \cdot 10^4$ |
| 2 | WX Psc | $3.4 \cdot 10^4$ | $8.5 \cdot 10^{-6}$ | 20.7 | 0.54 | $9.9 \cdot 10^3$ |
| | | | $1.2 \cdot 10^{-5}$ | 20.7 | 0.51 | $8.8 \cdot 10^3$ |
| | | | $2.4 \cdot 10^{-5}$ | 20.7 | 0.51 | $8.8 \cdot 10^3$ |
| 3 | W And | $4.4 \cdot 10^4$ | $8.0 \cdot 10^{-7}$ | 10.7 | 0.48 | $1.0 \cdot 10^3$ |
| | | | $9.7 \cdot 10^{-7}$ | 10.7 | 0.63 | $1.7 \cdot 10^3$ |
| 4 | *o* Cet | $8.1 \cdot 10^5$ | $5.0 \cdot 10^{-7}$ | 5.6 | 0.11 | $9.8 \cdot 10^3$ |
| | | | $5.7 \cdot 10^{-7}$ | 5.6 | 0.08 | $5.1 \cdot 10^3$ |
| | | | $1.0 \cdot 10^{-6}$ | 5.6 | 0.08 | $5.1 \cdot 10^3$ |
| | | | $1.0 \cdot 10^{-7}$ | 5.6 | 0.08 | $5.1 \cdot 10^3$ |
| | | | $2.1 \cdot 10^{-6}$ | 5.6 | 0.08 | $5.1 \cdot 10^3$ |
| 5 | RAFGL 618 | $7.8 \cdot 10^3$ | $6.7 \cdot 10^{-5}$ | 19.5 | 1.30 | $1.3 \cdot 10^4$ |
| | | | $5.6 \cdot 10^{-5}$ | 19.5 | 1.30 | $1.7 \cdot 10^4$ |
| 6 | IRAS 06088+1909 | – | – | – | – | – |
| 7 | Red Rect | – | – | – | – | – |
| 8 | IRC+40156 | $3.7 \cdot 10^3$ | $1.0 \cdot 10^{-5}$ | 16.3 | 1.60 | $9.5 \cdot 10^3$ |
| 9 | X CnC | $2.1 \cdot 10^4$ | $7.7 \cdot 10^{-7}$ | 9.7 | 0.69 | $1.0 \cdot 10^4$ |
| | | | $4.6 \cdot 10^{-7}$ | 9.7 | 0.64 | $8.6 \cdot 10^3$ |
| 10 | R LMi | $9.4 \cdot 10^4$ | $2.8 \cdot 10^{-7}$ | 7.0 | 0.33 | $1.0 \cdot 10^4$ |
| | | | $5.0 \cdot 10^{-7}$ | 7.0 | 0.35 | $1.2 \cdot 10^4$ |
| 11 | R Leo | $5.0 \cdot 10^5$ | $1.0 \cdot 10^{-7}$ | 8.5 | 0.14 | $9.8 \cdot 10^3$ |
| | | | $8.0 \cdot 10^{-8}$ | 8.5 | 0.30 | $4.5 \cdot 10^4$ |
| | | | $6.0 \cdot 10^{-7}$ | 8.5 | 0.24 | $2.9 \cdot 10^4$ |
| 12 | CW Leo | $6.6 \cdot 10^5$ | $4.8 \cdot 10^{-5}$ | 14.7 | 0.29 | $5.6 \cdot 10^4$ |
| | | | $2.2 \cdot 10^{-5}$ | 14.7 | 0.22 | $5.6 \cdot 10^4$ |
| 13 | CIT 6 | $6.9 \cdot 10^4$ | $6.0 \cdot 10^{-6}$ | 16.8 | 0.38 | $1.0 \cdot 10^4$ |
| | | | $2.6 \cdot 10^{-6}$ | 16.8 | 0.19 | $2.5 \cdot 10^3$ |
| | | | $4.8 \cdot 10^{-6}$ | 16.8 | 0.39 | $1.0 \cdot 10^4$ |
| | | | $7.5 \cdot 10^{-6}$ | 16.8 | 0.48 | $1.6 \cdot 10^4$ |
| 14 | Y CVn | $8.7 \cdot 10^4$ | $4.2 \cdot 10^{-7}$ | 8.2 | 0.34 | $1.0 \cdot 10^4$ |
| | | | $2.8 \cdot 10^{-7}$ | 8.2 | 0.35 | $1.1 \cdot 10^4$ |
| | | | $1.4 \cdot 10^{-6}$ | 8.2 | 0.35 | $1.1 \cdot 10^4$ |
| | | | $1.2 \cdot 10^{-7}$ | 8.2 | 0.41 | $1.5 \cdot 10^4$ |
| 15 | RT Vir | $1.3 \cdot 10^5$ | $7.4 \cdot 10^{-7}$ | 9.3 | 0.28 | $1.0 \cdot 10^4$ |
| | | | $1.3 \cdot 10^{-6}$ | 9.3 | 0.97 | $1.2 \cdot 10^5$ |
| | | | $6.0 \cdot 10^{-6}$ | 9.3 | 1.00 | $1.3 \cdot 10^5$ |
| | | | $4.9 \cdot 10^{-7}$ | 9.3 | 0.32 | $1.3 \cdot 10^4$ |
| 16 | S CrB | $2.3 \cdot 10^4$ | $5.8 \cdot 10^{-7}$ | 6.3 | 0.66 | $1.0 \cdot 10^4$ |
| | | | $6.0 \cdot 10^{-7}$ | 6.3 | 0.42 | $4.1 \cdot 10^3$ |
| 17 | WX Ser | $7.2 \cdot 10^3$ | $2.6 \cdot 10^{-6}$ | 8.8 | 1.20 | $1.0 \cdot 10^3$ |
| | | | $5.3 \cdot 10^{-7}$ | 8.8 | 0.72 | $3.7 \cdot 10^3$ |
| 18 | V CrB | $1.5 \cdot 10^4$ | $5.2 \cdot 10^{-7}$ | 7.8 | 0.82 | $1.0 \cdot 10^4$ |
| | | | $5.8 \cdot 10^{-7}$ | 7.8 | 1.02 | $1.6 \cdot 10^4$ |
| 19 | U Her | $3.2 \cdot 10^5$ | $2.6 \cdot 10^{-7}$ | 13.1 | 0.18 | $1.0 \cdot 10^4$ |

Table 5.4: continue.

| # | Source | $4\pi \cdot 1\text{kpc}^2 F_{total}$ $L_\odot$ | $\dot{M}$ [$M_\odot$ yr$^{-1}$] | $v_e$ [km s$^{-1}$] | d [kpc] | $L$ [$L_\odot$] |
|---|---|---|---|---|---|---|
| 20 | NSV 9118 | $1.6 \cdot 10^4$ | $9.7 \cdot 10^{-6}$ | 16.3 | 0.79 | $1.0 \cdot 10^4$ |
| | | | $2.0 \cdot 10^{-5}$ | 16.3 | 1.20 | $2.3 \cdot 10^4$ |
| | | | $1.6 \cdot 10^{-5}$ | 16.3 | 1.20 | $2.3 \cdot 10^4$ |
| 21 | AFGL 2205 | $1.1 \cdot 10^4$ | $2.1 \cdot 10^{-6}$ | 10.6 | 0.95 | $9.9 \cdot 10^4$ |
| 22 | NSV 11225 | $2.8 \cdot 10^4$ | $3.8 \cdot 10^{-6}$ | 14.2 | 0.60 | $1.0 \cdot 10^4$ |
| | | | $9.1 \cdot 10^{-6}$ | 14.2 | 0.79 | $1.7 \cdot 10^4$ |
| | | | $2.4 \cdot 10^{-6}$ | 14.2 | 0.79 | $1.7 \cdot 10^4$ |
| | | | $6.0 \cdot 10^{-6}$ | 14.2 | 0.64 | $1.1 \cdot 10^4$ |
| 23 | CRL 3068 | $1.1 \cdot 10^4$ | $8.4 \cdot 10^{-6}$ | 14.1 | 0.95 | $9.9 \cdot 10^3$ |
| | | | $6.4 \cdot 10^{-6}$ | 14.1 | 0.57 | $3.6 \cdot 10^3$ |
| | | | $1.2 \cdot 10^{-5}$ | 14.1 | 1.00 | $1.1 \cdot 10^4$ |
| | | | $2.1 \cdot 10^{-5}$ | 14.1 | 1.04 | $1.2 \cdot 10^4$ |

consequence of the selection process in which the targets to be observed were chosen. In order to maximize the $S/N$ ratio available with TIRCAM and CAMIRAS detectors, we have selected the brightest sources with the largest infrared excess available: in the case of the C-rich envelopes this favored the sources in the lower boundary of the color distribution, that is where the infrared excess is maximum. O-rich sources, on the contrary, are spread on the whole diagram.

### 5.3.4 One example of extended source: WX Psc

The limited aperture of TIRGO and SPM telescopes does not allow the necessary angular resolution to spatially resolve AGB circumstellar envelopes. The collected images were however analyzed to search for extended emission beyond the instrumental PSF. Figure 5.10 shows the image of the bright O-rich source WX Psc (alias CIT3) at 8.8 $\mu$m, which represents the best candidate for spatial extension among CAMIRAS sources.

This source has been recently observed at 11.5 $\mu$m at the Wyoming Infrared Observatory (Sudol et al., 1999), where the visibility curve in the E-W direction was derived, and no extension was found (leading to the conclusion that at that wavelength the circumstellar shell should have an angular diameter of 0.63" or less). Similarly, a far-IR search (60 and 100 $\mu$m) in the IRAS database conducted by Young et al. (1993) was not able to resolve extended emission from the source.

Near-IR speckle observations at the SAO 6m telescope (Irrgang et al, 1998), were able to identify two separate components in the circumstellar

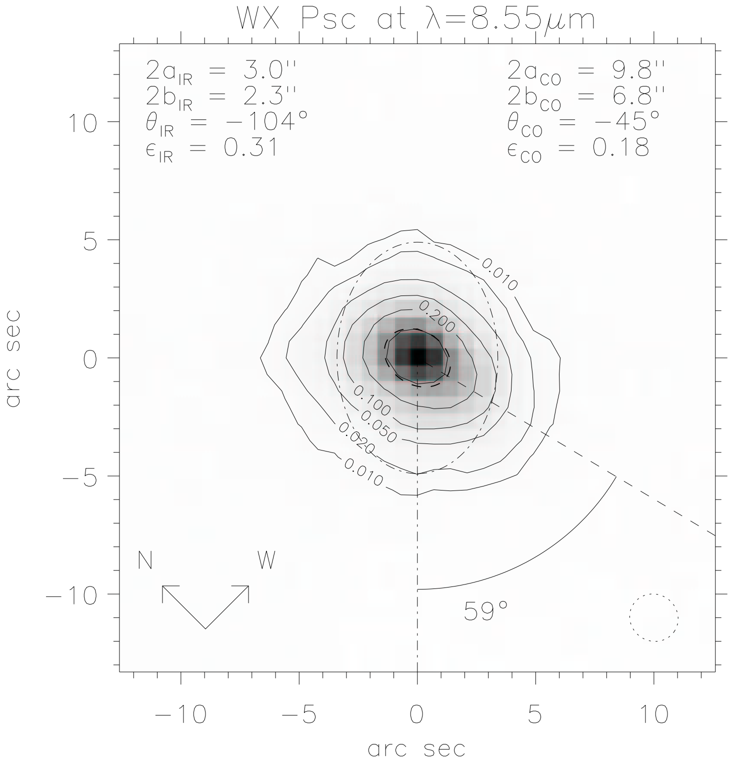

Fig. 5.10.— Images and contour plots of the O-rich AGB envelope WX Psc at 8.55 $\mu$m. Contour levels are shown at 0.01, 0.02, 0.05, 0.1, 0.2 and 0.5 of the source maximum, where the 0.01 contour corresponds to the $5\sigma$ noise level. The source radial brightness distribution is fitted with a 2D elliptical gaussian whose major and minor axis, orientation (from E direction, clockwise) and asymmetry are indicated in the left column. The "sizes" $a$ and $b$ of the interpolating elliptical gaussian are related to the FWHM by the relation FWHM = size $\cdot\sqrt{2\ln 2}$. The dashed contour and line are the half maximum ellipse of the fitting gaussian and the orientation of its major axis. The dot dashed contour and line indicate the size and orientation of the secondary gaussian component of the CO(J=1→0) emission as measured by Neri et al. (1998). The parameters of the CO fitting are indicated in the right column for comparison; note the 59° rotation between the orientation of the IR and the CO major axis. The dotted circle in the lower right corner is the beam size of the PSF, derived from the half maximum contour of a standard star.

envelope of the source, consisting of a partially resolved smaller structure (representing the innermost region of the envelope) and a fully resolved extended nebulosity that “[...] *might point to a change of the physical properties in the outflow*”.

High resolution $^{12}$CO (J=1→0) and (J=2→1) maps of the O-rich source have been obtained using radio interferometers able to resolve the molecular envelope of this object. In Neri et al. (1998), IRAM observations of WX Psc are fitted by using a double component envelope in which the primary component (of size ∼30”) is spherical, and the secondary elliptical, with asymmetry $\epsilon_{CO} = 0.18$ (major and minor sizes 9.8” and 6.8”) and major axis rotated by 45° from E to S.

We have attempted a similar 2D gaussian fit on our 8.55 $\mu$m image (not deconvolved with the PSF), and the results are shown in figure 5.10. The best fit parameters indicate an elongated shape (major and minor size of 3.0” and 2.3” respectively) with asymmetry $\epsilon_{IR} = 0.31$, oriented with the major axis at 104° from the E direction (counterclockwise). The comparison of the source image with the PSF derived from nearby standard stars (symmetrical and with FWHM of about 2.0”), implies an extension of WX Psc in the N-S direction, while the source remains unresolved along the E-W axis (in agreement with Sudol et al. (1999) observation). The extension of the source is less clear in our images at longer wavelengths.

The smaller dimensions of the mid-IR image, compared to the CO map, its larger asymmetry and the different orientation (59° rotation between the CO and IR envelope) suggest the possibility that the mid-IR and the CO observations refer to physically distinct regions of the envelope. This consideration, together with the failure to detect an extended dust emission at 60 and 100 $\mu$m, leads to the conclusion that in the envelope of WX Psc the dust appears to be concentrated only in the central regions. This further suggests that dust is condensed close to the photosphere of WX Psc, in a non spherical environment. At larger distances from the central star the dust is undetectable. The progressive decrease in the envelope asymmetry probed by the CO observations can be explained either assuming a disk-like geometry in the dust spatial distribution or, alternatively, assuming an axisymmetrical circumstellar envelope that becomes more and more spherical as it expands with the AGB wind.

The spatial resolution of our image does not help to clarify the underlying geometry of the source, but brings into evidence that even with a small aperture telescope it is possible to derive information on the spatial distribution of dust for some bright and close-by objects. A larger telescope and a more sensitive camera is a necessary step to confirm this observations and collect extended images for a larger sample of sources. An observational effort of this nature is described in the next section.

## 5.4 MIRAC imaging of extended AGB envelopes

The mid-IR camera MIRAC has been successfully operated in imaging projects devoted to advanced stages of stellar evolution, such as PN, pre-PN and post-AGB stars (Hora et al. 1990, 1993, 1996, Dayal et al. 1998, Meixner et al. 1999). These evolved objects constitute an ideal target for the camera, due to their strong infrared emission and large physical size. The strong departures from spherical symmetry already observed in high resolution optical and near-IR observations (see, e.g the HST "gallery" of PN and pre-PN) are confirmed in MIRAC images mapping the spatial distribution of the circumstellar dust.

AGB circumstellar envelopes are a greater challenge for the current state of mid-IR imaging. This is the consequence of many factors:

- post-AGB, pre-PN and PN have in general larger angular sizes than AGB circumstellar envelopes, which are a more difficult target for telescopes of median aperture.

- a dramatic increase in the mass loss rate is characteristic of the transition between the AGB and the post-AGB phase. Evolved objects as post-AGB and pre-PN have larger infrared excesses than AGB envelopes.

- the AGB stars and the inner parts of the mid-IR envelopes are orders of magnitude brighter than the extended dust envelopes; a large $S/N$ ratio is thus needed to separate the faint envelope emission from the stellar one.

On the other hand, many AGB sources are close to the solar system ($\lesssim$500 pc) and bright enough at 10 $\mu$m ($\gtrsim$500 Jy) that the conditions to attempt their imaging are satisfied by current mid-IR cameras and telescopes.

The scientific importance of such observations is to provide observational constraints on the physics of mass loss in late stages of stellar evolution. The questions raised in chapter 4, about a connection between stellar pulsations and dust production, can be directly tested by imaging the spatial structure of nearby AGB envelopes.

Growing evidences indicate an important role of non uniform density distributions in the dust forming regions of AGB stars (Le Bertre & Winters, 1998; Fleisher et al., 1992). Recent observations at different wavelengths support the idea that these inhomogeneities can propagate in the circumstellar envelope, giving rise to strong deviations from spherical symmetry. Clumpy structures in the dust forming regions of the C-rich AGB star IRC+10216 were found by near-IR masking and speckle interferometry at Keck and SAO telescopes (Monnier et al., 1997; Weigelt et al., 1998). A sequence of detached dust shells were also found around this source by deep optical imaging (Mauron & Huggins, 1999), suggesting a complex mass loss history similar to the one that characterized the more evolved post-AGB "Egg Nebula" (Sahai et al., 1998) or the O-rich Mira R Hya (Hashimoto et al., 1998). All these observations suggest that the asymmetry observed in many PN already starts during the AGB, where it shapes the evolution of the circumstellar envelope towards the Planetary Nebula phase.

This section describes an observational effort aimed to demonstrate the feasibility of AGB circumstellar envelopes mid-IR imaging with a mid-size infrared telescope. A technique developed for imaging objects having angular sizes comparable to the instrumental PSF is also described, and the results of the observations are presented.

### 5.4.1 The camera MIRAC3 at IRTF

MIRAC3 (Hoffmann et al., 1998) is a Mid-InfraRed Array camera which utilizes a Boeing HF16 128×128 Si:As hybrid BIB array. Reflective optics in the camera liquid-helium cryostat yield achromatic diffraction-limited imaging at a nominal scale on IRTF of 0.35"/pix, with zoom capability from 0.35 to 0.17"/pix. A PC with a Digital Signal Processor (DSP) card controls the telescope secondary chopper and data acquisition, storage, processing and display, and initiates telescope nod and offset motions via ethernet or RS232. From the full set of filters available for the camera, we have made use of the 10% filters centered at 8.8, 9.8, 11.7, 12.5 and 18.0 $\mu$m. The target sources were typically observed in all four chop-nod beams.

The observations were made with MIRAC3 at the 3 m aperture NASA InfraRed Telescope Facility (IRTF) on top of Mauna Kea (Hawaii). The project was awarded a total of 9 nights in November 1998 (3 full nights lost because of bad weather), June 1999 and September 1999.

Typical sensitivities expected at IRTF are 26 Jy arcsec$^{-2}$ at 11.7 $\mu$m and 170 mJy arcsec$^{-2}$ at 18.0 $\mu$m, all chop-nod, one minute total observing time.

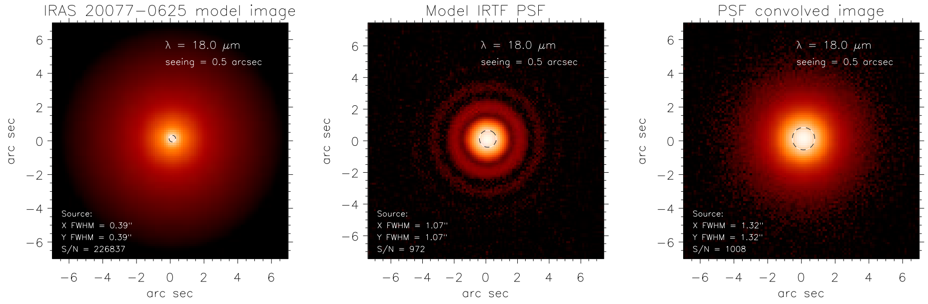

Fig. 5.11.— Simulated images of AGB circumstellar envelopes for the MIRAC3 camera at IRTF. Left panel shows the source model. The synthetic PSF with 0.5" and added noise is at the center. Final image (with $S/N \sim 1000$) is on the right.

### 5.4.2 Characterizing a sample of extended AGB sources

A critical part of our project was the selection of the sources to be imaged. To maximize the chances of extended emission detection one has to search for close-by objects having large optical depths, providing high infrared excess and extinction of the stellar radiation.

To find the best candidate meeting these criteria, we have modeled all AGB sources with $S/N \gtrsim 10$ in the IRAS LRS catalog by using the model grids described in chapter 3 for oxidic and carbonaceous dust. The sources were then selected with the following procedure:

1. the radial brightness distribution at 10 and 18 $\mu$m was computed for each envelope by fitting its IRAS Low Resolution Spectra;

2. a two dimensional image of each source was then derived from the intensity profile (figure 5.11, left panel);

3. the IRTF ideal diffraction limited PSF was simulated at 10 and 20 $\mu$m 10% passband filters. A more realistic PSF was then obtained by coadding many randomly displaced diffraction patterns in order to simulate a seeing of 0.5" (figure 5.11, center);

4. each source image was convolved with the PSF, and then resampled into the MIRAC3 final image array grid (0.32"/5, assuming a supersampling of 5×5 pixels in the image reduction processing as described in section 5.2.3);

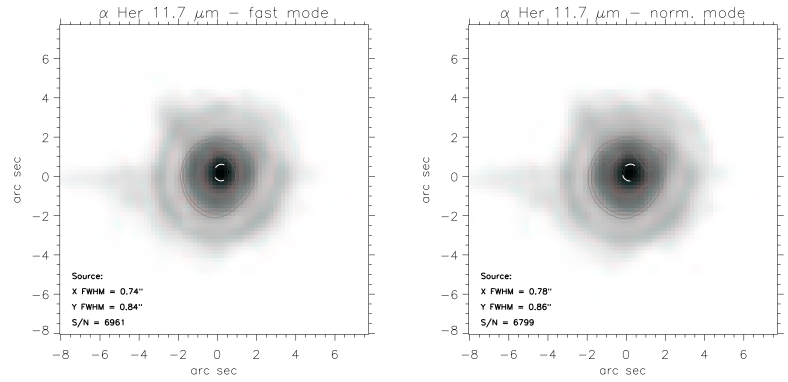

FIG. 5.12.— The reference star $\alpha$ Her at 11.7 $\mu$m. The image on the left was obtained using MIRAC3 fast mode, coadding about 1,600 single exposures of 0.17 sec (272 sec total); on the right is the coadding of 80 exposures of 10 sec each (800 sec total).

5. gaussian noise was added to all final images, to produce a peak S/N of ∼1,000, as expected for the real observations (figure 5.11, right);
6. the PSF was finally subtracted from the simulated images to map the excess of the source intensity with respect to the emission of a point source: detection of extended emission is expected only when this excess is above the noise level of the detector.

Note in figure 5.11 the well visible 2–3 diffraction rings in the model PSF, separated by dark annulus in which the flux of the PSF is below the noise. Note also in the right panel how the extended sources do not show the same pattern, having a much smoother profile. This is the main difference between extended sources of small angular size and point sources, and should be expected in the images of the observed AGB envelopes.

A criteria for selecting the sources showing a detectable extended emission is given by the ratio between the total excess flux and the normalized PSF in a standard 5” aperture:

$$ex = \frac{\sum_{ij}\left[\mathrm{image}(x_i, y_j) - \mathrm{PSF}(x_i, y_j)\right]}{\sum_{ij}\mathrm{PSF}(x_i, y_j)} \tag{5.13}$$

The best sources showing a detectable excess emission above the instrumental PSF in a minimum area of 6–8 arcsec in diameter were then selected for observations.

### 5.4.3 Observing technique

The circumstellar dust emission predicted by our models is typically characterized by a compact component, only partially resolved as an enlarged (in terms of the FWHM) PSF, plus a faint "halo" that can be separated by the "wings" of the PSF only when the S/N is of the order of ∼1,000 or larger. For a positive detection of these two components is necessary to maximize the achievable angular resolution and sensitivity. To meet these requirements, we used a rather short integration time (10 seconds), in order to reduce the effects of the atmospheric seeing. Hundreds of single chop-nod images were then taken, recentered and coadded as explained in section 5.2.3. This technique is possible in the case of AGB circumstellar envelopes because of the presence of a bright central source, which allows a precise recentering of the individual frames.

Another advantage of having many short integration time frames instead of a single long exposure, is a better spatial sampling of the images. To have even superior sampling we applied a dithering pattern to each beam position, by moving the sources in 5 offset positions on the detector array grid. An example of the full chop-nod sequence with dithering can be seen in the cumulative raw image shown in figure 5.5.

The optimal resolution can in principle be obtained by further reducing the single frame integration time. At mid-IR wavelengths, a frame time of the order to 0.1–0.2 sec is comparable to the timescale of the atmospheric convective cells turbulence. Setting this parameter to such a short time does in fact allow to "freeze" the atmospheric seeing, providing nearly perfect diffraction limited images. Again, this technique can be used only in case of very bright sources, for which a 0.1 sec integration time gives enough $S/N$ for a precise recentering. A very fast data acquisition electronic system is also required, in order to be able to collect images at a rate of nearly 10 Hertz. This is possible in the case of MIRAC3, thanks to the special "fast mode" which saves the large number of observed frames in a packed format, with only a small increase of wait time for readout, A/D conversion and save to disk operations.

The "fast mode" technique produced an effective increase in the spatial resolution of the sources for which it was tested. An example is shown in figure 5.12, where the standard star $\beta$ Her is shown, imaged with a frame time of 0.17 (left panel) and 10 seconds (right). The fast mode image is the coadd (with drizzling) of about 1,600 single exposures for a 272 sec total, while the normal integration was made with only 80 individual exposures (without drizzling), for a total time of 800 sec. Note the smaller FWHM of the fast mode image, and its higher $S/N$, despite the shorter integration time.

Our tests showed that the fast mode technique can enhance the spatial resolution at 10 $\mu$m by about 5%. This can be crucial when the sources to be observed are of comparable size with the PSF. The gain in the spatial resolution is however only effective when the telescope PSF remains stable between the observation of the source and the reference star. As shown in the next section, this is not always the case for the IRTF, whose mirror does not possess the necessary rigidity to guarantee a completely stable PSF while pointing at different coordinates in the sky. In this case the induced PSF deformations are larger than the loss of spatial resolution due to the seeing reduction between the 0.1 and 10 seconds frame time integration. This technique is however recommended at telescopes equipped with active optics systems, which can take full advantage of the increased angular resolution.

### 5.4.4 Observed sources

The list of the observed sources is shown in table 5.5. It consists of 26 objects, of which 20 are O-rich, 6 C-rich, 1 S-star and 1 pre-PN. The 10 $\mu$m fluxes goes from 100 to 5000 Jy, with an average of 500 Jy, which required a total integration time of 10–15 min for source, and for filter. The standard stars $\alpha$ Boo, $\alpha$ Her, $\alpha$ Tau, $\beta$ Peg, $\beta$ And and $\gamma$ Dra were observed for flux and PSF calibration.

The images were collected in the 10% passband filters at 8.5, 9.8, 11.7, 12.5 and 18.0 $\mu$m filters. A preference was given to the 18.0 $\mu$m filter, which our models show as having the best chance of detecting extended emissions above the PSF. This result of our simulations is not surprising, since the radiation emitted at 18 $\mu$m is originated in a colder region of the envelopes, which is thus more external. Since the temperature gradient in the envelopes goes as $T_d \sim r^{-0.3}$ (see equation 2.38), the region where a 20 $\mu$m photon is emitted is 8 times farther from the central star than the 10 $\mu$m photosphere. The 20 $\mu$m diffraction limited PSF is instead only 2 times larger than the 10 $\mu$m one (equation 5.7), and less subjected to the atmospheric seeing. It is thus easier to detect the extended emission of AGB circumstellar envelopes when the wavelength is longer. The only limit in this approach is in the lower brightness of 18 $\mu$m emissions. This is not a problem for our selected bright sources though it could be, for the standards which are in general less luminous than the AGB sources. The 11.7 $\mu$m filter was also favored, since it is in the middle of the 10 $\mu$m window, where the atmosphere is more transparent and the detector more sensitive.

Table 5.5 List of MIRAC3 sources

| Source | Type | IRAS name | F12 [Jy] | F25 [Jy] | Var. type |
|---|---|---|---|---|---|
| WX Psc | O-rich | 01037+1219 | 1160 | 968 | - |
| V370 And | O-rich | 01556+4511 | 499 | 291 | - |
| *o* Cet | O-rich | 02168−0312 | 4880 | 2260 | M |
| V656 Cas | O-rich | 02316+6455 | 481 | 314 | M |
| IRC+50096 | C-rich | 03229+4721 | 535 | 199 | - |
| IK Tau | O-rich | 03507+1115 | 4630 | 2380 | M |
| TX Cam | O-rich | 04566+5606 | 1640 | 635 | M |
| V Hya | C-rich | 10491−2059 | 1110 | 460 | - |
| V CVn | O-rich | 13172+4547 | 132 | 64 | SR |
| W Hya | O-rich | 13462−2807 | 4200 | 1190 | SR |
| OV Ser | O-rich | 15223−0203 | 101 | 67 | - |
| X Her | O-rich | 16011+4722 | 484 | 241 | SR |
| IRC+20370 | C-rich | 18397+1738 | 534 | 239 | M |
| IRC+10401 | C-rich | 19008+0726 | 454 | 182 | M |
| W Aql | S-star | 19126−0708 | 1575 | 670 | M |
| CH Cyg | O-rich | 19232+5008 | 565 | 191 | SR |
| V1302 Aql | pre-PN | 19244+1115 | 1350 | 2310 | - |
| GY Aql | O-rich | 19474−0744 | 460 | 271 | SR |
| BI Cyg | O-rich | 20194+3646 | 335 | 245 | - |
| V Cyg | C-rich | 20396+4757 | 665 | 234 | M |
| T Cep | O-rich | 21088+6817 | 753 | 267 | M |
| EP Aqr | O-rich | 21439−0226 | 637 | 321 | - |
| IRC+40540 | C-rich | 23320+4316 | 959 | 469 | - |
| R Aqr | O-rich | 23412−1533 | 1580 | 543 | M |
| TX Psc | C-rich | 23438+0312 | 163 | 40 | - |
| R Cas | O-rich | 23558+5158 | 1340 | 555 | M |

To minimize the spatial dependence of the PSF from the atmospheric conditions and telescope orientation we have always observed the closest standard before and after each source, in each filter.

The data reduction and photometric calibration was performed as described in section 5.2, using the IDL package we wrote and optimized for our

Table 5.6 Photometry of MIRAC3 sources

| Source | $F_{8.5}$ [Jy] | $F_{9.8}$ [Jy] | $F_{11.7}$ [Jy] | $F_{12.5}$ [Jy] | $F_{18.0}$ [Jy] | epoch |
|---|---|---|---|---|---|---|
| WX Psc | - | - | 1580 | 1370 | 2380 | Sep 99 |
| V370 And | - | - | 403 | 393 | - | Sep 99 |
| *o* Cet | - | 2710 | 2170 | - | 2020 | Sep 99 |
| V656 Cas | - | - | 214 | - | 231 | Sep 99 |
| IRC+50096 | - | - | 500 | - | 281 | Sep 99 |
| IK Tau | - | - | 2080 | - | 2060 | Sep 99 |
| TX Cam | - | - | 917 | 762 | 976 | Sep 99 |
| V Hya | - | - | 1120 | - | 628 | Jun 99 |
| V CVn | 105 | 175 | 109 | 88 | 115 | Jun 99 |
| W Hya | - | 2000 | 2940 | 2770 | 1780 | Jun 99 |
| | - | - | 2850 | - | - | Jun 99 |
| OV Ser | 78 | 101 | 87 | 77 | 81 | Jun 99 |
| X Her | 490 | - | 503 | 451 | 408 | Jun 99 |
| IRC+20370 | - | - | 994 | 781 | 440 | Jun 99 |
| IRC+10401 | - | - | 449 | 396 | 237 | Jun 99 |
| W Aql | - | - | 983 | 885 | 725 | Sep 99 |
| CH Cyg | - | - | 639 | 483 | 558 | Jun 99 |
| V1302 Aql | 788 | - | 1380 | - | 2570 | Jun 99 |
| GY Aql | - | - | 505 | 198 | 432 | Sep 99 |
| BI Cyg | - | - | 280 | 201 | 332 | Sep 99 |
| V Cyg | - | - | 20 | 19 | 312 | Jun 99 |
| T Cep | - | - | 554 | - | 377 | Sep 99 |
| EP Aqr | - | - | 499 | - | 481 | Sep 99 |
| IRC+40540 | - | 810 | 791 | 707 | 595 | Sep 99 |
| R Aqr | - | 1170 | - | - | 699 | Sep 99 |
| TX Psc | - | - | 105 | - | 54 | Sep 99 |
| R Cas | - | 2200 | 1640 | 1430 | 1310 | Sep 99 |

observing technique. The fluxes of the standard stars come from Hoffmann & Hora (1999).

The photometry of the sources is listed in table 5.6. Relatively stable conditions of the Mauna Kea sky on the timescale of each source-standard pair observations were met in most of our June and September 1999 runs. In these conditions the photometric accuracy computed for the flux density in table 5.6 are of ~5% for the 8.5, 9.8, 11.7 and 12.5 $\mu$m filters, and ~8% at 18 $\mu$m.

The measured photometry is mostly in accordance with the IRAS fluxes at 10 and 20 $\mu$m, taking into account the different filter profiles and effective wavelengths, and the long period variability of all the sources.

Table 5.7 FWHM of MIRAC3 sources, references and deconvolutions.

| Source | $\lambda$ | FWHM Source | | FWHM Reference | | FWHM Max Entropy | | FWHM Max Likelihood | | excess |
|---|---|---|---|---|---|---|---|---|---|---|
| | [$\mu$m] | X ["] | Y ["] | X ["] | Y ["] | X ["] | Y ["] | X ["] | Y ["] | |
| WX Psc | 11.7 | 0.77 | 0.86 | 0.75 | 0.83 | 0.22 | 0.29 | 0.23 | 0.29 | 0.0% |
| | 18.0 | 1.24 | 1.13 | 1.08 | 1.11 | 0.54 | 0.43 | 0.52 | 0.43 | **23.4%** |
| V370 And | 11.7 | 0.78 | 0.84 | 0.75 | 0.83 | 0.24 | 0.25 | 0.25 | 0.27 | 3.1% |
| | 12.5 | 0.87 | 0.84 | 0.85 | 0.83 | 0.26 | 0.27 | 0.26 | 0.27 | 4.2% |
| *o* Cet | 9.8 | 1.04 | 0.92 | 0.85 | 0.95 | 0.38 | 0.36 | 0.37 | 0.38 | 18.7% |
| | 11.7 | 0.93 | 1.03 | 0.85 | 0.95 | 0.35 | 0.35 | 0.35 | 0.38 | 15.5% |
| | 18.0 | 1.35 | 1.40 | 1.12 | 1.08 | 0.68 | 0.71 | 0.68 | 0.71 | **63.0%** |
| V656 Cas | 11.7 | 0.90 | 1.01 | 0.83 | 0.90 | 0.30 | 0.35 | 0.30 | 0.34 | **30.7%** |
| | 18.0 | 1.15 | 1.23 | 1.10 | 1.03 | 0.72 | 0.66 | 0.45 | 0.72 | **24.7%** |
| IRC+50096 | 11.7 | 0.87 | 0.90 | 0.88 | 0.78 | 0.28 | 0.39 | 0.27 | 0.39 | 8.3% |
| | 18.0 | 1.18 | 1.28 | 1.12 | 1.08 | 0.53 | 0.57 | 0.58 | 0.70 | **33.9%** |
| IK Tau | 11.7 | 0.81 | 0.83 | 0.88 | 0.78 | 0.21 | 0.28 | 0.22 | 0.27 | 0.0% |
| | 18.0 | 1.13 | 1.15 | 1.12 | 1.08 | 0.70 | 0.70 | 0.65 | 0.66 | 11.9% |
| TX Cam | 11.7 | 0.93 | 0.91 | 0.80 | 0.78 | 0.30 | 0.41 | 0.32 | 0.41 | **31.7%** |
| | 12.5 | 0.96 | 0.93 | 0.85 | 0.83 | 0.31 | 0.37 | 0.31 | 0.38 | **27.9%** |
| | 18.0 | 1.37 | 1.34 | 1.14 | 1.06 | 0.49 | 0.68 | 0.50 | 0.71 | **71.5%** |
| V Hya | 11.7 | 0.82 | 0.97 | 0.81 | 0.95 | 0.25 | 0.32 | 0.25 | 0.33 | 4.9% |
| | 18.0 | 1.15 | 1.35 | 1.07 | 1.23 | 0.53 | 0.80 | 0.48 | 0.63 | **21.4%** |
| V CVn | 8.8 | 0.73 | 0.90 | 0.76 | 0.87 | 0.24 | 0.31 | 0.23 | 0.31 | 4.8% |
| | 9.8 | 0.77 | 0.81 | 1.25 | 0.92 | 0.26 | 0.28 | 0.25 | 0.25 | 0.0% |
| | 11.7 | 0.87 | 0.83 | 0.82 | 0.99 | 0.29 | 0.23 | 0.29 | 0.24 | 0.0% |
| | 12.5 | 0.85 | 0.87 | 0.85 | 1.06 | 0.27 | 0.22 | 0.28 | 0.23 | 0.0% |
| | 18.0 | 1.09 | 1.13 | 1.05 | 1.14 | 0.50 | 0.56 | 0.38 | 0.36 | 19.7% |
| W Hya | 9.8 | 0.82 | 0.99 | 0.79 | 0.84 | 0.28 | 0.41 | 0.28 | 0.41 | **26.7%** |
| | 11.7 | 0.88 | 1.04 | 1.12 | 1.24 | 0.25 | 0.37 | 0.27 | 0.36 | **35.6%** |
| | 11.7 | 0.86 | 0.98 | 0.87 | 0.83 | 0.27 | 0.40 | 0.28 | 0.40 | 18.8% |
| | 12.5 | 0.98 | 1.06 | 0.85 | 0.89 | 0.35 | 0.45 | 0.36 | 0.46 | **44.7%** |
| | 18.0 | 1.19 | 1.43 | 1.10 | 1.17 | 0.48 | 0.80 | 0.48 | 0.80 | **45.6%** |
| OV Ser | 8.8 | 0.81 | 0.77 | 0.80 | 0.83 | 0.23 | 0.25 | 0.23 | 0.25 | 0.0% |
| | 9.8 | 0.83 | 0.92 | 1.25 | 0.92 | 0.27 | 0.38 | 0.26 | 0.33 | 0.0% |
| | 11.7 | 0.82 | 0.95 | 1.07 | 0.92 | 0.21 | 0.32 | 0.22 | 0.32 | 0.0% |
| | 18.0 | 1.20 | 1.33 | 1.24 | 1.21 | 0.47 | 0.86 | 0.46 | 0.85 | 4.4% |

Table 5.7: continue.

|  | $\lambda$ | FWHM Source |  | FWHM Reference |  | FWHM Max Entropy |  | FWHM Max Likelihood |  | excess |
|---|---|---|---|---|---|---|---|---|---|---|
|  | [$\mu$m] | X ["] | Y ["] | X ["] | Y ["] | X ["] | Y ["] | X ["] | Y ["] |  |
| X Her | 8.8 | 0.78 | 0.80 | 0.73 | 0.83 | 0.27 | 0.23 | 0.27 | 0.23 | 0.1% |
|  | 11.7 | 0.84 | 0.89 | 0.83 | 0.91 | 0.28 | 0.25 | 0.27 | 0.28 | 0.0% |
|  | 12.5 | 0.85 | 0.89 | 0.92 | 0.87 | 0.27 | 0.25 | 0.27 | 0.25 | 0.0% |
|  | 18.0 | 1.18 | 1.18 | 1.07 | 1.19 | 0.65 | 0.52 | 0.52 | 0.41 | 10.5% |
| IRC+20370 | 11.7 | 0.85 | 1.07 | 0.80 | 0.91 | 0.28 | 0.46 | 0.29 | 0.46 | 17.1% |
|  | 12.5 | 0.88 | 0.94 | 0.86 | 0.92 | 0.27 | 0.29 | 0.28 | 0.30 | 0.0% |
|  | 18.0 | 1.22 | 1.33 | 1.10 | 1.19 | 0.43 | 0.50 | 0.45 | 0.52 | **22.3%** |
| IRC+10401 | 11.7 | 0.83 | 0.92 | 0.80 | 0.91 | 0.25 | 0.29 | 0.26 | 0.29 | 5.3% |
|  | 12.5 | 0.84 | 0.91 | 0.86 | 0.92 | 0.22 | 0.27 | 0.24 | 0.27 | 0.0% |
|  | 18.0 | 1.15 | 1.28 | 1.10 | 1.19 | 0.33 | 0.48 | 0.37 | 0.46 | 11.6% |
| W Aql | 11.7 | 0.91 | 0.84 | 0.86 | 0.88 | 0.26 | 0.33 | 0.26 | 0.33 | 0.0% |
|  | 12.5 | 0.85 | 0.91 | 0.87 | 0.87 | 0.29 | 0.34 | 0.29 | 0.32 | 2.48% |
|  | 18.0 | 1.20 | 1.123 | 1.08 | 1.11 | 0.52 | 0.64 | 0.47 | 0.57 | **27.1%** |
| CH Cyg | 11.7 | 0.87 | 0.84 | 0.79 | 0.84 | 0.31 | 0.29 | 0.26 | 0.33 | 4.3% |
|  | 12.5 | 0.90 | 0.87 | 0.87 | 0.85 | 0.33 | 0.36 | 0.31 | 0.32 | 0.1% |
| V1302 Aql | 8.8 | 0.72 | 0.80 | 0.61 | 0.71 | 0.32 | 0.30 | 0.32 | 0.30 | **27.5%** |
|  | 11.7 | 0.88 | 0.94 | 0.74 | 0.84 | 0.35 | 0.35 | 0.35 | 0.35 | **28.3%** |
|  | 18.0 | 1.43 | 1.50 | 1.20 | 1.09 | 0.65 | 0.69 | 0.66 | 0.69 | **49.5%** |
| GY Aql | 11.7 | 0.85 | 0.85 | 0.88 | 0.82 | 0.26 | 0.30 | 0.26 | 0.30 | 0.0% |
|  | 12.5 | 0.84 | 0.89 | 0.91 | 0.84 | 0.29 | 0.29 | 0.27 | 0.28 | 0.9% |
|  | 18.0 | 1.20 | 1.13 | 1.10 | 1.03 | 0.62 | 0.66 | 0.50 | 0.63 | 19.3% |
| BI Cyg | 11.7 | 0.92 | 0.86 | 0.86 | 0.88 | 0.32 | 0.29 | 0.31 | 0.28 | 2.3% |
|  | 12.5 | 0.87 | 0.92 | 0.91 | 0.84 | 0.28 | 0.31 | 0.27 | 0.32 | 3.2% |
|  | 18.0 | 1.21 | 1.27 | 1.06 | 1.1 | 0.59 | 0.57 | 0.54 | 0.50 | **32.8%** |
| V Cyg | 11.7 | 1.16 | 1.13 | 0.77 | 0.85 | 0.84 | 0.87 | 0.84 | 0.80 | **101.5%** |
|  | 12.5 | 1.14 | 1.07 | 0.86 | 0.84 | 0.86 | 0.90 | 0.80 | 0.74 | **69.3%** |
|  | 18.0 | 1.17 | 1.17 | 1.14 | 1.07 | 0.61 | 0.57 | 0.48 | 0.46 | 17.1% |
| T Cep | 11.7 | 0.83 | 0.90 | 0.84 | 0.76 | 0.27 | 0.46 | 0.27 | 0.43 | 16.4% |
|  | 18.0 | 1.10 | 1.26 | 1.01 | 1.06 | 0.59 | 0.87 | 0.53 | 0.83 | **37.6%** |
| EP Aqr | 11.7 | 0.83 | 0.89 | 0.84 | 0.79 | 0.27 | 0.35 | 0.27 | 0.35 | 7.2% |
|  | 18.0 | 1.18 | 1.18 | 1.10 | 1.03 | 0.54 | 0.75 | 0.52 | 0.65 | **22.8%** |
| IRC+40540 | 9.8 | 0.77 | 0.89 | 0.90 | 0.75 | 0.23 | 0.32 | 0.24 | 0.32 | 3.6% |
|  | 11.7 | 0.86 | 0.90 | 0.89 | 0.80 | 0.26 | 0.32 | 0.26 | 0.32 | 6.8% |
|  | 12.5 | 1.00 | 1.10 | 0.85 | 0.87 | 0.41 | 0.55 | 0.41 | 0.57 | **48.9%** |
|  | 18.0 | 1.27 | 1.45 | 1.22 | 1.12 | 0.52 | 0.70 | 0.51 | 0.71 | **42.3%** |

Table 5.7: continue.

| | $\lambda$ | FWHM Source | | FWHM Reference | | FWHM Max Entropy | | FWHM Max Likelihood | | excess |
|---|---|---|---|---|---|---|---|---|---|---|
| | [$\mu$m] | X ["] | Y ["] | X ["] | Y ["] | X ["] | Y ["] | X ["] | Y ["] | |
| R Aqr | 9.8 | 0.89 | 1.00 | 0.85 | 0.95 | 0.31 | 0.35 | 0.31 | 0.35 | 8.7% |
| | 18.0 | 1.27 | 1.29 | 1.14 | 1.06 | 0.54 | 0.68 | - | - | **34.7%** |
| TX Psc | 11.7 | 0.85 | 0.81 | 0.83 | 0.90 | 0.28 | 0.23 | 0.28 | 0.23 | 0.0% |
| | 18.0 | 1.12 | 1.20 | 1.14 | 1.06 | 0.44 | 0.51 | 0.42 | 0.38 | 14.8% |
| R Cas | 9.8 | 0.88 | 0.86 | 0.90 | 0.75 | 0.27 | 0.32 | 0.27 | 0.33 | 13.0% |
| | 11.7 | 0.89 | 0.90 | 0.89 | 0.80 | 0.26 | 0.33 | 0.27 | 0.33 | 15.2% |
| | 12.5 | 1.00 | 1.13 | 0.85 | 0.87 | 0.38 | 0.55 | 0.38 | 0.56 | **55.9%** |
| | 18.0 | 1.32 | 1.52 | 1.22 | 1.12 | 0.56 | 0.78 | 0.57 | 0.79 | **67.6%** |

### 5.4.5 Discussion

Table 5.7 shows the extension of all observed sources, measured with the same criteria used for the source selection, which applies equation 5.13 to each source - reference pair renormalized to their peak value:

$$\text{source}' = \frac{\text{source}}{\text{MAX[source]}} \qquad , \qquad \text{reference}' = \frac{\text{reference}}{\text{MAX[reference]}} \tag{5.14}$$

Boldface numbers indicate source excess emission above 20% of the PSF total flux. Negative values have been set to zero (this is the case when the reference is more extended to the source, generally due to bad focusing of the telescope).

From a total of 75 observations, 28 show more than 20% of extended emission above the PSF, corresponding to 17 sources extended at least at one wavelength, on a sample of 26. In general, sources extended in one filter tend to show measurable infrared excess also in the other wavelengths, but in most cases the larger excess is measured at 20 $\mu$m. This result was fully expected, as explained in the previous section.

For each source and reference star, table 5.7 reports the FWHM in the X and Y direction, where X is oriented in R.A. and Y in declination. With only a few exceptions, all sources have a larger FWHM than the corresponding standards, with a difference that is in some cases larger than 1 MIRAC pixel (0.33" for June observations, 0.34" in September).

The maximum entropy and maximum likelihood (Lucy method) deconvolutions have been computed for all source and reference pair. The FWHM of the deconvolved images are also listed in table 5.7. Due to the limitations in the deconvolution algorithms, the given value should be used with caution, and considered only as an upper limit for the source "sizes". Tests made by convolving pairs of reference stars show that in general a residual image is left by both deconvolution processes, that can be as big as 1 MIRAC pixel.

### 5.4.6 Images of individual sources

The next pages show images of a few extended sources from our observed sample. Each figure plots the image of the source at a certain wavelength, the reference star in the same filter, the infrared excess image, obtained by subtracting the renormalized reference from the source, and the maximum entropy deconvolution. The orientation of the images is N up and W right. The source and reference image also show the contours at 0.01, 0.02, 0.05, 0.1, 0.2 of the maximum. The half maximum ellipse (contour at 0.5 of the maximum) is also plotted (dashed circle).

Most of the images are at 18 $\mu$m, where the extension is more evident, and the PSF is less dependent from the seeing. In some cases the images at shorter wavelengths are also shown for comparison.

Almost all sources show departures from spherical symmetry on angular size much larger than the telescope resolution. These deviation from sphericity however are generally present at a low brightness level, and can be due to the instability of the IRTF PSF with respect to the telescope orientation. We have indeed verified that the same standard observed in different positions on the sky can generate asymmetric features in the PSF. For this reason we cannot claim in some cases a specific symmetry of the observed sources, on the basis of our images alone. Active optics telescopes, providing a controlled shape of the primary mirror, can in principle overcome this difficulty, and allow the analysis of geometry of AGB circumstellar envelopes in greater detail.

Many deconvolved images appear to have ring like structures, analogous to detached shells. When the observed rings appear at the same position of the PSF diffraction minima, they are artifacts of the deconvolution process, which tends to concentrate the flux where the $S/N$ ratio is higher. In the case of our AGB envelopes, which have a smoother radial profile than the instrumental PSF (see e.g. figure 5.11) the maximum signal of the excess emission is precisely where the PSF disappears, that is in the minima of its diffraction pattern. The presence of the rings is a confirmation of the spatial extension of the source, and can give an idea of the real size of the envelopes. However, they cannot be considered as detached shells without independent observations.

The best case which suggests the presence of a detached envelope is the deconvolved image of W Hya (figure 5.23) at 18 $\mu$m. The high $S/N$ of both source and reference, and the net separation of the observed ring from the central source, is an indication that the shell can be physically disconnected from the star, by a phase of less intense mass loss. The shell is elongated in the N-S direction, and has a very different shape than the second diffraction ring of the PSF. The same structure is observed in the deconvolved images at other wavelengths. These are strong evidences that the detached appearence of the shell is not a spurious result of the deconvolution process.

Along with the detached shell, the source shows a second, compact envelope around the AGB star. This compact source is also extended (according to the FWHM of the deconvolved image), and very elongated, also in the N-S direction.

If the 18 $\mu$m shell observed in our image is detached, its separation from the central star ($\sim$ 2.5 arcsec) would correspond to a distance of $\sim$ 280 A.U. from the star, given the parallax of the source measured by HIPPARCOS (8.73mas, Perriman et al. 1997). With an expansion velocity of 8.2 km s$^{-1}$ (Loup et al., 1993), the timescale for the separation of the envelope would be $\sim$ 170 yr.

A detailed model of the source, fitting the observed radial brightness distribution, is in progress, and should give more information on the spatial structure of the source. A follow-up observation with a larger aperture telescope is also programmed.

Since W Hya is an O-rich SR variable, the presence of a detached shell, if confirmed, would be in nice agreement with the predictions made in chapter 4. Note, as a comparison, the symmetric shape of the deconvolved image of the Mira prototype *o* Cet (figure 5.22), which suggests an extended spherical envelope attached to the source. Even though shorther wavelength observations indicate asymmetries of *o* Cet photosphere (Karovska et al., 1997; Lopez et al., 1997), these deviations from spherical symmetry are not confirmed in our images.

Among the sources which show extension in our MIRAC3 data, there is also the O-rich AGB star WX Psc, which was already observed with the camera CAMIRAS (see section 5.3.4). An extended envelope is detected only at 18 $\mu$m, and does not show the asymmetry of figure 5.10 (the deconvolved image is symmetrical). The FWHM at 18 $\mu$m is elongated in the E-W direction, while the 11.7 $\mu$m FWHM is N-S elongated. This discrepancy is a suggestion that the asymmetries observed in CAMIRAS images may be due to an incorrect shape of the PSF.

Among the other observed sources, the largest extensions are shown by IRC+20370 (6"×8", probably asymmetrical), TX Cam (with a 6"×7" asymmetric halo) and the post-AGB V1302 Aql which is strongly extended at all wavelengths. This last source was previously imaged with MIRAC at the IRTF (Meixner et al., 1999), and was found extended and elongated, with major axis at 45° (9.8 $\mu$m) and 63° (20.6 $\mu$m) counterclockwise N to E. Our deconvolved images, which are characterized by a better angular resolution provided by the "fast mode" and drizzling technique used for this source, confirm the observed asymmetry. The full size of the envelope, given by the deconvolved images, is 4"×3" at 11.7 $\mu$m and $\sim$ 5" at 18.0 $\mu$m.

### 5.4.7 Conclusions

Our observations have demonstrated that high resolution imaging of AGB circumstellar envelopes is feasible with current mid-IR cameras and telescopes. All observed sources, selected by modeling their mid-IR spectrum, have shown some degree of extension, which in two third of the cases is larger than 20%.

The observed sources are more extended at 20 $\mu$m, where the radiation is emitted by the external regions of their envelopes. Deconvolution techniques are applied to the images, and reduce the effects of seeing and diffraction. The sub-arcsec angular resolution provided by our deconvolved images, allows to infer the spatial distribution of dust around the central stars. Despite some limitations due to the unstable PSF of the IRTF telescope, our deconvolutions give strong constraints on the symmetry of the sources, and the eventual presence of detached shells. Previously observed images of our sources, when available, confirm the symmetry and extension suggested by our images.

A follow-up campaign with the larger MMT telescope (6m aperture), equipped with active optics able to increase the stability of the PSF, is programmed. The new observations will be carried on to confirm the results of our survey, and extend the sample to lower luminosities. Radiative transfer modeling of the extended sources, fitting at the same time the spectra and the radial brightness distribution of the envelopes, is also programmed. This combined analysis, compared to more traditional techniques, offers stronger constraints on the parameters of the envelopes, and is less dependent on the PSF instability. This will allow a much better understanding of the physics of mass loss in evolved stars, until now precluded by the absence of high resolution data at mid-IR wavelengths.

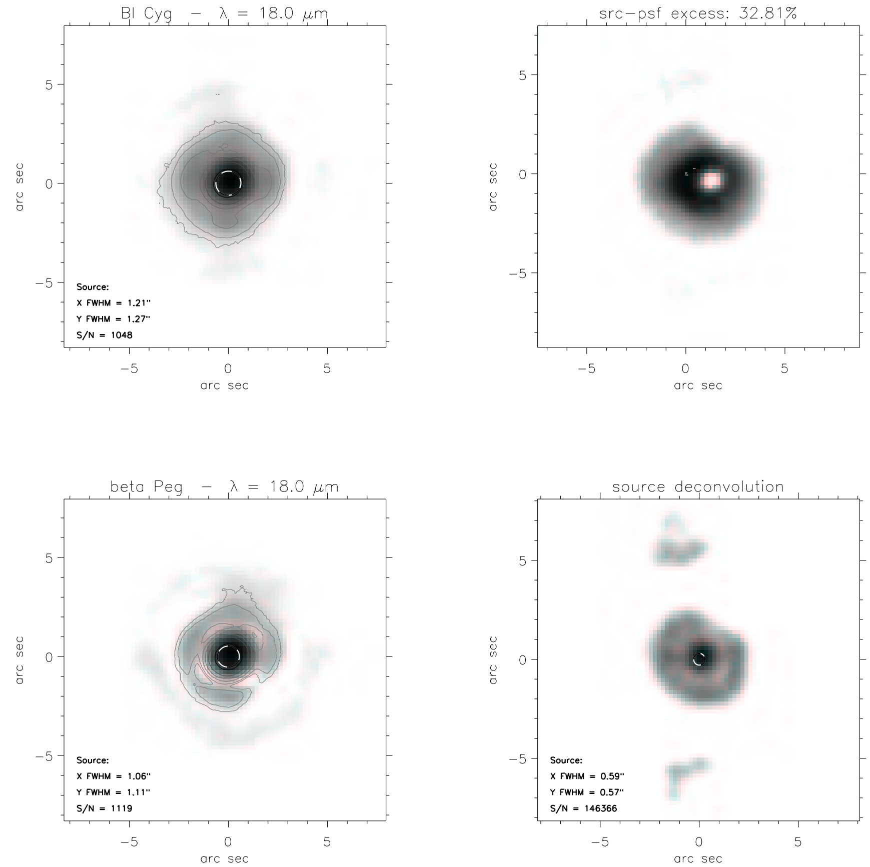

FIG. 5.13.— 18.0 $\mu$m image of the O-rich source BI Cyg, its reference star $\beta$ Peg, the infrared excess image and their deconvolution. The source is only extended at 18.0 $\mu$m, while at shorter wavelength it is a point source. The two structures in the N-S direction visible in the deconvolved image, are probably an artifact of the deconvolution process. The source appears symmetric, with a total diameter of the circumstellar emission of 5”.

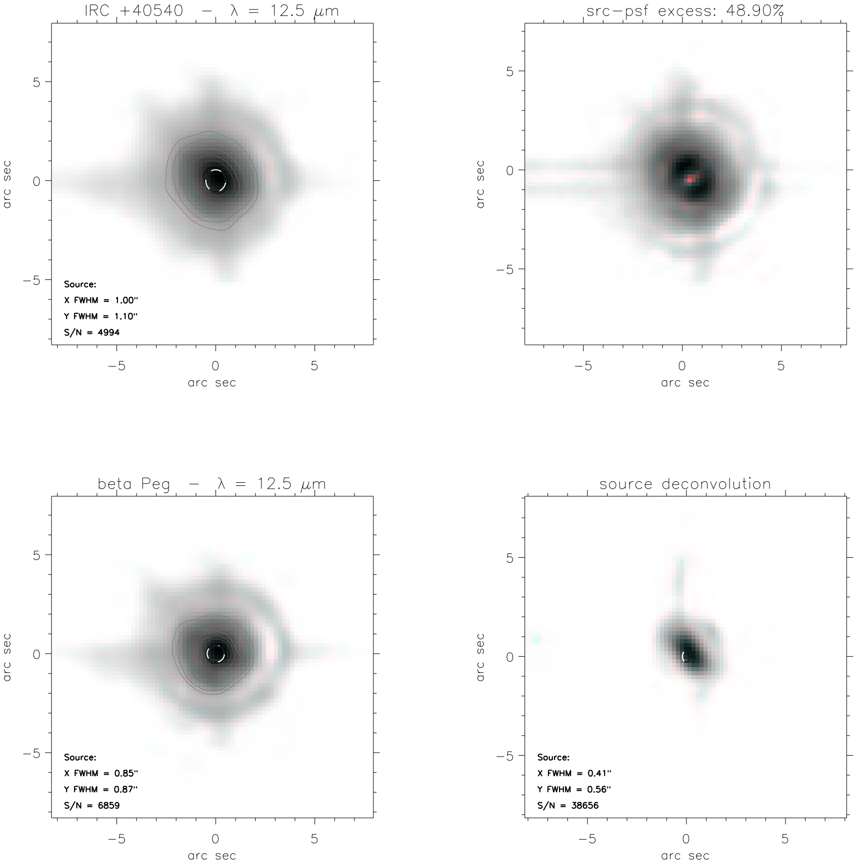

FIG. 5.14.— 12.5 $\mu$m image of the C-rich source IRC+40540, its reference star $\beta$ Peg, the infrared excess image and their deconvolution. The source is also extended at 18.0 $\mu$m, but not at shorter wavelength. The source is elongated in the NE-SW direction, with size 3”×3”.

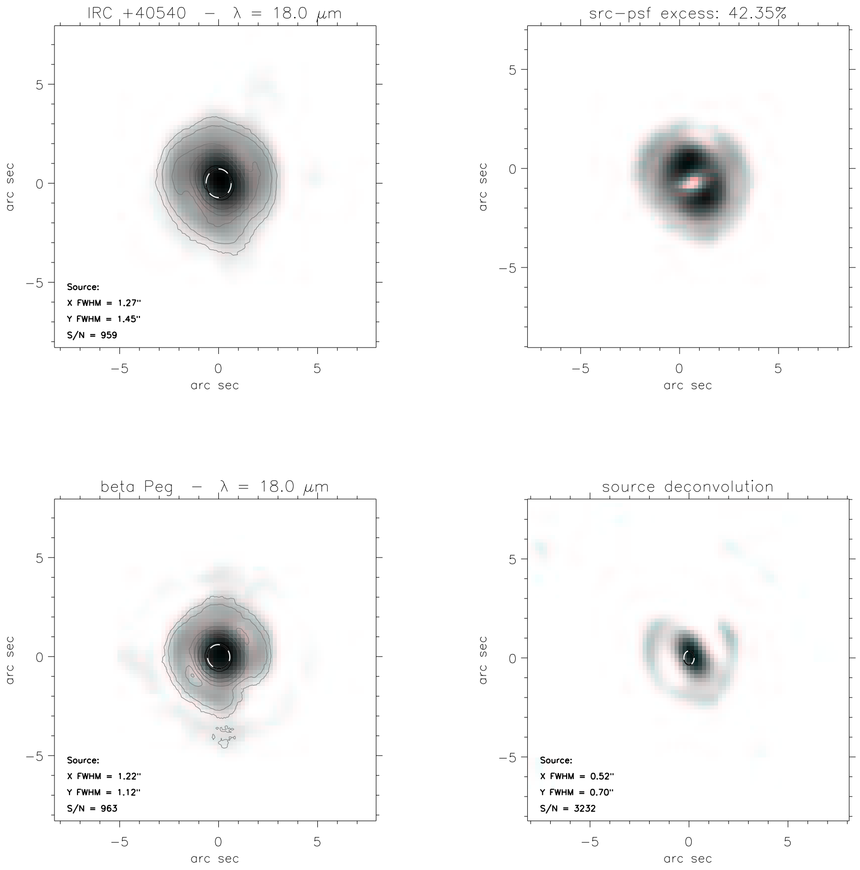

FIG. 5.15.— 18.0 $\mu$m image of the C-rich source IRC+40540, its reference star $\beta$ Peg, the infrared excess image and their deconvolution. The image shows the same elongation seen at 12.5 $\mu$m, but the extended emission is here detected as far as the second diffraction ring (5”).

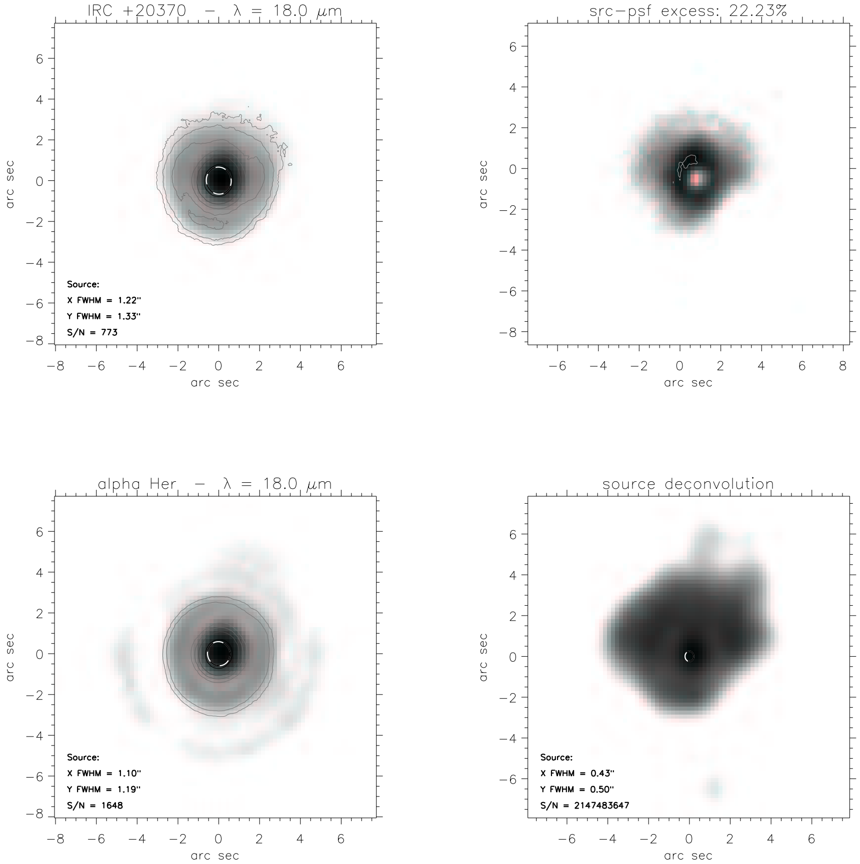

FIG. 5.16.— 18.0 $\mu$m image of the C-rich source IRC+20370, its reference star $\alpha$ Her, the infrared excess image and their deconvolution. The source appears also extended at 11.7 $\mu$m. The image in the 12.5 $\mu$m filter does not show extension because of low $S/N$ ratio. The source shows a rectangular shape with high $S/N$, and an extension of 6" ×8", mainly N of the central star.

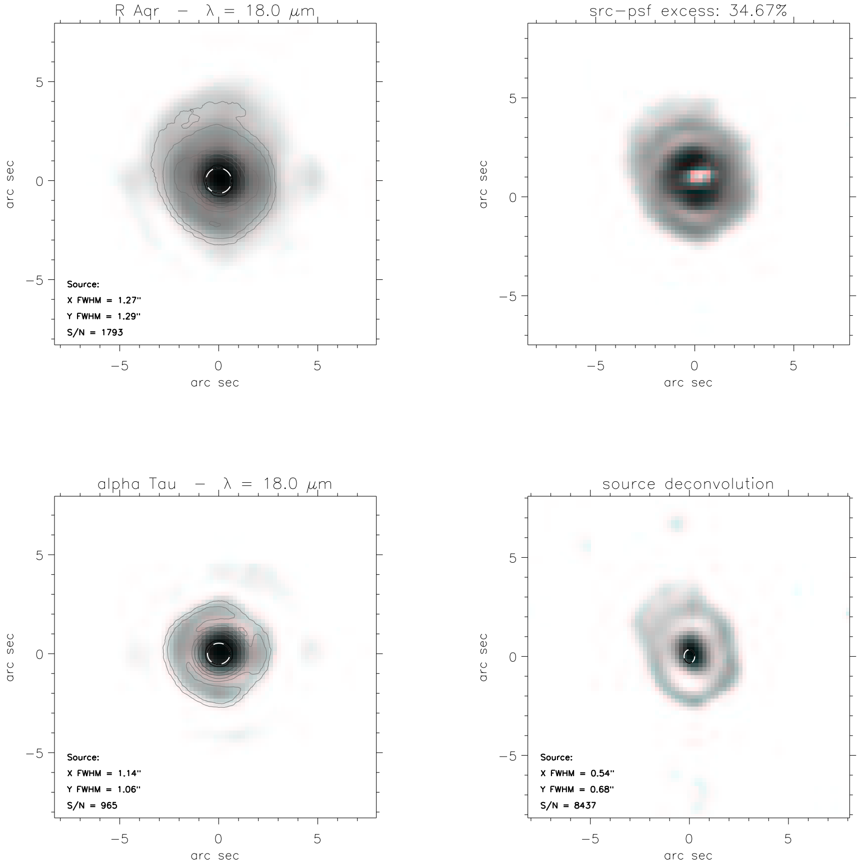

FIG. 5.17.— 18.0 $\mu$m image of the Mira O-rich source R Aqr, its reference star $\alpha$ Tau, the infrared excess image and their deconvolution. The source is not extended in MIRAC3 images at shorter wavelength. The extended emission is detected inside an area of 4" ×6" around the central source. The oval shape is probably due to a deformed PSF, since the source was observed with airmass $\gtrsim 1.3$.

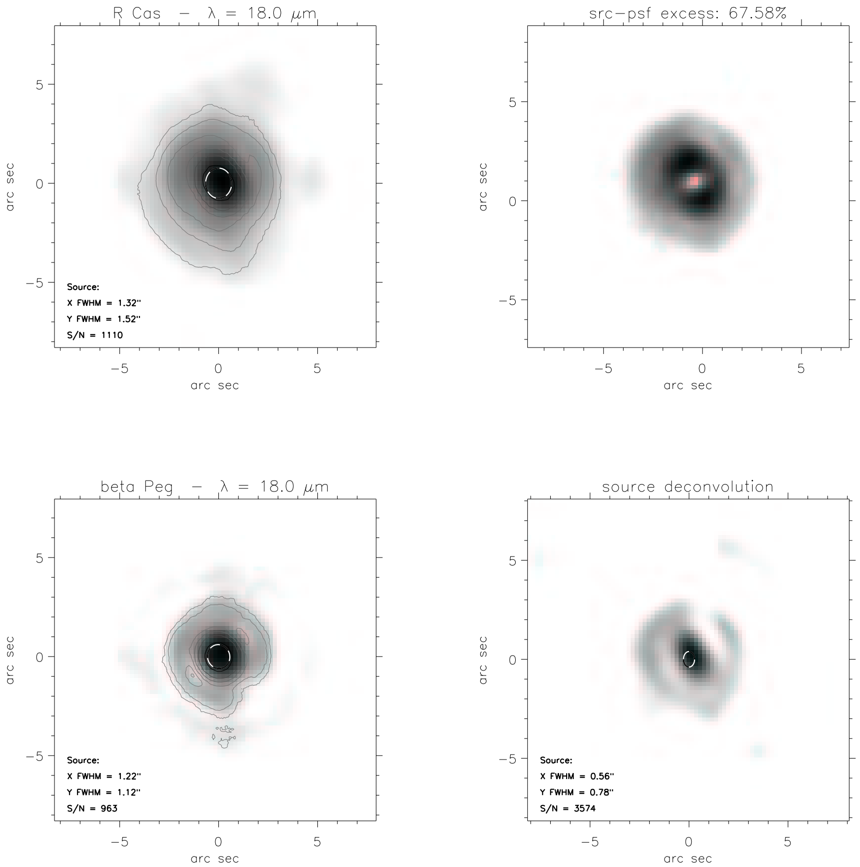

FIG. 5.18.— 18.0 $\mu$m image of the O-rich source R Cas, its reference star $\beta$ Peg, the infrared excess image and their deconvolution. The source is extended at all wavelengths, showing an oval compact emission 0.55"×0.76" plus an extended halo 6" in diameter.

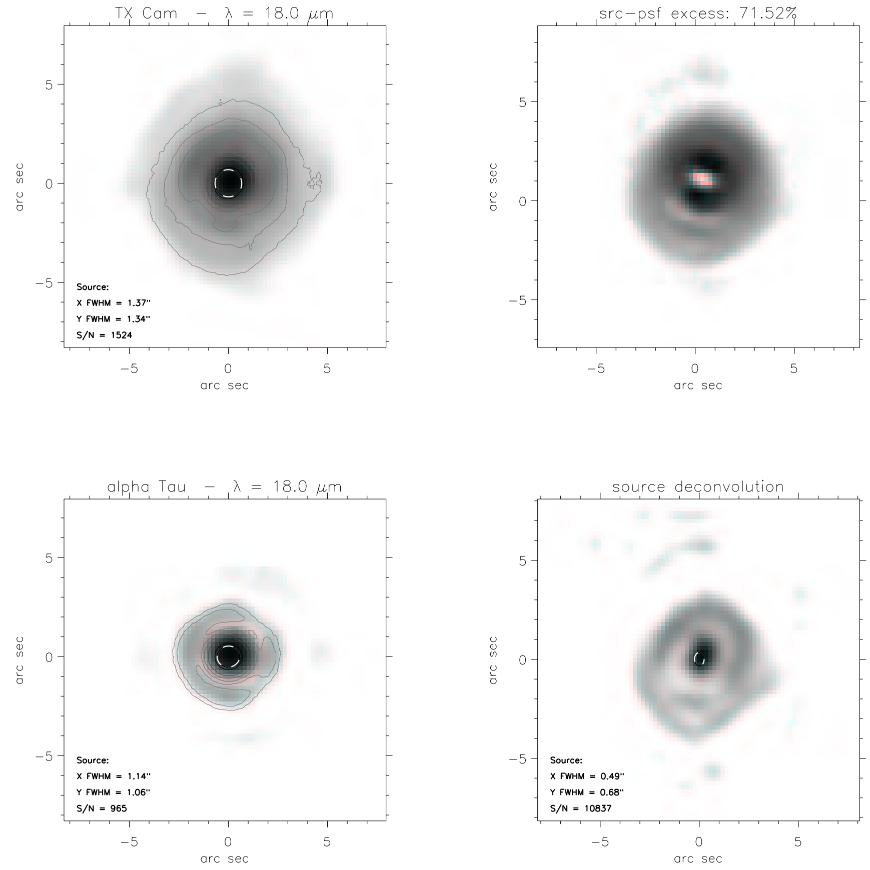

FIG. 5.19.— 18.0 $\mu$m image of the O-rich source TX Cam, its reference star $\alpha$ Tau, the infrared excess image and their deconvolution. The source is one of the more extended in our sample, with a 6"×7" halo. The source shows a larger and more diffuse IR excess S of the central star.

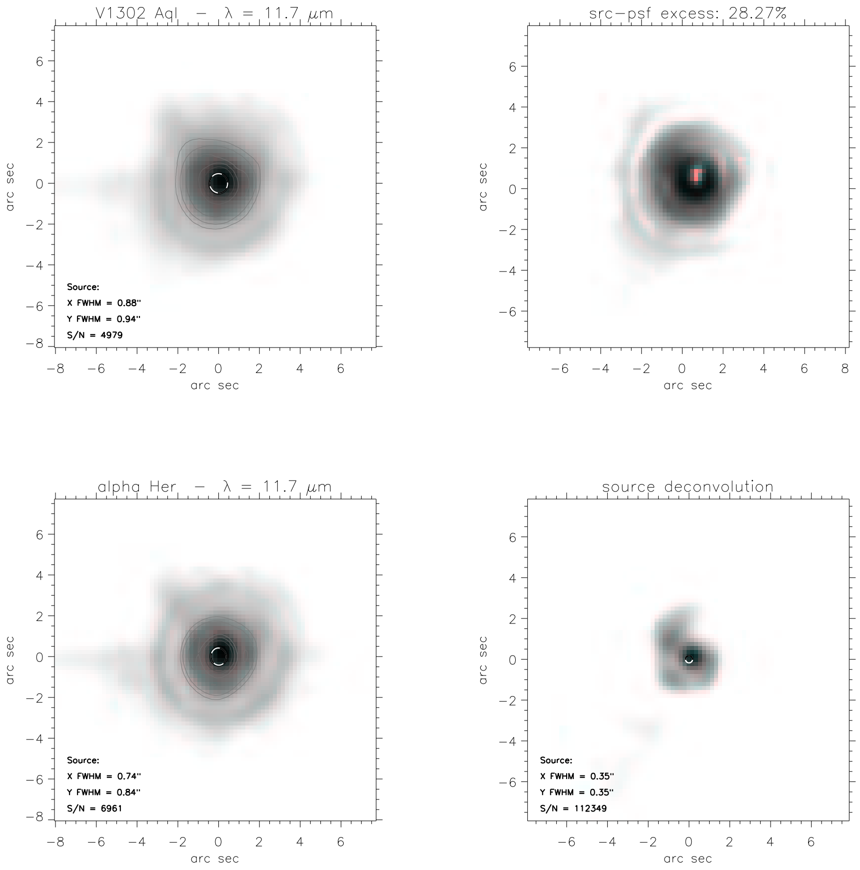

FIG. 5.20.— 11.7 $\mu$m image of the post-AGB source V1302 Aql, its reference star $\alpha$ Her, the infrared excess image and their deconvolution. The source is very extended in all filters, with a size of 4" even at short wavelength. The asymmetric structure of the source is confirmed by Meixner et al. (1999).

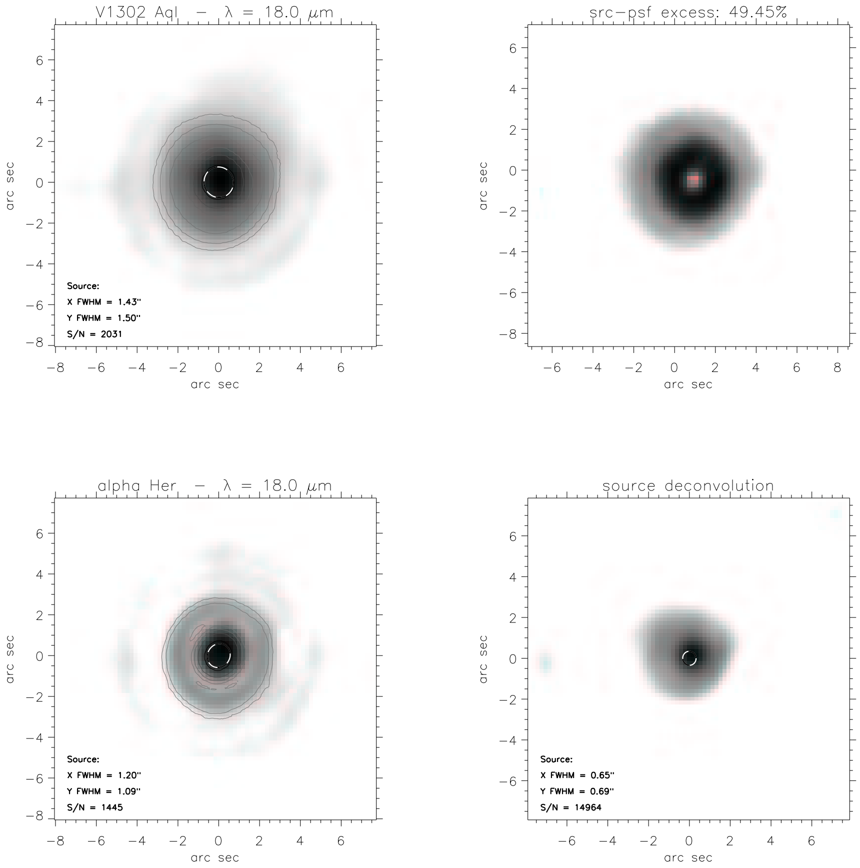

FIG. 5.21.— 18.0 $\mu$m image of the post-AGB source V1302 Aql, its reference star $\alpha$ Her, the infrared excess image and their deconvolution. The extension and symmetry of the source is confirmed, with a size of 5".

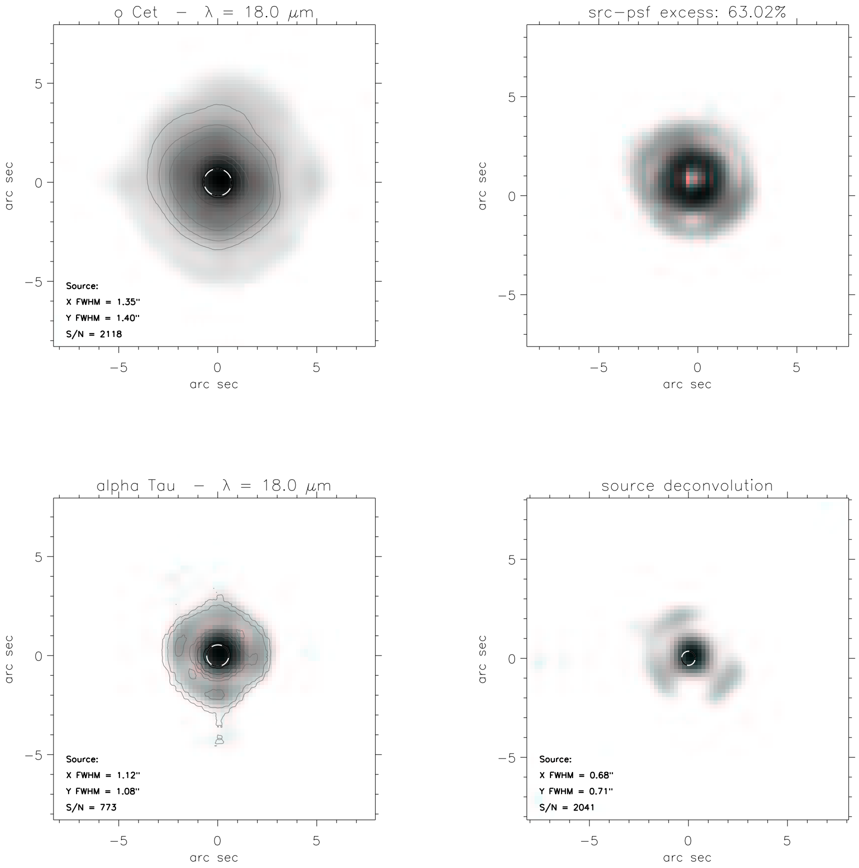

FIG. 5.22.— 18.0 $\mu$m image of the Mira prototype *o* Cet, its reference star $\alpha$ Tau, the infrared excess image and their deconvolution. The source is also extended at shorter wavelength with a size of 5" (after which the $S/N$ is "killed" by the second diffraction ring). The clumpy structure is probably a consequence of a deformed PSF (observed with airmass $\gtrsim 1.25$). The geometry of the envelope appears to be spherical at 18 $\mu$m, even though the source shows asymmetries and multiple shells at a much smaller spatial scale (Karovska et al., 1997; Lopez et al., 1997).

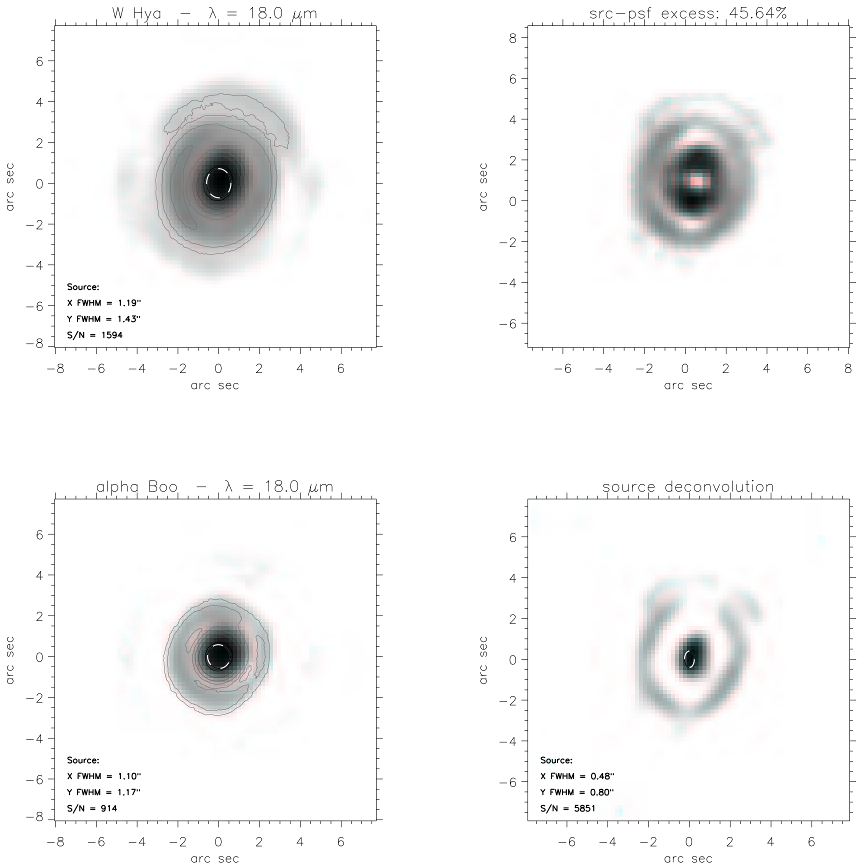

FIG. 5.23.— 18.0 $\mu$m image of the O-rich SR W Hya, its reference star $\alpha$ Boo, the infrared excess image and their deconvolution. The source appears extended at all wavelengths. Note the oval shape and the detached appearance of the deconvolved envelope.

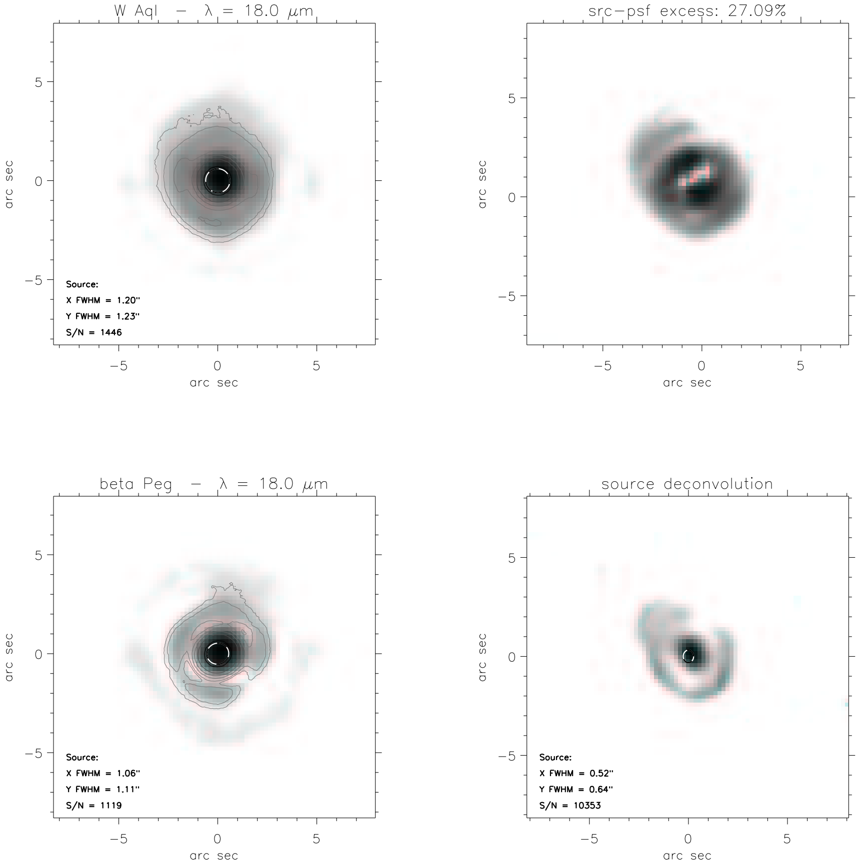

FIG. 5.24.— 18.0 $\mu$m image of the S-star W Aql, its reference star $\beta$ Peg, the infrared excess image and their deconvolution. The source is extended only at this wavelength, up to the second diffraction ring of the image (after which the $S/N$ is too low). The oval shape, as in the case of R Aql, is a consequence of the PSF.

## 5.5 AFGL 2591: detection of dust ejection in a massive YSO

During the MIRAC3 IRTF run, we have observed the bright Young Stellar Object (YSO) AFGL 2591. The images, taken at 11.7, 12.5 and 18.0 $\mu$m, revealed a knot of emission which may be evidence for a recent ejection event. This knot is roughly coincident with a previously seen near-IR reflection nebula and radio source, and lies within the known large-scale CO outflow. We also found a new faint NW source which may be an embedded low mass star. The results of the observations are described in this section, as published on Astrophysical Journal Letters (Marengo et al., 2000c).

### 5.5.1 Outflows in Young Stellar Objects

It is now generally agreed that most, if not all, stars produce energetic outflows during their formations (see Bachiller, 1996, for a review). Since the discovery of outflows almost 20 years ago (Snell et al., 1980), nearly 200 examples have been found, most of them associated with low luminosity YSO. Outflows can be studied using a variety of tracers including high velocity CO line emission (Bally & Lada, 1983), shock excited $H_2$ line emission (e.g. Lane, 1989) and optically visible Herbig-Haro (HH) jets (Reipurth 1989, 1999).

Even though all indications are that the flows emerge bipolarly from the stellar or circumstellar region, the physical processes giving rise to the outflows are not well understood. A primary wind originating at the star (e.g Shu et al., 1991) or at the accretion disk (e.g. Pudritz & Norman, 1983) is assumed to be responsible for the outward flow. A well collimated wind sweeps up the ambient molecular gas in its vicinity, forming two cavities in opposite directions from the star. The displaced molecular gas constitutes the CO outflows, and ionized "*knots*" of gas manifest themselves as HH objects. Outflows probably occur while the star is still accreting material, and may play a significant role in ejecting material of excess angular momentum.

The presence of "bullets" in the CO emission, and shocked "knots" visible in the optical and near-IR suggest that the mass ejection in YSO may occur intermittently, with an interval of $\sim 10^3$ yr between successive outbursts. The reasons for such modulation are not clear, but there are reasons to suspect a connection with variations in the accretion rate through a circumstellar disk (Hartmann & Kenyon, 1985). If this is true, it may be possible to probe the accretion history of protostars using detailed observations of their outflows (Reipurth, 1989).

One of the barriers to better understand the outflow process is the limited spatial resolution of CO observations. This is particularly true for YSOs which are embedded in dusty clouds responsible for large extinctions ($A_V \gg 10$).

These limitations can be overcome in the mid-IR, where sub-arcsec resolution can be provided by ground-based high resolution imaging, with the techniques explained in in section 5.2.

The observed source, AFGL 2591, was first recognized as an outflow by Bally & Lada (1983). The CO outflow is larger than 1' in extent, with the blue lobe extending west or southwest, and the red lobe in the northeast direction (Lada et al., 1984; Mitchell et al., 1992; Hasegawa & Mitchell, 1995). Optical and near-IR observations have revealed molecular hydrogen emission (40" east and west, Tamura & Yamashita 1992) and HH objects (10" and 20" west/southwest, Poetzel et al. 1992) near AFGL 2591. The distance of the source is not well established. Assuming a value of 1 kpc, it has a luminosity of $\sim 2 \cdot 10^4$ $L_\odot$ and an estimated stellar mass of 10 $M_\odot$.

### 5.5.2 Observations and data reduction

AFGL 2591 was observed with MIRAC3 at IRTF on June 3 and 4, 1999. We obtained images in the 11.6, 12.5 and 18.0 $\mu$m 10% passband filters, with a total on-source integration time of 600, 370 and 570 seconds respectively. The standard stars $\alpha$ Her and $\beta$ Peg, observed before and after the science target, were used for flux and PSF calibration.

The data acquisition and reduction was performed as for the AGB sources of the previous sections. The background was removed by using a standard beam switching technique, with the source in all four beams. Each individual nod cycle required a 10 second on-source integration, and the procedure was repeated for as many cycles as needed to obtain the requested total integration time.

### 5.5.3 Results and discussion

A schematic drawing of AFGL 2591 and its related structures is given in figure 5.25.

The images of AFGL 2591 are shown in figure 5.26, 5.27 and 5.28. The central source is not clearly resolved. It has FWHM of 0.84", 0.87" and 1.21" at 11.7, 12.5 and 18.0 $\mu$m respectively. An extended knot of emission ~6" SW from the central source is visible in all three images. A compact faint source is seen ~11" NW of AFGL 2591. We list mid-IR fluxes for the

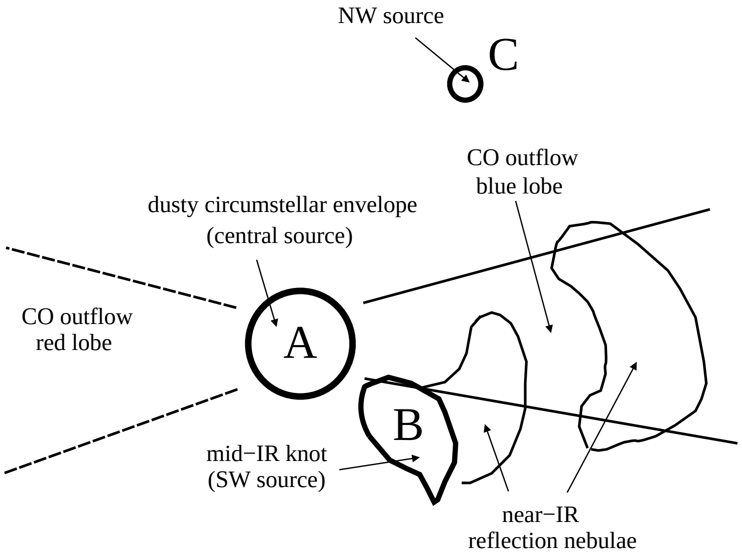

FIG. 5.25.— Schematic view of AFGL 2591 and related structures.

TABLE 5.8 PHOTOMETRY OF AFGL 2591

| Source | $F_{11.7}$ [Jy] | $F_{12.5}$ [Jy] | $F_{18.0}$ [Jy] | $T_{col}$ [K] |
|---|---|---|---|---|
| A | 440 | 745 | 753 | 320 |
| B | 18.4 | 15.9 | 79.6 | 110 |
| C | 1.8 | 2.1 | 16.2 | 110 |

three sources in Table 5.8. From the 12.5 and 18.0 $\mu$m fluxes we derived color temperatures of 300–350 K for the central source, and 100–120 K for the SW knot and the NW source.

The only previously published observation of AFGL 2591 in the mid-IR was obtained with TIRCAM at SPM (Persi et al., 1995), and does not reveal the SW knot or the NW compact source seen in the MIRAC3 images.

The flux of the central source rises dramatically from 11.7 to 12.5 $\mu$m, implying that the 11.7 $\mu$m flux may be suppressed by a large silicate absorption feature at $\sim$9.8 $\mu$m. Indeed, the IRAS LRS of the source shows deep absorption at that wavelength. Thus, it is likely that the protostar is

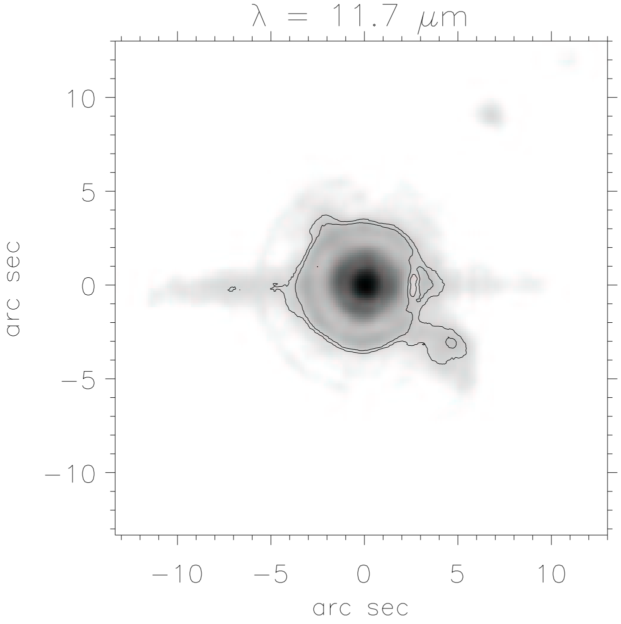

FIG. 5.26.— 11.7 $\mu$m image of AFGL 2591. Contours are plotted for 10 and 15 $\sigma$ levels.

surrounded by an optically thick dusty envelope, perhaps in free fall collapse onto the star (van der Tak et al., 1999). Our observations limit the radius of the envelope to ~2500 A.U.

Figure 5.29 shows the IRAS spectrum of the source, and the best fit we obtained by modeling the circumstellar envelope with DUSTY using the same technique described for the AGB envelopes of the previous chapters. The shown fit is for a spherically symmetric envelope with radial density profile $n(r) \propto r^{-2}$ around a central black body of $T_{eff} \simeq$ 25,000 K (van der Tak et al., 1999). The fit with $n(r) \propto r^{-1.5}$ (i.e. constant infall) was not as good, implying that the infalling envelope is likely to be surrounded by a fair amount of non-infalling cloud material. The model spectrum is not particularly sensitive to the $T_{eff}$ of the central source. Our best fit to the LRS suggests an $A_B$ of the order of 100.

AFGL 2591 is generally considered an example of a relatively isolated massive star formation. However, our detection of a faint point source 11" NW of it suggests the presence of other embedded low mass stars in the vicinity. A preliminary look at the Two-Micron All Sky Survey (2MASS) J,H

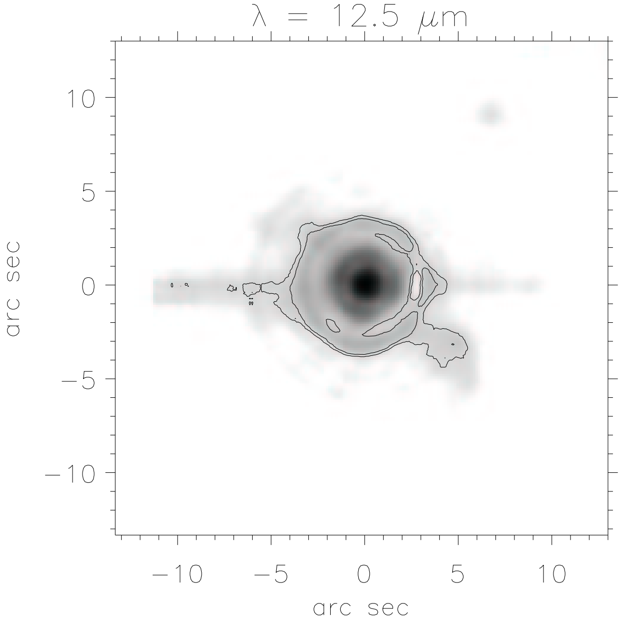

FIG. 5.27.— 12.5 $\mu$m image of AFGL 2591. Contours are plotted for 10 and 15 $\sigma$ levels.

and K images reveals at least two other sources within 40” of AFGL 2591. Deep mid-IR images of a larger area are needed to search for a possible cluster of low-mass protostars in the region.

The SW knot we detect appears close to the inner portion of a loop first observed in the near-IR by Forrest & Shure (1986). The near-IR emission is assumed to arise from scattering of photons from the main source off dust grains at the surface of a cavity cleared by the outflow. The loop, also seen in $NH_3$ observations by Torrelles et al. (1989), is indeed located in the blue outflow lobe, i.e., the one toward us. At 18 $\mu$m we derive an optical depth $\tau_{18} \simeq 1.2$, and therefore a mass estimate of $\gtrsim 0.2$ $M_\odot$ for this knot.

The SW knot is also coincident with a radio source as well as a knot of $H_2$ emission. The radio source, detected using interferometers at the Very Large Array (Campbell, 1984) and the Owens Valley Radio Observatory (van der Tak et al., 1999), has approximately flat spectrum between 6.1 and 0.3 cm, and is interpreted as free-free emission from an optically thin HII region. The $H_2$ emission is seen in an image taken with the BEAR imaging spectrometer on the Canada-France-Hawaii telescope using a narrow band filter

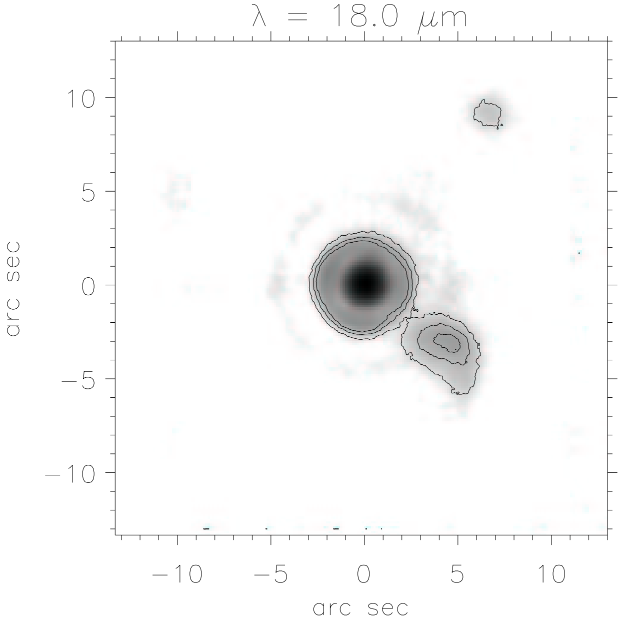

Fig. 5.28.— 18.0 $\mu$m image of AFGL 2591. Contours are plotted for 5, 10 and 15 $\sigma$ levels.

on the 1-0 S(1) line, after the continuum is subtracted (G. Mitchell, personal communication). The existence of the $H_2$ line implies shock collisional heating of the molecular gas in the outflow, which provides the necessary excitation energy ($T \gtrsim 2000$ K, see e.g. Smith & Brand 1990). On the other hand, the dust responsible for mid-IR emission is characterized by a much lower temperature of $T_d \sim 100$ K, as inferred from our photometry. It is likely that the $H_2$ emission comes from the shock itself, while the mid-IR color temperature is determined by the local thermodynamical equilibrium of the dust with the radiation fiels (which has a much lower energy than the shock).

Previous near-IR observations have also revealed a second, larger loop of emission at a projected separation of ∼ 19" from the star (Burns et al., 1989; Minchin et al., 1991; Tamura et al., 1991; Poetzel et al., 1992). The presence of multiple shells/loops is thought to be evidence for episodic mass loss outflows from AFGL 2591, as are molecular bullets seen in CO emission (Bachiller et al., 1991) and shocked knots observed in the optical and the near-IR (Reipurth, 1989) in other well known outflow sources. Up to $\sim 1 M_\odot$

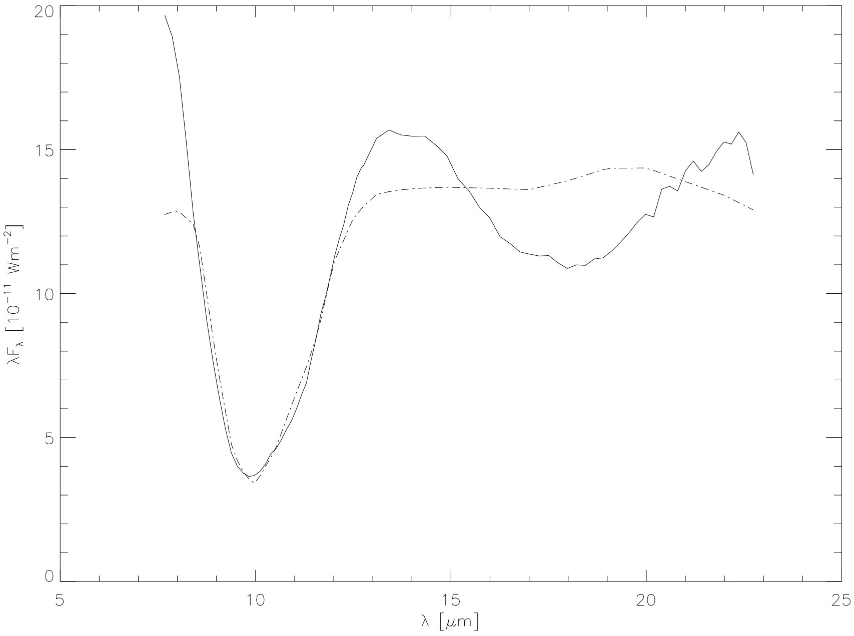

FIG. 5.29.— IRAS Low Resolution Spectrum of AFGL 2591 (thick line) and best fit model (dot-dashed line) for the 10 $\mu$m silicate feature. The heavy absorption is presumably due to an optically thick dusty envelope around the massive central star.

could be ejected in such eruptive events, though a few tenths of a solar mass is typical (Bachiller, 1996).

If we assume that the SW knot is associated with a recent mass ejection from AFGL 2591, we can estimate its dynamical timescale. Following Minchin et al. (1991), we take that the outflow is inclined from the plane of the sky by 55 degrees. In this case we estimate $\sim 10^4$ A.U. as the true distance from the star to the SW knot. Given a true outflow velocity of 26 km s$^{-1}$ (based on the line of sight velocity of the CO gas observed by Bally & Lada 1983), we get a dynamical timescale of $\sim$ 2000 yr. For the same assumptions, the outer loop seen in the near-IR would have a dynamical timescale of $\sim$ 6000 yr. Such timescales are consistent with the estimated $10^4$–$10^5$ yr total duration of the energetic outflow phase of YSOs (Bally & Lada, 1983).

In summary, our observations suggest that mid-IR imaging and spectroscopy can be powerful tools for probing the immediate circumstellar environment of embedded stars driving outflows. Such outflows appear to be rather common around young stars and are very likely associated with accretion processes from the early stages of protostars. They may play an important role in determining the mass of the star-disk system, and affect the evolution of the surrounding molecular cloud. Yet our understanding of the outflow process is far from satisfactory. High-resolution imaging with current mid-IR cameras and future millimeter interferometers could help develop a more unified picture of infall and outflow in star formation.

# Chapter 6

# Models of ICM dust

When in section 1.2.4 the question of dust presence in the hot intracluster medium (ICM) of galaxies was raised, a particular emphasis was given on the absence of convincing proofs of its survival in such a hostile medium. The attempts to quantify the amount of dust dispersed in the ICM by using extinction measurements have given contradicting results. The efforts to detect direct thermal emission from such dust have also yielded results which are not fully convincing.

For a better understanding of dust physics in hot plasmas, it is necessary to predict the expected emission, in view of the present and future observational campaigns. This requires a detailed model for the temperature distribution of ICM dust.

An algorithm which derives the temperature of dust embedded in a hot astrophysical plasmas was developed by Dwek (1986). In this chapter a new numerical implementation of this method is discussed, and a parallel code, able to compute the stochastic temperature distribution for a wide range of input parameters, is presented. The case of the Coma clusters of Galaxies is studied, and possible astrophysical applications, are suggested.

This work has been made under the supervision of Dennis W. Sciama at SISSA/ISAS (Trieste, Italy) and in collaboration with Avery Meiksin (now at University of Edinburgh, UK).

## 6.1 Characteristics of ICM dust

The basic characteristics of ICM dust are described in section 1.2.4. They are inferred from the status of the hot plasma that accumulates at the gravitational well of massive clusters of galaxies, which in turn are mainly derived by X-ray observations.

The physical status of dust and gas in the ICM is a fundamental ingredient to model the thermal structure of ICM dust, and is reviewed in this section in reference to the specific case of the Coma Cluster of galaxies.

### 6.1.1 The Coma Cluster of Galaxies

The Coma cluster of galaxies is considered as the archetype of a virialized cluster in state of thermodynamical equilibrium (Kent, 1982). The distance $D \simeq 138$ Mpc, and the high luminosity $L_X \simeq 1.7 \cdot 10^{45}$ erg s$^{-1}$ (Mushotzky et al., 1978) makes the Coma cluster an ideal observational target. It was, in fact, the original cluster in which what has come to be known as dark matter was discovered (Zwicky, 1933).

Even though there are evidences of substructures inside the cluster, its status of disequilibrium is probably not too severe (Briel et al., 1992). The virialization of the galaxies in the cluster allows to derive a smooth law for their distribution, which have been measured by Henriksen & Mushotzky (1986):

$$g(r) = \left[1 + \left(\frac{r}{r_G}\right)^2\right]^{-3/2} \qquad \text{with} \qquad r_G \simeq 0.25 \text{ Mpc} \tag{6.1}$$

The dynamical equilibrium of the cluster is also reflected by the enormous quantities of gas which constitutes the intracluster medium. This gas supports itself in hydrostatic equilibrium against the gravitational field of the cluster, which requires a kinetic temperature of the order of $10^6$–$10^8$ K. The main energy loss at such high temperature is through bremsstrahlung radiation, responsible for the diffuse X-radiation which is the main cooling mechanism for the ICM.

X-ray images of the Coma cluster have been obtained with the ROSAT satellite, and measure its radial brightness distribution. A best fit analytical representation of the azimuthally averaged surface luminosity of the cluster is given by Briel et al. (1992), and corresponds to a modified isothermal King profile (King, 1966):

$$F_X(r) \simeq 3.5 \cdot 10^{-8}\, \text{erg cm}^{-2}\, \text{sr}^{-1} \left[1 + \left(\frac{r}{r_X}\right)^2\right]^{-1.75} \tag{6.2}$$

where $r_X \simeq 0.42$ Mpc is the core radius of the cluster.

The gravitational binding mass that is inferred for the cluster is $M_{tot} \simeq 1.8 \cdot 10^{15}$ M$_\odot$, assuming a Hubble constant $H_0 \simeq 50$ km s$^{-1}$ Mpc$^{-1}$ (Briel

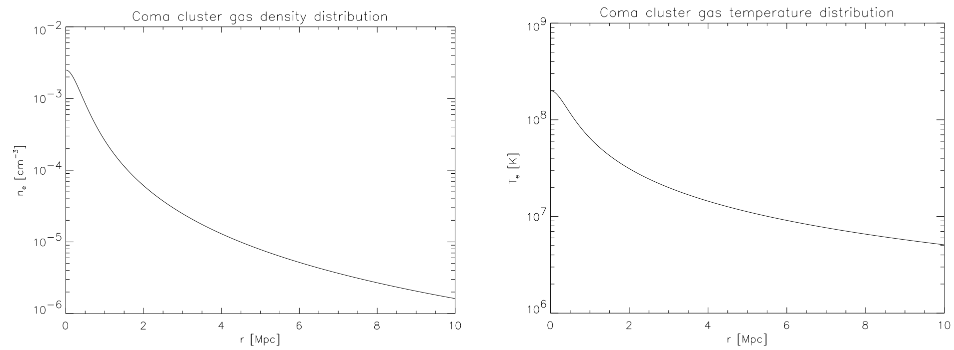

FIG. 6.1.— Radial profiles for ICM gas temperature and density profiles for Coma Cluster. Derived from Henriksen & Mushotzky (1986).

et al., 1992). Since the total mass of the gas ($M_g \simeq 10^{14}$ M$_\odot$) is at least an order of magnitude less (Dwek et al., 1990), one should conclude that most of the gravitational force in the cluster is produced by Dark Matter (DM).

### 6.1.2 The ICM gas

As for the Coma cluster, the total X-ray luminosity of a rich cluster of galaxies is of the order of $10^{43}$–$10^{45}$ L$_\odot$ (Fabian, 1994b). It is from the analysis of this radiation that most of the information on the status of the ICM gas are derived. Emission lines of highly ionized Fe are observed in bright clusters, with ∼0.3 solar abundances. Many other metals are also detected, which equal and even exceed solar abundance (Fabian, 1988). This confirms that the ICM gas is chemically enriched, and cannot be primordial. Its origin is uncertain (see section 1.2.4), but its chemical enrichment suggests its provenience from the galaxies in the clusters.

The spatial density and temperature distribution of ICM gas is also fitted by X-ray surface brightness maps. Best fit profiles for the Coma cluster are plotted in figure 6.1, as given by Henriksen & Mushotzky (1986):

$$n_g(r) \simeq 2.5 \cdot 10^{-3}\ \mathrm{cm}^{-3}\, f(r) \tag{6.3}$$

$$T_g(r) \simeq 2 \cdot 10^{8}\ \mathrm{K}\, f(r)^{1/2} \tag{6.4}$$

where

$$f(r) = \left[1 + \left(\frac{r}{r_c}\right)^2\right]^{-1.14} \qquad \text{with} \qquad r_c \simeq 0.4 \text{ Mpc} \tag{6.5}$$

These expressions will be used in section 6.2.4 to compute the temperature distribution of dust at different distances from the center of the cluster.

### 6.1.3 Size and spatial distribution of the grains

The size and density distribution of dust in the ICM is determined by the time for which the grains have been exposed to the sputtering action of the hot gas. Since typical interstellar grains are smaller than 0.5 $\mu$m (see equation 1.1), according to equation 2.70 they cannot survive longer than $10^8$ yr in the central region of a rich cluster. Thus, if dust is present in the ICM, it cannot be primordial. As shown in section 1.2.4, injection of dust from the cluster's galaxies is the most plausible hypothesis to explain its presence in the ICM, as inferred by extinction measurements.

Assuming a galactic origin of ICM dust, an initial size distribution similar to MRN distribution (equation 1.1), as for the ISM, is to be expected: $n_d \sim a^{-k}$, with $k = 3.5$. The initial gas to dust mass ratio should also be equal to the galactic value, or $Z_d = 0.0075$.

Once the dust is transferred into the ICM, it is rapidly eroded by the sputtering action of the gas. To guarantee a continuous presence of dust, the injection episodes should occur with a relative frequency (less than $10^8$ yr), otherwise the dust disappears. If the dust is continually replenished by the galaxies, a steady state size-diffusion equation can be written (Dwek et al., 1990):

$$\frac{\mathrm{d}n_d(a,r)}{\mathrm{d}a} = \left[\frac{\tau_{sputt}(a,r)}{a}\right]\left[\frac{\mathrm{d}n_{d,i}(a,r)}{\mathrm{d}t}\right] \tag{6.6}$$

where $\mathrm{d}n_d(a,r)$ is the grain number density at distance $r$ and in the size interval $a$ and $a + \mathrm{d}a$, and $\mathrm{d}n_{d,i}(a,r)/\mathrm{d}t$ is the initial injection rate of dust particles of radius $a$. Assuming all the ICM gas originated in the galaxies, and a constant gas outflow during the lifetime $\tau_0$ of the cluster, then

$$\frac{\mathrm{d}n_{d,i}(a,r)}{\mathrm{d}t} \sim \frac{n_{d,i}(a,r)}{\tau_0} \tag{6.7}$$

where $n_{d,i}(a,r) = n_{d,i}(0) \cdot g(r) \cdot a^{-k}$ is the initial size-density distribution of the injected dust. The dust density at the center of the cluster $n_{d,i}(0)$ is:

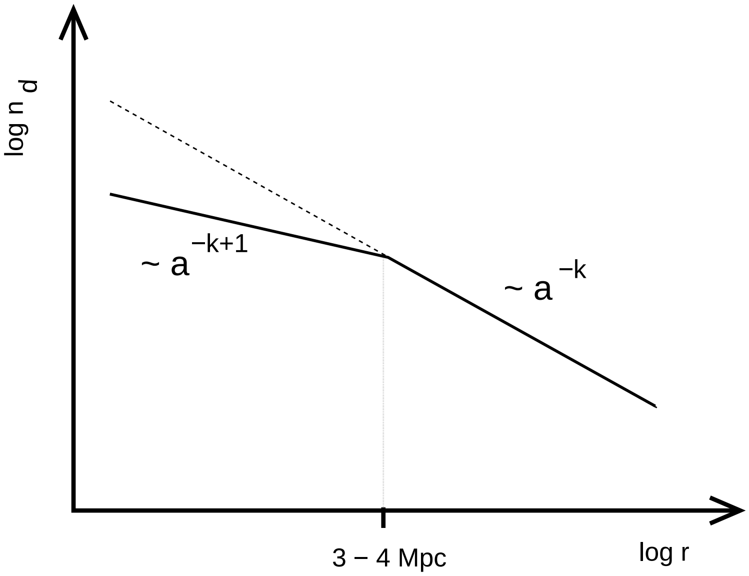

FIG. 6.2.— Schematic profile of Coma cluster dust, with steady state $\sim a^{-k+1}$ radial size distribution in the inner core of the cluster, and ISM like distribution outside the central region, where the dust is not effectively sputtered.

$$n_{d,i}(0) = \frac{\mu_g n_g(0) m_H Z_d}{\langle m_d \rangle} \tag{6.8}$$

where $\mu_g \cdot m_H$ is the mean atomic weight of the gas and $\langle m_d \rangle$ the average mass of the grains in the MNR size interval. From equation 2.70, since $\tau_{sputt} \propto a/n_g$:

$$\tau_{sputt}(a, r) = \frac{\tau_{sputt}(a, 0)}{f(r)} \tag{6.9}$$

Then:

$$\mathrm{d}n_d(a, r) = \frac{\tau_{sputt}(a, 0)}{\tau_0} \cdot \frac{n_{d,i}(0)}{a} \cdot \frac{g(r)}{f(r)} \cdot a^{-k} \,\mathrm{d}a \tag{6.10}$$

The last equation can be integrated with respect to $a$. Since $\tau_{sputt}/a \sim const(a)$, the only term of equation 6.10 which depends from $a$ is the MRN distribution factor $a^{-k}$, and then:

$$n_d(a,r) = \frac{\tau_{sputt}(a,r)}{\tau_0} \cdot \frac{\mu_g n_g(0) m_H Z_d}{\langle m_d \rangle} \left[\frac{g(r)}{f(r)}\right] \left(\frac{a^{-k}}{k-1}\right) \tag{6.11}$$

This relation is valid only at distances in which the sputtering time does not exceed the age of the cluster. For the Coma cluster this is true only in the central 3–4 Mpc region, outside of which the dust is not effectively sputtered, and the dust density monotonically increases if continuously ejected by the galaxies (Dwek et al., 1990). The resulting radial profile is shown in figure 6.2.

Equation 6.11 shows that, since $\tau_{sputt} \propto a^{-1}$, steady state ICM dust has a size distribution $n_d(a) \propto a^{-(k+1)}$, which makes it different from the newly injected MNR distribution $n_{d,i}(a) \propto a^{-k}$. A second characteristic of the steady state dust distribution is the radial dependence $g(r)/f(r)$ which reflects the distribution of the dust sources (the galaxies) and destructors (the gas).

### 6.1.4 Dust properties

Equation 2.77 shows that the cooling rate necessary to derive the thermodynamics of grains, depends on the dust Planck averaged absorption efficiency. This quantity depends on the optical properties of the dust, and thus on its composition and grain size.

Opacities for dust in Active Galactic Nuclei (AGNs) have been derived by Laor & Draine (1993) by applying Mie theory to model grains in the $5 \cdot 10^{-3}$–10 $\mu$m size, over the 1000 $\mu$m–1 Å range. The optical constants are available for silicates, graphite and SiC, and have been derived by fitting the observed spectra of AGNs from the IR to X.

We have computed the Planck averaged absorption efficiency of silicates and graphite in order to provide the cooling rates of carbonaceous and oxidic dust having different sizes. Our grain size range have been restricted to the $1 \cdot 10^{-3}$–0.1 $\mu$m interval, on a grid made of 41 points. For small grains, $Q_\nu(a) \sim a$, and thus $Q_P/a$ is roughly constant. For $\lambda \gtrsim 20$ $\mu$m, $Q_\nu \sim \lambda^{-2}$, and thus equation 2.79 gives $Q_P(a,t)/a \propto \lambda^2$. This power-law is valid in our grain size range for low temperatures, where the black body emission is peaked at short wavelength. An example of Planck averaged absorption efficiency for dust grains having $a \simeq 0.01$ $\mu$m is given in figure 6.3.

A second ingredient which is used to compute the grain radiative cooling time is their heat capacity (see equation 2.81), which is available as a fit for

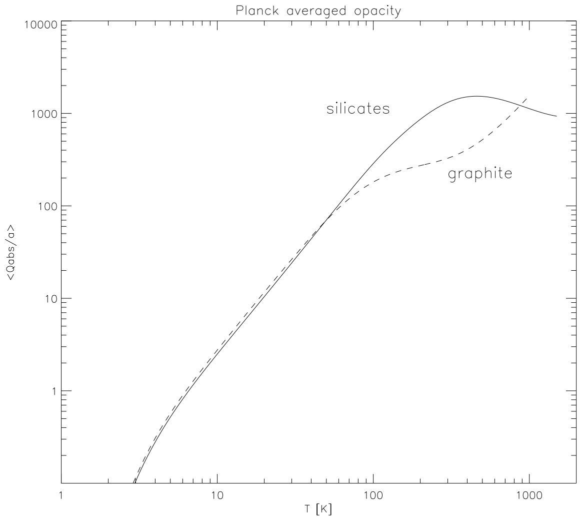

FIG. 6.3.— Planck averaged opacity for Laor & Draine (1993) silicate and graphite grains (the grains size $a$ is in cm).

laboratory data. We have used the power-laws given by Dwek (1986) for graphite grains, and by Draine & Anderson (1985) for silicates.

## 6.2 Temperature distribution

The thermodynamical status of ICM dust is determined by the balance between radiative cooling and heating. Two heating mechanisms prevails: radiative heating by the background radiation flux in the cluster, and collisional heating due to the electrons of the ICM plasma (see section 2.3.4). If the radiative heating due to the background can be considered continuous, collisional heating depends on the timescales $\tau_{coll}$ between two successive grain - electron collisions. If $\tau_{coll} \gtrsim \tau_{cool}$ the grains receive from the gas enough energy to maintain a constant equilibrium temperature, while in the opposite case ($\tau_{coll} \ll \tau_{cool}$) the grains temperature oscillates at each collision.

This section describes our implementation of the model developed by Dwek (1986). First the equilibrium temperature for grains continuously heated is evaluated, and then a method to compute the statistical temperature distribution of stochastically heated grains is explained, and applied to the case of the Coma cluster.

### 6.2.1 Equilibrium temperature

The equilibrium temperature for collisional heated dust is given by equating the total heating rate provided by the collisions and by the radiation background $H_{coll}(T_d) + H_0(T_0)$, with the radiative cooling rate $\Lambda_{rad}(T_d)$. The background heating rate is in general given by two components: a low energy background caused by the Cosmic Microwave Background Radiation (CMBR), and a high energy flux due to the cluster X-ray emission:

$$H_0 = F_X + 4\pi a^2\, Q_P(T_{CMBR})\, \sigma T_{CMBR}^4 \tag{6.12}$$

The collisional heating rate is given by equation 2.73, and depends on the gas parameters ($T_e$ and $n_e$), the grain size $a$ and the critical energy $E_*$ which regulates the absorption of energy from the colliding electron. For high gas temperatures $E_*/kT_e \gg 1$ the integral in equation 2.73 can be solved with an analytical approximation, giving $H_{coll} \propto a^2 n_g E_*^{3/2}$. Since $E_* \propto a^{2/3}$, then $H_{coll} \propto a^3 n$.

The cooling rate is given by equation 2.77. Using the approximation of the Planck averaged absorption efficiency valid for small grains and low temperatures ($Q_P(a, T_d) \propto aT_d^2$), one has $\Lambda_{rad} \propto a^2\, T_d^4\, Q_P(a, T_d) \sim a^3 T_d^6$.

In thermal equilibrium, heating and cooling rate are equal. Neglecting the contribution of the background flux, in this approximation the equilibrium temperature is independent by the grain size and the gas temperature, and is only a function of the gas density. The complete calculation of this result was given by Dwek (1987):

$$T_{eq} \simeq 57\mathrm{K}\, n_g^{1/6} \tag{6.13}$$

with $n_g$ in cm$^{-3}$, and for $T_e \gtrsim 3 \cdot 10^7$ K. We have tested this relation by solving the equilibrium temperature equation for $T_e$ in the interval $10^6$–$10^9$ K, and $n_e \sim 10^{-6}$–$10^{-2}$ cm$^{-3}$. The result is shown in figure 6.4. Even though the approximate solution is in the same range of temperature of the exact computation, a certain spread of the equilibrium temperatures is still present, in function of the gas temperature $T_e$.

Figure 6.4 shows that the equilibrium temperature of ICM dust heated by hot ICM gas goes from $\sim T_{CMBR}$ to 40 K. When the X-ray background flux is added, this temperature can be higher, but our calculations show that the main heating factor are the collisions with the gas.

Note that with dust temperatures in this range, the peak of emission would be in the far-IR or millimetric. However,this is not always the case. When the collisions are sporadic and the temperature of the grains is allowed

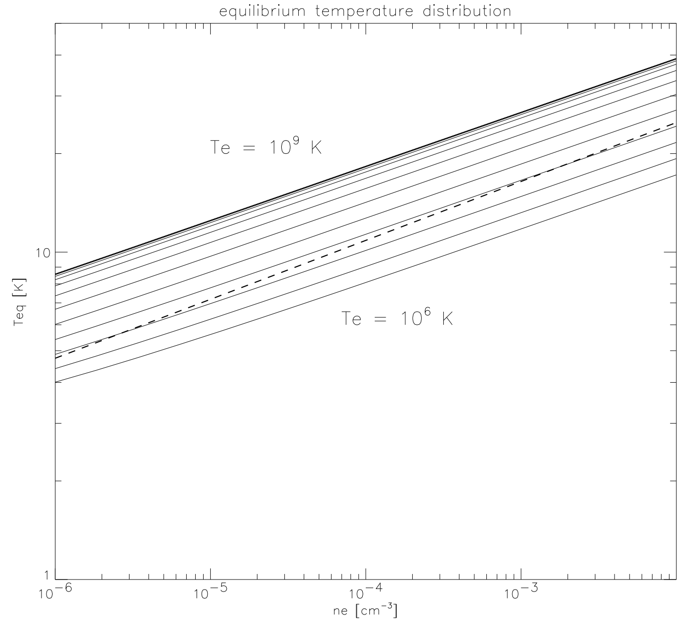

FIG. 6.4.— Equilibrium temperature for ICM dust, computed on a logarithmic grid of electron kinetic temperatures from $10^6$ to $10^9$ K. The dashed line is the Dwek (1987) approximation in equation 6.13.

to oscillate, a statistical distributions is extablished, as shown in the next section.

### 6.2.2 Stochastic heating

When the cooling time is much shorter than the interval between collisions of gas particles with the grains, thermodynamical equilibrium cannot be established. In this situation, the idea of "equilibrium temperature" does not make sense anymore, since different grains at different times will not have the same temperature. The only quantity that can be defined in these conditions is a *probability* that a grain of given size $a$ will have temperature $T_d$ when observed.

Assume that, at time $t_0$, a dust grain of size $a$ is at temperature $T_i$. Then a collision with a free plasma electron occurs, and a fraction $\zeta(E)$ of the impact energy $E$ is transferred to the lattice of the grain. The final temperature $T_f$, that is a function of the electron energy and the initial status of the grain, is given by the following equation:

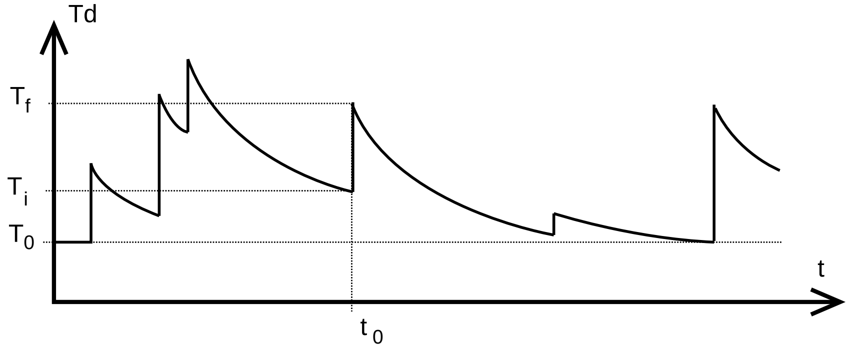

FIG. 6.5.— Temperature oscillations of a stochastically heated dust grain.

$$E\zeta(E) = \int_{T_i}^{T_f} c_V(T)\,\mathrm{d}T \tag{6.14}$$

After the collision, the grain cools down asymptotically toward the minimum temperature $T_0$ set by the background, until a new scatter raises again its temperature to a different value $T'_f$, according to the energy of the new electron (see figure 6.5).

The rate at which the grain cools down to the minimum temperature $T_0$ is given by equation 2.80. Since the heat capacity $c_V \propto a^3$ and the Plank averaged absorption efficiency $Q_P \propto a$, this cooling time does not depend on the grain size $a$:

$$\tau_{cool} \sim \frac{c_V(T_d)}{a^2\, Q_P(a, T_d)} \sim const(a) \tag{6.15}$$

The expected cooling time for silicate and graphite grains ranges from $10^5$ s (for $T_f \sim 10$ K) to $10^{-1}$ s (for $T_f \sim 1000$ K). The expected collision time for ICM with $T_e \sim 10^8$ K and $n \sim 10^{-3}$ cm$^{-3}$ is $\sim 10^3$ s, for grains with $s \sim 5 \cdot 10^{-2}$ $\mu$m. Only larger grains (which have a larger cross section and heat capacity) will experience enough collisions to reach thermal equilibrium with the gas. Smaller grains are instead heated to higher $T_f$ (smaller $c_V \propto a^3$), and cool down to lower temperature before another collision (due to their smaller cross sections). These small grains are not in equilibrium with the rest of the ICM.

The fraction of the time spent by a grain cooling down from $T_d + \mathrm{d}T_d$ to $T_d$ with respect to the collision time is given by (Purcell, 1976):

$$P_E(a, T_d)\,\mathrm{d}T_d = \frac{\mathrm{d}t}{\tau_{coll}}\, e^{-\frac{\tau_{cool}}{\tau_{coll}}} \tag{6.16}$$

The probability that a grain of size $a$ is heated to a certain temperature $T_d$ from $T_i$ is obtained by averaging $P_E$ over the flux distribution of the incident electrons:

$$\mathbb{A}_{T_i,T_d} = \langle P_E(a, T_d)\rangle_{nva^2 f(E)} \tag{6.17}$$

For a Maxwellian kinetic temperature distribution of the ICM gas (equation 2.71), the explicit expression of the *transition matrix* $\mathbb{A}(T_d, T_i)$ is:

$$\mathbb{A}_{T_i,T_d} = \theta(T_d) \int_0^\infty e^{-\int_{T_d}^{T_f(x,T_i)} \theta(T)\,\mathrm{d}T} x e^{-x}\,\mathrm{d}x \tag{6.18}$$

where $x = E/kT_e$ and $\theta(T)\mathrm{d}T$ is the *fractional cooling rate*:

$$\theta(T)\mathrm{d}T = \frac{\mathrm{d}T}{\tau_{coll}} \left|\frac{\mathrm{d}T}{\mathrm{d}t}\right|^{-1} \tag{6.19}$$

The transition matrix $\mathbb{A}(T_d, T_i)$ computes the temperature distribution of the grains after one collision, for a grain population of initial temperature $T_i$:

$$g^{(k)} \equiv G(a, T_d; T_i) \rightarrow g^{(k+1)} = \mathbb{A}g^{(k)} \tag{6.20}$$

After many collisions ($k \rightarrow \infty$), the grain population reaches a "steady state" $g \equiv G(a, T_d)$ in which their temperature distribution does not change after another collision:

$$(1 - \mathbb{A})g = 0 \tag{6.21}$$

This final state is called *stochastic temperature distribution*, and gives the probability $G(a, T_d)\,\mathrm{d}T$ that a grain of size $a$, in *statistical equilibrium* with the ICM gas, has the temperature $T_d$.

### 6.2.3 Numerical approach

An iterative method to compute the "steady state" stochastic distribution $G(a, T_d)$ has been proposed by Dwek (1986). One starts from a stochastic distribution $g^{(0)} = \delta_{T_0,T_i}$ in which grains with all sizes are at the minimum temperature $T_0$. Then a distribution $g^{(1)}$ is derived by applying the transition matrix to $g^{(0)}$. In other words, this is equivalent to compute the distribution of the grains after one single collision:

$$g^{(1)} = g^{(0)}\,\mathbb{A}_{T_i,T_d} = \delta_{T_0,T_i}\,\mathbb{A}_{T_i,T_d} \tag{6.22}$$

The process is repeated by applying $\mathbb{A}$ to the result of the previous iteration, until convergence is achieved:

$$g^{(k)} = \mathbb{A}\,g^{(k-1)} \to G(a, T_d) \qquad \text{for}\, k \to \infty \tag{6.23}$$

The main computational problem consists mainly in computing the transition matrix $\mathbb{A}$. This requires solving the integral 6.18 for all the combinations of $T_i$ and $T_f$, ranging from the minimum temperature $T_0$ to the dust sublimation temperature $T_{subl}$, and for each grain size $a$. Since the problem scales as $N_T^2$, it is necessary to limit the size of the temperature grid, in order to maintain the required computation time at a reasonable level. We used a logarithmic grid for $a$ and $T_d$, with $N_a = 11$ and $N_{T_d} = 256$.Once the transition matrix is evaluated, one can perform as many iterations as necessary, since the time required for that scales linearly.

The iterations are done only when necessary, i.e. when the collisional time is shorter than the cooling time (the grain does interact with the gas more than once in its lifetime). In the other cases, which are typical of very small grains (with negligible cross sections) only the first iteration is required. For larger grains, a heuristic criteria to determine the number of required iteration is given by:

$$n_{it} \lesssim \frac{\tau_{cool}(T_{eq})}{\tau_{coll}} \tag{6.24}$$

The iterations may be stopped before reaching $n_{it}$, in case the difference between two successive distribution is less than the allowed precision.

The integrand over $x$ in equation 6.18, should be set to zero when the final temperature $T_f$ is high enough to destroy the grain ($T_F \gtrsim T_{subl}$, see figure 6.6). In this case the grain is removed from the population, and should not contribute to the final statistical distribution. The values of $x$ for which this happens depend on the respective values of the critical energy $E_*$ with the sublimation energy $kT_{subl}$. To ensure high precision in the integration, without increasing the computation time, the integration is done on an adaptive grid $N_x = 512$ only where the integrand is not zero, and the zero points are computed with a semi-analytic formula.

Since the transition matrix for each set of parameters is evaluated independently, the problem is easily parallelizable, and ideally scales with the number of CPUs that are employed. We have thus written a parallel version of the program, running either using the parallel library MPI (Message

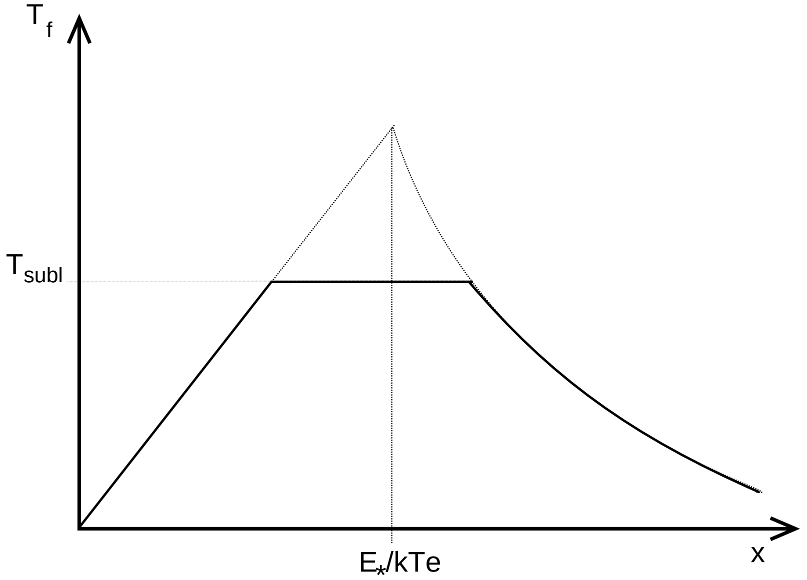

FIG. 6.6.— Final grain temperature as a function of incident electron energy. For $x = E_*/kT_e \gtrsim T_{subl}$ the grain is destroyed, and its contribution to the statistical equilibrium of temperatures should be removed.

Passing Interface, Gropp et al. 1999) or PVM (Parallel Virtual Machine, Geist et al. 1994). The code is able to compute a full grid of 15 $T_e$,$n_e$ pairs (e.g. the status of the the ICM gas in 15 radial annuli from the center of a cluster) in about 6 hours, with the SISSA SP2 cluster using 15 nodes.

### 6.2.4 Modeling results

As a benchmark test for the numerical code, we have computed the stochastic temperature distributions for silicate and graphite dust in the case of the Coma cluster. The radial size-density distribution was evaluated by using equation 6.11, and the ICM gas temperature and density profiles with equations 6.4 and 6.3. The X-ray background flux was estimated by using equation 6.2. The distributions $G(a, T_d)$ have been computed on a logarithmic radial grid of 15 points, from the center of the cluster, to 5 Mpc.

The equilibrium temperatures of the grains are given in table 6.1, for different distances from the center of the cluster, and for different grain-sizes. Note that $T_{eq}$ is largely independent from $a$, as found by Dwek (1987).

A selection of the dust stochastic temperature distributions is shown in figure 6.7 for silicates, and 6.8 for graphite.

Table 6.1 Dust equilibrium temperature for Coma cluster.

| Radius | $T_{eq}$ [K] silicate dust | | | $T_{eq}$ [K] graphite dust | | |
|---|---|---|---|---|---|---|
| (Mpc) | 0.001 $\mu$m | 0.01 $\mu$m | 0.01 $\mu$m | 0.001 $\mu$m | 0.01 $\mu$m | 0.01 $\mu$m |
| 0.00 | 29.3 | 30.2 | 30.2 | 30.6 | 30.7 | 30.7 |
| 0.20 | 28.0 | 30.0 | 30.0 | 29.4 | 29.4 | 29.4 |
| 0.26 | 27.3 | 28.3 | 28.3 | 28.7 | 28.8 | 28.8 |
| 0.33 | 26.4 | 27.4 | 27.4 | 27.8 | 27.8 | 27.8 |
| 0.42 | 25.3 | 26.2 | 26.2 | 26.7 | 26.7 | 26.6 |
| 0.54 | 23.9 | 24.8 | 24.8 | 25.2 | 25.3 | 25.2 |
| 0.69 | 22.3 | 23.3 | 23.1 | 23.7 | 23.7 | 23.5 |
| 0.88 | 20.7 | 21.6 | 21.4 | 22.0 | 22.0 | 21.8 |
| 1.13 | 19.0 | 19.2 | 19.6 | 20.3 | 20.3 | 19.9 |
| 1.45 | 17.4 | 18.2 | 17.7 | 18.7 | 18.7 | 18.1 |
| 1.86 | 15.9 | 16.7 | 15.9 | 17.1 | 17.1 | 16.2 |
| 2.38 | 14.5 | 15.2 | 14.2 | 15.6 | 15.6 | 14.4 |
| 3.05 | 13.3 | 13.8 | 12.5 | 14.3 | 14.2 | 12.7 |
| 3.90 | 12.1 | 12.5 | 10.9 | 13.0 | 12.8 | 11.0 |
| 5.00 | 11.0 | 11.3 | 9.3 | 11.8 | 11.6 | 9.5 |

Note the flat shape of the small grain distributions, which are peaked at a temperature close to $T_0$, but have a long tail reaching high temperatures, up to $T_{subl}$. This high temperature tail is responsible to a broadening of the emission spectra, which is important due to the dominance of the size distribution towards small grains.

Large grains, as expected, tend instead to the equilibrium temperature. The larger the grain radius, and the more the temperature distribution resembles a $\delta$-function peaked to the equilibrium temperature $T_{eq}$:

$$G(a, T_d) = \begin{cases} \delta(T_d - T_0) & \text{for } a \rightarrow 0 \\ \delta(T_d - T_{eq}) & \text{for } a \rightarrow \infty \end{cases} \tag{6.25}$$

Note also the dependence of the $G(a, T_d)$ shape on the dust gas temperature and density: in the more external regions of the cluster, where the gas is colder and more rarefied, even large dust grains cannot experience enough collisions to approach the equilibrium temperature, resulting in broader temperature distributions.

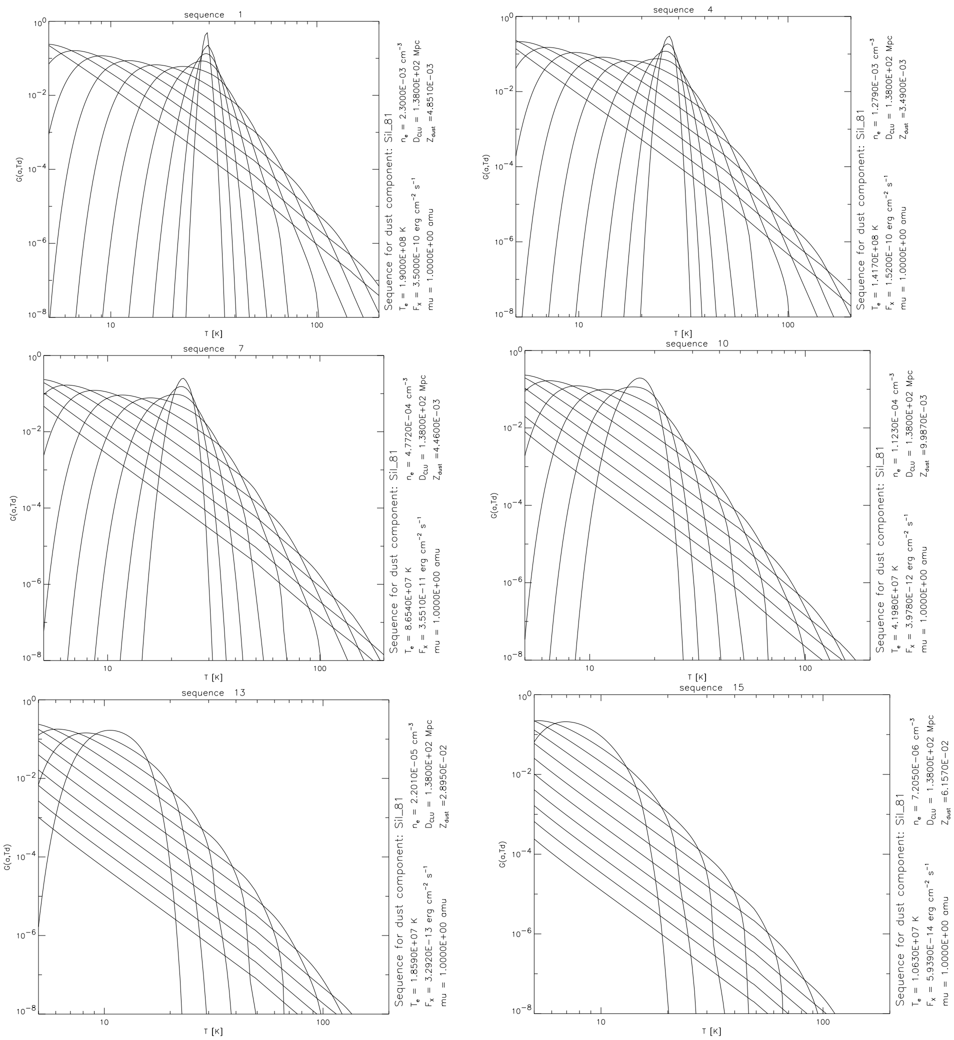

FIG. 6.7.— Stochastic temperature distribution for silicate grains, computed for various annuli from the center of the Coma cluster. Each curve corresponds to a particular grain size, from $a \simeq 0.001$ $\mu$m (flat distribution) to 0.1 $\mu$m (peaked distribution). The ICM parameters are written on the side of each panel.

As a test we tried to run the same sequence without the X-ray background flux, finding that the contribution of the X-ray to the temperature distribution is of the order of 1 K in the minimum temperature $T_0$. This confirms that the energy balance of the ICM dust is dominated by the collisions with the hot gas.

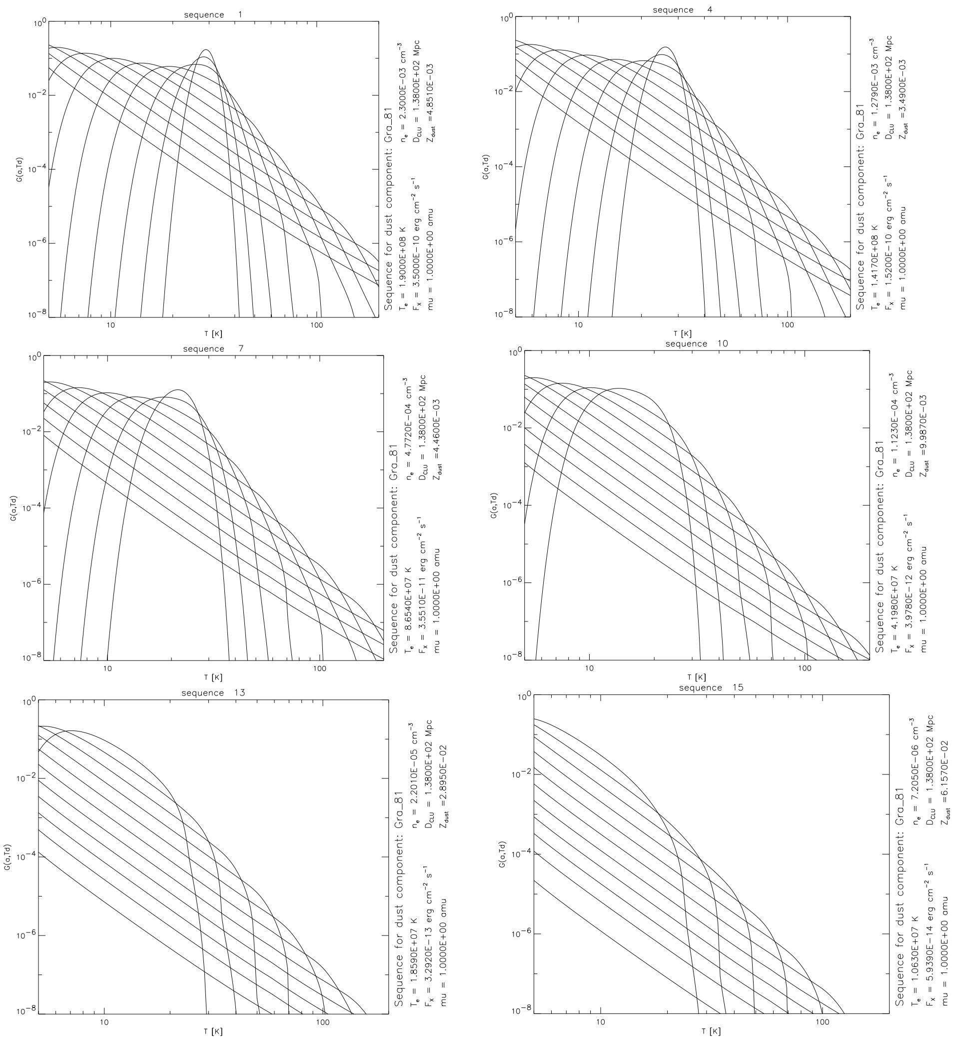

FIG. 6.8.— Stochastic temperature distribution for graphite grains, computed for various annuli from the center of the Coma cluster. Each curve corresponds to a particular grain size, from $a \simeq 0.001$ $\mu$m (flat distribution) to 0.1 $\mu$m (peaked distribution). The ICM parameters are written on the side of each panel.

## 6.3 Possible applications

The numerical code here developed is able to compute with excellent accuracy and efficiently the stochastic temperature distribution of dust in hot plasma, subjected by a background radiation field. The most direct application of the code is to compute the spectrum and IR - millimetric surface brightness of a real cluster, given a map of the temperature and density of the gas, with arbitrary geometry.

In spherical geometry the intensity of the dust radiation can be calculated by extending equation 2.31 to the stochastic temperature case. In optically thin conditions:

$$I_\nu(y) = \int \mathrm{d}\ell \int \mathrm{d}a\, \pi a^2\, Q_\nu(a)\, n_d(a,\ell)\, \langle B_\nu(T_d)\rangle \tag{6.26}$$

where the Planck emissivity is substituted with its average on the statistical distribution $G(a, T_d)$:

$$\langle B_\nu(T_d)\rangle = \int_0^\infty G(a,T_d)\, B_\nu(T_d)\, \mathrm{d}T_d \tag{6.27}$$

Note that in equation 6.26 $Q\nu(a) \sim a$, $n_d(a,\ell) \sim a^{1-k}$ for steady state dust injection from the galaxies, and $n_d(a,\ell) \sim a^{-k}$ for unique episode of sudden injection. In the two cases the emissivity is:

$$I_\nu \propto \begin{cases} a^{4-k} \sim a^{1/2} & \text{for steady state dust injection} \\ a^{3-k} \sim a^{-1/2} & \text{for sudden injection} \end{cases} \tag{6.28}$$

This result shows that from the IR - millimetric spectra of ICM dust it is possible to infer the origin of the dust, and test the interactions between the ISM of the cluster's galaxies, and the ICM. For the Coma cluster the expected flux is of the order of $10^{-1}$ mJy at 10 $\mu$m and $10^3$ mJy at 100 $\mu$m, which is above the expected sensitivity of the SIRTF photometers.

Another interesting application is to test the effect which dust emission has on the Sunyaev-Zel'dovich (SZ) effect (Sunyaev & Zel'dovich, 1972). The SZ effect is a consequence of Compton scattering of CMBR photons by the hot ICM gas, which results in a characteristic spectral signature. As a consequence of the comptonization of the CMBR, the cluster becomes a "positive" radiation source in the sub-millimeter band, and a "negative" one at larger wavelengths.

This effect is of cosmological interest because it serves as a probe of intracluster gas and its evolution and, when combined with X-ray observations, can be used to estimate the Hubble constant, independent of the distance ladder (Birkinshaw & Hughes, 1994). The SZ effect has been measured in numerous clusters of galaxies, and in particular in the Coma cluster (Herbig et al., 1995; Silverberg et al., 1997).

The measurement of the SZ effect at radio frequencies is complicated by the presence of weak background sources, which may lead to significant systematic errors of either sign. At millimetric wavelengths, high quality ground-based measurements have been obtained using different techniques with an array of detectors (Wilbanks et al., 1994), or with balloon-borne instruments (Cheng et al., 1994). Given the temperature distribution of ICM dust a certain contribution to the effect from the dust should be expected at millimetric wavelengths.

This contribution can be evaluated as follows. The comptonization parameter of the radiation along the line of sight is a function of the gas density and temperature:

$$y = \left(\frac{k\sigma_T}{mc^2}\right) \int n_e \, T_e \, \mathrm{d}\ell \tag{6.29}$$

The difference in the CMBR intensity at a frequency $\nu$, along different line of sight $\ell$, then is (Rephaeli, 1995):

$$\Delta I = \frac{2\,(kT_{CMBR})^3}{(hc)^2} g(x) \Delta y \tag{6.30}$$

where $x = h\nu / kT_{CMBR}$ and

$$g(x) = \frac{x^4 e^x}{(e^x - 1)^2} \left[x \coth\left(\frac{x}{2}\right) - 4\right] \tag{6.31}$$

By using the equations 6.3 and 6.4 it is is possible to compute $\Delta I$, and then compare its spectrum with the spectrum of the expected dust emissions for different dust to gas mass ratios. Alternatively, the millimetric measurements of the SZ effect can be used to derive an estimate (or an upper limit) of the dust density in the cluster, providing an independent test for the survival of dust in the ICM.

# Bibliography

Aguirre, A. 1999, ApJ 525, 583

Annis, J., Jewitt, D. 1993, MNRAS 264, 593

Bachiller, R. 1996, ARA&A 34, 111

Bachiller, R., Martín-Pintado, J., Planesas, P. 1991, A&A 251, 639

Baines, M.J., Williams, I.P., Asebismo, A.S. 1965, MNRAS 130, 63

Bally, J., Lada, C.J. 1983, ApJ 256, 824

Barnard, E.E. 1913, ApJ 38, 501

Barthès, D., Mattei, J.A. 1997, AJ 113, 373

Becker, S.A., Iben, I. Jr. 1979, A&A 232, 831

Begemann, B., Dorschner, J., Henning, T., Mutschke, H., Thamm, E. 1994, ApJ 423, L71

Birkinshaw, M., Hughes, J.P. 1994, ApJ 420, 33

Blöcker, T., Schönberner, D. 1991, A&A 244, 43

Bogart, R.S., Wagoner, R.V. 1973, ApJ 181, 609

Boyle, B.J., Fong, R., Shanks, T. 1988, MNRAS 231, 879

Bregman, J.N., McNamara, B.R., O'Connell, R.W. 1990, ApJ 351, 406

Bregman, J.N., Cox, C.V. 1997, in proc. *Extragalactic Astronomy in the Infrared*, G.A. Mamon, Trinh Xuan Thuan, and J. Trân Thanh Vân (eds.), Editions Frontières, Gif-sur-Yvette, p. 215 (`astro-ph/9712171`)

Briel, U.G., Henry, J.P., Böhringer, H. 1992, A&A 259, L31

Burns, M.S., Hayward, T.L., Thronson, H.A.Jr., Johnson, P.E. 1989, AJ 98, 659

Busso, M., Gallino, R., Lambert, D.L., Raiteri, C.M., Smith, V.V., ApJ 399, 218

Busso, M., Lambert, D., Beglio, L., Gallino, R., Raiteri, C.M., Smith, V.V. 1995, ApJ 446, 775

Busso, M., Origlia, L., Marengo, M., Persi, P., Ferrari-Toniolo, M., Silvestro, G., Corcione, L., Tapia, M., Bohigas, J. 1996, A&A 311, 253

Busso, M., Gallino, R., Wasserburg, G.J. 1999, ARA&A, 37, 239

Campbell, B. 1984, ApJ 287, 334

Cheng, E.S., Cottingham, D.A., Fixsen, D.J., Inman, C.A., Kowitt, M.S., Meyer, S.S., Page, L.A., Puchalla, J.L., Silverberg, R.F. 1994, ApJ 456, L71

Cherchneff, I., Barker, J.R., Tielens, A.G.G.M. 1992, ApJ 401, 269

Chiosi, C., Bertelli, G., Bressan, A. 1992, ARA&A 30, 235

Cohen, M., Walker, R.G., Witteborn, F.C. 1992, AJ 104, 2030

Cox, C.V., Bregman, J.N., Schombert, J.M. 1995, ApJS 99, 405

Cox C.V., Bregman, J.N. 1997, in *American Astronomical Society Meeting* no. 191, 106.03

Dayal, A., Hoffmann, W.F., Bieging, J.H., Hora, J.L., Deutsch, L.K., Fazio, G.G 1998, ApJ 492, 603

Dominik, C., Sedlmayr, E., Gail, H.P. 1993, A&A 277, 578

de Vancouleurs, G., de Vancouleurs, A., Corwin, H.G. Jr. 1972, AJ 77, 285

Dorschner, J., Friedemann, V., Gurtler, J. 1978, Astronomische Nachrichten, 299, 269

Dorschner, J., Henning, T. 1995, A&A Rev. 6, 271

Draine, B.T., Salpeter, E.E. 1979, ApJ 231, 77

Draine, B.T., Anderson, N. 1985, ApJ 292, 494

Dwek, E. 1986, ApJ 302, 363

Dwek, E. 1987, ApJ 322, 812

Dwek, E., Werner, M.W. 1981, ApJ 248, 138

Dwek, E., Rephaeli, Y., Mather, J.C. 1990, ApJ 350, 104

Dwek, E., Arendt, R.G. 1992, ARA&A 30, 11

Engelke, C.W. 1992, AJ 104, 1248

Fabian, A.C. 1988, *Cooling Flows in Clusters and Galaxies*, Dordrecht: Kluwer

Fabian, A.C., Johnstone, R.M., Daines, S.J. 1994, MNRAS 271, 958

Fabian, A.C. 1994(b), ARA&A 32, 277

Feast, M. 1999, in proc. "Asymptotic Giant Branch Stars", I.A.U. Symposium no. 191, eds.T. Le Bertre, A. Lèbre and C. Waelkens, p. 151

Ferguson, H.C. 1993, MNRAS 263, 343

Fleisher, A.J., Gauger, A., Sedlmayr, E. 1992, A&A 266, 321

Forrest, W.J., Shure, M.A. 1986, ApJ 311, L81

Frost, C.A., Cannon, R.C., Lattanzio, J.C., Wood, P.R., Forestini, M. 1998, A&A 332, 17

Fruchter, A.S., Hook, R.N. 1998, `astro-ph/9808087`

Gallino, R., Busso, M., Picchio, G., Raiteri, C.M. 1990, Nature 348, 298

Geist, A., Beguelin, A., Dongarra, J., Weicheng, J., Manchek, R., Sunderam, V. 1994, *PVM: Parallel Virtual Machine. A Users' Guide and Tutorial for Networked Parallel Computing*, MIT Press, Janus Kowalik (ed.), Cambridge, MA. Also at `http://www.netlib.org/pvm3/book/pvm-book.html`

Gezari, D.Y. 1993, NASA publ.

Grabelsky, D.A., Ulmer, M.P. 1990, ApJ 355, 401

Greisen, E.W., Harten, R.H. 1981, A&AS 44, 371

Griffin, I.P. 1990, MNRAS 247, 591

Gropp, W., Lusk, E., Skjwllum, A. 1999, *Using MPI - 2nd Edition. Portable Parallel Programming with the Message Passing Interface*, MIT Press.

Grøsbol, P., Harten, R.H., Greisen, E.W., Wells, D.C. 1988, A&AS 73, 359

Gunn, J.E., Gott, R. III 1972, ApJ 176, 1

Habing, H.J. 1990, *From Miras to Planetary Nebulæ: Which Path for Stellar Evolution?*, eds. M.O. Mennessier, A. Omont, p.16

Habing, H.J. 1996, ARA&A 7. 97

Hanner, M.S. 1988, NASA Conf. Pub. 3004, 22

Harten, R.H., Grøsbol, P., Greisen, E.W., Wells, D.C. 1988, A&AS 73, 365

Hartmann, L., Kenyon, S.J. 1985, ApJ 299, 426

Hasegawa, T.I., Mitchell, G.F. 1995, ApJ 451, 225

Hashimoto, O. 1995, ApJ 442, 286

Hashimoto, O., Izumiura, H., Kester, D.J.M., Bontekoe, T.J.R. 1998, A&A 329, 213

Henriksen, M.J., Mushotzky, R.F. 1986, ApJ 302, 287

Herbig, T., Lawrence, C.R., Readhead, A.C.S., Gulkis, S. 1995, ApJ 449, L5

Hoffleit, D. 1996, Journal of the AAVSO 25, no. 2

Hoffmann, W.F., Hora, J.L., Fazio, G.G., Deutsch, L.K., Dayal, A. 1998, in proc. *Infrared Astronomical Instrumentation*, A.M. Fowler (ed.), Proc. SPIE 3354, p. 647

Hoffmann, W.F., Hora, J.L. 1999, MIRAC3 User's Manual, Steward Observatory, University of Arizona, and Harvard-Smithsonian Center for Astrophysics

Höfner, S., Dorfi, E.A. 1997, A&A 319. 684

Hofner, S. 1999, in proc. "Asymptotic Giant Branch Stars", I.A.U. Symposium no. 191, eds.T. Le Bertre, A. Lèbre and C. Waelkens, p. 159

Hora, J.L., Hoffmann, W.F., Deutsch, L.K., Fazio, G.G. 1990, ApJ 353, 549

Hora, J.L., Deutsch, L.K., Hoffmann, W.F., Fazio, G.G., Shivanandan, K. 1993, ApJ 413, 304

Hora, J.L., Deutsch, L.K., Hoffmann, W.F., Fazio, G.G 1996, AJ 112, 2064

Hoyle, F., Wickramasinghe, N.C. 1969, Nature 223, 459

Hollis, J.M., Dorband, J.E., Yusef-Zadeh, F. 1992, ApJ 368, 293

Hron, J., Aringer, B., Kerschbaum, F. 1997, A&A 322, 280

Hu, E.M. 1992, ApJ 391, 608

Hubble, E. 1926, ApJ 64, 321

Hubble, E 1934, ApJ 79, 8

IRAS Catalogues and Atlases, Atlas of Low Resolution Spectra, IRAS Science Team 1986, A&AS 65, 607

IRAS Catalogues and Atlases, Catalogue of Point Sources, IRAS Science Team 1986, IPAC

IRAS Catalogs and Atlases, vol.1, Explanatory Supplement 1988, ed. C. Beichman, G. Neugerbauer, H.J Habing, P.E. Clegg, T.J. Chester, NASA RP-1190, Washington D.C.:GPO

Iben, I. Jr. 1991, ApJS 76, 55

Iben, I. Jr., Renzini, A. 1983, ARA&A 21, 271

Icke, V., Franck, A., Heske, A. 1992, A&A 258, 341

Irrgang, P., Balega, Y.Y., gauger, A. Osterbart, R., Schniggenberg, G., Weigelt, G. 1998, poster P4-08 presented at the I.A.U. Symposium no. 191 on Asymptotic Giant Branch Stars, Montpellier, France, Aug 28-Sept 1, 1998

Ivezić, Ž., Elitzur, M. 1995, ApJ 445, 415

Ivezić, Ž., Elitzur, M. 1997, MNRAS 287, 799

Ivezić, Ž., Knapp, G.R. 1998, `astro-ph/9812421`

Ivezić, Ž., Nenkova, M., Elitzur, M. 1999, *User Manual for DUSTY*, University of Kentucky Internal Report, available at `http://www.pa/uky.edu/∼moshe/dusty/`

Jackson, J.D. 1962, *Classical Electrodynamics, Second Edition*, J. Wiley, New York

Jones, M., Merrill, K.M. 1976, ApJ 389, 400

Jones A.P., Tielens, A.G.G.M, Hollenbach, D.J., McKee, C.F. 1994, ApJ 433, 797

Jones, A.P., Tielens, A.G.G.M. 1994 in *The Cold Universe*, T. Montmerle, Ch.J. Lada, I.F. Mirabel, J. Trân Thanh Vân (eds.), Editions Frontières, Gif-sur-Yvette, p. 35

Jura, M., Kleinmann, S.G. 1992, ApJS 83, 329

Justtanont, K., Tielens, A.G.G.M. 1992, ApJ 389, 400

Karachentsev, I.D., Lipovetskii, V.A. 1969, SvA 12, 909

Karovska, M., Hack, W., Raymond, J., Guinan, E. 1997, ApJ 482, L175

Kent, S.M., Gunn, J.E. 1982, ApJ 87, 945

Kerschbaum, F., Hron, J. 1992, A&A 263, 97

Kerschbaum, F., Hron, J. 1996, A&A 308, 486

Kim, S.H., Martin, P.G., Hendry, P.D. 1994, ApJ 442, 164

King, I.R. 1966, AJ 71, 64

King, I.R. 1971, PASP 83, 199

Kholopov, P.N., Samus, N.N., Frolov, M.S., Goranskij, V.P., Gorynya, N.A., Karitskaya, E.A., Kazarovets, E.V., Kireeva, N.N., Kukarkina, N.P., Kurochkin, N.E., Medvedeva, G.I., Pastukhova, E.N., Perova, N.B., Rastorguev, A.S., Shugarov, S.Y. 1988, Combined General Catalogue of Variable Stars, 4.1 Ed (II/214A)

Kwok, S., Purton, C.R., Fitzgerald, P.M. 1978, ApJ 219,125

Lada, C.J., Thronson, H.A.Jr., Smith, H.A., Schwartz, P.R., Glaccum, W. 1984, ApJ 286, 302

Lagage, P.O., Jouan, R., Masse, P., Mestreau, P., Tarrius, A. 1992, in proc. *42nd ESO Conf. on "Progress in Telescope and Instrumentation Technologies"*, M.H. Ulrich (ed.), ESO-Munich, p. 601

Lane, A.P. 1989, in proc. ESO Workshop on *Low Mass Star Formation and Pre-Main Sequence Objects*, Bo Reipurth (ed.), Garching bei München: ESO, p. 331

Laor, A., Draine, B.T. 1993, ApJ 401, 441

Le Bertre, T., Winters, J.M. 1998, A&A 334, 173

Lebtzer, Th., Hron, J. 1999, A&A 351, 533

Little, S.J., Little-Marenin, I.R., Bauer, W.H. 1987, AJ 94, 981

Little-Marenin, I.R. 1986, ApJ 307, L15

Little-Marenin, I.R., Little, S.J. 1988, ApJ 333,305

Little-Marenin, I.R., Little, S.J. 1990, AJ 99, 1173

Lopez, B., Mékarnia, D., Lefèvre, J. 1995, A&A 296, 752

Lopez, B., Danchi, W.C., Bester, M., Hale, D.D.S., Lipman, E.A., Monnier, J.D., Tuthill, P.G., Townes, C.H., Degiacomi, C.G., Geballe, T.R., Greenhill, L.J., Cruzalebes, P., Lefevre, J., Mekarina, D., Mattei, J.A., Nishimoto, D., Kervin, P.W. 1997, ApJ 488, 807

Loreta, E. 1934, Astron. Nachr. 254, 151

Loup, C., Forveille, T., Omont, A., Paul, J.F. 1993, A&AS 99, 291

Lucy, L.B. 1974, AJ 79, 745

Mamon, G.A., Glassgold, A.E., Huggins, P.J. 1988, ApJ 328, 797

Maoz, D. 1995, ApJ 455, L115

Marengo, M., Canil, G., Silvestro, G., Origlia, L., Busso, M., Persi, P. 1997, A&A 322, 924

Marengo, M., Busso, M., Silvestro, G., Persi, P., Lagage, P.O. 1999, A&A 348, 501

Marengo, M., Busso, M., Fazio, G.G., Ivezić, Ž. 2000, in proc, *The Changes in Abundances in Asymptotic Giant Branch Stars*, Mem. SAIt., 71, 615

Marengo, M., Fazio, G.G., Hora, J.L, Hoffmann, W.F., Dayal, A., Deutsch, L.K. 2000(b), in proc. *Asymmetrical Planetary Nebulæ II: From Origins to Microstructures*, ASP Conference Series, Vol. 199, 2000, J.H. Kastner, N. Soker & S. Rappaport (eds.)

Marengo, M., Jayawardhana, R., Fazio, G.G., Hoffmann, W.F., Hora, J.L., Dayal, A., Deutsch, L.K. 2000(c), ApJ 541, L63

Marengo, M., Ivezić, Ž., Knapp, G.R. 2001, MNRAS 324, 1117

Matteucci, F., Gibson, B.K. 1995, A&A 304, 11

Mathis, J.S., Rumpl, W., Nordsieck, K.H. 1977, ApJ 217, 425

Mathis, J.S. 1990, ARA&A 28, 37

Mauron, N., Huggins, P.J. 1999, A&A 349, 203

Meixner, M., Ueta, T., Dayal, A., Hora, J.L., Fazio, G.G., Hrivnak, B.J., Skinner, C.J., Hoffmann, W.F., Deutsch, L. 1999, ApJS 122, 221

Mihalas, D. 1978, in *Stellar Athmospheres*, W.H Freeman (ed.), San Francisco, ch. 2

Minchin, N.R., Hough, J.H., McCall, A., Aspin, C., Hayashi, S.S., Yamashita, T., Burton, M.G. 1991, MNRAS 251, 508

Mitchell, G.F., Hasegawa, T.I., Schella, J. 1992, ApJ 386, 604

Moffat, A.F.J. 1969, A&A 3, 455

Monnier, J.D., Tuthill, P.G., Danchi, W.C., Haniff, C. 1998, AAS Meeting 191, 114.05

Mushotzky, R.F., Serlemitsos, P.J., Smith, B.W., Boldt, E.A., Holt, S.S. 1978, ApJ 225, 21

Neri, R., Kahane, C., Lucas, R., Bujarrabal, V., Loup, C. 1998, A&AS 130, 1

Ney, E.P. 1977, Science 195, 541

Nuth, J.A.III, Hecht, J.H. 1990, Ap&SS 163, 79

Omont, A., Loup, C., Forveille, T., te Lintel Hekkert, P., Habing, H., Silvagnanam, P. 1993, A&A 267, 515

Onaka, T., de Jong, T., Willems, F.J. 1989, A&A 218, 169

Ossenkopf, V., Henning, Th., Mathis, J.S. 1992 A&A 261, 567

Paczynzki, B. 1970, Acta Astron. 20, 47

Pégourié, B. 1988, A&A 194, 335

Perryman, M.A.C., Lindegren, L., Kovalevsky, J., Hoeg, E., Bastian, U., Bernacca, P.L., Crézé, M., Donati, F., Grenon, M., van Leeuwen, F., van der Marel, H., Mignard, F., Murray, C.A., Le Poole, R.S., Schrijver, H., Turon, C., Arenou, F., Froeschlé, M., Petersen, C.S. 1997, A&A 323, L49

Persi, P., Ferrari-Toniolo, M., Marenzi, A.R., Busso, M., Corcione, L., Ferrari, A., Gai, M., Nicolini, G., Racioppi, F., Robberto, M., Shivanandan, K., Tofani, G. 1994, Exp. Astr. 5, 363

Persi, P., Ferrari-Toniolo, M., Marenzi, A.R., Busso, M., Corcione, L., Marengo, M., Tapia, M. 1995, Ap&SS 224, 535

Poetzel, R., Mundt, R., Ray, T.P. 1992, A&A 262, 229

Pudritz, R.E., Norman, C.A. 1983, ApJ 274, 677

Purcell, E.M. 1976, ApJ 206, 685

Reimers, D. 1975, Mem. Soc. Roy. Sci. Liege $6^{th}$ Ser., 8, 369

Reipurth, B. 1989, Nature 340, 42

Reipurth, B., 1999, *A General Catalog of Herbig-Haro Objects*, available electronically at `http://casa.colorado.edu/hhcat`

Rephaeli, Y. 1995, ARA&A 33, 541

Renzini, A., Fusi Pecci, F. 1988, ARA&A 26, 199

Renzini, A., Voli, M. 1981, A&A 94, 175

Richardson, W.H. 1972, J. Opt. Soc. Am. 62, 55

Romani, R.W., Maoz, D. 1992, ApJ 386, 36

Roth, J. 1983, in *Sputtering by Particle Bombardment II*, ed R. Berisch, p. 91, Springer-Verlag, Berlin

Rowan-Robinson, M. 1980, ApJS 44, 403

Sackmann, I.-J., Boothroyd, A.I. 1992, ApJ 392, 71

Sahai, R., Trauger, J.T., Watson, A.M., Stapelfeldt, K.R., Hester, J.J., Burrows, C.J., Ballister, G.E., Clarke, J.T., Crisp., D., Evans, R.W., Gallagher, J.S.III, Griffiths, R.E., Hoessel, J.G., Holtzman, J.A., Mould, J.R., Scowen, P.A., Westphal, J.A. 1998, ApJ 493, 301

Salpeter, E.E. 1974, ApJ 193, 585

Silverberg, R.F., Cheng, E.S., Cottingham, D.A., Fixsen, D.J., Inman, C.A., Kowitt, M.S., Meyer, S.S., Page, L.A., Puchalla, J.L., Rephaeli, Y. 1997, ApJ 485, 22

Scalo, J.M., Haff, P.K., Switkowski, Z.E., Tombrello, T.A. 1977, Phys. Lett. 70B, 137

Seares, F.H. 1940, PASP 52, 80

Sedlmayr, E. 1994, in *Molecules in the Stellar Environment*, U.G. Jørgensen (ed.), Springer, Berlin, p. 163

Shu, F.H., Ruden, S.P., Lada, C.J., Lizano, S. 1991, ApJ 370, 31

Simpson, J.P. 1991, ApJ 368, 570

Sloan, G.C., Price, S.D. 1995, ApJ 451, 758

Sloan, G.C., Price, S.D. 1998, ApJS 119, 141

Smith, M.D., Brand, P.W.J.L. 1990, MNRAS 245, 108

Smith, V.V., Lambert, D.L. 1989, ApJ 345, L75

Snell, R.L., Loren, R.B., Plambeck, R.L. 1980, ApJ 239, 17

Sopka, R.J., Hildebrand, R., Jaffe, D.T., Gatley, I., Roellig, T., Werner, M., Jura, M., Zuckerman, B. 1985, ApJ 294, 242

Speck, A.K. 1998, Ph.D. Thesis, University College London, Gower Street, London WC1N 1AS

Speck, A.K., Hofmeister, A.M., Barlow, M.J. 1999, ApJ 513, L87

Spitzer, L. 1978, *Physical processes in the Interstellar Medium*, Wiley, New York

Steffen, M., Szczerba, R., Schoenberner, D. 1998, A&A 337, 149

Stencel, R.E., Nuth, J.A.III, Little-Marenin, I.R, Little, S.J. 1990, ApJ 350, L45

Stetson, P. 1987, PASP 99, 191

Straniero, O., Gallino, R., Busso, M., Chieffi, A., Raiteri, C.M., Limongi, M., Salaris, M. 1995, ApJ 440, 85

Staniero, O., Chieffi, A., Limongi, M., Busso, M., Gallino, R., Arlandini, C. 1997, ApJ 478, 332

Sudol, J.J., Dyck, H.M., Stencel, R.E., Klebe, D.I., Creech-Eakman, M.J. 1999, AJ 117, 1609

Sugimoto, D. 1971, Progr. Theor. Phys. 45, 761

Sunyaev, R.A., Zel'dovich, Y.B. 1972, Comments Ap. Space Phys 4, 173

Tamura, M., Gatley, I., Joyce, R.R., Ueno, M., Suto, H., Sekiguchi, M. 1991, ApJ 378, 611

Tamura, M., Yamashita, T. 1992, ApJ 391, 710

Tielens A.G.G.M. 1989, in *Interstellar Dust*, L.J. Allamandola, A.G.G.M. Tielens (eds.), I.A.U. Symp. 135, Kluwer, Dordrecht, p. 239

Torrelles, J.M., Ho, P.T.P., Rodríguez, L.F., Cantó, J. 1989, ApJ 343, 222

Trumpler, R.J. 1940, ApJ 91, 186

Tuchman, Y. 1999, in proc. "Asymptotic Giant Branch Stars", I.A.U. Symposium no. 191, eds. T. Le Bertre, A. Lèbre and C. Waelkens, p. 123

Ueta, T., Meixner, M., Bobrowsky, M. 2000, ApJ 528, 861

Uus, U. 1970, Nauch. Inform. Acad. Nauk. 17, 3

van de Hulst, H.C. 1957, *Light Scattering by Small Particles*, Wiley, New York

van der Tak, F.F.S., van Dishoeck, E.F., Evans, N.J.II, Bakker, E.J., Blake, G.A. 1999, ApJ 522, 991

van der Veen, W.E.C.J., Habing, H.J. 1988, A&A 194, 125

Vardya, M., de Jong, T., Willems, F. 1986, ApJ 304, L29

Vassiliadis, E., Wood, P.R. 1993, ApJ 413, 641

Volk, K., Kwok, S. 1988, ApJ 331, 435

Weigelt, G., Balega, Y., Blöcker, T., Fleisher, A.J., Osterbart, R., Winters, J.M. 1998, A&A 311, L61

Wallerstein, G., Knapp, G.R., 1998, ARA&A 36, 369

Waters, L.B.F.M., Molster, F.J., de Jong, T., Beintema, D.A., Waelkens, C., Boogert, A.C.A., Boxhoorn, D.R., de Graauw, T., Drapatz, S., Feuchtgruber, H., Genzel, R., Helmich, F.P., Heras, A.M., Huygen, R., Izumiura, H., Justtanont, K., Kester, D.J.M., Kunze, D., Lahuis, F., Lamers, H.J.G.L.M., Leech, K.J. Loup, C. lutz, D., Morris, P.W., Price, S.D. Roelfsema, P.R., Salama, A., Schaeidt, S.G., Tielens, A.G.G.M., Trams, N.R., Valentijn, E.A., Vandenbussche, B., van den Ancker, M.E., van Dishoeck, E.F., van Winckel, H., Wesselius, P.R., Young, E.T. 1996, A&A 315, L361

Wells, D.C., Greisen, E.W., Harten, R.H. 1981, A&AS 44, 393

Wilbanks, T.M., Ade, P.A.R., Fisher, M.L., Holzapfel, W.L., Lange, A.E. 1994, ApJ 427, 75

Willems, F.J., de Jong, T. 1986, ApJ 309, L39

Windsteig, W., Dorfi, E.A., Höfner, S., Hron, J., Kerschbaum, F. 1997, A&A 324, 617

Winters, J.M., Dominik, C., Sedlmayr, E. 1994, A&A 288, 255

Winters, J.M. 1998, Ap&SS 255, 257

Wise, M.W., Michael, W., O'Connell, R.W., Bregman, J.N., Roberts, M.S. 1993, ApJ 405, 94

Wolf, N.J., Ney, E.P. 1969, ApJ 155, L181

Wood, P.R., Sebo, K.M. 1996, MNRAS 282, 958

Wood, P.R. Alcock, C., Allsman, R.A., Alves, D., Axelrod, T.S., Becker, A.C., Bennet, D.P., Cook, K.H., Drake, A.J., Freeman, K.C., Griest, K., King, L.J., Lehner, M.J., Marshall, S.L., Minniti, D., Peterson, B.A., Pratt, M.R., Quinn, P.J., Stubbs, C.W., Sutherland, W., Tomaney, A., Vandehei, T., Welch, D.L. 1999, in proc. “Asymptotic Giant Branch Stars”, I.A.U. Symposium no. 191, eds.T. Le Bertre, A. Lèbre and C. Waelkens, p. 151

Young, K., Phillips, T.G., Knapp, G.R. 1993, ApJS 86, 517

Zwicky, F. 1933, Helv. Phys. Acta 6, 110

Zwicky, F. 1957, PASP 69, 518

# Index